

INFORMATION TO USERS

This manuscript has been reproduced from the microfilm master. UMI films the text directly from the original or copy submitted. Thus, some thesis and dissertation copies are in typewriter face, while others may be from any type of computer printer.

The quality of this reproduction is dependent upon the quality of the copy submitted. Broken or indistinct print, colored or poor quality illustrations and photographs, print bleedthrough, substandard margins, and improper alignment can adversely affect reproduction.

In the unlikely event that the author did not send UMI a complete manuscript and there are missing pages, these will be noted. Also, if unauthorized copyright material had to be removed, a note will indicate the deletion.

Oversize materials (e.g., maps, drawings, charts) are reproduced by sectioning the original, beginning at the upper left-hand corner and continuing from left to right in equal sections with small overlaps. Each original is also photographed in one exposure and is included in reduced form at the back of the book.

Photographs included in the original manuscript have been reproduced xerographically in this copy. Higher quality 6" x 9" black and white photographic prints are available for any photographs or illustrations appearing in this copy for an additional charge. Contact UMI directly to order.

UMI

A Bell & Howell Information Company
300 North Zeeb Road, Ann Arbor MI 48106-1346 USA
313/761-4700 800/521-0600

A STUDY OF THE β -DELAYED NEUTRON DECAY OF ^{14}Be

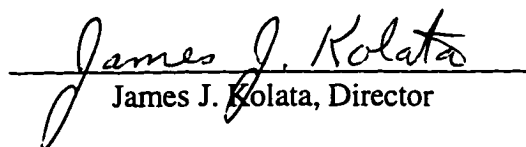
A Dissertation

Submitted to the Graduate School
of the University of Notre Dame
In Partial Fulfillment of the Requirements
of the Degree of

Doctor of Philosophy

by

Michael David Belbot, B.S., M.S.


James J. Kolata, Director

Department of Physics
Notre Dame, Indiana
September 1996

UMI Number: 9701129

UMI Microform 9701129
Copyright 1996, by UMI Company. All rights reserved.
This microform edition is protected against unauthorized
copying under Title 17, United States Code.

UMI
300 North Zeeb Road
Ann Arbor, MI 48103

A STUDY OF THE
 β -DELAYED NEUTRON DECAY OF ^{14}Be

Abstract

by

Michael David Belbot

Two experiments were performed to investigate the β -delayed neutron spectroscopy of ^{14}Be , at the National Superconducting Cyclotron Laboratory at Michigan State University and at the Institute for Physical and Chemical Research (RIKEN) in Wako, Saitama, Japan. Our motivation was that the neutron spectroscopy of ^{14}Be had not previously been measured. Since this nucleus is so far from stability, it is believed to have unusual structure, and a study of its β decay can provide important tests of the shell-model.

In both experiments, a pulsed ^{14}Be beam was stopped so that the activity was accumulated while the beam was on and the decay was measured while the beam was off. Individual neutron groups were measured using plastic scintillators to measure the neutron flight time. Gamma-neutron coincidence was measured by using high purity germanium γ -ray detectors. Beta-delayed charged-particle decays were also measured in the RIKEN experiment using silicon-surface barrier detectors.

Almost all of the ^{14}Be neutron emission corresponds to a very strong group with a branching ratio and $\log ft$ measured to be $82 \pm_{31}^4\%$ and $3.70 \pm_{0.04}^{0.20}$, respectively.

Michael David Belbot

We determined that the width of the final state was 60 ± 5 keV, and the half-life of ^{14}Be was 4.36 ± 0.13 ms. A much weaker neutron group was also measured with branching ratio and $\log ft$ equal to $0.29 \pm 0.12\%$ and $5.67 \pm 0.15_{0.24}$, respectively. Insufficient statistics were obtained to see γ - n coincidence. A charged-particle group was observed but is believed to be due a known daughter decay. The $\log f_1 t$ (first-forbidden) corresponding to $0n$ emission has been estimated and was found to be much stronger than similar transitions in other nuclei. Several possible explanations are presented.

The results are discussed and compared to shell-model calculations that agree rather well with the measurements. The techniques of the two experiments are compared and recommendations for improvement are made. The most important elements of future work include a more reliable determination of detection efficiencies, more coincidence statistics, a renewed search for charged-particle decays, and better shell-model calculations.

TABLE OF CONTENTS

CHAPTER 1 INTRODUCTION	1
1.1 Beta decay	1
1.2 Nuclear Shell-Model	4
1.2.1 Infinite spherical potential	4
1.2.2 Harmonic oscillator potential	6
1.2.3 Intermediate form and spin-orbit potential	8
1.2.4 Parity and angular momentum coupling	10
1.2.5 Shell-model calculations for particle-hole configurations	12
1.3 Fermi Theory of Decay	13
1.5 Isobaric Analog State	24
1.6 Beta-delayed Neutron Decay	26
1.7 Background Information on ^{14}Be	28
CHAPTER 2 EXPERIMENTAL METHOD FOR THE NSCL EXPERIMENT ..	31
2.1 Radioactive Beam Production at the NSCL	31
2.2 The NSCL Neutron Detector Array and Associated Hardware	35
2.3 Beam-on/Beam-off Duty Cycles	41
2.4 Real Time Clock	44
2.5 Calibration Runs	44
2.5.1 Gamma-ray calibration	44
2.5.2 Time-of-flight calibration run	46
2.5.3 ^{17}N calibration run	46
2.5.4 Pu-Be calibration run	46
2.6 Neutron Flight Path Calibration	47

2.7 Neutron Efficiency Calibration.....	51
2.7.1 ^{17}N data points	51
2.7.2 ^{16}C data of Scheller <i>et al.</i>	53
2.7.3 Pu-Be data points	55
2.7.4 Monte Carlo calculation and determination of neutron efficiency curve.....	61
 CHAPTER 3 ANALYSIS AND RESULTS OF THE NSCL EXPERIMENT	68
3.1 Analysis of β -decay Activity	68
3.1.1 Analysis of the ungated decay curve	68
3.1.2 Analysis of the decay curve requiring β - n coincidence.....	76
3.2 Analysis of the Neutron Time-of-Flight Data.....	77
3.2.1 Calibration of the time-of-flight data.....	77
3.2.2 Fit to the raw time-of-flight spectrum.....	79
3.2.3 Correction for ^{11}Li contamination.....	83
3.3 Branching Ratios and $\text{Log}ft$ Values.....	93
3.3.1 Determination of branching ratios and $\text{log}ft$ values for $1n$ states	93
3.3.2 Determination of the branching ratio for $2n$ emission.....	96
3.4 Analysis of the γ -Ray Data	99
3.4.1 Energy calibration of the γ -ray detector.....	99
3.4.2 Detection efficiency calibration of the γ -ray detector.....	102
3.4.3 Branching ratio and $\text{log}ft$ value for the observed γ -ray state.....	107
3.5 Determination of the β -detection efficiency	110
3.6 Missing Neutrons	111
 CHAPTER 4 EXPERIMENTAL METHOD FOR THE RIKEN EXPERIMENT	113
4.1 ^{14}Be Radioactive Beam Production at RIKEN	113
4.2 The RIKEN Neutron Detector Array and Associated Hardware.....	115
4.3 Beam-on/Beam-off Duty Cycles.....	123
4.4 Calibration Runs	124

4.4.1	Gamma ray calibration.....	124
4.4.2	Time-of-flight calibration run.....	124
4.4.3	^{17}N calibration run	124
4.4.4	Energy calibration of neutron detectors.....	125
4.4.5	SSD stack energy calibration	125
4.4.6	Horizontal position calibration	126
4.5	Flight Path Determination.....	126
4.5.1	Geometrical flight path correction.....	126
4.5.2	Distance calibration	132
4.6	Neutron Detection Efficiency Calibration	133
4.6.1	Raw detection efficiency.....	133
4.6.2	Corrected neutron detection efficiency.....	140
 CHAPTER 5 ANALYSIS AND RESULTS OF THE RIKEN EXPERIMENT ...		146
5.1	Analysis of β -decay Activity	146
5.1.1	Analysis of the ungated decay curve	146
5.1.2	Analysis of the decay curve requiring β - n coincidence.....	150
5.2	Analysis of the Neutron Time-of-Flight Data.....	152
5.2.1	Calibration of the time-of-flight data.....	152
5.2.2	Fit of the low energy neutron group	153
5.3	Determination of Branching Ratio and $\text{Log}ft$ Values of Neutron States	159
5.4	Analysis of the γ -Ray Data	161
5.4.1	Energy calibration of the γ -ray detector.....	161
5.4.2	Detection efficiency calibration of the γ -ray detector.....	163
5.4.3	Branching ratio and $\text{log}ft$ value for the observed γ -ray state.....	164
5.5	Analysis of Charged-Particle Data.....	165
5.5.1	Relative gain matching of the SSD energy signals.....	165
5.5.2	Reduction of peak interference	165
5.5.3	Half-life of the charged-particle group	170

5.5.4 Absolute energy calibration of the SSD energy spectra	172
5.5.5 Branching ratio of the charged-particle group	174
5.6 Determination of the Natural Width of the Low Energy Neutron Group ..	176
CHAPTER 6 DISCUSSION AND CONCLUSION	179
6.1 Discussion of ^{14}Be Half-life.....	179
6.2 Discussion of Low Energy Neutron State.....	180
6.3 Discussion of Higher Energy Neutron States	182
6.4 Discussion of γ -ray State.....	183
6.5 Discussion of Observed Charged-particle Group	187
6.6 Discussion of Zero neutron Emission	189
6.7 Decay Scheme of ^{14}Be β decay.....	196
6.8 Comparison to Shell-model Calculation.....	197
6.9 Comparison of Experimental Methods	198
6.9.1 Neutron detectors	198
6.9.2 Implantation and start detectors	199
6.9.3 On-line monitoring of impurities	200
6.9.4 Other detectors present in the RIKEN experiment	200
6.10 Future work.....	201
6.10.1 Gamma-neutron coincidence	201
6.10.2 Neutron-neutron coincidence.....	203
6.10.3 Neutron detection efficiencies	204
6.10.4 Other improvements.....	205
6.10.5 Future experiments.....	206
6.11 Conclusion	207
APPENDIX A ELECTRONICS DIAGRAMS FOR THE NSCL EXPERIMENT	209
A.1 DIAGRAMS FOR E AND E DETECTORS	209
A.2 DIAGRAM OF IMPLANTATION DETECTOR ELECTRONICS	210
A.3 DIAGRAM FOR NEUTRON ARRAY DETECTORS.....	211

A.4 DIAGRAM FOR HP-Ge γ -RAY DETECTOR.....	212
A.5 DIAGRAM FOR ELECTRONICS ASSOCIATED WITH THE MASTER GATE.....	213
A.6 DIAGRAM OF ELECTRONICS ASSOCIATED WITH THE CPU AND THE CYCLOTRON-RF	214
A.7 DEFINITION OF TERMS AND SYMBOLS USED IN APPENDIX A.....	215
APPENDIX B REFERENCES FOR γ -RAY SOURCES.....	216
APPENDIX C ELECTRONICS DIAGRAMS OF THE RIKEN EXPERIMENT	217
C.1 ELECTRONICS DIAGRAM FOR START (BETA) DETECTORS	217
C.2 ELECTRONICS DIAGRAM FOR THE SSD STACK.....	218
C.3 ELECTRONICS ASSOCIATED WITH F2 AND F3 SCINTILLATORS.....	219
C.4 ELECTRONICS ASSOCIATED WITH NEUTRON AND VETO DETECTORS.....	220
C.5 ELECTRONICS ASSOCIATED WITH HP Ge DETECTOR.....	221
C.6 ELECTRONICS ASSOCIATED WITH BEAM-ON AND -OFF SIGNALS	222
C.7 DEFINITION OF NEW TERMS USED IN APPENDIX C.....	223
REFERENCES	224

LIST OF TABLES

1.1 SELECTION RULES FOR β DECAY	21
2.1 SETTINGS FOR HIGH ACCEPTANCE MODE OF A1200.....	33
2.2 LIST OF ABSORBERS.....	37
2.3 PURITY OF BEAM	39
2.4 CALIBRATED γ -RAY LINES IN NIST SOURCE.....	45
2.5 CENTROID, VELOCITY, AND CALIBRATED DISTANCE FOR ^{17}N NEUTRON PEAKS	50
2.6 YIELD AND NEUTRON DETECTION EFFICIENCY FOR ^{17}N PEAKS	54
2.7 CALIBRATED DISTANCE OF STANDARD DETECTOR (^{17}N PEAKS) ..	57
2.8 NEUTRON EFFICIENCY AND RELATED INFORMATION FOR EACH ENERGY BIN.....	61
3.1 BEAM-ON AND -OFF ACTIVITIES.....	73
3.2 RAW ^{14}Be NEUTRON PEAKS	83
3.3 RAW ^{11}Li NEUTRON PEAKS	84
3.4 CORRECTED ^{11}Li NEUTRON PEAKS.....	88
3.5 CORRECTED ^{14}Be NEUTRON PEAKS.....	92
3.6 BRANCHING RATIOS AND $\log ft$ VALUES OF CORRECTED ^{14}Be NEUTRON GROUPS	93
3.7 THE a_n USED TO CALCULATE $\log ft$ VALUES FOR THE β DECAY OF ^{14}Be	94
3.8 CORRECTION FACTORS FOR THE RADIOACTIVE DECAY OF SOURCES	105
3.9 γ -RAY DETECTION EFFICIENCY.....	105
4.1 MAXIMUM SETTINGS FOR RIPS.....	114
4.2 PURITY OF BEAM	119
4.3 CALIBRATED DISTANCE CORRESPONDING TO ^{17}N NEUTRON PEAKS.....	133

4.4	INFORMATION REGARDING FIT OF ^{17}N PEAKS.....	134
4.5	^{17}N NEUTRON DETECTION EFFICIENCY	139
4.6	CORRECTED ^{17}N DETECTION EFFICIENCIES	144
5.1	INFORMATION REGARDING ^{14}Be NEUTRON PEAKS	155
5.2	BRANCHING RATIOS AND $\text{Log}ft$ VALUES OF NEUTRON GROUPS.....	160
5.3	VARIOUS WIDTHS ASSOCIATED WITH THE ^{17}N NEUTRON PEAKS.....	177

LIST OF FIGURES

1.1	(a) The energy levels determined from a infinite spherical potential well. The circled numbers are the number of particles required to close major shells. The labeling of a sub-shell is on the left and its degeneracy is on the right. (b) Same as Fig. 1.1a but for a harmonic oscillator potential [Kr88e].	7
1.2	Wood-Saxon [Wo54] potential for a nucleus with $A = 14$. The symbol R_0 is the mean radius, and the skin thickness is defined as the distance in which the potential changes from $-0.9V_0$ to $-0.1V_0$.	8
1.3	(a) Energy levels corresponding to the potential of Fig. 1.2. The labeling is the same as Fig. 1.2 except that the cumulative number of nucleons is at the extreme right. (b) Same as Fig. 1.3a but with the spin-orbit interaction added. The expressions below each column of numbers gives a general expression for the degeneracy [Kr88f].	9
1.4	The shell-model configuration for the ^{14}B ground state. Occupied states (filled circles) are called particles and empty states (open circles) are called holes. The symbols π and ν are abbreviations for protons and neutrons as indicated above.	11
1.5	Plots of various β -decay energy distributions: (a) a fictitious distribution for $Z = 29$ and endpoint energy (E_0) = 1.0 MeV without the correction for the nuclear Coulomb field, (b) the energy distribution of the β^- decay of ^{64}Cu ($E_0 = 0.5782$ MeV [Ha79]), (c) the energy distribution of the β^+ decay of ^{64}Cu ($E_0 = 1.67449$ MeV [Ha79]).	18
1.6	Plot of experimentally measured $\log ft$ values versus the number of reported cases for each order of forbiddenness [Kr88g].	24
1.7	Hypothetical decay scheme for ^{14}Be showing the energetics of β -delayed neutron decay. The dashed-lines indicate the neutron thresholds.	27
1.8	The predicted level scheme of the β decay of ^{14}Be given in [Cu88].	30
2.1	Diagram of A1200 Beam Analysis Device [Sh91].	33
2.2	Schematic of NSCL neutron detector array [Ha91].	36

2.3	Diagram of the hardware located at the center of the NSCL array [Ha91].	37
2.4	Plot of the timing signal referenced to the cyclotron RF (TOF) versus energy loss in the ΔE detector.	40
2.5	Same as Fig. 2.4 but gated on the E-veto detector.	40
2.6	Typical time-of-flight spectrum for ^{14}Be data.	43
2.7	Time-of-flight spectrum for ^{17}N data.	50
2.8	Plot of raw ^{17}N decay spectrum (bottom histogram) and that corrected for dead time (top).	54
2.9	Refit of the ^{16}C data of K. W. Scheller <i>et al.</i> [Sc94]. The energies of the peaks here and below are clearly shown (including the ^{17}N impurity).	56
2.10	A refit of the ^{17}N data Scheller <i>et al.</i> [Sc94].	56
2.11	Plot of light output vs. neutron energy (calculated from time-of-flight) in the standard detector for the ^{17}N data.	58
2.12	Plots of the time-of-flight spectra of the standard detector [a] and array detector [b] (sum of all 15) for the Pu-Be source.	60
2.13	Plot of neutron energy versus light output for neutron detectors. Note that the line a, as shown in Fig. 2.11, is very difficult to determine here.	62
2.14	Plot of the measured neutron efficiency data points and the fit (solid line) obtained from KSUEFF. The dashed lines are the best estimate of the error in the fit due to the error in the threshold.	62
2.15	Plot of the χ^2 as a function of the threshold of the neutron detectors. The histogram is the χ^2 curve and the bold line is a quadratic fit to that curve using the program XVGR (see text).	65
2.16	Plot of the light output of the neutron detectors measured by R. Harkewicz [Ha91] for a ^{60}C and ^{134}Cs γ -ray source. The position of the Compton edge and the method of finding the resolution are shown for the plot of the ^{60}Co source.	67
3.1	Fit of the raw 40 ms beam-off β -decay spectrum showing the parent, daughter, impurity, and background components.	75
3.2	Fit of the decay curve requiring β - n coincidence and using the 10 ms beam-off data.	77
3.3	Figure 3.3 Typical time calibration spectrum (detector 1 right). The sharp	

spikes are 10 ns apart, and listed at the top of the figure are the time and centroids of these peaks. (See text for more details.)	79
3.4 Raw 10 ms beam-off activity spectrum showing the location of the lower gate required to eliminate direct beam contaminants from the beam-off data. ...	80
3.5 Schematic showing the geometry of a typical neutron decay. The symbol "PM" is an abbreviation for photomultiplier. Note that the diagram is not drawn to scale.	81
3.6 (a) Fit of the sum of the time-of-flight spectra of all fifteen neutron detectors. (b) Time-of-flight spectrum of one of the neutron detectors (number 1) for comparison.	82
3.7 Fit of the ^{11}Li component of the decay curve where β - n coincidence has been applied.	85
3.8 Raw ^{11}Li time-of-flight spectrum obtained from Ref. [Mo93].	87
3.9 Ratio (solid line) between the neutron detection efficiency in the ^{14}Be experiment to that of the ^{11}Li experiment.	91
3.10 Time-of-flight spectrum for the sum of all 15 neutron detectors with ^{11}Li contamination removed.	92
3.11 Plot of γ -ray energy calibration points as a function of channel number. The solid line is a linear fit to these points (see text).	100
3.12 (a) Measured centroids versus difference between an unweighted linear fit and the accepted energies for the γ -ray energy calibration points. (b) A similar fit using a quadratic function. The dashed lines represent the statistical uncertainty in each fit.	101
3.13 Fit of γ -ray peak due to daughter decay of ^{14}Be (see text).	102
3.14 Plot of γ -ray detection efficiency as a function of γ -ray energy (see text for details).	108
4.1 Diagram of the RIPS radioactive beam facility.	115
4.2 Schematic of experimental setup viewed from above with enlarged detail of the stopper (implantation detector) and the aluminum degrader. This figure is not drawn to scale, and it was, in part, obtained from [Ki93].	116
4.3 Energy spectra of SSD's 2-4 using an aluminum degrader with thickness of 300 μm tilted at 30° (see text).	118

4.4	Plot of the ratios Si_2/Si_3 and Si_3/Si_4 versus the effective degrader thickness. The angle of the aluminum degrader relative to the beam axis (see text) for each data point is also indicated.	118
4.5	Plot of the energy deposited in the F2 scintillator versus flight time between F2 and F3.	120
4.6	Same as Fig. 4.5 but gated in coincidence with the downstream β detector.	120
4.7	Diagram showing the geometry of the neutron and veto walls; it is not drawn to scale.	121
4.8	Schematic of the neutron detectors, as seen from above, showing the dimensions, geometry, and distance of these detectors from the SSD stack. ...	127
4.9	Diagram showing the geometry of a scintillator bar (as the beam sees it) and the locations of the β source used in the horizontal calibration.	128
4.10	Typical horizontal position spectrum using timing information and the function of Eq. 4.3.	130
4.11	(a) A fit of the sum of all calibrated timing position spectra from which the timing horizontal position resolution was determined (b) The same as Fig. 4.11b but corresponding to energy signals.	131
4.12	Time-of-flight spectrum of ^{17}N data showing the fit from which neutron detection efficiency was determined.	134
4.13	Plot of showing the severe distortion in the ^{17}N activity curve.	136
4.14	The ^{17}N decay curve that was fitted to obtain the total number of ^{17}N β decays. The vertical long-dashed lines indicate the regions excluded from consideration in the fit. See text for more details.	136
4.15	Plot of the energy deposited in the F2 scintillator versus flight time between F2 and F3 for the ^{17}N data.	137
4.16	Same as Fig. 4.15 but gated in coincidence with the downstream β detector.	137
4.17	(a) Plot of the corrected neutron detection efficiencies obtained from the ^{17}N data and of the fitted efficiency curve. (b) Blow up of Fig. 4.17a showing how the curves were extrapolated to zero energy to obtain the threshold in terms of neutron energy.	143

4.18	A fit to the uncorrected 0.3828 MeV ^{17}N data point (solid line) using KSUEFF [Ce79] where the dashed lines represent the systematic error and the left data point represents the corresponding efficiency at 287 keV.	145
5.1	Fit of the raw 20 ms beam-off β -decay spectrum showing the parent, daughter, impurity, and background components.	147
5.2	A diagram illustrating the difference between extendable and non-extendable dead time [Kn95e].	148
5.3	Portion of time-of-flight spectrum showing the ^{14}Be 287 keV β -delayed neutron peak as a function of elapsed time after the start of the beam-off period.	151
5.4	Plot of the decay curve requiring coincidence with the 287 keV neutron peak.	151
5.5	Portion of the time-of-flight spectrum showing the low energy neutron group at 287 keV.	154
5.6	Plot of veto time-of-flight spectrum showing the lower software cut applied to the anti-coincidence data. Events corresponding to counts located to the left of the dashed line were not eliminated.	156
5.7	(a) Plot of the neutron time-of-flight spectrum without β veto (anti-coincidence) applied. (b) Same as Fig. 5.7a but with β veto applied. Note that the channel scale has been compressed by a factor of four relative to Fig. 5.5.	157
5.8	Enlarged portion of Fig. 5.7b showing a fit to the higher energy neutron groups.	158
5.9	Plot of veto detector time-of-flight spectrum showing the ^{17}N β -delayed neutron groups.	159
5.10	A plot showing the residuals for the linear fit used to determine the energy of the observed γ -ray line. The dashed lines represent the uncertainty in the fit, and the error bars are the uncertainties in the accepted energies.	162
5.11	Fit of γ -ray peak due to daughter decay of ^{14}Be (see text).	162
5.12	Plot of the γ -ray detection efficiency as a function of γ -ray energy (see text for details).	164
5.13	A typical energy spectrum (SSD 1) showing the pedestal and pulser peak.	166

5.14	An energy spectrum of the ^{14}Be data from SSD 1 showing the various groups.	167
5.15	Diagram showing the geometry for a typical β decay and cuts used to reduce the interference caused by the β -particle peak for the type of event shown (see text).	170
5.16	(a) Plot of SSD energy spectrum after cuts were applied that reduced the interference of the β -particle peak (see text). (b) Same as Fig. 5.16a showing a fit to the charged-particle group and plotted on a vertically enlarged linear scale.	171
5.17	Fitted activity curve to the measured charged-particle data assuming a daughter decay using the procedure described in the text.	172
5.18	Fit to the charged-particle group that was used to determine its branching ratio (see text).	175
6.1	Diagram of the two possible decay schemes corresponding to the observed γ -ray decay with energy 3.680 MeV. The γ -ray intensity (I_γ) and branching ratio (p) are given where known.	184
6.2	(a) For daughter $Z = 6$, an extrapolation of the tabulated values of $\log_{10}(f_1/f_0)$ obtained from Ref. [Go71] versus β decay energy using the function given in Eq. 6.1 (see text). (b) A fit to the same values as Fig. 6.2a for the entire energy range given in [Go71], again using Eq. 6.1.	192
6.3	Plot obtained from Ref. [Al74] showing measurement of 6.73 MeV γ -ray state ("peak of interest") that has established the spin/parity of the ^{14}B ground state (see text for details).	194
6.4	Plot showing an example of adding a Gaussian distribution "simulated peak" to determine the limit in the branching ratio of an unobserved charged-particle group.	195
6.5	The 2σ upper limit in the branching ratio of an unobserved charged-particle group.	195
6.6	Decay scheme for the β decay of ^{14}Be	197

ACKNOWLEDGEMENTS

First of all I would like to thank my advisor James Kolata for his guidance, and attention to detail that made this work possible. His knowledge of and enthusiasm for physics have never ceased to amaze me. I would also like to thank him for giving me what has been a very interesting thesis project. It has been exciting to be the first to measure the neutron spectroscopy of the β decay of ^{14}Be . In this sense, my thesis project has truly been original research, and has also at times been fun.

Next I would like to thank Kent Scheller for helping with the analysis of my first thesis experiment, for the use of his half-life code `LIFE5`, and the use of his data. Special thanks goes to Chris Friedman who wrote programs to translate the data taken at the NSCL and RIKEN to an appropriate format for analysis at Notre Dame. He has been a good friend, and invaluable for maintaining our computer systems and for answering my computer questions. Good luck with your new job at IUSB, Chris; you will be missed. Thanks also go to Nori Aoi, one of my RIKEN collaborators, who answered many of my questions regarding the second experiment in this work, and who bought up many important points that became a vital part of this work. Lastly, I thank John Yurkon for helping me run the neutron detection efficiency code `KSUEFF`, and Alec Brown for his shell-model calculations.

Even though this work does not include an experiment done at Notre Dame, I have gained much experience from the experiments I have participated in our Lab. Therefore, I thank the various people that work our lab. Ed Berners and

his successor Larry Lamm have maintained the tandem VanDeGraaf accelerator, and have taught me a lot about tandem accelerators work. Jim Kaiser has maintained the electronics and computer hardware, and has taken on much extra work by becoming system administrator after Chris Friedman left. Our secretaries Pat Joblonski, who, sadly, died about a month before this acknowledgement section was written, and her successor Sandy Trobaugh have been very helpful and nice to talk to.

Next I would like to thank the various graduate students and postdocs I have met in my seven years here who have been good friends and have often been very helpful with question. Unfortunately, there are too many of you to mention here. In particular, I thank the present members of our group that have helped out in my thesis experiments and other experiments that our group has done: Pete Santi, Don Peterson, and Johannes VonSchartzenberg. I also thank the past members of our group: Rich Tighe, Bob Kryger, Won Chung, Sunil Dixit, Robin Smith, Jaimie Vega, Mohammed Zahar, and most importantly my long time officemate Ken Lamkin. Thanks for being a good friend, Ken. It was nice sharing an office with you for five and half years. Who would have ever guessed that would rejoin you again in my new job at Western Kentucky University. By the way, Ken, I'm still not going to rub your feet.

Lastly, I would like to thank my parents for their love, support and encouragement. Thanks Mother and Dad for having cancelled your vacation plans three times in trying to be here for my commencement, which kept getting delayed. It is too bad that I am defending in the middle of a school year, and most likely will not attend commencement. I am sorry that you didn't have the chance to be there.

CHAPTER 1

INTRODUCTION

In this work we report the results of two experiments in which the β -delayed neutron spectroscopy of ^{14}Be was measured. The first experiment was performed in November 1991 at the National Superconducting Cyclotron Laboratory (NSCL) at Michigan State University in East Lansing, Michigan. The second was performed in October 1993 at the Institute of Physical and Chemical Research (RIKEN) in Wako, Saitama, Japan. For brevity the first experiment shall be referred to as simply the "NSCL experiment" or the "first experiment", and the second as the "RIKEN experiment" or "second experiment". In both experiments the half-life of ^{14}Be was measured along with the energies and intensities of emitted neutrons and γ -rays from the β^- decay of this nuclide. In the RIKEN experiment, the energies and intensities of delayed charged-particle decays were also measured. First we will give an overview of on β decay, β -delayed neutron decay, and ^{14}Be . Next the experimental details and results of the NSCL experiment will be presented, followed by that for the RIKEN experiment. Lastly the two experiments will be compared, and the results of both will be discussed in the context of a shell-model calculation.

1.1 Beta decay

Beta decay is the process by which an unstable nucleus that has an excess number of neutrons or protons becomes more stable by converting one of its nucleons (neutrons or protons) from one species to another. Depending on whether neutrons or

protons are in excess, two different types of β decay processes can result [Kr88]:

$${}^A_Z X_N \rightarrow {}^A_{Z+1} X'_{N-1} + e^- + \bar{\nu}_e \quad (1.1)$$

$${}^A_Z X_N \rightarrow {}^A_{Z-1} X'_{N+1} + e^+ + \nu_e, \quad (1.2)$$

where Eq. 1.1 is β^- decay resulting from a neutron excess and Eq. 1.2 is β^+ decay resulting from a proton excess. The symbol ν_e represents the electron neutrino and $\bar{\nu}_e$ the electron anti-neutrino. In equations 1.1 and 1.2 the parent is element X with atomic number Z, atomic mass A, and neutron number N. The daughter is element X' with the same atomic mass, but an atomic number increased or decreased by one for β^- decay and β^+ , respectively. It is possible for the daughter itself to be unstable with respect to β decay (although in excited states other processes can compete with β decay, for example γ and nucleon emission). The total energy release (or Q value) resulting from β decay to the ground state is the energy equivalent of the mass difference between the initial and final states of the system. For β^- decay [Kr88]:

$$Q_{\beta^-} = [m_N(X) - m_N(X') - m_e]c^2, \quad (1.3)$$

where $m_N(X)$ is the *nuclear* mass of the parent, $m_N(X')$ is the nuclear mass of the daughter, m_e is the mass of the electron, and the neutrino is assumed to be massless. Usually the atomic masses of the neutral atoms, denoted $m(X)$, are tabulated instead of nuclear masses. We can convert from nuclear to neutral atomic masses by adding constituent energies associated with the neutral atom [Kr88]:

$$m(X)c^2 = m_N(X)c^2 + Zm_e c^2 - \sum_{i=1}^Z B_i, \quad (1.4)$$

where Z is that of the parent and B_i is the binding energy of the i th electron. Inserting Eq. 1.4 into 1.3 for both $m_N(X)$ and $m_N(X')$ gives us the following result:

$$Q_{\beta^-} = \{ [m(X) - Zm_e] - [m(X') - (Z+1)m_e] - m_e \} c^2 + \left\{ \sum_{i=1}^Z B_i - \sum_{j=1}^{Z+1} B_j \right\}. \quad (1.5)$$

If the very small difference in electron binding energy is neglected, the above reduces to

$$Q_{\beta^-} = [m(X) - m(X')]c^2 = [m(X) - m(X')] \cdot 931.502 \text{ MeV/u}, \quad (1.6)$$

where the extreme right expression can be used if the atomic masses are given in atomic mass units. If one performs the same calculation for β^+ decay, the result is [Kr88]:

$$Q_{\beta^+} = [m(X) - m(X')] \cdot 931.502 \text{ MeV/u} - 1.022 \text{ MeV}. \quad (1.7)$$

Note here the electron masses do not cancel.

Because β decay will often populate excited states in the daughter, the study of the emitted γ -rays and nucleons can reveal much information about both the β decay and the structure of the populated states of the daughter. It is difficult to learn much just by measuring the energy of the β particle, for several reasons. First, because β decay is a three-body process, the β particle and neutrino are not emitted with unique energies but rather with a broad distribution of energies. Neglecting the usually very small recoil energy of the daughter nucleus, the total kinetic energy is shared between the electron and neutrino. Second, the β particles are usually highly relativistic due to their high kinetic energies (several MeV) relative to their rest mass energy (0.511 MeV). Thus the β particles travel essentially at the velocity of light, and methods that measure the electron energy using its flight time are not very useful. Third, the neutrino itself is undetected because of its negligibly small cross section with typical solids (1.2×10^{-19} barns or 1.2×10^{-42} cm² [Kr88b]); therefore one cannot directly measure the kinetic energy carried by the neutrino. Last, precise electron energy measurements are difficult, because electrons tend to scatter out of the active volume of the detector before depositing their full energy. Large changes in direction and velocity of the electrons produce electromagnetic radiation called

bremssstrahlung (German for "braking radiation") which is often high in energy and which escapes the detector. For these reasons, much of the information regarding the emitted β particles must be inferred from γ rays and nucleons emitted in coincidence with the β decay.

1.2 Nuclear Shell-Model

In the next section regarding β decay, we shall find that this mode of decay is very important in probing the structure of the nucleus. We discuss here the "shell model", because it is one of the most successful and universal models that describes the structure of the nucleus. Nuclear physicists have found evidence of shell-model effect. At particular numbers of neutrons or protons (2, 8, 20, 28, 50, 82, 126, and 184, the "magic numbers") in the nucleus, distinct and sudden changes in various measured quantities have been observed. For example, the neutron capture cross-section (the probability that a nucleus will absorb a neutron) drops dramatically when the number of neutrons in the nucleus equals one of the magic numbers. The nuclear charge radius also changes suddenly when the number of neutrons equals a magic number. (See K. S. Krane [Kr88c].) This indicated that whenever the number of neutrons or protons equals a magic number, a very tightly bound structure is formed (the closure of a nuclear shell). In the following paragraphs we shall follow some of the treatment on this topic given by K. S. Krane [Kr88c, Kr88d].

1.2.1 Infinite spherical potential

One important question is: can one find a correct potential $V(r)$ (assumed to be dependent on only r) that when inserted into the Schödinger time-independent equation:

$$-\frac{\hbar^2}{2m}\nabla^2\psi + V(r)\psi = E\psi, \quad (1.8)$$

(where E and m are the energy and mass of the particle [nucleon], respectively) will reproduce the correct magic numbers and explain the observed phenomena? The simplest potential is a spherical infinite well, where $V(r) = 0$ for $r < a$ and $V(r) = \infty$ for $r > a$, where "a" is a constant. The absolute square of the wave function ψ gives the probability for finding the particle (nucleon) at a particular point in space, and in spherical coordinates we assume a separable solution of the form [Kr88d]:

$$\psi(r, \theta, \phi) = R(r) \Theta(\theta) \Phi(\phi). \quad (1.9)$$

Solving Eq. 1.8 for $\Phi(\phi)$, we get the following differential equation [Kr88d]:

$$\frac{d^2\Phi}{d\phi^2} + m_l^2 \Phi = 0$$

(where m_l^2 is the separation constant) with the solution [Kr88d]:

$$\Phi_{m_l}(\phi) = \frac{1}{\sqrt{2\pi}} e^{im_l\phi}. \quad (1.10)$$

Here, $m_l = 0, \pm 1, \pm 2, \dots$. We also get the following for $\Theta(\theta)$ [Kr88d]:

$$\frac{1}{\sin\theta} \frac{d}{d\theta} \left(\sin\theta \frac{d\Theta}{d\theta} \right) + \left[l(l+1) - \frac{m_l^2}{\sin^2\theta} \right] \Theta = 0, \quad (1.11)$$

with the solution [Kr88d]:

$$\Theta_{l m_l}(\theta) = \left[\frac{2l+1}{2} \frac{(l-m_l)!}{(l+m_l)!} \right]^{1/2} P_l^{m_l}(\theta), \quad (1.12)$$

where $l = 0, 1, 2, 3, \dots$ and $m_l = 0, \pm 1, \pm 2, \pm 3, \dots, \pm l$ corresponding to each respective l . The normalized functions $Y_{l m_l}(\theta, \phi) = \Theta_{l m_l}(\theta) \cdot \Phi_{l m_l}(\phi)$ are the spherical harmonics, which (see [Kr88d]) are the same for all central potentials $V(r)$, since such potentials do not depend on ϕ or θ . Thus, to obtain the energy levels only the radial equation needs to be solved [Kr88d]:

$$-\frac{\hbar^2}{2m} \left(\frac{d^2R}{dr^2} + \frac{2}{r} \frac{dR}{dr} \right) + \left[V(r) + \frac{l(l+1)\hbar^2}{2mr^2} \right] R = E \cdot R. \quad (1.13)$$

The above is solved with the help of a set of oscillatory functions known as spherical Bessel functions where we apply the condition: $j_l(ka) = 0$ (the condition that the walls are impenetrable). The functions are given by [Kr88d]:

$$j_l(kr) = \left(-\frac{r}{k}\right)^l \left(\frac{1}{r} \frac{d}{dr}\right)^l j_0(kr), \quad (1.14)$$

where $j_0 = (\sin kr)/kr$, and k is a constant. (The explicit solutions for the lowest l have been listed in [Kr88d].) Equations 1.14 are transcendental and must be solved numerically. The energy $E = (\hbar^2 k^2)/2m$, and using the zeros of the j_l [Ab65] (where $r = a$), we find the energy levels.

The resulting levels are shown in Fig. 1.1a. It is apparent that there are large gaps in the energy levels, which indicates a shell structure. The number of particles required to fill each shell is designated by the circled numbers. Note, that unlike the situation in atomic physics, the principal quantum number n does not enter into the expression for energy. This number merely counts the levels with the same value l . Also note that the energy level are not dependent on m_l either, and this results in a degeneracy equal to $2l(l + 1)$, where the factor of two results from the fact that the spin $\frac{1}{2}$ particles have an additional intrinsic degeneracy that has two values: $+\frac{1}{2}$ (spin up) or $-\frac{1}{2}$ (spin down). The quantity l is the orbital angular momentum and has been given a notation in analogy with atomic physics: s, p, d, f, g, h, i, j corresponding to $l = 0, 1, 2, 3, 4, 5, 6, 7$, respectively. Note that this potential does not reproduce all of the magic numbers, or the correct spacing between energy levels.

1.2.2 Harmonic oscillator potential

The harmonic oscillator potential is a logical next choice, because small oscillations about more complicated potentials have often been approximated with this type of potential, where $V(r) = \frac{1}{2}kr^2$. We shall not solve this problem here but direct

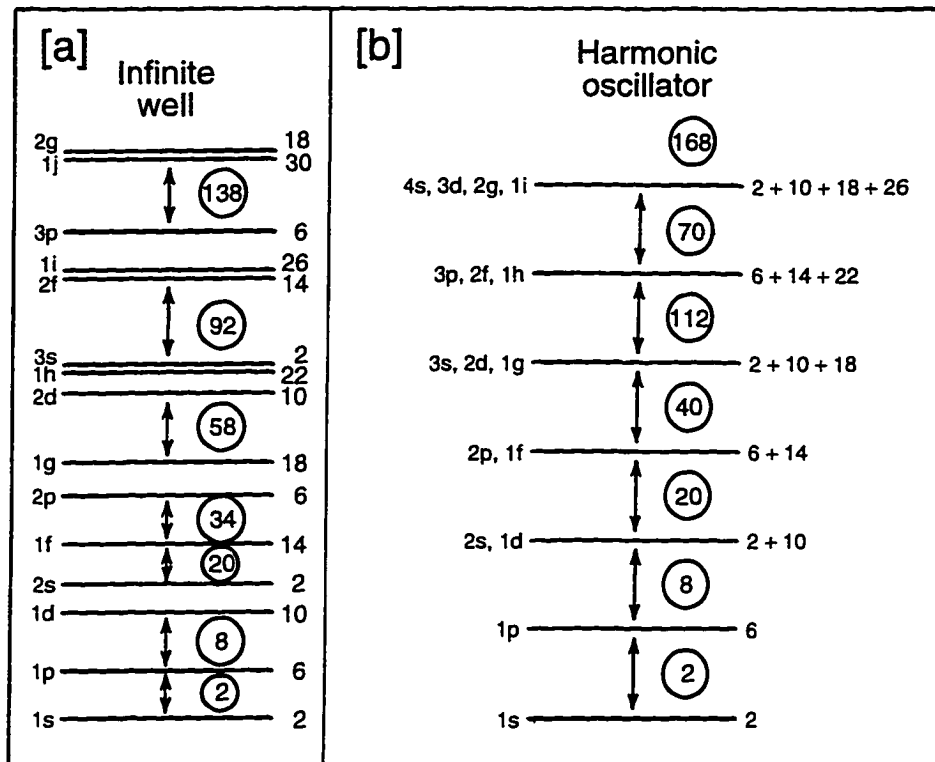


Figure 1.1 (a) The energy levels determined from a infinite spherical potential well. The circled numbers are the number of particles required to close major shells. The labeling of a sub-shell is on the left and its degeneracy is on the right. (b) Same as Fig. 1.1a but for a harmonic oscillator potential [Kr88e].

the reader to references [Wi86] and [Kr88d]. The energy levels are given by [Kr88d]:

$$E_n = \hbar^2 \omega_0 (n + \frac{1}{2}), \quad (1.15)$$

where n is a non-negative integer. The energy levels E_n do not depend on l but not all values of l are allowed. At most, $l = n$ and can only be even or odd as n is even or odd. There is an additional degeneracy of $(2l + 1)$ for each value of l , because the energy levels do not depend on m_l . This results in a total degeneracy of $\frac{1}{2}(n + 1)(n + 2)$ for each energy level. The shell structure, assignments, and degeneracies of the energy levels are shown in Fig. 1.1b. Notice that with the above two potentials only the lowest three magic numbers have been reproduced (2, 8, and 20).

1.2.3 Intermediate form and spin-orbit potential

The infinite spherical well is not satisfactory, because nuclei do not present such a sharp edge, and it requires infinite separation energies to liberate a nucleon from the nucleus. The harmonic oscillator is equally unsatisfactory, because this potential does not have a sharp enough edge and never levels off to zero at large distances from the nucleus as we expect the correct potential should. It was discovered that the following form (Wood-Saxon [Wo54]) gave the best result:

$$V(r) = \frac{-V_0}{1 + e^{[(r - R_0)/a_0]}} \quad (1.16)$$

where the parameters V_0 , R_0 , and a_0 are the well depth, mean radius, and skin thickness parameter, respectively (Fig. 1.2). Various experiments have determined that $V_0 = 50$ MeV, $R_0 = 1.22$ fm [Kr88i], and $a_0 = 0.524$ fm. The energy levels obtained from this potential are shown in Fig. 1.3a. The first three magic numbers are once again reproduced. Something had to be added to produce the other magic numbers, without making a radical change in the potential, because Fig. 1.3a is already a reasonably good representation of the level spectrum.

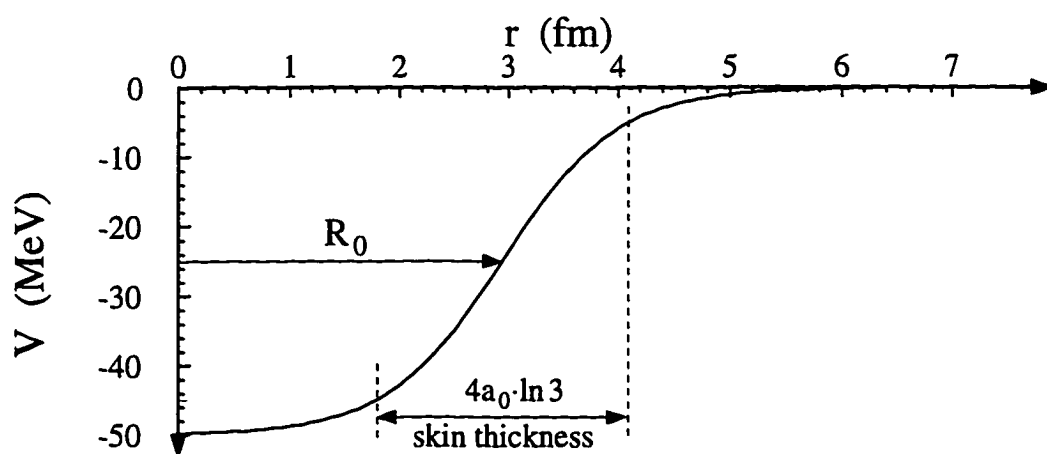


Figure 1.2 Wood-Saxon [Wo54] potential for a nucleus with $A = 14$. The symbol R_0 is the mean radius, and the skin thickness is defined as the distance in which the potential changes from $-0.9V_0$ to $-0.1V_0$.

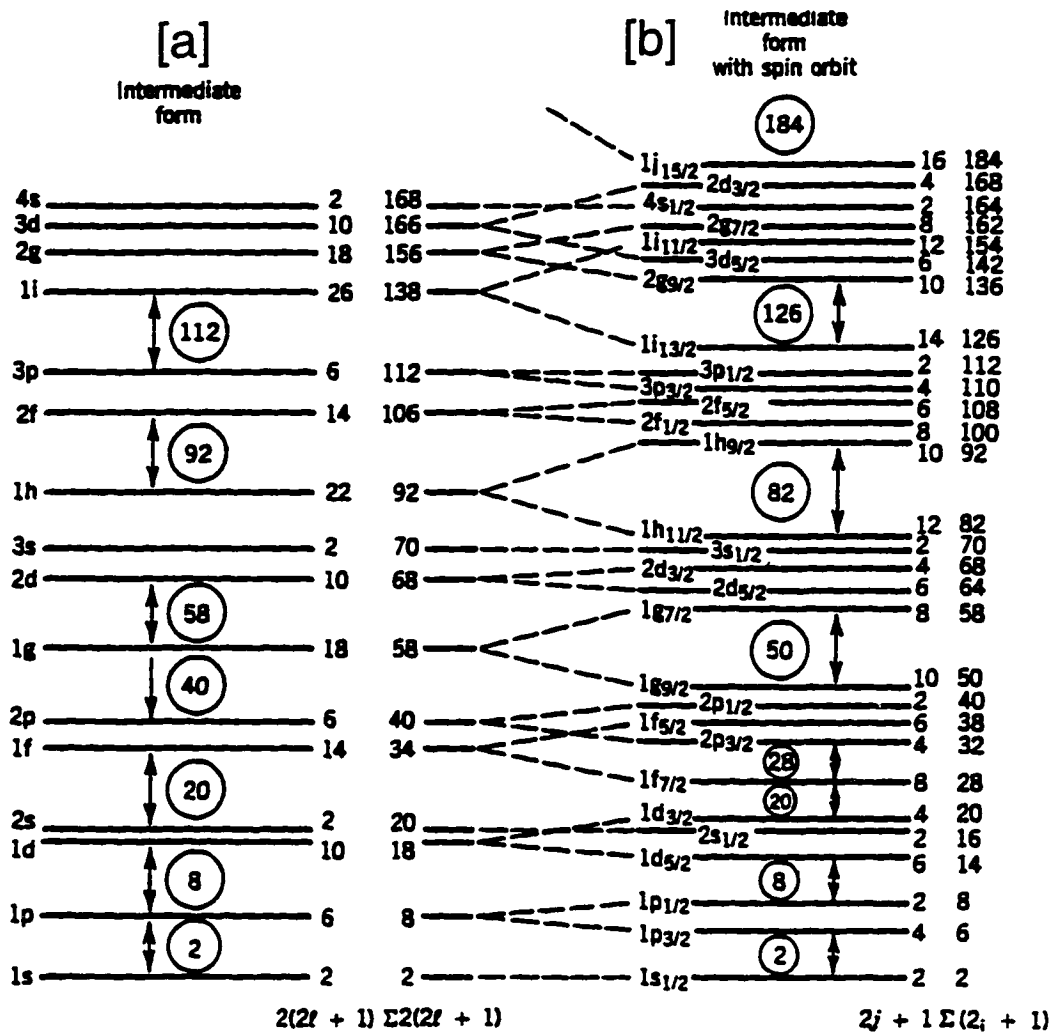


Figure 1.3 (a) Energy levels corresponding to the potential of Fig. 1.2. The labeling is the same as Fig. 1.2 except that the cumulative number of nucleons is at the extreme right. (b) Same as Fig. 1.3a but with the spin-orbit interaction added. The expressions below each column of numbers gives a general expression for the degeneracy [Kr88f].

Maxel, Haxel, Suess, and Jensen showed in 1949 that adding a spin-orbit potential gave the correct spacing to the sub-shells and reproduced the correct magic numbers (Fig. 1.3b). In atomic physics, the spin-orbit interaction is caused by the interaction of the magnetic moment of the electron with the magnetic field generated by its orbiting around the nucleus. In nuclear physics, the electromagnetic interaction would not be strong enough to produce the desired

splitting and reordering of sub-shells, but the interaction is given the same form: $V_{so}(r)l \cdot s$. The form of V_{so} is not so important, but the $l \cdot s$ is what causes the reordering of levels. The states are labeled according to their total angular momentum, where $j = l + s$. Because the neutron and proton are nonidentical particles, they are counted separately with a level scheme for each. Their assumed intrinsic spin of $\frac{1}{2}$ means that, for every value of l , there are two possible values for j : $j = l + \frac{1}{2}$ and $j = l - \frac{1}{2}$ (except for $l=0$ for which only $j = \frac{1}{2}$ is possible). For example, $l = 0$ gives only the $s_{\frac{1}{2}}$ level, but $l = 1$ gives the $p_{\frac{1}{2}}$ and $p_{\frac{3}{2}}$ levels, $l = 2$ gives the $d_{\frac{3}{2}}$ and $d_{\frac{5}{2}}$ levels, and so on. Moreover, the principal quantum number n is merely an index that counts the j levels. (Some conventions start at 1 like Fig. 1.3, others at 0, which represents the actual l value.) For a specific nucleus, it is easiest to visualize the filling of sub-shells with diagrams like Fig. 1.4. This shows the filling of the shell-model energy levels for the ground state of ^{14}B (a nuclide of interest for this thesis). Note that, in the ground state, the lowest sub-shells are completely filled before the nucleons start filling the next one above, and the total number of nucleons required to fill a sub-shell is equal to the degeneracy given in Fig. 1.3b. The arrangement of nucleons (Fig. 1.4) is known as a shell-model configuration. For each shell-model configuration there are associated wave functions ψ for both the neutrons and protons (the same one that was described in Sec. 1.2.2). More details regarding the shell model can be found in references [Kr88c] and [La80].

1.2.4 Parity and angular momentum coupling

The parity of a state or wave function $\psi(\mathbf{r})$ is defined as even or positive if $\psi(-\mathbf{r}) = \psi(\mathbf{r})$ and odd or negative if $\psi(-\mathbf{r}) = -\psi(\mathbf{r})$. Because the magnitude of the radial component of the wave function depends only on the magnitude of r , it is

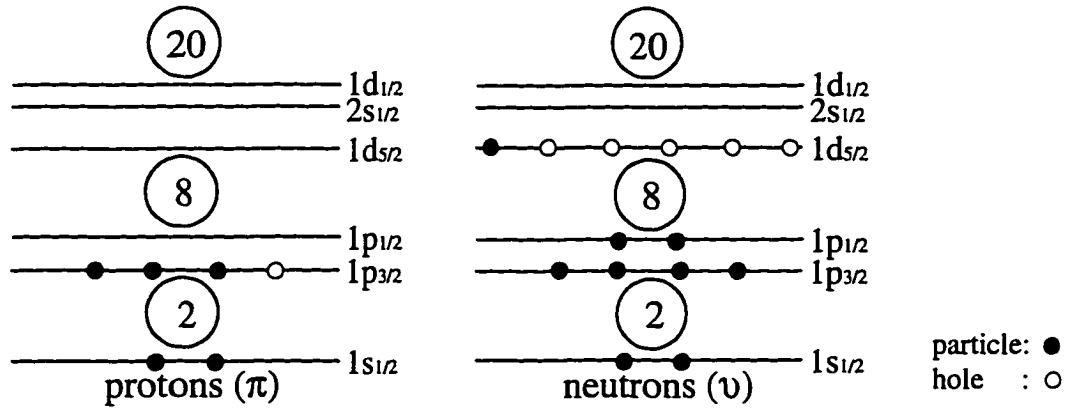


Figure 1.4 The shell-model configuration for the ^{14}B ground state. Occupied states (filled circles) are called particles and empty states (open circles) are called holes. The symbols π and ν are abbreviations for protons and neutrons as indicated above.

invariant under the parity operation ($\mathbf{r} \rightarrow -\mathbf{r}$). Thus, parity is solely dependent on the spherical harmonics [Kr88d]:

$$Y_{lm_l}(\pi - \theta, \phi - \pi) = (-1)^l Y_{lm_l}(\theta, \phi), \quad (1.17)$$

where the factor $(-1)^l$ gives the parity of the nuclear state.

Next, suppose that one has two states (1 and 2) with angular momenta j_1 and j_2 and parities π_1 and π_2 ; then, the total j of the state must be an integer such that $|j_1 - j_2| \leq j \leq (j_1 + j_2)$ (see [Sa85] for a formal discussion). The parity can be found from:

$$\begin{aligned} \psi_1(\mathbf{r}) \cdot \psi_2(\mathbf{r}) &\rightarrow \psi_1(-\mathbf{r}) \cdot \psi_2(-\mathbf{r}) = [Y_1(\pi - \theta, \phi - \pi) R_1(r)] \cdot [Y_2(\pi - \theta, \phi - \pi) R_2(r)] \\ &= (-1)^{l_1} [Y_1(\theta, \phi) R_1(r)] \cdot (-1)^{l_2} [Y_2(\theta, \phi) R_2(r)] = (-1)^{l_1} (-1)^{l_2} [\psi_1(\mathbf{r}) \cdot \psi_2(\mathbf{r})], \end{aligned} \quad (1.18)$$

where the subscripts of the Y stand for the l and m_l for each state 1 and 2. The parity of the total state is then just $(-1)^{l_1} (-1)^{l_2}$. For example, if a $p_{3/2}$ state is coupled with a $d_{5/2}$ state (with l equal to 1 and 2, respectively), the total possible $j = 1, 2, 3$, or 4 with parity -1 . For brevity, the total state is said to have a total spin/parity denoted as J^π , which for the above would be $1^-, 2^-, 3^-,$ or 4^- .

It has been found that the ground states of all nuclei with even numbers of neutrons and protons (even-even) have spin/parity of 0^+ [Bo69], and almost all nuclei with an even number of one species of nucleons and an odd number of the other species possess a spin/parity equal to that of the odd nucleon. This led to the development of the *extreme independent particle model*, where the spin/parity is determined by the last unpaired nucleon. This is an oversimplification, and the next approximation is that all nucleons outside closed sub-shells (valence nucleons) contribute to the spin/parity where an empty state or "hole" can act like a particle. This is analogous to atomic physics where the valence electrons determine the structure of the atom and the closed sub-shells contribute nothing. See Ref. [Ca90] for a detailed treatment of the extreme independent particle model and two-particle and multiparticle (where a particle here mean a particle or a hole) configurations.

1.2.5 Shell-model calculations for particle-hole configurations

The shell-model configuration shown for ^{14}B presents an interesting theoretical problem, for it represents the simplest non-trivial shell-model problem: two-particle configuration. It represents the coupling of a neutron in the $1d_{5/2}$ state and a proton hole in the $1p_{3/2}$ state (a particle-hole configuration), which can be abbreviated as $\pi(d_{5/2})^{+1}\nu(p_{3/2})^{-1}$, where the subscripts $+1$ and -1 mean one particle and one hole, respectively. There have been many sophisticated and complicated formalisms that have been devised to calculate the predicted energies and spin/parities for the excited levels using the shell-model. We shall go into details here but direct the reader to two such formalisms (mentioned later in this thesis) that have been used to make calculations of particle-hole interactions: the Millener-Kurath (MK) interaction [Mi75] and the Warburton-Brown (WBT) interaction [Wa92].

1.3 Fermi Theory of β Decay

The purpose of this section is to briefly outline some of the major points of the Fermi theory of β decay that will be useful for understanding the material that follows in this work. A more complete description can be found in almost any introductory nuclear physics text. Here we shall follow the explanation given by K. S. Krane, *Introductory Nuclear Physics* [Kr88] and by P. Marmier and E. Sheldon, *Physics of Nuclei and Particles* [Ma69]. Fermi treated the β decay interaction as a weak perturbation and derived the relationship, known as Fermi's Golden Rule, between the decay probability λ and the properties of the initial and final nuclear states:

$$\lambda = \frac{2\pi}{\hbar} |V_{fi}|^2 \rho(E_f), \quad (1.19)$$

where the quantity $\rho(E_f)$ is the density of final states, expressed as dn/dE_f , the number of states dn in the energy interval dE_f . This implies that a β -decay transition is more probable if there are more final states available. The matrix element V_{fi} is the overlap between the initial and final states [Kr88]:

$$V_{fi} = \int \Psi_f^* V_x \Psi_i dv, \quad (1.20)$$

where V_x is the interaction potential. In this work we will not be concerned with the exact form of V_x . For β decay this interaction matrix element can also be written as [Kr88]:

$$V_{fi} = g \int [\Psi_f^* \varphi_e^* \varphi_\nu^*] V_x \Psi_i dv, \quad (1.21)$$

where Ψ_f refers to the final *nuclear* wave function of the daughter. The terms φ_e and φ_ν refer to the electron and neutrino wave functions, respectively. The quantity in square brackets is the total final state of the system after the β -decay. The constant g (equal to about $0.88 \times 10^{-4} \text{ MeV}\cdot\text{fm}^3$ [Kr88]) gives the strength of the weak interaction, just as e (the electronic charge) gives the strength of the

electromagnetic interaction. For a given transition we shall let the momentum of the electron be represented by \mathbf{p} and that of the neutrino by \mathbf{q} . Since we are only interested in the shape of the energy spectrum, the directions of \mathbf{p} and \mathbf{q} do not matter.

The quantity $\rho(E_f)$ is the density of all possible final states accessible in the phase space of the electron and neutrino. We assume that each are confined to a box of volume V to normalize the wave functions, where V will cancel from the final result. Considering only the electron for the moment, the probability that $p < |\mathbf{p}| < p + dp$ is proportional to the volume of a spherical shell with radius p and thickness dp which is equal to $4\pi p^2 dp$. (If dp is very small relative to p then this volume can be approximated by a right prism with cross sectional area $4\pi p^2$ and height dp which converges to the exact result as $dp \rightarrow 0$.) In the phase space defined by (x, y, z, p_x, p_y, p_z) , the total probability that an electron is confined within the volume V with the proper momentum is proportional to the product of the above two probabilities: $4\pi p^2 dp V$. The uncertainty principle tells us that $\Delta x \Delta p_x \approx h$ or analogously in six-dimensional phase space $\Delta x \Delta y \Delta z \Delta p_x \Delta p_y \Delta p_z \approx h^3$. Thus each final state cannot occupy a volume smaller than h^3 in the electron phase space, and therefore we divide this into the above probability to find the number of electron states [Kr88]:

$$dn_e = \frac{4\pi p^2 dp V}{h^3}. \quad (1.22)$$

Similarly the number of neutrino states is

$$dn_\nu = \frac{4\pi q^2 dq V}{h^3}. \quad (1.23)$$

The total number of states with the proper momenta for both the electron and

neutrino is then [Kr88]:

$$dn = dn_e dn_\nu = \frac{(4\pi)^2 V^2 p^2 dp q^2 dq}{h^6}. \quad (1.24)$$

We shall assume that the electron and neutrino wave functions have their usual free particle (plane-wave) forms [Kr88]:

$$\begin{aligned} \varphi_e(\mathbf{r}) &= \frac{1}{\sqrt{V}} e^{(i\mathbf{p}\cdot\mathbf{r})/\hbar} \\ \varphi_\nu(\mathbf{r}) &= \frac{1}{\sqrt{V}} e^{(i\mathbf{q}\cdot\mathbf{r})/\hbar}. \end{aligned} \quad (1.25)$$

One can make a Taylor Series expansion of the exponential terms in Eq. 1.25 if the magnitude of the exponents are known, which requires estimating $|\mathbf{p}|$ and $|\mathbf{q}|$ (which shall be represented as just p and q , respectively). For a particle of nonzero mass, the relativistic relationship between the total energy of the particle E and its momentum p is given by

$$E^2 = p^2 c^2 + m_0^2 c^4, \quad (1.26)$$

where m_0 is the rest mass of the particle in question. The total energy is simply the sum of the kinetic energy E_k and the rest mass energy:

$$E = E_k + m_0 c^2. \quad (1.27)$$

By combining equations 1.26 and 1.27 we get the following expression:

$$p = \frac{\sqrt{E_k^2 + 2E_k m_0 c^2}}{c}. \quad (1.28)$$

Because neutrinos are considered to be massless, Eq. 1.28 reduces to

$$q = \frac{E_k}{c}. \quad (1.29)$$

The quantity E_k is in this case is the kinetic energy of the neutrino. For the average

energies encountered in this work, $E_k < 5 \text{ MeV}$. Given the mass of the electron, approximately $0.511 \text{ MeV}/c^2$, $p < 5.5 \text{ MeV}/c$ and $q < 5 \text{ MeV}/c$ at $E_k < 5 \text{ MeV}$. Since the radius of the nucleus $r \sim 1 \text{ fm} = 10^{-15} \text{ m}$, $\hbar = 6.582 \times 10^{-22} \text{ MeV}\cdot\text{s}$, and $c = 2.998 \times 10^8 \text{ m/s}$, the absolute value of the exponents in Eq. 1.25 are $(i\mathbf{p}\cdot\mathbf{r})/\hbar < (0.028)i$ and $(i\mathbf{q}\cdot\mathbf{r})/\hbar < (0.025)i$ (the case where \mathbf{p} and \mathbf{q} are parallel or antiparallel to \mathbf{r}). Even at the maximum possible energy (the end point energy of ^{14}Be is equal to 16.22 MeV [Au93]), $(i\mathbf{p}\cdot\mathbf{r})/\hbar \leq 0.09i$ and $(i\mathbf{q}\cdot\mathbf{r})/\hbar \leq 0.08$. Thus to a fair approximation we can expand the exponential about $(i\mathbf{p}\cdot\mathbf{r})/\hbar = 0$ and $(i\mathbf{q}\cdot\mathbf{r})/\hbar = 0$. Keeping only the first term of the expansion yields [Kr88]:

$$e^{(i\mathbf{p}\cdot\mathbf{r})/\hbar} = 1 + \frac{i\mathbf{p}\cdot\mathbf{r}}{\hbar} - \frac{(\mathbf{p}\cdot\mathbf{r})^2}{2\hbar^2} + \dots \cong 1$$

$$e^{(i\mathbf{q}\cdot\mathbf{r})/\hbar} = 1 + \frac{i\mathbf{q}\cdot\mathbf{r}}{\hbar} - \frac{(\mathbf{q}\cdot\mathbf{r})^2}{2\hbar^2} + \dots \cong 1. \quad (1.30)$$

This is known as the *allowed approximation*. In this case, $\varphi_e(\mathbf{r})^* = \varphi_\nu(\mathbf{r})^* = 1/(V)^{1/2}$, and Eq. 1.21 becomes

$$V_{fi} = (g/V) \int \psi_f^* \mathbf{V}_x \Psi_i \, dv. \quad (1.31)$$

The term $M_{fi} = \int \psi_f^* \mathbf{V}_x \Psi_i \, dv$ is called the *nuclear matrix element*. Thus we get $|V_{fi}|^2 = (g/V)^2 |M_{fi}|^2$, and the decay probability becomes

$$\lambda = \frac{2\pi}{\hbar V^2} g^2 |M_{fi}|^2 \frac{dn}{dE_f}. \quad (1.32)$$

Substituting Eq. 1.24 into Eq. 1.32 yields

$$\lambda = \frac{2\pi}{\hbar} g^2 |M_{fi}|^2 (4\pi)^2 \frac{p^2 dp q^2}{h^6} \frac{dq}{dE_f}. \quad (1.33)$$

If E_e and E_ν are the electron and neutrino energy, respectively, the final energy $E_f = E_e + E_\nu$. From Eq. 1.29 $E_\nu = qc$. Thus $E_f = E_e + qc$, $dE_f = dq/c$ at a given E_e , and

$dq/dE_f = 1/c$. Then Eq. 1.33 becomes [Kr88]:

$$d\lambda = \lambda = \frac{2\pi}{\hbar} g^2 |M_{fi}|^2 (4\pi)^2 \frac{p^2 dp q^2}{ch^6}, \quad (1.34)$$

where we have chosen to express λ as $d\lambda$, because λ above is really the partial transition probability for electrons with momenta from p to $p + dp$. We shall assume that M_{fi} is not dependent on p or q and gather all the constant terms in Eq. 1.34 into a single constant $C = [(2\pi)/\hbar c] g^2 |M_{fi}|^2 [(4\pi)^2/h^6]$. This gives us [Kr88]:

$$N(p) dp = d\lambda = Cp^2 q^2 dp, \quad (1.35)$$

where $N(p)$ is the electron momentum distribution. If we ignore the negligible nuclear recoil energy, then $Q = E_f = E_e + E_\nu$, and [Kr88]:

$$q = \frac{Q - E_e}{c} = \frac{Q - \sqrt{p^2 c^2 + m_e c^4} + m_e c^2}{c}. \quad (1.36)$$

The electron kinetic energy E_e was found by solving Eq. 1.28 for E_k with $m_e = m_0$.

Substituting this into Eq. 1.35, we find that [Kr88]:

$$N(p) dp = \frac{C}{c^2} p^2 [Q - \sqrt{p^2 c^2 + m_e c^4} + m_e c^2]^2 dp. \quad (1.37)$$

Frequently one is more interested in the energy spectrum, because that is what is usually measured. From Eq. 1.28 we get $p^2 = (E_e^2 + 2E_e m_e c^2)/c^2$, and $dp = (1/c)(E_e^2 + 2E_e m_e c^2)^{1/2}(E_e + m_e c^2)$. Inserting these expressions into Eq. 1.35 along with the expression for q in terms of E_e (Eq. 1.36), we get

$$N(E_e) dE_e = \frac{C}{c^5} (Q - E_e)^2 (E_e + m_e c^2) \sqrt{E_e^2 + 2E_e m_e c^2} dE_e. \quad (1.38)$$

The shape of the distribution indicated by Eq. 1.38 is plotted in Fig. 1.5a. Notice that there is a definite upper cutoff in the distribution at $E_e = Q$ (neglecting the usually small effect of the daughter recoil), which is called the endpoint energy. This represents the condition in which the maximum kinetic energy is imparted to the β particle, indicated in Fig. 1.5 as " E_0 ". The distribution also vanishes at $E_0 = 0$.

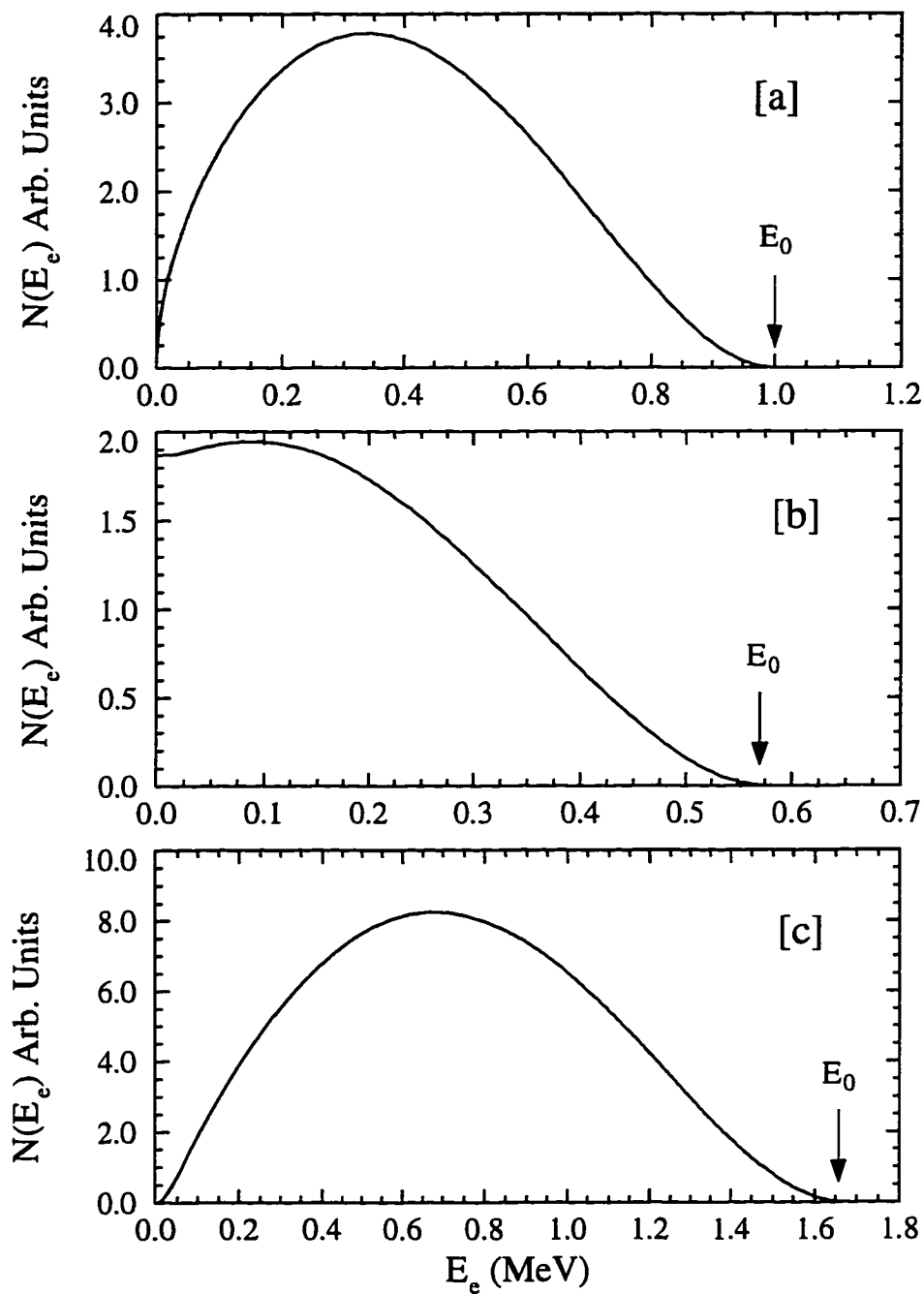


Figure 1.5 Plots of various β -decay energy distributions: (a) a fictitious distribution for $Z = 29$ and endpoint energy (E_0) = 1.0 MeV without the correction for the nuclear Coulomb field, (b) the energy distribution of the β^- decay of ^{64}Cu ($E_0 = 0.5782$ MeV [Ha79]), (c) the energy distribution of the β^+ decay of ^{64}Cu ($E_0 = 1.67449$ MeV [Ha79]).

The distribution shown in Fig. 1.5a is not what is actually measured, because the effect of the nuclear Coulomb field has been ignored. Equation 1.38 must be multiplied by a correction factor called the *Fermi function* to obtain the proper distribution, which is written as $F(Z', E_e)$, where Z' is the atomic number of the daughter nucleus. Figures 1.5b and 1.5c show ^{64}Cu as an example, because it is both a β^- and β^+ emitter. By comparing these two spectra we can see the effects of the Coulomb field on both β^- and β^+ decay. Notice that in Fig. 1.5b (β^- decay) the probability for low energy β particles is greatly enhanced, and the distribution approaches a constant value greater than zero at $E_e = 0$. Figure 1.5c is an example of β^+ decay where the probability of low energy β particles is reduced. In both cases, near the end point energy, the distribution approaches that of the uncorrected distribution shown in Fig. 1.5a. Semiclassically we can interpret figures 1.5b and 1.5c in the following way: β^- decay produces more low energy β particles because of Coulomb attraction, β^+ decay produces fewer low energy β particles because of Coulomb repulsion, and at higher decay energies the β particles are not affected very much by the nuclear Coulomb field. The correct quantum mechanical explanation is that the Coulomb field changes the wave function of the electron (or positron) from that given in Eq. 1.30. Because we shall deal with the decay of ^{14}Be , a β^- emitter, we shall only consider this type of β decay for the remainder of this work. So far we have assumed that the nuclear matrix element M_{fi} was not dependent on p and does not affect the shape of the β -decay energy distribution. This is the allowed approximation. This approximation cannot be used when M_{fi} vanishes to first order. In this case the next higher order of Eq. 1.30 would have to be used. Cases of this sort are called *forbidden* decays, which is something of a misnomer, because these decays are not truly forbidden but just much less probable than allowed decay. If the second term in the expansion must be used to find a

nonvanishing matrix element, then this is called a *first*-forbidden decay; if the third term must be used, then it is called *second*-forbidden decay, and so on.

In the allowed approximation, the electron and neutrino wave functions are assumed to begin at the origin; therefore, they cannot carry any orbital angular momentum ($l = 0$). Then, only the spins of the electron and neutrino can cause a change in angular momentum. Since both particles are fermions, they have a spin $s = 1/2$. There are only two possibilities: the spins aligning parallel or antiparallel. When the spins align **antiparallel**, the total spin $S = 0$; this is called *Fermi* decay. Thus the change in angular momentum $\Delta I = |I_i - I_f| = 0$, where I_i is the initial angular momentum, and I_f is the final angular momentum. *Gamow-Teller* decay results when the spins are aligned **parallel** and $I_i = I_f + 1$. Here $\Delta I = 0$ or 1 . When one has a $I_i = 0$ to $I_f = 0$ transition it is not possible for a vector of length 1 to couple with the initial state to form a final state with $I_f = 0$, so Fermi decay is the only possible transition. With the exception of a $0^+ \rightarrow 0^+$ transition, if $\Delta I = 0$ there is a mixture of Fermi and Gamow-Teller decay. The change in parity $\Delta\pi$ associated with orbital momentum l is given by $(-1)^l$, where $\Delta\pi = -1$ implies a change in parity. For allowed decay $l = 0$, and there is no change in parity.

The $(0^+ \rightarrow 0^+)$ transition for $N = Z$ nuclei is called superallowed and is among the strongest (smallest $\log ft$ value) β decays known. It is where a neutron is transformed to a proton (or vice versa) in the same shell configuration for the initial and final state; these are known as mirror nuclei. In this case, the nuclear matrix element $|M|_{fi} = \sqrt{2}$ [Kr88], and its large value implies that the initial and final wave functions or shell-model configurations are very similar, because they differ only by the exchange of a proton and neutron. Because $|M|_{fi}$ is a constant for superallowed decay the corresponding $\log ft$ values should be similar (see Ref.

[Go71]). Since the strong force is assumed to act on neutrons and protons equally, then the difference in the wave functions is solely due to the perturbation of the Coulomb force, and a very strong overlap would be expected.

In the case of **first-forbidden** decay, $l = 1$, and $S = 0$ or 1 . Thus the two vectors can couple to form a vector with $\Delta I = 0, 1$, or 2 . There is also a parity change, since $(-1)^l = -1$. There are two types of first-forbidden decay, unique and non-unique. Unique first-forbidden is the case where the β is forbidden because of the change in parity ($\Delta\pi = -1$) and the change in spin ($\Delta I = 2$) are both not permissible under allowed decay. Other first-forbidden transitions (where $\Delta I = 0$ or 1) are called non-unique. We can continue this process and find the selection rules for second-, third-, and fourth-forbidden decays (higher levels of forbiddenness have not been observed). The angular momentum selection rules (up to second-forbidden) are given below in Table 1.1.

TABLE 1.1
SELECTION RULES FOR β DECAY

Decay Type	ΔI	$\Delta\pi^a$
Allowed (Fermi)	0	+1
Allowed (Gamow-Teller)	0, 1	+1
First-forbidden (non-unique)	0, 1	-1
First-forbidden (unique)	2	-1
Second-forbidden	2, 3	+1

NOTE: See [Kr88] for the selection rules of third and fourth forbidden decays. The transition $0^+ \rightarrow 0^+$ is the pure Fermi type.

^aThe notation +1 means no change in parity and -1 means a change in parity.

Now we wish to calculate the total transition probability from Eq. 1.37 by integrating over all possible values of p . For allowed decay we obtain [Kr88]:

$$\lambda = \int N(p) dp = \frac{g^2 |M_{fi}|^2}{2\pi^3 \hbar^7 c^3} \int_0^{p_{\max}} F(Z', p) p^2 (Q - E_e)^2 dp. \quad (1.39)$$

We can simplify this further by introducing the *Fermi integral* given by [Kr88]:

$$f(Z', E_0) = \frac{1}{(m_e c)^3 (m_e c^2)^2} \int_0^{p_{\max}} F(Z', p) p^2 (E_0 - E_e)^2 dp, \quad (1.40)$$

where Q has been replaced with the endpoint energy E_0 and the constant $1/[(m_e c)^3 (m_e c^2)^2]$ has been introduced to make the Fermi integral dimensionless. (Here the energy is expressed in units of $m_e c^2$ and the momentum p in units of $m_e c$.) Inserting Eq. 1.40 into Eq. 1.39 gives

$$\lambda = \frac{g^2 m_e^5 c^4 |M_{fi}|^2}{2\pi^3 \hbar^7} f(Z', E_0). \quad (1.41)$$

Using the relationship between the decay constant and half-life $t_{1/2}$ [$\lambda = \ln(2)/t_{1/2}$] and

abbreviating $f(Z', E_0)$ as simply f we get [Kr88]:

$$ft_{1/2} = \frac{2 \ln(2) \pi^3 \hbar^7}{g^2 m_e^5 c^4 |M_{fi}|^2}, \quad (1.42)$$

where the quantity on the left side is known as the *ft value* or *comparative half-life*. Notice that the right side of Eq. 1.42 is only a function the nuclear matrix element M_{fi} . Thus the *ft* value measures differences in the nuclear wave function independent of the density of states (which is included in f). Usually, the right side of Eq. 1.42 is not calculated directly, but the comparative half-life is found by computing f and measuring the half-life of a given transition. The quantity f has been tabulated for various values of E_0 and Z' (the exact method by which it was computed in this work is given in Sec. 3.3). When there are several decay modes,

one defines the partial ft value for the transition in question, which is given by

$$ft = \frac{f(Z', E_0) t_{1/2(\text{total})}}{\text{B.R.}}, \quad (1.43)$$

where $t_{1/2(\text{total})}$ is the total half-life (the half-life actually measured) and B.R. is the branching ratio (or the fraction of the total number of decays) of the transition in question. Because ft values can vary over as many as seventeen orders of magnitude, it is convenient to express the comparative half-life as $\log_{10} ft$ or simply $\log ft$. Generally, the higher the level of forbiddenness the higher the $\log ft$ value.

Figure 1.6 shows some general trends in $\log ft$ values. The most probable of allowed decays are called *superallowed* and are $0^+ \rightarrow 0^+$ Fermi transitions. They have $\log ft$ values between 2.5 and 4. The rest of the allowed decays have $\log ft$ values that range from about 4 to 7.5. Most of the first forbidden decays have $\log ft$ values from 6 to 10, the rarer second-forbidden decays from 10 to 13.5, and the very rare third- and fourth-forbidden decays are found above $\log ft$ 13.5 (see [Kr88]). One can see that, although there is much overlap among the various level of forbiddenness, $\log ft$ values are very useful for their *predictive* ability. If the initial state spin and parity are known, then we can make a reasonable guess for the spin and parity of the final state. Let us take ^{14}Be as an example. In this work we shall assume that the β decay of ^{14}Be originates from the 0^+ ground state [Aj91], since a nucleus so far from stability is very unlikely to be produced in an isomeric excited state.) If a measured β -decay transition has a $\log ft$ value of about 5.7 (Table 3.6), then according to the selection rules given in Table 1.1 and Fig. 1.6, we would say that the most likely assignment for the final state is 1^+ . According to the rules given in Table 1.1, an assignment of 0^+ is also possible, but this would imply a $0^+ \rightarrow 0^+$ superallowed transition which generally would have a $\log ft$ value less than 4.0. Later we will see how this was used in the analysis of both experiments presented in this work.

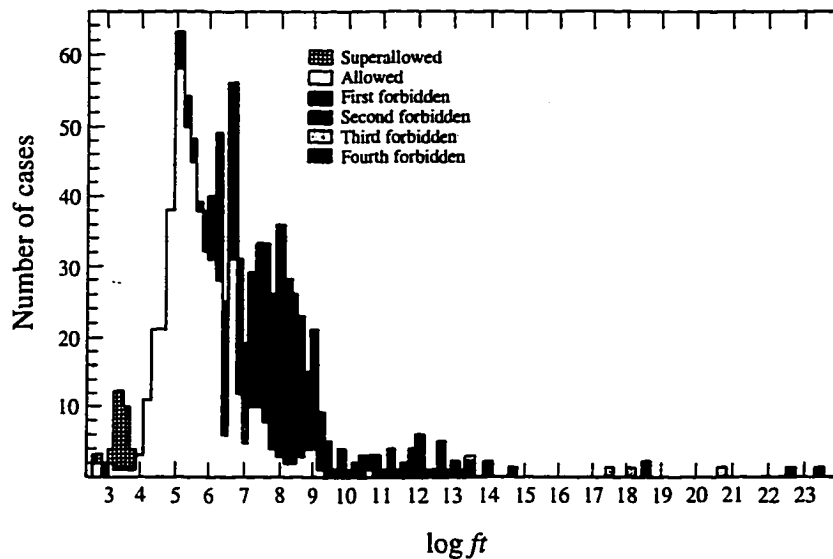


Figure 1.6 Plot of experimentally measured $\log ft$ values versus the number of reported cases for each order of forbiddenness [Kr88g].

1.4 Isobaric Analog State

In the previous section we have discussed superallowed ($0^+ \rightarrow 0^+$) β decay transitions. These transitions are just one kind of a general class of β decay which includes transitions between isobaric analog states. Before discussing the isobaric analog further, a short discussion of isospin is necessary.

Isospin[§] symmetry is the idea that the strong force interaction does not distinguish between neutrons and protons. (In the following discussion we shall follow the treatment on isospin given by K. S. Krane [Kr88h].) Just as in the shell-model where the individual protons and neutrons in a nucleus possess nuclear spin, it has been found that one can refer to a general particle called the nucleon that has an isospin with quantum number $t = \frac{1}{2}$, where the neutron and proton are considered differ intrinsic isospin states of the same particle. The neutron is

[§]Because isospin describes the properties of nuclei with same atomic mass (isobars), this was given the name "isobaric spin" or "isospin".

arbitrarily assigned a spin $m_t = -1/2$ (spin-down) and the proton is assigned a spin $m_t = +1/2$. The coupling of nucleons follows the same rules that have already been discussed in Sec. 1.2.4. The z-axis projection (T_z) of the total isospin T is the sum of the total z-axis projections of the individual nucleons ($t_z = m_t \hbar$):

$$T_z = \frac{1}{2}(Z - N). \quad (1.44)$$

In Eq. 1.44 above, T_z is given in units of \hbar not explicitly stated and Z and N are the number of protons and neutrons in the nucleus, respectively. The total isospin T can take any integral value between $-|T_z|$ and $+|T_z|$. For example, a two-nucleon system could have total isospin $T = 0$ or 1 , where the first state has $|T_z| = 0$ and the second has $|T_z| = -1, 0, \text{ or } +1$. Only one such system exists in nature: the deuteron, where $T = 0$ and $|T_z| = 0$ (one neutron and one proton).

Isospin T has been found to be a useful quantum number in predicting nuclear reactions. We shall not give a discussion of this here (see [Kr88h] for details), except for a discussion of isobaric analog states. A β transition between two isobaric analog states is the case where the initial and final shell-model configurations are identical except for the exchange of a proton for a neutron (β^- decay) or vice versa (β^+ decay).

Because a transition between isobaric analog states result from the transmutation of a proton for a neutron (we shall only refer to β^- decay for simplicity), the difference in energy between this state and its isobaric analog can only be due to the difference in binding energy of the one nucleon and the difference in Coulomb energy. The excitation energy in the daughter [$\Delta E(A, Z)$] of the isobaric analog of the parent ground state (for β^- decay) has been given in Ref. [La80]:

$$\Delta E(A, Z) = BE({}_Z^A Y_N) - BE({}_{Z-1}^A X_{N+1}) + \Delta E_c(A, Z), \quad (1.45)$$

where ${}_Z^A Y_N$ is the daughter nucleus, ${}_{Z-1}^A X_{N+1}$ is the parent nucleus, $\Delta E_c(A, Z)$ is the difference in Coulomb energy between the two, and the binding energies BE were

taken from Ref. [Au93]. The Coulomb energy E_c has been computed in Ref. [Sw58] and is given by

$$E_c = \frac{3}{5} \frac{e^2 Z^2}{4\pi\epsilon_0 R} \left(1 - \frac{c}{Z^{2/3}} \right), \quad (1.46)$$

where e is the electronic charge (1.602×10^{-19} C), ϵ_0 is the permittivity of free space (8.854×10^{-12} C²J⁻¹m⁻¹), Z and R are the atomic number and radius of the daughter nucleus, and c is parameter which for light nuclei ($Z < 10$) is

$$c = 0.7636 - e^{-0.38Z}. \quad (1.47)$$

The nuclear radius R assumes that the density of nuclear matter is a constant throughout the nucleus [Kr88i], meaning that

$$\frac{A}{\frac{4}{3}\pi R^3} \sim \text{constant}. \quad (1.48)$$

Thus,

$$R \propto A^{1/3} = R_0 A^{1/3}. \quad (1.49)$$

where R_0 (about 1.22 fm) has been found from scattering experiments and varies from 1.2 to 1.25 fm [Kr88]. If R is in fermis and E_c in MeV then Eq. 1.46 becomes

$$E_c = \frac{0.8640 \cdot Z^2}{R} \left(1 - \frac{c}{Z^{2/3}} \right). \quad (1.50)$$

The difference in Coulomb energy used in Eq. 1.45 is given by

$$\Delta E_c(A, Z) = E_c(Z, A) - E_c(Z-1, A), \quad (1.51)$$

where $E_c(Z, A)$ and $E_c(Z-1, A)$ are the Coulomb energies of the daughter and parent.

1.5 Beta-delayed Neutron Decay

Next we shall discuss the specific type of decay mechanism that leads to neutron emission from the β decay daughter. This process is called *β -delayed neutron decay*. For convenience we shall refer only to neutron emission in this

section, but the following can apply equally to other types of delayed transitions, such as proton or α particle emission. Figure 1.7 shows the energetics and a generalized decay scheme of ^{14}Be as an example. The original nucleus (^{14}Be), known as the *precursor*, β decays to excited states in the *emitter* (^{14}B) which then neutron decay to states in the *daughter* (^{13}B or ^{12}B) or γ decays to the ground state of the emitter depending on the excitation energy of the level populated. The half-life for neutron emission is very short ($\sim 10^{-20}$ s), because neutron decay involves the strong force. Thus, the neutron decay exhibits a half-life that is essentially that of the precursor β decay. Quite often, the emitter is also loosely referred to as a "daughter" of the precursor. If the excitation energy of the emitter is greater than the energy required to liberate a neutron (the separation energy), then neutron emission will occur (although γ decay to lower levels of the emitter may be a competing process if the neutron energy is very low). Otherwise, the only possible way for the emitter to de-excite is through γ decay. It is also possible for the daughters to be unstable with respect to neutron, γ , or β decay. The process continues until a stable state is reached.

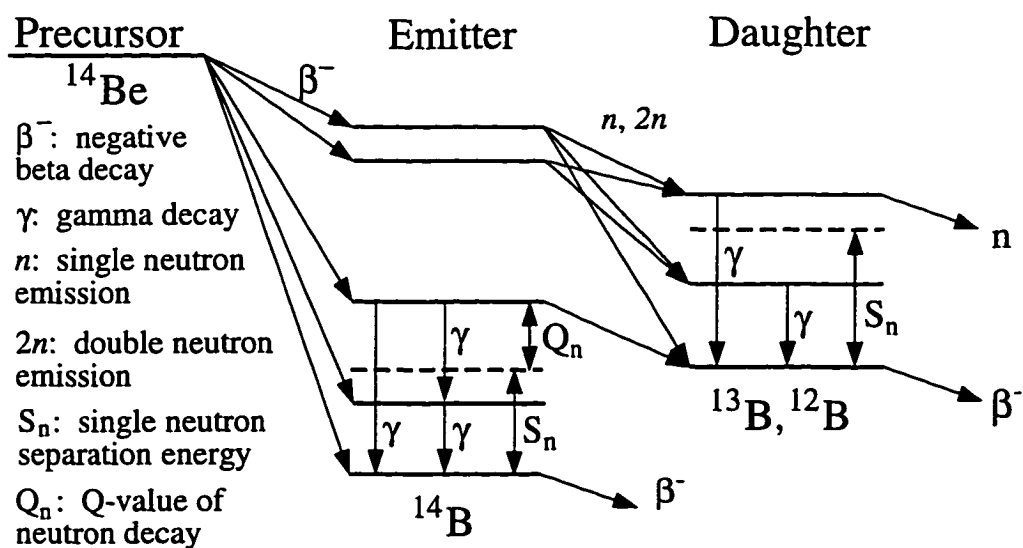


Figure 1.7 Hypothetical decay scheme for ^{14}Be showing the energetics of β -delayed neutron decay. The dashed-lines indicate the neutron thresholds.

Because information regarding the β decay must be inferred from measurements of the coincident neutron and γ emission, one needs a starting point when trying to construct the decay scheme. Therefore it is usually assumed that the daughter and emitter states are reasonably well-known. For example, as stated above, the half-life of the β decay of the precursor can be determined by measuring the half-life for neutron emission. If one can assume that two or more states of the precursor do not β decay to the same level of the emitter, then the branching ratio of the neutron state relative to the total number of β decays gives the branching ratio of the β transition that populates that state. If the nuclear masses of the precursor and daughter are known, then the Q value of the ground state β decay can be calculated. This information, together with the measured energies of coincident nucleons and coincident γ rays, can be used to determine the excitation energy of the emitter state in question. If the spin/parity of the precursor state from which β decays originate is known, and the $\log ft$ value can be calculated, then one can determine probable spin/parity assignments for the populated states.

1.6 Background Information on ^{14}Be

Now we shall discuss ^{14}Be specifically. It is of considerable importance, because it is the heaviest (or most neutron-rich) particle stable isotope of beryllium. (The term "particle stable" means that the nuclide β decays first before emitting nucleons.) It is stable against prompt (immediate) nucleon emission. Furthermore the nucleus ^{13}Be is particle unstable. It is believed that ^{14}Be has an unusual structure, because it is so far from stability, and the extra binding energy to achieve particle stability must come entirely from the neutron pairing force. The β decay population of excited states in the daughter ^{14}B may reveal information about the structure of that nuclide and provide tests of the shell-model for nuclei far from stability.

The nuclide ^{14}Be was first observed by Bowman *et al.* [Bo73] by impinging 4.8 GeV protons on a uranium target. The first ^{14}Be half-life measurement (4.2 ± 0.7 ms) was performed by Curtin *et al.* [Cu86] at the NSCL. Even as recently as 1988, only the ^{14}Be half-life was known. The total branching ratios for $0n$ ($14 \pm 3\%$), $1n$ ($81 \pm 4\%$), and $2n$ ($5 \pm 2\%$) emission were then measured by Dufour *et al.* [Du88]. (The half-lives of the corresponding daughters are 13.8 ± 1.0 ms [Aj91], 17.36 ± 0.16 ms [Aj91], and 20.20 ± 0.02 ms [Aj90] for ^{14}B , ^{13}B , and ^{12}B , respectively.) In that work, the half-life (4.35 ± 0.17 ms) was also determined to better accuracy than in the work of Curtin *et al.* Because Dufour *et al.* used a π liquid scintillator to measure the neutron multiplicity of ^{14}Be , no information was obtained regarding the energies or intensities of the delayed neutrons. Thus nothing was known about the energies, branching ratios, or $\log ft$ values of β transitions to specific states in ^{14}B . Since the level scheme of ^{14}B was also poorly known, we were motivated to perform a detailed measurement of the intensities and energies of specific β -delayed neutron transitions from ^{14}Be .

A shell-model calculation by Curtin and Brown [Cu85] predicts a very strong β -decay branch to a state just below the $1n$ emission threshold. A much weaker branch is predicted to another state that is below the threshold for $2n$ emission. The theoretically predicted half-life of these β transitions is 6.3 ms. Figure 1.8 shows the predicted level scheme of ^{14}Be given in [Cu85]. The $\log ft$ values listed in Fig. 1.8 were calculated using the theoretical decay energies and branching ratios to calculate f as given in [Wi74] and Sec. 3.3. The theoretical branching ratios for the various neutron multiplicities of ^{14}Be have also been calculated by Dufour *et al.* [Du88] using the formalism of Takahashi [Ta72]. The theoretically predicted branching ratios are 61% for $1n$ decay, 14.5% for $2n$ decay, and 0.3% for $3n$ decay. Note that β -delayed $3n$ decay, while theoretically predicted, is unobserved. Compare these values to the

experimentally determined values given above: the discrepancy between these values and the measured and predicted half-life of ^{14}Be was another reason that motivated us to perform a detailed study of the β -delayed neutron decay of ^{14}Be .

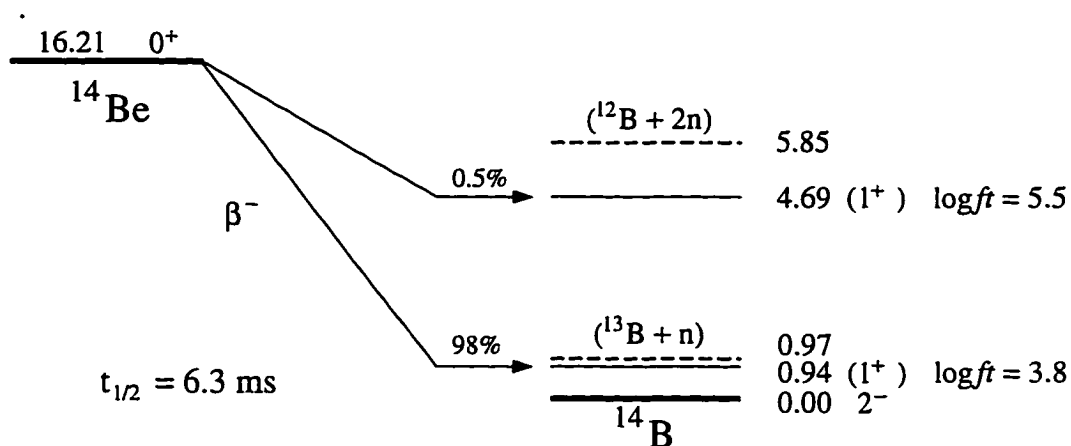


Figure 1.8 The predicted level scheme of the β decay of ^{14}Be given in [Cu88]. The dashed lines are the thresholds for one- and two-neutron emission. Level energies are given in MeV with respect to the ground state of ^{14}B . The spin/parity of the predicted states are enclosed in parentheses, and the properties of the ground states and thresholds have been obtained from [Aj91]. (See text for more details.)

CHAPTER 2

EXPERIMENTAL METHOD FOR THE NSCL EXPERIMENT

This chapter describes the experimental method for the first experiment carried out in this work. First, the method of ^{14}Be radioactive beam production and separation using the A1200 fragment mass separator (see below) is given. Next the detector array [Ha91] used to detect the β -delayed neutrons (designed and built at the NSCL), its associated hardware, and the γ -ray detectors used for γ -n coincidence measurements [Be95] are described. Because a pulsed beam was necessary, the various beam on/off cycles that we used are discussed. Last, the various calibration runs required to determine neutron detection efficiency, to perform an energy and detection efficiency calibration of the γ -ray detectors, and to make a time and distance calibration of the time-of-flight detectors are discussed.

2.1 Radioactive Beam Production at the NSCL

The first experiment was performed at the National Superconducting Cyclotron Laboratory (NSCL) at Michigan State University (MSU). Due to the short half-life of ^{14}Be (4.35 ± 0.17 ms) [Du88], an implanted beam was necessary to perform the β -decay study. The ^{14}Be beam was produced by projectile fragmentation of an 80 MeV per nucleon $^{18}\text{O}^{6+}$ beam. The primary beam, produced by the K1200 cyclotron, impinged on a ^9Be target (thickness 190 mg/cm^2) that was placed at the object position of the A1200 radioactive beam

facility. This device is a fragment mass separator, used to collect and separate the ^{14}Be ions, that consists of two sets of superconducting 22.5° dipole magnets that bend in opposite directions and fourteen superconducting quadrupole magnets (see Fig. 2.1). It was operated in the high acceptance achromatic mode with the parameters shown in Table 2.1 [Sh91]. The beam fragments are forward focused (that is, their momentum in the beam direction is much larger than that perpendicular to the beam) and have essentially the primary beam velocity. The magnetic force exerted on the fragments by the first dipole of the A1200 supplies the centripetal acceleration. Thus

$$qvB = \frac{mv^2}{r}, \quad (2.1)$$

where q and m are the charge and mass of the particle, respectively, v is its velocity, B is the magnetic field of the dipole, and r is the radius of curvature of the first dipole. Solving for r , we get

$$r = \frac{mv}{qB} = \frac{v}{B} \left(\frac{1}{q/m} \right). \quad (2.2)$$

Since v and B are constants, the first dipole magnet selects reaction products according to their charge-to-mass ratio. Undesired fragments were stopped inside this magnet. For fully stripped ^{14}Be ions, the magnet was set to $B \cdot r = 4.079 \text{ T}\cdot\text{m}$, which allowed ions with a mass-to-charge ratio of 3.5 to pass. A thin plastic scintillator (7.84 mg/cm^2) [Ha91] was placed at the image #1 location (see Fig. 2.1) of the A1200 to provide a start signal for measuring the time-of-flight of the reaction products.

The first dipole was insufficient to completely separate the desired fragments, since many isotopes can have the same approximate charge-to-mass ratio. Thus it was necessary to introduce a wedged-shaped aluminum energy

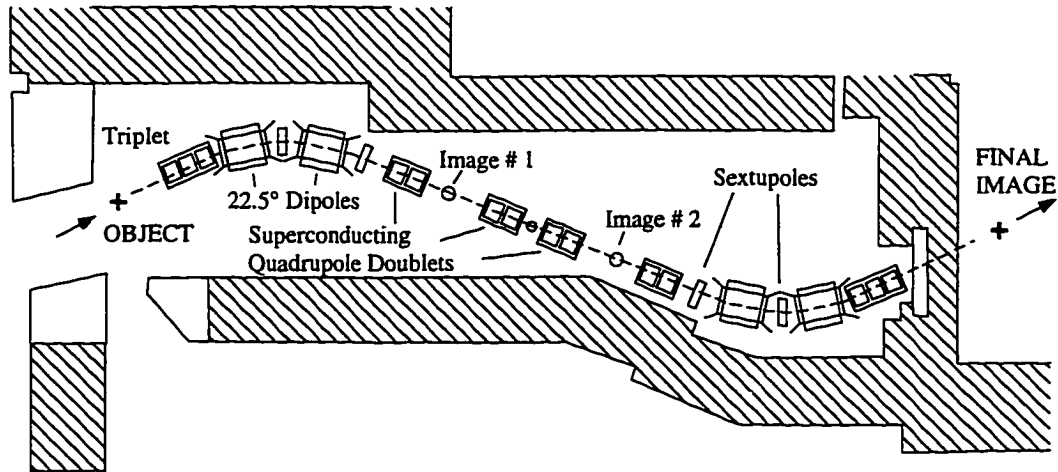


Figure 2.1 Diagram of A1200 Beam Analysis Device [Sh91].

TABLE 2.1

SETTINGS FOR HIGH ACCEPTANCE MODE OF A1200

parameter	value
solid angle acceptance	4.3 msr
theta acceptance	54 mrad
phi acceptance	80 mrad
momentum acceptance ($\Delta p/p$)	3.0 %
rigidity	5.4 Tm

SOURCE: Ref. [Sh91]

degrader (central thickness 425 mg/cm^2 and wedge angle 3.5 mrad , corresponding to achromatic separation [Sh91]) at image # 2 to further separate the ions and to focus different nuclides at different points along the final image of the A1200 according to their differential energy loss. (See [Du86] for a detailed discussion of projectile fragmentation and the way in which a wedge-shaped degrader preserves the achromatism of a fragment mass separator and, thereby, improves the mass

resolution at the final image.) Because the fragments had essentially the primary beam velocity, their energy was roughly equal to (actually somewhat less than) that of the primary beam (80 MeV/A). This is considerably less than the rest mass energy of a nucleon, about 931 MeV/A, so the fragments can be treated classically. The Bethe-Bloch formula for energy loss in this energy regime is dominated by the multiplicative factor q^2/v^2 [Kn79]. Thus

$$\frac{dE}{dx} \propto \frac{q^2}{v^2} \propto \frac{Z^2 A}{E} \quad (\text{for fully stripped ions}). \quad (2.3)$$

Since the energy loss through the degrader wedge is usually small, we can treat it as a thin absorber. In this case the stopping power is roughly constant throughout the absorber and [Kn79b]:

$$\Delta E = \left(-\frac{dE}{dx} \right)_{\text{avg.}} \cdot t, \quad (2.4)$$

where ΔE is the total energy loss, $(-dE/dx)_{\text{avg.}}$ the average stopping power, and t the thickness of the absorber. Combining equations 2.3 and 2.4 we get $\Delta E \propto t(q^2/v^2) = k(q^2/v^2)$, where k is a constant. Squaring the r value given in Eq. 2.2 and expressing it in terms of fragment energy, and subtracting ΔE from the total energy E , we get:

$$r'^2 = \frac{2mE'}{qB'} = \frac{2m(E - \Delta E)}{qB'} = \frac{2m}{qB'} \left[E - k \left(\frac{q^2}{v^2} \right) \right] = \frac{m^2 v^2}{qB'} - \frac{kmq^2}{B'v^2}, \quad (2.5)$$

where r' is the radius of curvature, and B' is the magnetic field of the second dipole. Here, $E' = E - \Delta E$, and v is the velocity of the particle after it has passed through the first dipole, given by $(q/m)Br$, where B and r are the radius of curvature and magnetic field, respectively, of the first dipole. Substituting this into Eq. 2.5 above gives

$$r' = \frac{qB^2 r^2}{B'} - \frac{km^3}{B'B^2 q^2 r^2}. \quad (2.6)$$

Because a constant charge-to-mass ratio has been selected by the first dipole, it is useful to express Eq. 2.6 in terms of q/m :

$$r' = m \left[\left(\frac{q}{m} \right) \frac{B^2 r^2}{B'} - \left(\frac{1}{q/m} \right)^2 \frac{1}{B' B^2 r^2} \right]. \quad (2.7)$$

Note that all the quantities inside the square brackets are constants when the first dipole has been set for a desired q/m . Thus Eq. 2.7 dependent only on the mass of the particles, which are thereby separated by into groups of unique mass and charge. See [Sh91] for more details regarding the A1200.

2.2 The NSCL Neutron Detector Array and Associated Hardware

The ^{14}Be beam was stopped inside a piece of plastic scintillator (BC412,* 2.0 cm by 2.5 cm by 1.0 cm deep), the "implantation detector", that was located at the center of the NSCL neutron detector array (see Fig. 2.2 and Ref. [Ha91]). Two 1.9 cm diameter HAMAMATSU H3167 photomultiplier tubes, optically coupled to the implantation detector, provided the "start" signal that indicated the β decay of implanted nuclei. We required that both scintillators fired to minimize the probability of random starts. Since the beam that emerged from the A1200 was too high in energy to stop inside the implantation detector, it was necessary to first degrade its energy. The ^{14}Be ions were energetic enough so that the detector array could be placed in air, which simplified the setup by eliminating the need for a vacuum chamber. A 0.25 mm thick Kapton® [Go87] window was attached to the end of the beamline to separate the vacuum from the air. About 8 mm of aluminum was introduced between the Kapton® window and the implantation detector to adjust the depth to which the ^{14}Be ions were implanted.

*Density 1.032 g/cm³ and hydrogen-to-carbon 1.104.

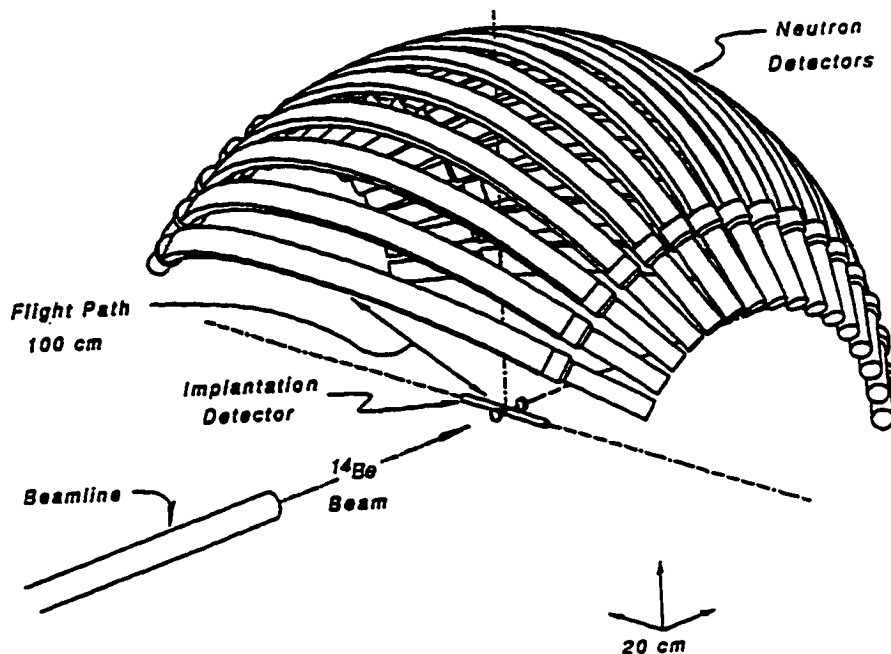


Figure 2.2 Schematic of NSCL neutron detector array [Ha91].

A thin (ΔE) silicon surface barrier detector 0.2 mm thick and 300 cm² in area was placed in front of the implantation detector (as the beam sees it) to monitor the purity of the beam (see Fig. 2.3). A thicker silicon surface barrier detector (E-veto, 1 mm thick) was placed behind the implantation detector to monitor the composition of the beam that passed through the implantation detector. The program STOPX [Aw83], which uses the formulas and parameters of J. F. Ziegler [Zi80], was run after the experiment to calculate the distance to which the ions had penetrated into the plastic, which turned out to be 0.9 ± 0.3 cm (including energy straggling and a 6% energy spread in the incident beam). This was determined from the initial beam energy (60 ± 4 MeV per nucleon, found by running the program INTENSITY [Wi92]) and the density and composition of the various absorbers (see Table 2.2). Thus, some of the ^{14}Be ions did not stop in the implantation detector. However, this did not affect the experiment, since the decay of these ions did not trigger the start scintillator.

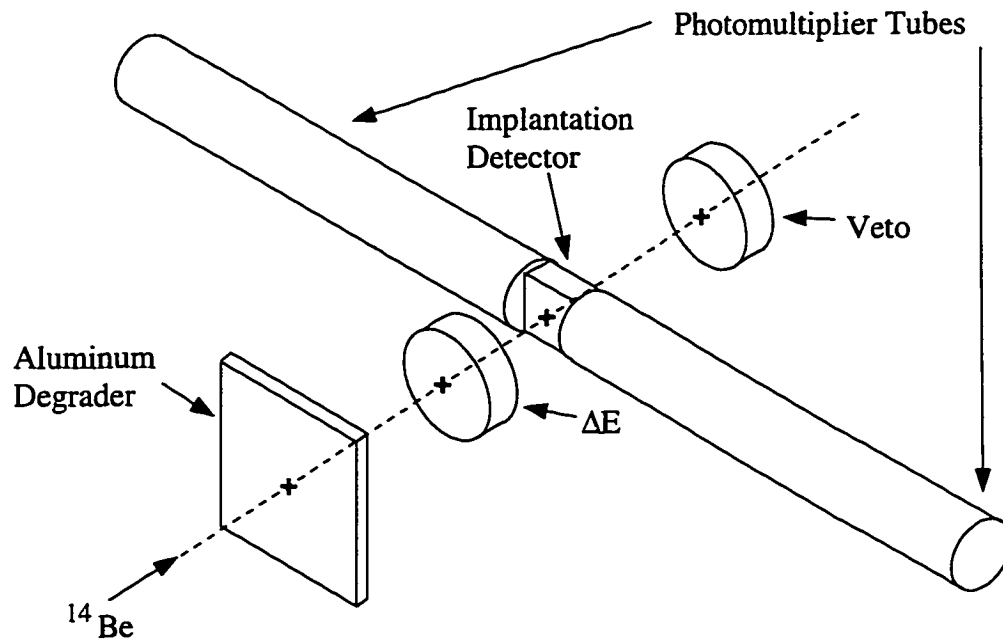


Figure 2.3 Diagram of the hardware located at the center of the NSCL array [Ha91].

TABLE 2.2

LIST OF ABSORBERS

absorber	thickness (cm)
air ^a	8.6 ±0.5
Kapton ^{® b}	0.025±0.001
aluminum (nat.)	0.80 ±0.01
silicon (nat.)	0.020±0.001

NOTE: Nat. is an abbreviation for natural.

^aconsidered as a mixture of 78.1% N₂, 20.9% O₂, and 0.9% Ar [Li91] at 760 torr.

^bsee Ref. [Go87]; ionic formula C₅H₅O₃N and density 1.42 g/cm².

A plot of the energy loss in the ΔE detector versus the timing signal from the scintillator located at image location #1 of the A1200 (relative to the cyclotron RF) yields clear Z and A separation (Fig. 2.4). We get the exit velocity of the ions after each dipole by solving for v in Eq. 2.1:

$$v = \frac{q}{m}(Br), \quad (2.8)$$

where B, r, and v are the respective magnetic field, radius of curvature, and ion velocity. If Br is a constant (that is, set for a specific ion), then the velocity is approximately proportional to (and thus the flight time inversely proportional to) q/m. From Eq. 2.3:

$$\frac{dE}{dx} \propto \frac{q^2}{v^2} = q^2 \left[\frac{m^2}{q^2} \frac{1}{(Br)^2} \right]. \quad (2.9)$$

If the ions are fully stripped then the energy loss dE/dx is proportional to Z^2 . Applying Eq. 2.8 for the second dipole, where $B'r'$ is a constant, the velocity is proportional to charge-to-mass ratio, and since the flight time is inversely proportional to the velocity, the flight time is proportional to the **mass-to-charge** ratio. Thus, the mass-to-charge ratio increases to the right (increasing flight time) along the x-axis of Fig. 2.4 for each band of Z (there is a wraparound, because the time is measured relative to the pulsed logic signal of the cyclotron RF). The purity of the beam was determined by obtaining the yields of the various groups seen in Fig. 2.4. A summary of the beam composition is given in Table 2.3 below. A similar plot gated in coincidence with the E-veto detector, placed behind the implantation detector, yielded the number and species of particles which passed through this detector (see Fig. 2.5). The composition of the beam which stopped in the implantation detector was obtained by subtracting the yields of each nuclide obtained in Fig. 2.5 from those in Fig. 2.4. The purity of the beam implanted was $90 \pm 1\%$ and a summary of the beam

composition is given in Table 2.3, where the uncertainties listed include an estimate of systematic error. A diagram of the electronics associated with the ΔE and E-veto detectors is given in Appendix A.1, and a diagram of the electronics associated with the implantation detector is shown in Appendix A.2.

TABLE 2.3
PURITY OF BEAM

Purity of beam		Purity of beam implanted	
Isotope	Yield (%)	Isotope	Yield (%)
^{14}Be	63.4 ± 0.7	^{14}Be	$90. \pm 1.$
^{11}Li	9.3 ± 0.3	^{11}Li	3.7 ± 0.5
^8He	1.9 ± 0.4	^8He	1.2 ± 0.7
^6He	4.2 ± 0.3	^6He	1.2 ± 0.6
^3H	21.2 ± 0.4	^3H	3.7 ± 0.6

The β -delayed neutrons were detected in an array of fifteen plastic scintillators (referred to as the NSCL neutron detector array). The neutrons are detected by scintillation light due to the recoil of protons in the plastic. Each neutron detector consisted of a BC 412 plastic bar (the same type as the implantation detector) that was 157 cm long by 7.6 cm wide by 2.54 cm thick and bent in a 1 m radius of curvature (see Fig. 2.2). The solid angle of each detector was approximately 120 msr as given in Ref. [Ha91]. The total solid angle subtended by all fifteen detectors was 1.78 ± 0.03 sr or $14.2 \pm 0.2\%$ geometrical efficiency. The geometry of the NSCL array insured that the flight path to the center of each detector was a constant to within a few millimeters. Both ends of the plastic scintillator were optically coupled to a 7.6 cm diameter THORN EMI 9821B photomultiplier tube that has both a timing and energy output.

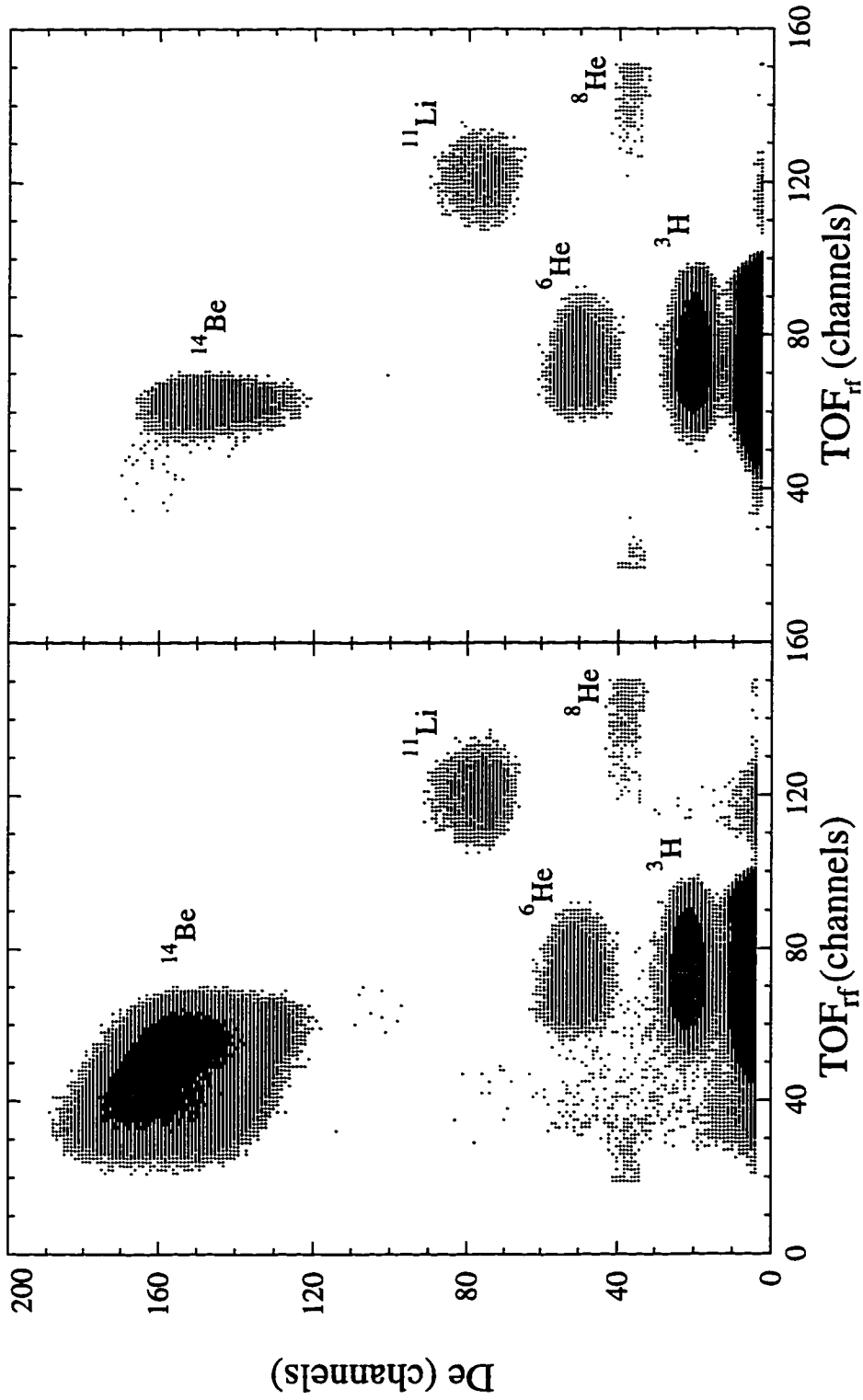


Figure 2.4 Plot of the timing signal referenced to the cyclotron RF (TOF) versus the energy loss in the ΔE detector. Figure 2.5 Same as Fig. 2.4 but gated on the E-veto detector.

The logical OR of all the timing outputs served as the "stop" for the time-of-flight measurement. In the off-line analysis, we required that both photomultiplier tubes fired and used the mean time as the "stop" signal. (This is discussed in more detail below.) The sum of the two energy signals measured the intensity of the scintillation light, which is proportional to the energy deposited. A diagram of the electronics associated with the neutron detectors is given in Appendix A.3, where the symbol $R \cap L$ indicates the AND of the right and left timing signals. (This is distinguished from $L \cap R$ which represents the AND of the left and right timing signals of the **implantation detector**.)

One must measure the γ -ray transitions coincident with neutron decay to fully reconstruct the decay scheme of ^{14}Be . In this experiment, an EG&G ORTEC GEM 90220-P Plus-S high purity germanium detector (HP Ge) was used for this purpose. The detector was placed so that it did not block the beam, nor the view of the implantation detector by any of the neutron detectors. It had a resolution of 1.97 keV (FWHM) and an efficiency of 88.4% of that of NaI at 1.33 MeV. The crystal was 75.8 mm in diameter and 92.9 mm in length with its front face 83 ± 3 mm away from the center of the implantation detector. A diagram of the electronics associated with the HP Ge detector is shown in Appendix A.4.

2.3 Beam-on/Beam-off Duty Cycles

In both experiments described in this work, the beam was pulsed at regular intervals so that the ^{14}Be ions were implanted while the beam was on and decays were detected while the beam was off. This provided clean conditions for the observation of the β -delayed neutron decay, free from interference from the direct beam. The beam was turned on and off for fixed periods of a time by using a LeCroy 222 Dual Gate Generator (see Appendix A.5). This module produced a

TTL logic pulse that shut off the beam by dephasing one of the "dees" of the K1200. The acquisition of the beam-off data began about 40 μ s [Mi88] after the primary beam was shut off. At the end of the beam-off period the gate generator sent another logic pulse to the fast phase shifter in the rf-transmitter which started the primary beam again by rephasing the appropriate "dee". The majority of the ^{14}Be data were taken with a duty cycle of 10.3 ms on/10.3 ms off, and the rest 10.3 ms on/40 ms off. The first duty cycle yielded higher statistics, because the beam-on period accounted for a greater fraction of the total time; the second allowed for a more accurate determination of the half-life due to the longer beam-off period.

The neutron spectroscopic information was derived from time-of-flight data. The start of the time-of-flight measurement was the detection of a β decay event in the implantation detector. A valid "start" consisted of a logical AND between both photomultiplier tubes ("L \cap R", left and right) to reduce the possibility of triggering on noise. This signal was then ANDed with the computer not-busy signal, and the resultant logical gate, called the Master Gate, started the acquisition system. It was also split with a FI/FO (fan-in/fan-out) module to trigger various CAMAC modules (for example the ADC Strobe, the TDC Stop, the QDC Gate, etc., see Appendix A.5). The signals BIT 1 and BIT 2, shown in Appendix A.5, were read by the computer interface to distinguish between beam-on and beam-off events, respectively.

A typical time-of-flight spectrum is shown in Fig. 2.6. The largest peak in the spectrum labeled the "prompt peak", was caused by β and γ rays. The β particles are produced with a distribution of energy (because β decay is a three-body process) with average energies on the order of a few MeV. Therefore, they are highly relativistic and travel essentially at the velocity of light. The sharp

prompt (or beta) peak served as a convenient time reference, since it was always located at about the same position in the time-of-flight spectrum regardless of electron energy. For completeness, the actual relativistic velocity of the β particles was calculated, using the average energy of the β decay (which is one-third of the endpoint energy) weighted by the branching ratios and decay energies of the system in question. (This will be discussed in detail later in this work.)

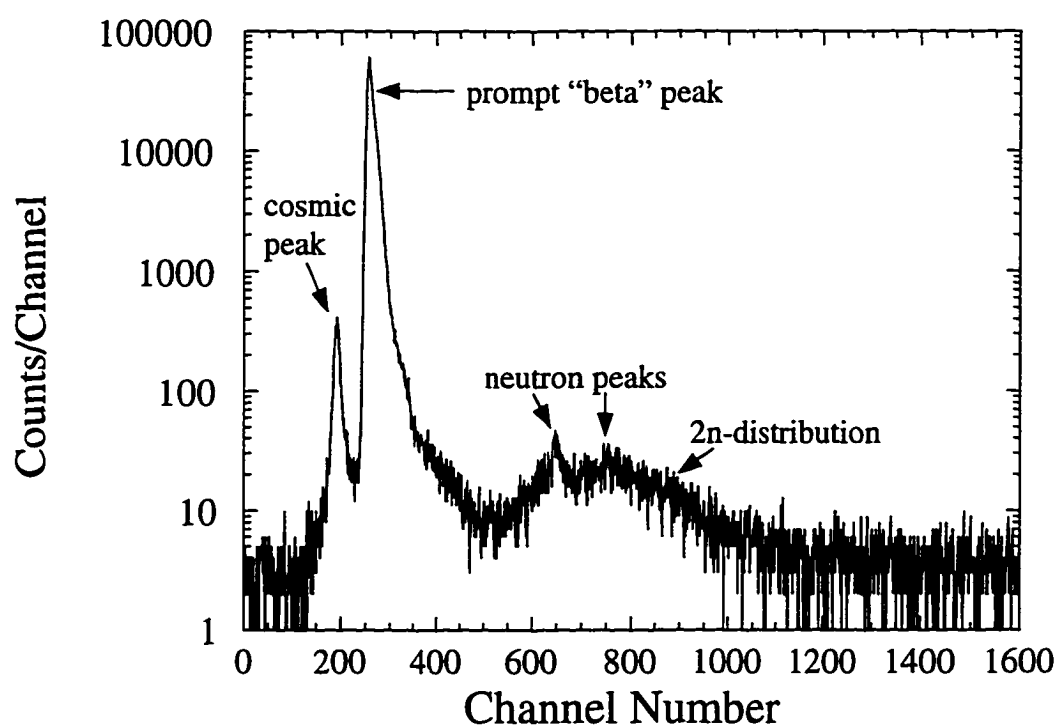


Figure 2.6 Typical time-of-flight spectrum for ^{14}Be data.

The broad peaks seen later (at higher channel numbers) in the spectrum are caused by neutrons. The time-of-flight of the neutrons was found by converting the channel difference between the centroid of the prompt peak and the neutron peak to a flight time and adding the time required for the electrons to reach the time-of-flight detectors. The velocity and thus the energy of the neutrons were

calculated by using the nominal distance of one meter between the implantation detector and the time-of-flight detector (details on how this distance was calibrated will be given below).

The peak labeled "cosmic peak" resulted from cosmic rays that struck one of the neutron detectors first, followed by the implantation detector. Therefore this peak appears at an earlier time than the prompt peak.

2.4 Real Time Clock

The half-life of ^{14}Be was determined by using an Ortec RC014 Real Time Clock [Or73] to measure the time between the start of the beam-off period and the β decay in the implantation detector. At the beginning of the beam-off period the real time clock was zeroed and began to count. When an event occurred, the value of the counter was written to magnetic tape, and it continued to count until the beam-off period ended. The beam-on and beam-off periods were obtained by measuring the time width of the corresponding portions of the pulsed signal going to the cyclotron dephaser (see Appendix A.5). See Ref. [73Or] for more details on the real time clock.

2.5 Calibration Runs

2.5.1 Gamma-ray calibration

An energy calibration of the γ -ray detector was performed by using the following γ -ray sources (approximately 10 μCi each): ^{60}Co , ^{228}Th , ^{152}Eu , ^{137}Cs , ^{133}Ba and a NIST (National Institute of Standards and Technology) standard source. The standard is a point source that is a mixture of ^{125}Sb , ^{154}Eu , and ^{155}Eu for which emission rates have been accurately calibrated within 1.3% (on

September 1, 1988), and it was used to obtain γ -ray branching ratios as discussed later. Table 2.4 lists the lines that have been used in the calibration. Further details on this standard source are given in [Na88]. Each calibration run was approximately five minutes long. All the sources were placed 83 ± 3 mm away from the center of the front face of the high purity Ge detector. The NIST source was 22 ± 3 mm off-axis, and the remaining sources were 20 ± 3 mm off-axis.

TABLE 2.4
CALIBRATED γ -RAY LINES IN NIST SOURCE

Source	γ -ray Energy (keV)	Emission Rate (γ /s)	Error (%)
^{155}Eu	86.062 ± 0.005	8.503×10^3	0.9
^{155}Eu	105.306 ± 0.002	5.922×10^3	1.3
^{154}Eu	123.070 ± 0.001	3.460×10^4	0.8
^{125}Sb	176.313 ± 0.002	4.133×10^3	0.6
^{154}Eu	247.930 ± 0.008	5.864×10^3	0.6
^{125}Sb	427.875 ± 0.006	1.796×10^4	0.8
^{125}Sb	463.365 ± 0.004	6.315×10^3	0.7
^{154}Eu	591.762 ± 0.005	4.197×10^3	0.6
^{125}Sb	600.600 ± 0.004	1.067×10^4	0.7
^{125}Sb	635.954 ± 0.005	6.820×10^3	0.6
^{154}Eu	723.305 ± 0.005	1.703×10^4	0.6
^{154}Eu	873.190 ± 0.005	1.304×10^4	0.7
^{154}Eu	996.262 ± 0.006	8.850×10^3	0.9
^{154}Eu	1004.725 ± 0.007	1.534×10^4	0.7
^{154}Eu	1274.436 ± 0.006	2.958×10^4	0.5
^{154}Eu	1596.495 ± 0.018	1.503×10^3	0.7

SOURCE: Ref. [Na88]

2.5.2 Time-of-flight calibration run

The neutron time-of-flight spectra were calibrated by using an EG&G Ortec 462 Time Calibrator. This module was set so that it emitted very narrow pulses (about 0.25 ns wide) that were spaced 10 ns apart for a fixed period of time. The time calibrator was connected to the output of each side of the photomultiplier tube (both left and right) so that the same length cable and delays were used as in the ^{14}Be data run. This ensured that the pulses recorded from the various photomultiplier tubes by the acquisition system have the same relative offsets as they would in the actual experiment so that the time-of-flight spectra can be gain matched and the events added together (this will be described in detail later in Sec. 3.2.1).

2.5.3 ^{17}N calibration run

A ^{17}N beam was run to experimentally measure the intrinsic neutron detection efficiency of the plastic time-of-flight detectors. The isotope ^{17}N was chosen as a standard by which to measure neutron efficiency, because it is a beam that is easily made at the NSCL and has very well known decay energies (0.3828 ± 0.0009 , 0.884 ± 0.021 , 1.1709 ± 0.0008 , 1.7003 ± 0.0017 MeV) and branching ratios (38.0 ± 1.3 , ~ 0.6 , 50.1 ± 1.3 , $6.9 \pm 0.5\%$, respectively) [Aj82]. Just as in the ^{14}Be runs, the beam was turned on and off at regular periodic intervals, with a beam-on period of 4 s and beam-off period of 8 s.

2.5.4 Pu-Be calibration run

A Pu-Be source (placed at the center of the array) was used to extend the neutron efficiency measurements to higher energies. Useful statistics were obtained for 1.4 to 7.3 MeV neutrons. A Pu-Be source produces neutrons through

the ${}^9\text{Be}({}^4\text{He}, n){}^{12}\text{C}^*$ reaction, where ${}^{12}\text{C}^*$ decays to the ground state by emitting a 4.4 MeV γ ray coincident with the neutron emission. Since there was no beam during this run, a cylindrical BaF_2 detector (5 cm in diameter and 10 cm deep) was used as the start counter by detecting the 4.4 MeV γ ray.

2.6 Neutron Flight Path Calibration

It was necessary to calibrate the neutron flight path because of imperfections in the geometry of the neutron array, the non-zero thickness of the implantation and array detectors, and the width of the beam spot. One cannot assume that ${}^{14}\text{Be}$ ions decayed at the center of the implantation detector, nor that the neutrons were detected at the center of each array detector; therefore the flight path could deviate somewhat from geometrical considerations alone. An accurate measurement of this distance was necessary, because neutron energy was determined using the time-of-flight method.

Only two of the ${}^{17}\text{N}$ peaks yielded useful statistics (1.1709 and 1.7003 MeV [Aj82]). The 0.3828 MeV peak was below the threshold of the neutron detectors (0.77 ± 0.13 MeV), and the 0.808 MeV peak (branching ratio $\sim 0.6\%$) [Aj82] was too small to observe.

Since the energies of the neutrons are known, their velocities can be calculated by using the relativistic expression for total energy

$$E = mc^2 = E_0 + E_k \quad (2.10)$$

$$\gamma m_0 c^2 = m_0 c^2 + E_k; \quad \gamma = \frac{1}{\sqrt{1 - (v^2/c^2)}}, \quad (2.11)$$

where m is the relativistic mass of the neutron, m_0 its rest mass, E_0 its rest mass energy, E_k its kinetic energy, c the velocity of light, v the velocity of the neutron,

and γ the Lorentz factor. Solving Eq. 2.11 for v we get

$$v = c \sqrt{1 - \frac{1}{[(E_k/m_0c^2) + 1]^2}}. \quad (2.12)$$

If E_k is expressed in MeV, then the following quantities can be conveniently expressed as: $c = 29.979$ ns/cm and $m_0c^2 = 939.566$ MeV/ c^2 . Most energies measured in this experiment (a few MeV) are much smaller than the neutron rest mass energy; therefore the classical expressions could be replaced above to a very good approximation. The relativistic formulas were used for completeness.

Reference [Ra96] reports an experiment performed by G. Raimann *et al.* that studied the β -delayed neutron decay of ^{17}C . There they describe the neutron peak shape as being asymmetric: a gaussian with an exponential tail on the longer time-of-flight (lower energy) side to account for the scattered neutrons. We have adopted this line shape for most of the time-of-flight data in the two experiments presented in this work. The program FITS [Di93] can employ a hypergaussian line shape to reproduce the low energy tail. Because it is non-standard, this type of line shape requires some explanation. The hypergaussian peak shape was obtained from [Ke81] and consists of four regions: a left exponential tail, an asymmetrical central hypergaussian where the left and right width can differ, and a right exponential region. The program matches the four regions to one another until a smooth curve is obtained and varies the parameters until the reduced χ^2 is minimized. The functional form for the central region is very similar to that of a gaussian and is given by $y = h \cdot \exp\{-\ln 2 [(2|x_0 - x|)/\Gamma_{L,R}]^\gamma\}$, where h is the height, x_0 the centroid, x the channel number, and $\Gamma_{L,R}$ the left/right width (Γ_L for $x < x_0$ and Γ_R for $x > x_0$). This shape is a *hypergaussian* because the exponent γ can be a value other than 2 (as it is for a gaussian), where values less than 2 give flat tops and values greater than 2 give pointed tops. The complete line shape is best

described as a *asymmetric hypergaussian with tails* (referred to as simply a hypergaussian). A complete description of FITS, including the exact functional form of the hypergaussian line shape, is given in [Di93]. The line shape for the fit shown in Fig. 2.7 consisted of hypergaussian with a symmetric central region, a tail on the right (longer time-of-flight) side, and no tail on the left side. We fitted the spectrum with the same γ values for both peaks (but allowed to vary) and found that allowing the parameters of the exponential tail of each peak to vary independently resulted in the best fit.

Information on the ^{17}N neutron peaks shown in Fig. 2.7 is listed below in Table 2.5, where the neutron velocities were calculated from Eq. 2.12, and the method for finding the calibrated distances is given below. If C_β and C_n are the centroids of the prompt and neutron peaks, respectively, k is the conversion from time-of-flight channels to time (here equal to 0.1 ns/chan), d is the flight path, and t_{total} is the total time-of-flight, then the velocity of the neutrons v_n can be written as

$$v_n = \frac{d}{t_{\text{total}}} = \frac{d}{k(C_n - C_\beta) + t_\beta}, \quad (2.13)$$

where t_β is the time-of-flight of the β particles. Therefore

$$t_\beta = \frac{d}{v_\beta} \text{ and } v_n = \frac{d}{k(C_n - C_\beta) + (d/v_\beta)}. \quad (2.14)$$

The energy used for calculating v_β was the average β -decay energy of ^{14}Be , E_β , (equal to one-third of the end-point energy). Because of the lack of information on the decay scheme of ^{14}Be (at the start of the analysis for this experiment), it was assumed that the decay was entirely to the ground state. Since the β particles are highly relativistic, v_β differed very little from c and neglecting the decay scheme of

^{14}Be resulted in negligible changes in $v_\beta = 0.995c$. Solving Eq. 2.14 for the flight path we get

$$d = \frac{v_n \cdot v_\beta \cdot k(C_n - C_\beta)}{v_n - v_\beta}. \quad (2.15)$$

The calibrated distance used for the analysis, 100.9 ± 0.3 cm, was simply the average of above two values, where the error is dominated by the systematic error, taken from the differences of the two measurements.

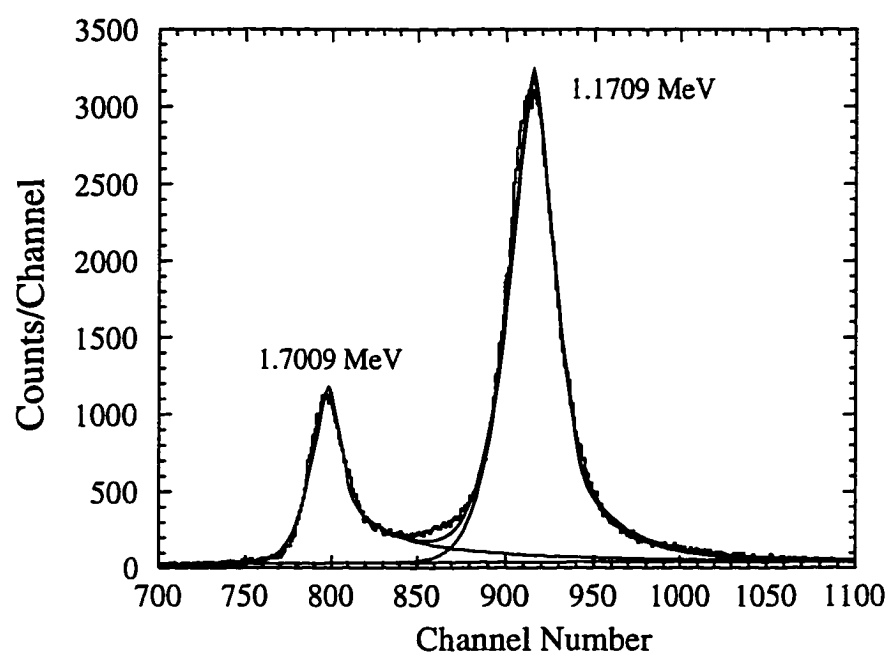


Figure 2.7 Time-of-flight spectrum for ^{17}N data.

TABLE 2.5

CENTROID, VELOCITY, AND CALIBRATED DISTANCE
FOR ^{17}N NEUTRON PEAKS

Energy (MeV)	Centroid	FWHM	Velocity (cm/ns)	Distance (cm)
1.7003 ± 0.0017	798.13 ± 0.11	22.77	1.8012 ± 0.0009	101.12 ± 0.03
1.1709 ± 0.0008	915.14 ± 0.06	30.84	1.4953 ± 0.0005	100.59 ± 0.09

2.7 Neutron Efficiency Calibration

The measured intrinsic neutron efficiency data points were found from three sources. First the efficiency for the 1.1709 and 1.7003 MeV ^{17}N neutron peaks were obtained from their known branching ratios [Aj82] (listed in Sec. 2.5.3). Second the efficiencies for the 0.810 and 1.714 MeV groups of the β -delayed neutron decay of ^{16}C were obtained by a reanalysis of the data of Scheller *et al.* [Sc94] who used the same neutron detector array and discriminator settings as in the present experiment. Last, the Pu-Be source was used to obtain the efficiencies for 1.7, 2.2, 2.8, 3.4, 4.0 and 4.6 MeV neutrons, determined in this experiment by direct comparison to the count rate found in a small cylindrical neutron detector of known efficiency. These measured data points were compared to a Monte Carlo calculation using the code KSUEFF [Ce79] that is based on a program [Ku64] written by R. J. Kurz.

2.7.1 ^{17}N data points

Intrinsic efficiency is the percentage of incident neutrons of a given energy that are detected and does not include the solid angle subtended by the detector. It is a property of the detector material, the threshold setting, and the geometry (as will be explained below). For the ^{17}N data, the intrinsic efficiency (ϵ_{int}) for a particular neutron group is found from

$$\epsilon_{\text{int}} = \frac{\text{no. detected}}{\text{no. impinged}} = \frac{\text{no. detected}}{\epsilon_{\text{geo}} \cdot \text{B.R.} \cdot N_{\beta}}, \quad (2.16)$$

where the geometrical efficiency is given by $\epsilon_{\text{geo}} = \Omega/4\pi$, and Ω is the solid angle subtended by the detector. The number of β particles (N_{β}) that are emitted during the beam-off period was found from a fit of the raw (ungated) decay spectrum. The branching ratios for the ^{17}N neutron peaks are well known and were given in Sec.

2.5.3 [Aj82]. The solid angle of the fifteen detectors used (as given in Sec. 2.2) was 1.78 ± 0.03 sr or $14.2 \pm 0.2\%$ geometrical efficiency.

The ^{17}N decay curve was subject to considerable rate dependent dead time that distorted its shape (Fig. 2.8). On semilog plot an exponential decay curve should be represented by a straight line, but notice that in Fig. 2.8 the plot curves downward at small times (compared to the corrected histogram). This indicates that the dead time is greater at the beginning of the curve, consistent with a rate dependent dead time. We were able to determine the total dead time for the ^{17}N data (18.5%) by using two scalers: one measuring the total number of events, and the other measuring the total number of events while the computer was live. In any detection system, when an event is recorded, the acquisition system is unable to process data or is dead for a length of time τ called the dead time period. If the actual event rate n is small enough so that the probability that two events will have overlapping dead time periods is small (assumed here because the dead time given by the scalers was not large), then the observed event rate m , corrected for dead time, is given by [Kn79c]:

$$m = n(1 - n\tau), \quad (2.17)$$

where n represents the number of events per unit time, and the product $n\tau$ is the total dead time per unit time or the fraction of the total elapsed time the computer is dead. Solving for n we get the doubled valued solution:

$$n = \frac{1 \pm \sqrt{1 - 4\tau m}}{2\tau}. \quad (2.18)$$

Because of the small rate limit, $n \rightarrow 0$ as $m \rightarrow 0$, and, thus, $n = [1 - (1 - 4\tau m)]/2\tau$

Equation 2.17 was used to correct the spectrum of Fig. 2.8 for dead time, channel by channel, and the resulting spectrum was fitted with a single exponential and constant background using LIFE5 [Sc94]. (This program will be described later in Sec. 3.1.2.) The period τ was optimized by minimizing the reduced χ^2 of the fit shown in

Fig. 2.8. Allowing the half-life and the constant background to vary resulted in $\chi^2 = 1.15$, $\tau = 140 \mu\text{s}$, a half-life of 4.33 s, and a total ^{17}N yield of 2.40×10^7 . The total live time corresponding to this correction was found by dividing the total number of raw counts (2.04×10^7 , Fig. 2.8) by the total number of corrected counts (2.41×10^7 , Fig. 2.8), resulting in a live time of 84.6% (dead time 15.4%). This is quite comparable with the dead time found from the scaler information (18.5%). Another fit was performed with the half-life fixed to the accepted value (4.17 s [Oh76]) to determine the systematic error in the fit, which resulted in $\chi^2 = 1.21$, $\tau = 160 \mu\text{s}$, a ^{17}N yield of 2.48×10^7 , and a total dead time equal to 18.0%. The two results were averaged to obtain the resultant yield and the systematic error was determined from the two ^{17}N components of the activity curves and the various dead times obtained. This resultant yield N_β was $(2.4 \pm 0.2) \times 10^7$ (where the statistical error was negligible). The raw yields of the ^{17}N β -delayed neutron groups (column 2, Table 2.6) were divided by their corresponding live times to account for the fact that the live time is folded into the time-of-flight spectrum, and these results are listed in Table 2.6 (column 3).

The neutron efficiencies listed in Table 2.6 below were found by inserting the following values in Eq. 2.16: the corrected yields given in Table 2.6 (no. detected), the geometrical efficiency given above (ϵ_{geo}), the branching ratios listed in Sec. 2.5.3 (B.R.), and the ^{17}N yield above (N_β).

2.7.2 ^{16}C data of Scheller *et al.*

Just prior to the NSCL experiment, another experiment was performed by Scheller *et al.*, who measured the β -delayed neutron decay of ^{18}N [Sc94] using the same detector as in the present experiment. During that experiment, a ^{16}C beam was used, and because the same thresholds were used as the present experiment, we could directly compare the data of both experiments.

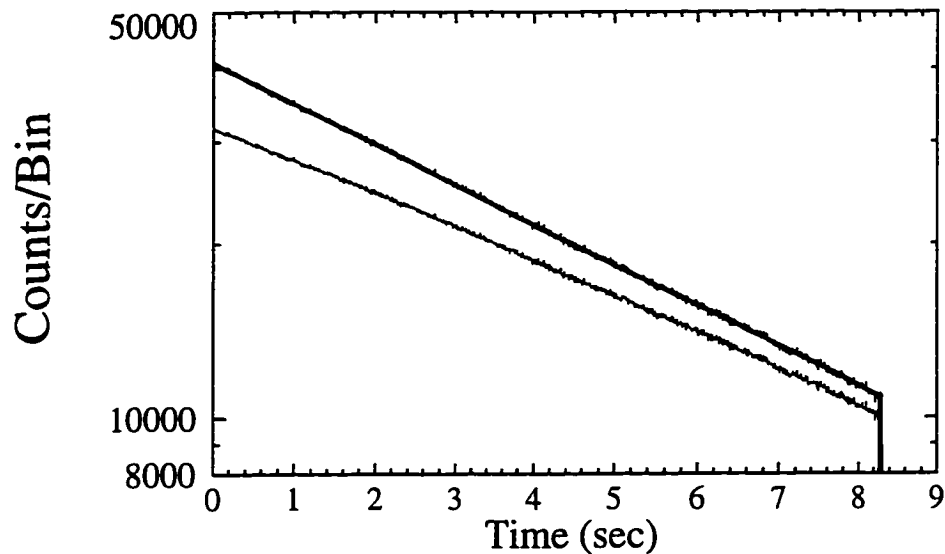


Figure 2.8 Plot of raw ^{17}N decay spectrum (bottom histogram) and that corrected for dead time (top). The distortion caused by rate dependent dead time is clearly seen in the bottom histogram. The top histogram was fitted with a single exponential and constant background (bold line). See text.

TABLE 2.6

YIELD AND NEUTRON DETECTION EFFICIENCY FOR ^{17}N PEAKS

Energy (MeV)	Raw Yield (counts)	Corrected Yield (counts)	Efficiency (%)
1.7003 ± 0.0017	$44200 \pm 400 \pm 9500$	$52200 \pm 500 \pm 11200$	$22. \pm 6.$
1.1709 ± 0.0008	$121900 \pm 600 \pm 7500$	$144100 \pm 700 \pm 8900$	8.5 ± 0.7

Scheller *et al.* fitted the time-of-flight data by using a hypergaussian line shape with a background consisting of a constant background plus a polynomial to represent the slowing increasing component toward lower neutron energies [Sc92]. Unlike Raimann *et al.* [Ra96], Scheller *et al.* allowed the shape parameters for the various peaks in the fit to vary independently [Sc92]. Because the line shape is more properly described as a hypergaussian (or perhaps gaussian) with an exponential

tail on the long time-of-flight side only, we decided to reanalyze their data, so that the fits obtained would be more consistent with our analysis. The ^{16}C data of Scheller *et al.* [Sc94] is shown below in Fig. 2.9. Notice that the 1.1703 MeV ^{17}N neutron peak was present as an impurity. Because the 1.714 MeV ^{16}C neutron peak has nearly the same energy as the 1.7003 MeV ^{17}N peak, the two were indistinguishable, and it was necessary to subtract the ^{17}N impurity from the ^{16}C peak. This was determined from ^{17}N data obtained during the same experiment. The fit of the ^{17}N data is shown in Fig. 2.10. The ratio of the 1.7003 MeV yield to that at 1.1709 MeV was $0.218 \pm 0.006 \pm 0.040$. The correct 1.714 MeV ^{16}C yield ($5990 \pm 80 \pm 260$) was found by multiplying the above ratio and the ^{17}N 1.1709 MeV yield shown in Table 2.7 ($660 \pm 30 \pm 30$) and subtracting the result from the raw (uncorrected) ^{16}C yield listed in Table 2.7 ($6140 \pm 80 \pm 260$). Next, Eq. 2.16 was used to calculate the neutron efficiency, where the geometrical efficiency was the same as in the present experiment. The number of ^{16}C β decays [Sc94] was found by fitting the decay spectrum of ^{16}C with a two component exponential (including the ^{17}N impurity) and a constant background using LIFES [Sc94]. The intrinsic neutron efficiencies found were $0.92 \pm 0.03 \pm 0.06\%$ for the 0.808 MeV peak and $17 \pm 2 \pm 2\%$ for the 1.714 MeV peak.

2.7.3 Pu-Be data points

A Pu-Be source was used to obtain measured neutron efficiency data in the energy range of 1.4 to 7.3 MeV, thus extending the neutron efficiency curve to higher energies. The efficiency was found by direct comparison to the count rate in a small, cylindrical liquid scintillator, the "standard" detector (BC 501,[§] radius 3.38 cm and depth 3.6 cm), whose efficiency could reliably be calibrated to within

[§]Density 0.901 g/cm^3 and hydrogen-to-carbon ratio 1.287.

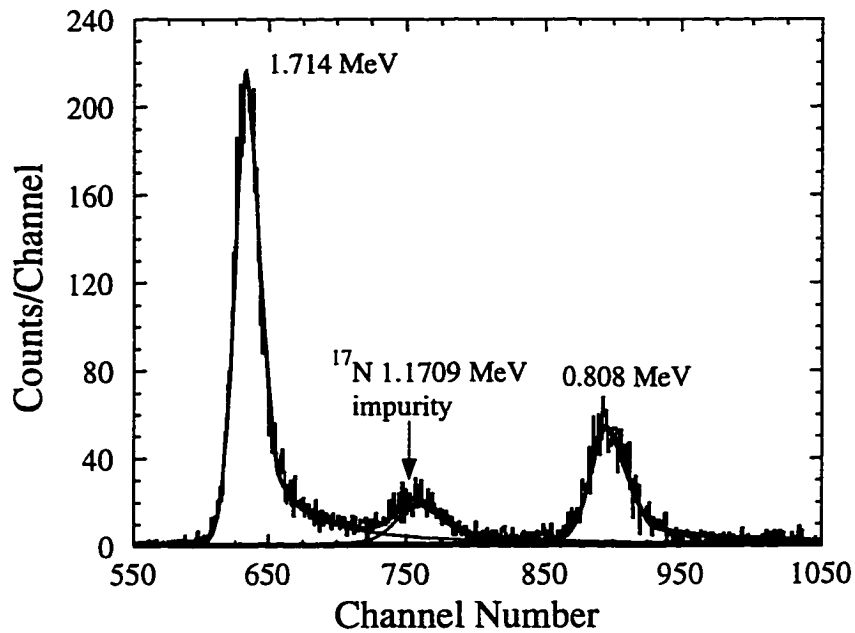


Figure 2.9 Refit of the ^{16}C data of K. W. Scheller *et al.* [Sc94]. The energies of the peaks here and below are clearly shown (including the ^{17}N impurity).

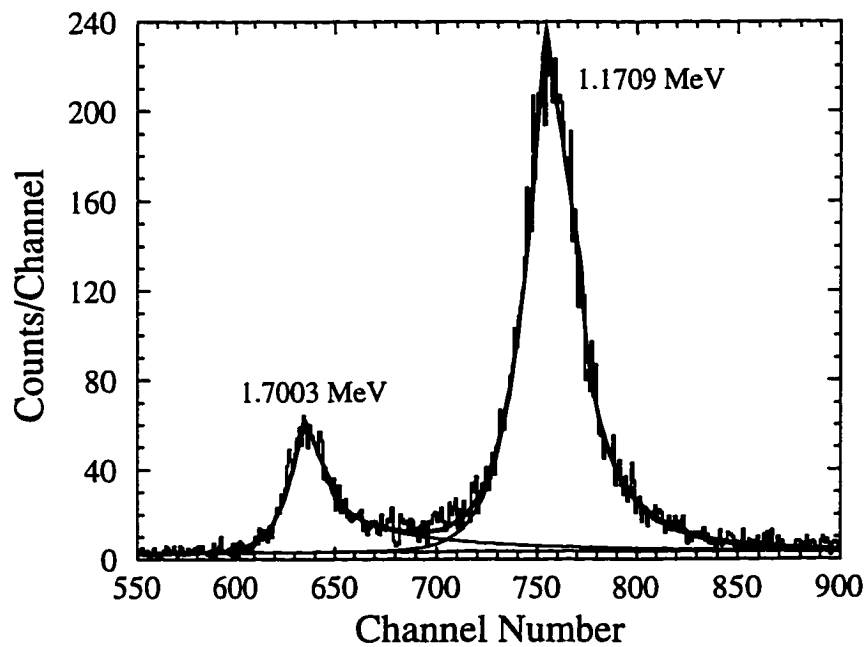


Figure 2.10 A refit of the ^{17}N data Scheller *et al.* [Sc94].

10% using the Monte Carlo code KSUEFF [Ce79]. (Details on this code will be given below.) The ^{17}N data were used to calibrate the flight path of the standard detector (see Sec. 2.6). The threshold of this detector was low enough so that the 0.3828 MeV peak was clearly visible. Therefore it was possible to get three measurements of the distance (Table 2.7). The calibrated distance used in the analysis was the average of the three values (weighted by their respective uncertainties), 99.2 ± 0.6 cm. We assumed that the neutrons stopped at the center of the detector, and therefore the average distance to the front face of the detector would simply be the above distance minus one-half of the depth of this detector (1.8 cm), giving 97.4 ± 0.6 cm. The solid angle subtended by the detector, 3.77 ± 0.06 msr, was found by running the Monte Carlo code of Wielopolski [Wi77], which assumes a point source.

TABLE 2.7
CALIBRATED DISTANCE OF STANDARD DETECTOR (^{17}N PEAKS)

Energy (MeV)	Distance (cm)
0.3828 ± 0.0009	98.7 ± 0.4
1.1709 ± 0.0008	100.0 ± 0.3
1.7003 ± 0.0017	98.8 ± 0.4

The threshold of the detector was determined by plotting the light output of the standard detector versus the energy of the neutrons as derived from time-of-flight data, as shown in Fig. 2.11. The time-of-flight spectrum was converted to an energy spectrum by rebinning the data according to the equation below

$$E_k = m_0 c^2 (\gamma - 1) = m_0 c^2 \left(\frac{1}{\sqrt{1 - (v_n^2/c^2)}} - 1 \right), \quad (2.19)$$

obtained by solving for E_k in Eq. 2.11. The quantity v_n was found from Eq. 2.14, where $v_\beta = c$, because the prompt peak is due to photons instead of electrons. The

light output is proportional to the energy deposited by the neutrons, and the energy from time-of-flight is a measure of their kinetic energy. Depending on how the neutrons scatter, a wide range of energies can be deposited in the scintillator but never more than the kinetic energy of the neutrons (indicating that they have completely stopped). Because both axes of Fig. 2.11 measure neutron energy in two independent ways, they are linearly related to one another and the curve which corresponds to where the energy deposited equals the kinetic energy of the neutrons is a straight line (indicated in Fig 2.11 by α). All the real neutron events must lie below this line. There is also a small y-value (light output) below which no events occurred (marked by β in Fig. 2.11) that was due to the threshold of the detector. The energy corresponding to the intersection of α and β is the threshold of the detector. In this case, it was 210 ± 30 keV, where the main systematic uncertainty came from determining α and β . After finding the threshold, we calculated the efficiency of the standard detector using KSUEFF.

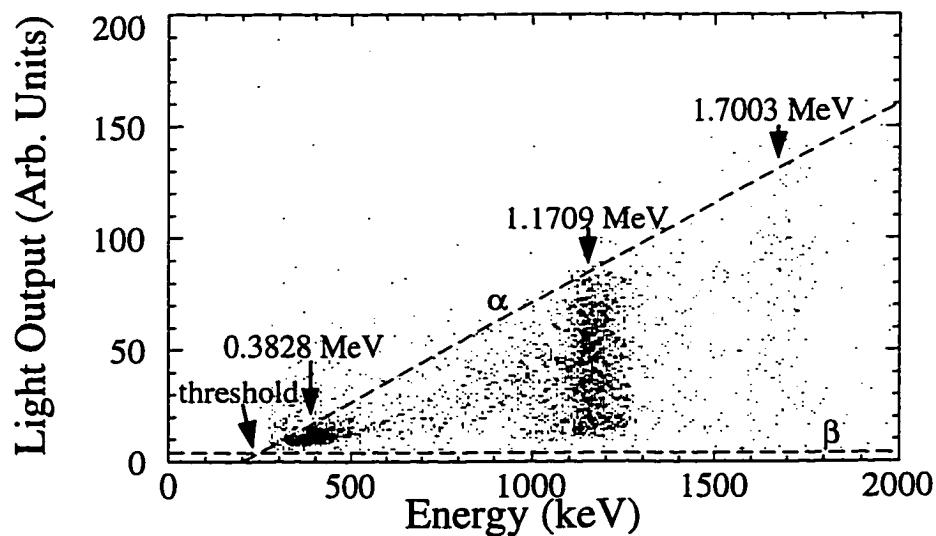


Figure 2.11 Plot of light output vs. neutron energy (calculated from time-of-flight) in the standard detector for the ^{17}N data. Note that the 1.7003 MeV group is very difficult to see in this two-dimensional plot. This plot was used to determine the threshold of the standard detector.

The Pu-Be spectrum was divided into energy bins for both the neutron and standard detector time-of-flight spectra (see Fig. 2.12). The energy bins chosen are listed in Table 2.8 and indicated by dashed lines in figures 2.12a and 2.12b. Equations 2.19 and 2.14 were used to convert the energies into channel numbers. The neutron efficiency of the detector array was found by starting with the definition of intrinsic efficiency (Eq. 2.16):

$$\epsilon_{\text{array}} = \frac{\text{no. detected}}{\text{no. impinged}}, \quad (2.20)$$

where ϵ_{array} is the intrinsic efficiency of the array detectors. The total number of neutrons emitted can be expressed in terms of measured quantities associated with this detector: $\text{no.}_{\text{stand.}} / [(\Omega_{\text{stand.}}/4\pi) \cdot \epsilon_{\text{stand.}}]$, where $\text{no.}_{\text{stand.}}$ is the sum of the neutron counts above background in the energy bin in question for the standard detector, the quantity $\Omega_{\text{stand.}}$ is the solid angle of the standard detector (the geometrical efficiency is then $\Omega_{\text{stand.}}/4\pi$), and $\epsilon_{\text{stand.}}$ is the intrinsic neutron efficiency of the standard detector for an energy equal to the average energy of the bin. The total number of neutrons emitted times the geometrical efficiency of the array, $\Omega_{\text{array}}/4\pi$, gives the number of neutrons that impinge on the array. Dividing this into the number of neutrons detected by the array detector, $\text{no.}_{\text{array}}$ gives us the following expression for ϵ_{array} :

$$\epsilon_{\text{array}} = \frac{\text{no.}_{\text{array}}}{\text{no.}_{\text{stand.}}} \cdot \frac{\Omega_{\text{stand.}}}{\Omega_{\text{array}}} \cdot \epsilon_{\text{stand.}}, \quad (2.21)$$

where the relative error in ϵ_{array} is found by adding the relative errors of the terms above in quadrature. (The errors in $\text{no.}_{\text{array}}$, $\text{no.}_{\text{stand.}}$, and $\epsilon_{\text{stand.}}$ are given in Table 2.8 below. The error in $\Omega_{\text{stand.}}$ was given above in this section, and Ω_{array} was given in Sec. 2.2).

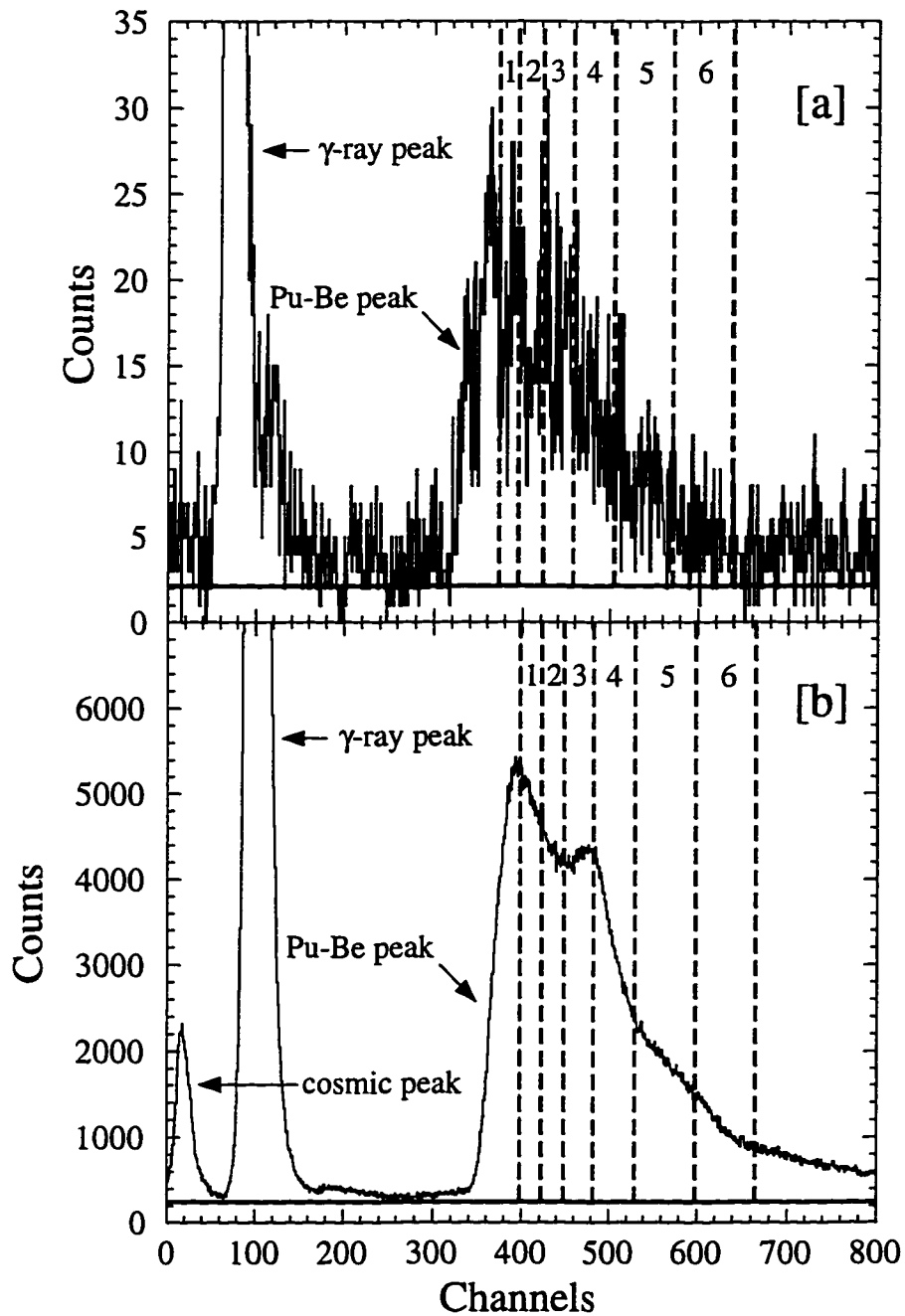


Figure 2.12 Plots of the time-of-flight spectra of the standard detector [a] and array detector [b] (sum of all 15) for the Pu-Be source. Both diagrams show the energy bins (dashed lines) used to determine neutron detection efficiency from this source. The solid bold line is the constant background used. See text for more details.

TABLE 2.8

NEUTRON EFFICIENCY AND RELATED INFORMATION
FOR EACH ENERGY BIN

No. ^a	Ave. Energy (MeV)	Energy Limits (MeV)	Counts Above Background		Neutron Efficiency	
			Standard Detector	Array Detector	Standard Det. (%)	Array Det.'s (%)
1	1.7	1.5 – 1.9	220±20	60500±300	38.6±3.9	22.0±2.8
2	2.2	1.9 – 2.5	400±30	114200±400	36.2±3.6	21.7±2.7
3	2.8	2.5 – 3.1	480±30	143600±400	33.3±3.3	21.0±2.5
4	3.4	3.1 – 3.7	510±30	140800±400	31.6±3.2	18.6±2.3
5	4.0	3.7 – 4.3	420±30	112100±400	30.3±3.0	17.2±2.1
6	4.6	4.3 – 4.9	360±30	109500±300	28.2±2.8	18.0±2.2

2.7.4 Monte Carlo calculation and determination of neutron efficiency curve

The code KSUEFF [Ce79] is a Monte Carlo program that models the neutron detection process and calculates the neutron detection efficiency as a function of neutron energy, given the composition, geometry, and threshold of a plastic or liquid scintillator. The thresholds of the neutron detectors were not well known, since the method of determining the threshold discussed in Sec. 2.7.4 did not work well for the neutron detectors as it was difficult to determine the line α in the plot of light output versus energy derived from time-of-flight for these detectors (Fig. 2.13). Therefore we matched the measured data points (Fig. 2.14) to a fit using KSUEFF to produce a smooth neutron efficiency curve. This was done by varying the threshold (which is an input parameter to KSUEFF) and minimizing χ^2 . A limited description of KSUEFF is given below and a more complete description of the algorithm and program logic is given in [Ce79].

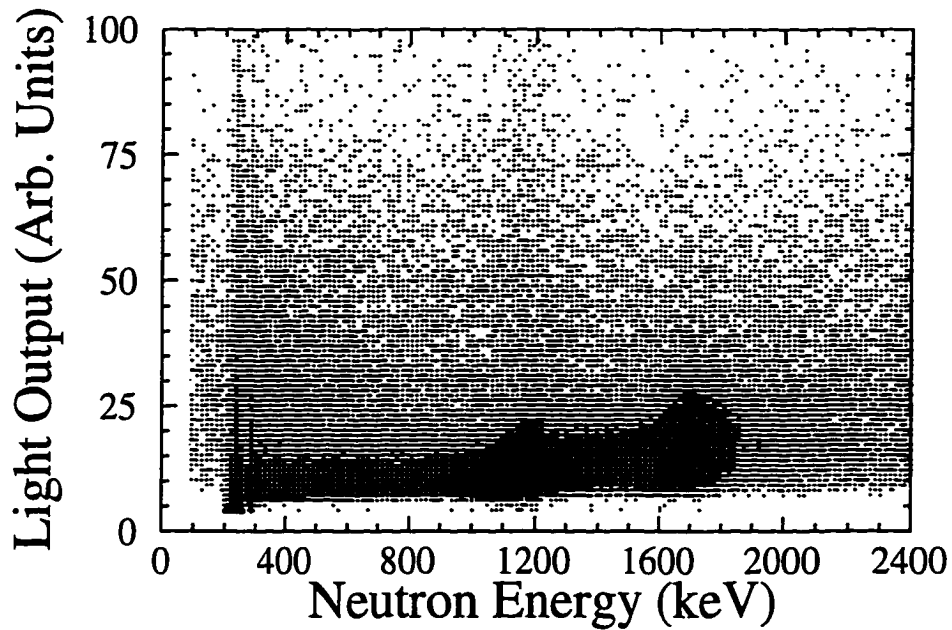


Figure 2.13 Plot of neutron energy versus light output for neutron detectors. Note that the line a, as shown in Fig. 2.11, is very difficult to determine here.

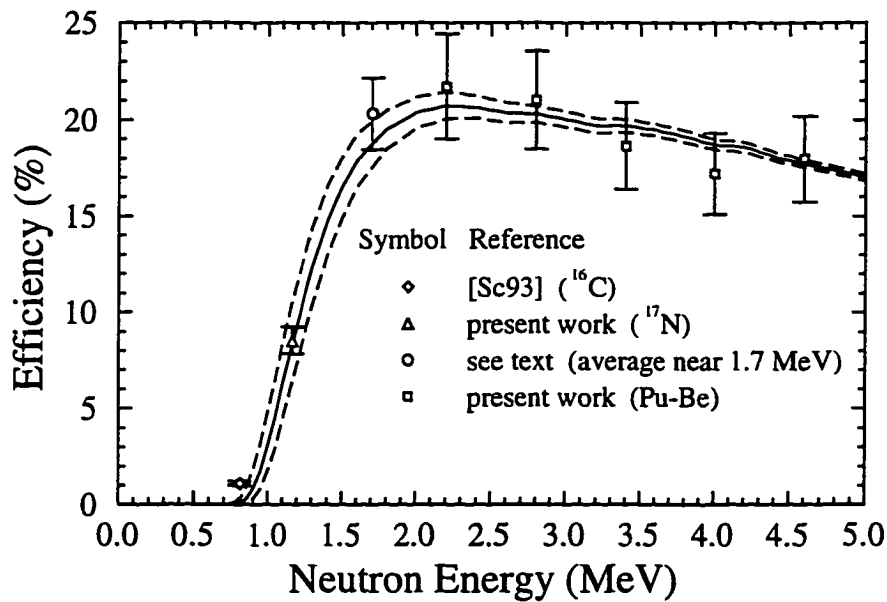


Figure 2.14 Plot of the measured neutron efficiency data points and the fit (solid line) obtained from KSUEFF. The dashed lines are the best estimate of the error in the fit due to the error in the threshold.

The program KSUEFF calculates neutron efficiency by tracing the path of randomly distributed neutrons as they scatter within the detector. This program determines what fraction of neutrons impinging on the detector deposit a given minimum amount of energy (the threshold) and considers these neutrons to have been detected. Neutrons that scatter out of the active volume of the detector without depositing the minimum required energy are not counted. Because neutrons are uncharged particles, they are detected only by the interactions they make with the protons and carbon atoms that are present in the scintillator. The program KSUEFF uses the cross sections (as a function of energy) of the following reaction channels to calculate the amount of energy deposited: (1) elastic scattering from protons, $n + p \rightarrow n + p$, (2) elastic scattering from carbon, $n + C \rightarrow n + C$, (3) inelastic scattering from carbon, $n + C \rightarrow n + C + \gamma$, and the following inelastic reactions: (4) $n + C \rightarrow \alpha + {}^9\text{Be}$, (5) $n + C \rightarrow n + 3\alpha$, and (6) $n + C \rightarrow p + {}^{12}\text{B}$ [Ce79]. At the neutron energies encountered in this analysis (about 0 – 5 MeV) only the elastic reaction channels, (1) and (2), are significant [Ce79]. The energy deposited in the scintillator is defined in terms of *electron equivalent energy*, which is the kinetic energy of a stopped electron that would yield the same amount of light as the impinging neutron. The conversion factor used in the program [Ce79] is given as

$$T_e = a_1 \cdot T_p - a_2 [1 - \exp(-a_3 \cdot T_p^{a_4})], \quad (2.22)$$

where T_e is the electron equivalent energy, T_p the proton (or neutron) energy and a_1 , a_2 , a_3 , and a_4 are constant "light coefficients". The light coefficients for a number of different types of scintillators are listed in [Ce79]. For BC-412, we used the coefficients for NE-102 ($a_1 = 0.95$, $a_2 = 8.0$, $a_3 = 0.1$, and $a_4 = 0.90$), because it is a plastic scintillator with density and hydrogen-to-carbon ratios identical to those of BC-412. Since there was no exact match for BC-501, we chose a material that matched it most closely: NE-213, a liquid scintillator with density 0.874 g/cm^3 and

hydrogen-to-carbon ratio 1.213. (Compare to density 0.901 g/cm² and hydrogen-to-carbon ratio of 1.287 for BC-501.) The light coefficients for NE-213 are $a_1 = 0.83$, $a_2 = 2.82$, $a_3 = 0.25$, and $a_4 = 0.93$ (used for the standard detector). The hemispherically bent rectangular detector illuminated by a point source was approximated by a simpler geometry of a rectangular prism uniformly illuminated at normal incidence. Once the parameters associated with the detector composition and geometry and the light coefficients were determined, the only parameter that was allowed to vary was the threshold.

In Fig. 2.14, the data point at 1.7 MeV ($20.3 \pm 1.9\%$) was the weighted average of the three measured points: $22.0 \pm 2.8\%$ (1.7 MeV, Pu-Be data), $22.4 \pm 5.9\%$, (1.7003 MeV, ¹⁷N data), $17.5 \pm 2.3\%$ (1.714 MeV, ¹⁶C data). The threshold was varied and the best fit to the data was found by minimizing the χ^2 of the fit. Reference [Ce79] states that KSUEFF is reliable to at least 10% for neutron energies above 1 MeV. Because the efficiency is ill-defined near threshold, we assigned a constant absolute uncertainty equal to 10% of the calculated efficiency at 1.7 MeV (near the maximum) to the entire curve. The uncertainty in the fit was determined by plotting the χ^2 (not the reduced χ^2) as a function of the threshold and using the relationship between the standard deviation (with respect to each fitted parameter) σ_j and the second derivative of the χ^2 with respect to the fitted parameters a_j [Be92]:

$$\sigma_j^2 = 2 \left(\frac{\partial^2 \chi^2}{\partial a_j^2} \right)^{-1} \quad (2.23)$$

Figure 2.15 shows χ^2 as a function of the threshold (expressed in electron equivalent). According to P. Bevington [Be92], the χ^2 varies quadratically near the minimum. Therefore, we made a non-linear fit to a parabola using a program XVGR [Tu92]. The resulting equation of the fitted curve (bold line) was $y = 147.12 + 1722.4x + 5131.5x^2$. The resulting threshold was 0.168 ± 0.014 MeV ee (electron

equivalent) with a reduced χ^2 of 0.370. The second derivative, $d^2y/dx^2 = 10263$, was used in Eq. 2.23 above to find the error in the threshold.

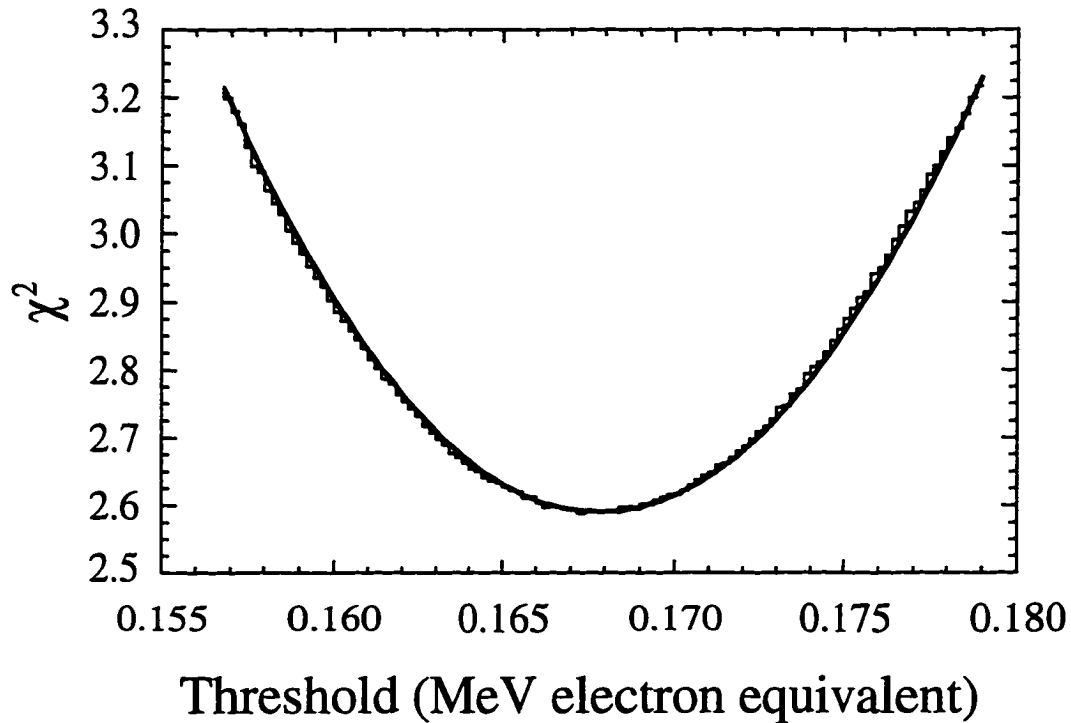


Figure 2.15 Plot of the χ^2 as a function of the threshold of the neutron detectors. The histogram is the χ^2 curve and the bold line is a quadratic fit to that curve using the program XVGR (see text).

No calibration of the neutron detector light output was performed, but the same detector array was used in Ref. [Ha91] as the present experiment. Therefore the energy resolution of these detectors was approximated by using the data in the above reference, where the Compton edges for ^{60}Co and ^{134}Cs were measured (Fig. 2.16). The edge was considered to be at the location corresponding to $\frac{1}{2}$ the total height of the edge (see Fig. 2.16), and the resolution was considered to be the difference in light output (electron equivalent energy) between the locations corresponding to $\frac{1}{4}$ and $\frac{3}{4}$ of the total height. The resolution for each plot was then

defined as

$$\text{Resolution} = \frac{CH_{1/4} - CH_{3/4}}{CH_{\text{edge}}} \cdot E_{\text{edge}}, \quad (2.24)$$

where $CH_{1/4}$, $CH_{3/4}$, and CH_{edge} are the location in channels of one-fourth, three-fourths, and one-half of the total height of the Compton edge, respectively, and E_{edge} is the energy of the edges as indicated in Fig. 2.16. The resolution obtained were 0.11 MeV for the ^{60}Co edge, and 0.064 and 0.058 MeV for the 0.61 and 0.43 ^{134}Cs edges, respectively. From Ref. [Kn79d], the energy resolution of a scintillator should be proportional to the square root of the energy. Thus, scaling all these resolutions to 0.43 MeV yields 0.072 MeV for the ^{60}Co edge and 0.054 MeV and 0.058 MeV for the 0.61 MeV and 0.43 MeV ^{134}Cs edges, respectively. We used the average of these three numbers, 0.061 MeV at 0.43 MeV (electron equivalent), as an estimate of the resolution of the neutron detectors. Scaling this resolution to the energy at threshold (0.168 MeV) yields 0.038 MeV. Consequently, the effective threshold considering the finite resolution of the neutron detectors is $0.130 \pm_{0.014}^{0.041}$ MeV ee. The lower uncertainty is simply the error in the threshold determined from Fig. 2.14 (0.014 MeV), and the upper uncertainty is this error (0.014 MeV) and the resolution (0.038 MeV) added quadratically. Because neutron energy is the experimentally measured quantity, one would like to know the threshold in terms of neutron energy, which can be found from Eq. 2.22. This equation cannot be solved analytically, but we used the program MAPLE [Wa94] to solve for the effective threshold above (0.130 MeV) and obtained a neutron threshold of 0.77 ± 0.13 MeV.

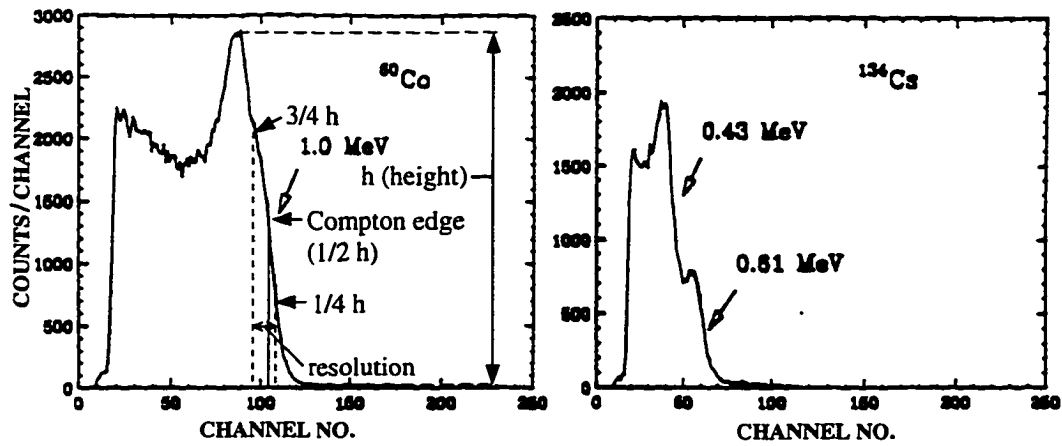


Figure 2.16 Plot of the light output of the neutron detectors measured by R. Harkewicz [Ha91] for a ^{60}Co and ^{134}Cs γ -ray source. The position of the Compton edge and the method of finding the resolution are shown for the plot of the ^{60}Co source.

CHAPTER 3

ANALYSIS AND RESULTS OF THE NSCL EXPERIMENT

This chapter describes the analysis and presents the results for the first experiment performed at the NSCL. First, the analysis and results for the β decay activity spectrum (both assumed and that in coincidence with emitted neutrons) are presented. Second, the neutron time-of-flight analysis and results (including the subtraction of a ${}^{11}\text{Li}$ contamination) are described. Third, the analysis and results of the γ -ray data are discussed. Finally, some of the results are briefly discussed in the context of the second experiment.

3.1 Analysis of β -decay Activity

The analysis of the raw β -decay activity is important because it determines the total number β -decays that occurred during the beam-off period, from which the branching ratios and $\log ft$ values of various β transitions corresponding to observed neutron and γ -ray lines can be computed. The analysis of the decay curve requiring β - n coincidence accurately determines the half-life of the β -decay, and verifies that the observed neutron groups do indeed result from the decay of ${}^{14}\text{Be}$.

3.1.1 Analysis of the ungated decay curve

The total number of ${}^{14}\text{Be}$ β decays was determined by fitting the ungated (raw) decay spectrum obtained from the Ortec RC014 Real Time Clock [Or73]. The 10 ms on/40 ms off duty cycle was used for this fit, because it allowed a more accurate

determination of the contribution of the daughter decays. The fit was complicated by the presence of the three daughter activities (^{14}B , ^{13}B , and ^{12}B with half-lives 13.8 ± 1.0 ms [Aj91], 17.36 ± 0.16 ms [Aj91], 20.20 ± 0.02 ms [Aj90], respectively) that not only have half-lives on the same order of magnitude as the beam-off period but also do not differ enough from each other to be easily distinguished. A computer program called GRAPH [Be92b] was written to model the growth and decay of ^{14}Be , its daughters, and the impurities for each beam-on/off cycle.

Initially, we could not assume that ^{14}Be , its daughters, and the impurities were detected by the start detector with equal efficiency. The β -decay end point energies of these nuclides (weighted by the branching ratios and Q values for decay to daughter states) are very high, ranging from about 13.1 MeV (for ^{13}B [Aj91]) to 16.2 MeV (for ^{14}Be [Au93] where we have assumed decay to the ground state). Since the average β^- decay energy is one-third of the end point energy, the average electron energy ranges from 4.4 to 5.4 MeV, and consequently the electrons are minimum ionizing and should have approximately identical energy losses. We used Ref. [Pa72] to calculate these energy losses in terms of the mass stopping power [$1/\rho(dE/dx)$], where ρ is the density and (dE/dx) is the linear stopping power. The mass stopping power for hydrogen and carbon were interpolated from the values given in Ref. [Pa72], and the value for BC 412 was found using the relationship [Le87]:

$$\frac{1}{\rho} \left(\frac{dE}{dx} \right) = w_1 \frac{1}{\rho_1} \left(\frac{dE}{dx} \right)_1 + w_2 \frac{1}{\rho_2} \left(\frac{dE}{dx} \right)_2, \quad (3.1)$$

where the subscripts refer to each element i of the compound or mixture and w represents the fractional abundance by weight of each element. For BC 412, the ratio of the number of hydrogen to carbon atoms (hydrogen-to-carbon ratio) was 1.104. Given the atomic weights of 1.0079 g/mol. for hydrogen and 12.011 g/mol. for carbon, the fractional abundance by weight in BC 412 was 0.0848 for hydrogen and 0.9152 for carbon. It was necessary to multiply the result by the density of BC 412

(1.032 g/cm³) to obtain the linear stopping power. Using Ref. [Pa72] we determined that the linear stopping power for electrons in BC412 in the energy range of 4.4 to 5.4 MeV varied from 1.98 to 2.03 MeV/cm, differing by only 2.5%. Because the energy loss of the electrons is much greater than the threshold energy of the implantation detector as indicated by its high β -detection efficiency ($79 \pm 14\%$, see Sec. 3.5), the β -detection efficiencies for ¹⁴Be and its daughters are nearly identical. Since the impurities are not implanted at the same depth into the plastic, their β -detection efficiencies cannot be assumed to be the same as that of ¹⁴Be, but (as shown below) such impurities were found to be negligibly small (well within systematic error) in the fit of the raw β -decay curve. Therefore the β -detection efficiencies for all nuclei (parent, daughters, and impurities) were assumed to be the same.

The first step in fitting the β -decay curve is to determine the mathematical form of the β -decay activity as a function of time, which comes from three sources: the ¹⁴Be parent, the daughters (¹²B, ¹³B, and ¹⁴B), and the impurities (³H, ⁶He, ⁸He, and ¹¹Li). During the beam-on period, the number of parent nuclei N_1 increases due to the implantation of nuclei at rate R and decreases due to its radioactive decay with decay constant λ_1 . The decay constant is the probability per unit time that an atom will decay, so that the number of atoms that decay per unit time is λN . Thus

$$\frac{dN_1'}{dt'} = R - \lambda_1 N_1', \quad (3.2)$$

where dN_1'/dt' is the rate at which the number of parent nuclei changes. The primes indicate beam-on quantities and the subscripts 1, 2, and 3 refer to parent, daughter, and impurity respectively. If t' is the elapsed time since the start of the beam-on period, the solution to the above differential equation is

$$N_1'(t') = \frac{R}{\lambda_1} (1 - e^{-\lambda_1 t'}). \quad (3.3)$$

We measure the activity $\mathcal{A}(t')$, which is equal to the number of decays per unit time λN ; therefore

$$\mathcal{A}_1(t') = \lambda_1 N_1' = R(1 - e^{-\lambda_1 t'}). \quad (3.4)$$

The daughter activities decrease due to radioactive decay but also increases because of the decay of the parent. If we represent the decay constant of the daughter by λ_2 and the number of daughter nuclei by N_2 , then

$$\frac{dN_2'}{dt'} = \lambda_1 N_1' - \lambda_2 N_2' = R(1 - e^{-\lambda_1 t'}) - \lambda_2 N_2'. \quad (3.5)$$

Solving for the activity of the daughter $\mathcal{A}_2(t')$ yields

$$\mathcal{A}_2'(t') = \lambda_2 R \left[- \left(1 - \frac{\lambda_2}{\lambda_1 - \lambda_2} \right) e^{-\lambda_2 t'} - \frac{\lambda_2 e^{-\lambda_1 t'}}{\lambda_2 - \lambda_1} + 1 \right]. \quad (3.6)$$

If more than one daughter is present, then it is necessary to multiply Eq. 3.6 by the branching ratio p_i of the daughter i . Because the impurities build up and decay in a similar manner as the parent, we simply use Eq. 3.4 and multiply it by f_i , the fractional yield of the impurity i (for the present experiment see Table 2.3). If any of the daughters or impurities also had radioactive daughters, then it was necessary to use Eq. 3.6 iteratively, where $\lambda_2 R$ was replaced by the production rate of the process that created this daughter, until stable isotopes are reached. Unless the beam-off period is sufficiently long, it is possible there will be some residual activity at the start of the beam-on period. If \mathcal{A}_0 is the residual activity, then the change in the number of residual nuclei per unit time is

$$\frac{dN}{dt} = -\lambda N. \quad (3.7)$$

The solution is $(N_0/\lambda)e^{-\lambda t'}$, and the activity is given by

$$\mathcal{A}_0 e^{-\lambda t'}, \quad (3.8)$$

where N_0 and \mathcal{A}_0 are the initial yield and activity, respectively, and λ is the decay constant of the nuclide in question. If $t_{1/2}$ (the half-life) is defined as the time required for the parent activity to decay to half of its initial activity, it is related to the decay constant through the following equation:

$$\frac{1/2 \mathcal{A}_0}{\mathcal{A}_0} = \frac{1}{2} = e^{-\lambda t_{1/2}}. \quad (3.9)$$

Taking the natural logarithm of both sides of Eq. 3.9 we get

$$\begin{aligned} \ln 1/2 &= -\lambda t_{1/2}, \\ t_{1/2} &= \frac{\ln 2}{\lambda}. \end{aligned} \quad (3.10)$$

Thus this term was added to each of the activities found above, and all the equations that were used to calculate the beam-on activities are summarized in Table 3.1.

Since there is no production of the parent during the beam-off period, its activity is given by Eq. 3.8. The activity of each impurity is of the same form as Eq. 3.8 except that its initial activity is equal to that of the parent times f_i . The activity of the daughter is increased by the decay of the parent and decreased by its own decay yielding

$$\frac{dN_2}{dt} = \lambda_1 N_1 - \lambda_2 N_2. \quad (3.11)$$

Multiplying the solution by λ_2 gives the beam-off daughter activity:

$$\mathcal{A}_2 = \frac{\mathcal{A}_{10} \lambda_2}{\lambda_2 - \lambda_1} (e^{-\lambda_1 t} - e^{-\lambda_2 t}), \quad (3.12)$$

where \mathcal{A}_{10} is the initial activity of the parent. All the formulas for calculating beam-off activity are summarized below in Table 3.1.

TABLE 3.1
BEAM-ON AND -OFF ACTIVITIES

Beam-on activity		
No.	Type	Equation
1	parent	$\mathcal{A}'_1 = R(1 - e^{-\lambda_1 t'}) + \mathcal{A}'_{10} e^{-\lambda_1 t'}$
2	daughter	$\mathcal{A}'_2 = p_i \lambda_2 R \left[- \left(1 - \frac{\lambda_2}{\lambda_1 - \lambda_2} \right) e^{-\lambda_2 t'} - \frac{\lambda_2 e^{-\lambda_1 t'}}{\lambda_2 - \lambda_1} + 1 \right] + \mathcal{A}'_{20} e^{-\lambda_2 t'}$
3	impurity	$\mathcal{A}'_3 = f_i R(1 - e^{-\lambda_3 t'}) + \mathcal{A}'_{30} e^{-\lambda_3 t'}$

Beam-off activity		
No.	Type	Equation
4	parent	$\mathcal{A}_1 = \mathcal{A}_{10} e^{-\lambda_1 t}$
5	daughter	$\mathcal{A}_2 = \frac{\mathcal{A}_{10} \lambda_2}{\lambda_2 - \lambda_1} (e^{-\lambda_1 t} - e^{-\lambda_2 t}) + \mathcal{A}_{20} e^{-\lambda_2 t}$
6	impurity	$\mathcal{A}_3 = f_i \mathcal{A}_{10} e^{-\lambda_3 t}$

NOTE: The primes indicate beam-on quantities, and unprimed quantities indicate beam-off quantities. The symbol \mathcal{A}_x is the activity as a function of the time t (or t') where x is 1, 2, or 3 indicating parent, daughter or impurity, respectively. The initial activity at the start of each corresponding period is given by \mathcal{A}_{x0} . The quantities p_i and f_i are the branching ratio for the daughter i and the fractional yield for the impurity i , respectively.

The algorithm of GRAPH [Be92b] is as follows. First it was assumed that all activities were equal to zero at the start of the data run. Next, the beam-on activities of the ^{14}Be parent, daughters ^{12}B , ^{13}B , and ^{14}B , and impurities ^8He and ^{11}Li at the end of the first beam-off period were calculated using equations 1–3 of Table 3.1. (The impurities ^3H and ^6He were treated as part of the constant background because of their long half-lives (12.3 yr [Ti87] and 806.7 ms [Aj88], respectively.) These activities were then used as the initial beam-off activities (\mathcal{A}_1 , \mathcal{A}_2 , and \mathcal{A}_3 , Table 3.1) for the subsequent beam-off period. Equations 4–6 of Table 3.1 were then used to calculate the activities at the end of the beam-off period. These activities were taken to be the

initial residual activities (\mathcal{A}_{10} , \mathcal{A}_{20} , and \mathcal{A}_{30} , see Table 3.1) for the next beam-on period. New activities were calculated for each cycle in the data run. The beam-off activity for each component (parent, daughters, and impurities) was accumulated and binned separately into a histogram, where the width of each channel in time was the same as that in the decay spectrum. Once the accumulation was complete, the activities were added together to get the total curve. In addition, a constant background was also added to account for random coincidences and long-lived impurities. Finally, the calculated total curve was compared with the data, and the reduced χ^2 of the fit to the data was computed and used to optimize the parameters.

We used the data with the longer beam-off period (40 ms) to perform the fit shown in Fig. 3.1, because this period was equal to about 10 half-lives of the parent, when only 0.1% of the initial activity is still present. This allowed a better estimate of the background and the contribution of the daughters and the impurities. The background was determined by fitting the last 9.3 ms of the decay curve using a program called LIFES [Sc94] (this will be described in Sec. 3.2) with a two-component exponential and constant background where the half-lives are fixed to the accepted values for ^{14}B and ^{13}B (13.8 ± 1.0 ms and 17.36 ± 0.16 ms, respectively [Aj91]). The daughter ^{12}B was excluded because its branching ratio was too small ($5 \pm 2\%$) [Du88] to fit accurately, and its exclusion had a negligible effect on the background determination. The relative abundances of the remaining two nuclides were held fixed for the purpose of determining the background, where the branching ratios determined by Dufour *et al.* (14% for ^{14}B and 85% for ^{13}B) were used.

For the total fit, the background found above was used and held fixed, and the relative abundance of ^{12}B (measured by Dufour *et al.* [Du88]) was used and held

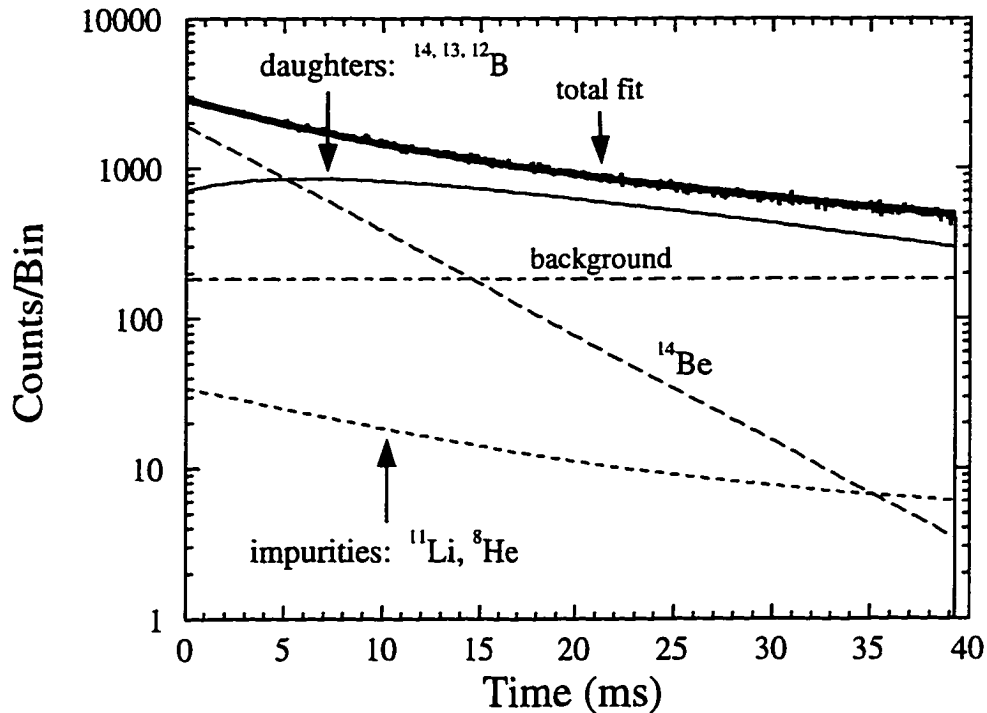


Figure 3.1 Fit of the raw 40 ms beam-off β -decay spectrum showing the parent, daughter, impurity, and background components.

held fixed, as well as those for ^{13}B and ^{14}B . The half-lives of these daughters were also held fixed to the accepted values [Aj91]. The computed implantation rate of ^{14}Be and its half-life were optimized by minimizing the χ^2 of the fit, giving a half-life equal to $4.8 \pm 0.4 \pm 0.2$ ms (whenever two uncertainties are given the first is statistical and the second is systematic) and an implantation rate of 60.4 ± 0.6 ions per second with a reduced $\chi^2 = 0.98$. The error in estimating the half-life and implantation rate contributed the majority of the systematic error. A fit was also performed with the half-life fixed to the value measured by Dufour *et al.* (4.35 ± 0.17 ms [Du88]) to get an estimate of the systematic error in the measured ^{14}Be yield. The fit shown in Fig. 3.1 resulted in a ^{14}Be yield of $(2.200 \pm 0.005 \pm 0.260) \times 10^5$. We used the yield of the β peak (Fig. 2.6), which should be proportional to the total number of β decays, to scale this to the total data set. Each β peak was fitted

with an asymmetric hypergaussian having a tail on the long time-of-flight side (see Sec. 2.6) to account for the distribution of β -particle energies (see Sec. 1.2). The background was insignificant. The yield of the β peak corresponding to the 40 ms beam-off data set was 93700 ± 300 , and that corresponding to the total data set was $(8.702 \pm 0.009) \times 10^5$. Thus the total ^{14}Be yield was $(2.04 \pm 0.01 \pm 0.24) \times 10^6$.

3.1.2 Analysis of the decay curve requiring β - n coincidence

Due to the complexity of the fit to the raw decay curve, it is difficult to accurately determine the half-life of ^{14}Be from these data. As discussed in Sec. 1.3, the neutrons resulting from the β decay of ^{14}Be should exhibit a half-life that is essentially that of the parent. Thus, by observing at the decay spectrum in coincidence with neutron groups, one should obtain a decay spectrum that consists of a single exponential curve plus a constant background resulting from random coincidences and very long-lived daughters and impurities.

We used the program LIFE5 [Sc94] to perform the above fit. This program can fit as many as five parent isotopes, along with a number of daughters and a constant background, where the total number of components is ten or less. The functional form for the decay of the parent and daughter during the beam-off period have already been given in equations 4 and 5 of Table 3.1. The program uses the Marquardt [Ma63] method, which searches the parameter space to optimize and to estimate the uncertainties of the parameters by using chi-squared minimization. Many of the algorithms for fitting a nonlinear function were obtained from Ref. [Be69]. See Ref. [Sc94] for more details.

We used the 10.3 ms on/10.3 ms off data, which represented the majority of the data, to perform the fit, because the β - n coincidence data had low statistics. This spectrum consisted of a single exponential component (the parent ^{14}Be) and a

constant background. Despite the shorter beam-off period, there were no daughters and since 10.3 ms is about 2.4 half-lives, the activity drops to about 20% of its initial value. We obtained a half-life of 4.0 ± 1.2 ms with a reduced $\chi^2 = 1.7$ (Fig. 3.2). The errors bars shown in this figure are statistical, and the histogram was compressed by a factor of eight relative to Fig. 3.1 yielding a bin width of 0.49 ms.

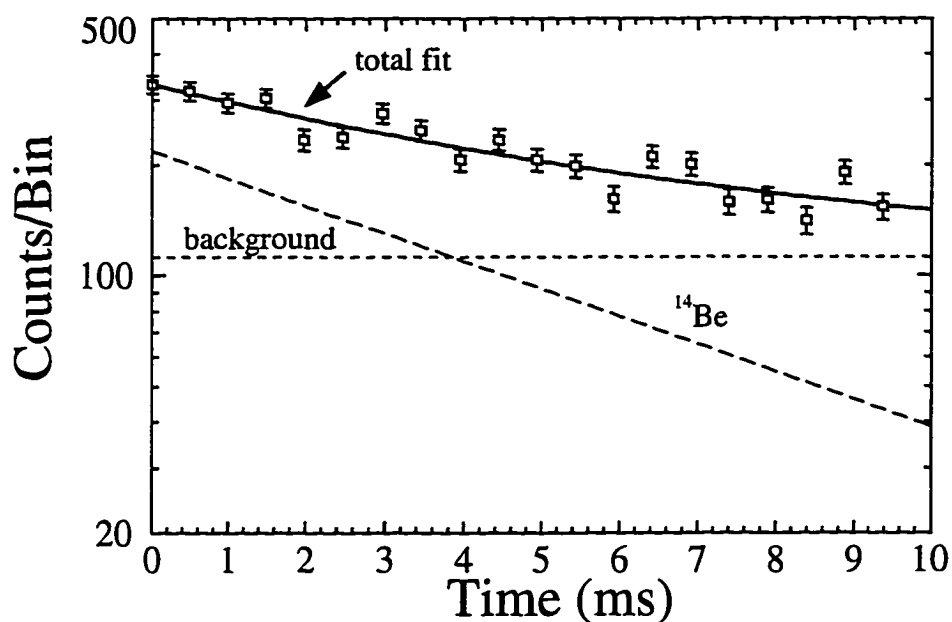


Figure 3.2 Fit of the decay curve requiring β - n coincidence and using the 10 ms beam-off data.

3.2 Analysis of the Neutron Time-of-Flight Data

The analysis of this data set determines the energy and intensities of emitted neutron groups that were used to determine the branching ratios and $\log ft$ values of the observed neutron groups.

3.2.1 Calibration of the time-of-flight data

Ideally one would like to analyze individual neutron detectors, because the neutron detection threshold varies for each photomultiplier tube [Ha91].

Unfortunately, there were insufficient statistics in the present experiment to do this. Therefore it was necessary to gain match all thirty photomultiplier tubes so that the corresponding time-of-flight spectra could be added together. As mentioned in Sec. 2.5.2, the EG&G Ortec 462 Time Calibrator used to perform the time calibration emitted very narrow pulses spaced exactly 10 ns apart. A typical spectrum (photomultiplier tube 1 right [see Fig. 2.2]) is shown in Fig 3.3. We arbitrarily chose the first spike to be located at a time equal to 0 ns, the next one at 10 ns, and so on. We performed a least squares linear fit on the time calibration data of each of the photomultiplier tubes, where the error in the centroids of the peaks are negligible. Thus each of the data points is assigned equal weight. The fit resulting from Fig. 3.3 was

$$y = (0.08538 \text{ ns/chan})x - 24.72 \text{ ns}, \quad (3.13)$$

where y is the time in nanoseconds and x is the channel number. The slopes and offsets varied over rather small ranges from 0.0853 ns/chan to 0.1000 ns/chan, and from -24.44 ns to -32.20 ns, respectively, for the different photomultiplier tubes. Because one wants equal channel numbers to represent equal flight times, we arbitrarily chose to calibrate all detectors to a slope of 0.1 ns/chan (a convenient value) and an offset of -25.6 ns (so that channel 256 is equal to zero time). If we represent the old (raw) calibration curve by

$$y = mx + b, \quad (3.14)$$

where m is the slope, b is the offset, and x is the old channel number, and the new (corrected) one by

$$y' = m'x' + b', \quad (3.15)$$

where the corrected quantities are indicated by primes, and for a given event the

flight times are equal ($y = y'$), then new channel number is

$$x' = \frac{mx + b - b'}{m'} \quad (3.16)$$

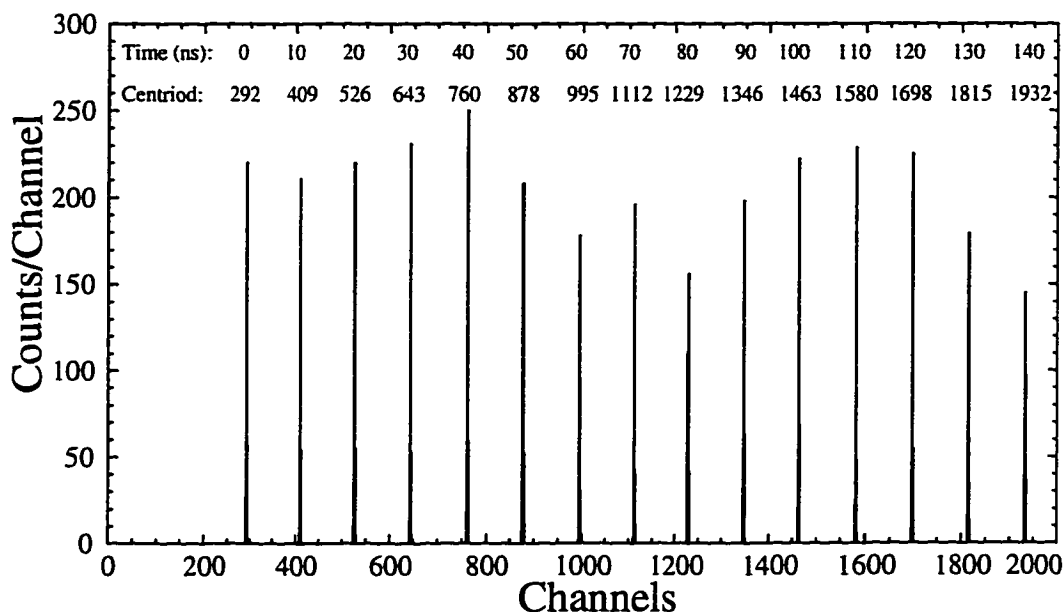


Figure 3.3 Typical time calibration spectrum (detector 1 right). The sharp spikes are 10 ns apart, and listed at the top of the figure are the time and centroids of these peaks. (See text for more details.)

3.2.2 Fit to the raw time-of-flight spectrum

We discovered that there was a small amount of beam-on contamination in the beam-off data. Even though the cyclotron was turned off at the end of the bombardment phase, the beam must still traverse about 30 m of beam line, which results in some beam being present at the beginning of the counting cycle. Moreover 40 μ s [Mi88] are required before the fast phase shifter shuts off the primary beam. This problem was indicated by a sharp spike present at the beginning of the half-life curve (Fig. 3.4). We solved this problem by excluding those events associated with the sharp spike. This lower software gate is indicated by a dashed

line that was located at a time equal to about 0.40 ms. As long as the lower spike (Fig. 3.4) is excluded, the exact location of the gate is not crucial, because the same cut was applied to all data sets and the decay curves were corrected for their true beginning. The upper software gate (not shown) was chosen so that it just excluded the upper spike caused by events overflowing the half-life TDC.

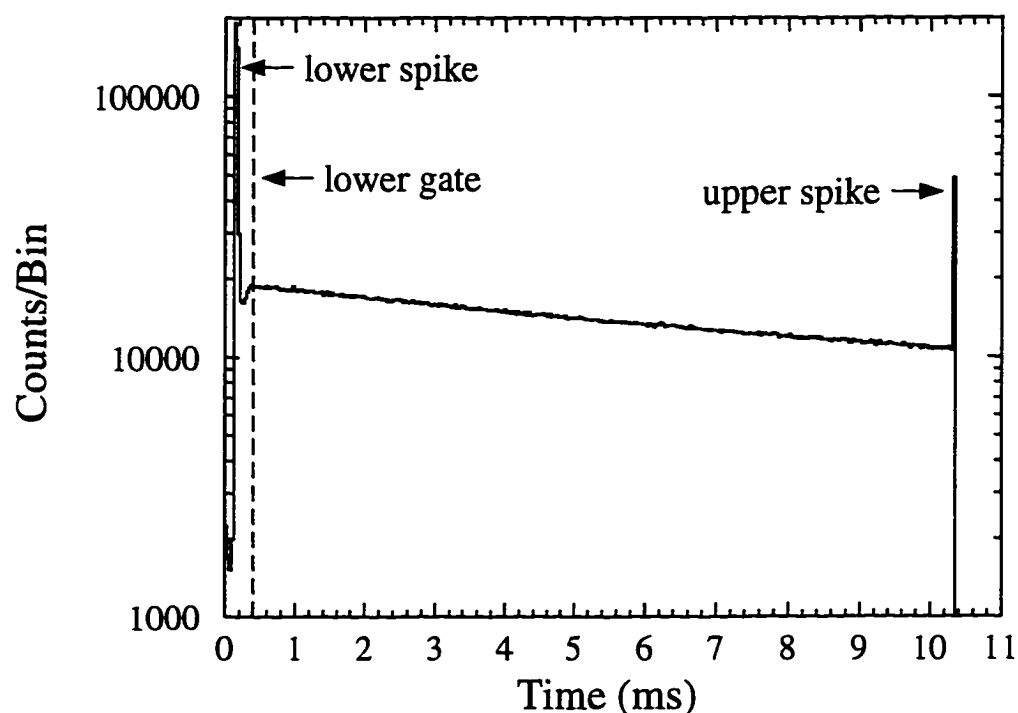


Figure 3.4 Raw 10 ms beam-off activity spectrum showing the location of the lower gate required to eliminate direct beam contaminants from the beam-off data.

Once this correction was done, we calculated the mean flight time for each detector because of the finite time required for light to travel to each end of the plastic scintillator. For example, Fig. 3.5* shows the geometry of a typical neutron decay, where l is the length of the plastic scintillator (1.57 m, see Sec. 2.2 and Ref.

*Note that Fig. 3.5 is an idealization, because the actual ray of light would be a zigzagged line as it bounces between the plastic-air interface. Thus l_1 and l_r are actually somewhat longer than what would be expected from this figure.

[Ha91]), α is the location of the stopped neutron, and l_r and l_l are the distance along the length of the scintillator from α to the right and left scintillators, respectively. Given that the decay is isotropic, the values of l_r and l_l can vary from 0 to l . Since the refractive index of the plastic is 1.58 [Bi90], and the velocity light in a vacuum is about 0.30 m/ns, the velocity of light in the plastic is 0.47 m/ns. The time required for light to travel the distance l is 8.3 ns with the time-of-flight calibration of 0.1 ns/chan this corresponds to 83 channels. Since the time-of-flight signals would vary about 42 channels from their mean position, one can see that it is necessary to plot the mean of the left and right timing signals, effectively placing all events at the center of the neutron detector (that is, $[l_l + l_r]/2 = l/2$). After this is done, the data for all fifteen detectors can be added together (Fig. 3.6a). For comparison Fig. 3.6b shows the spectrum of one of the neutron detectors (no. 1) after the mean time correction is applied. Clearly, an analysis of an individual detector would have been very difficult.

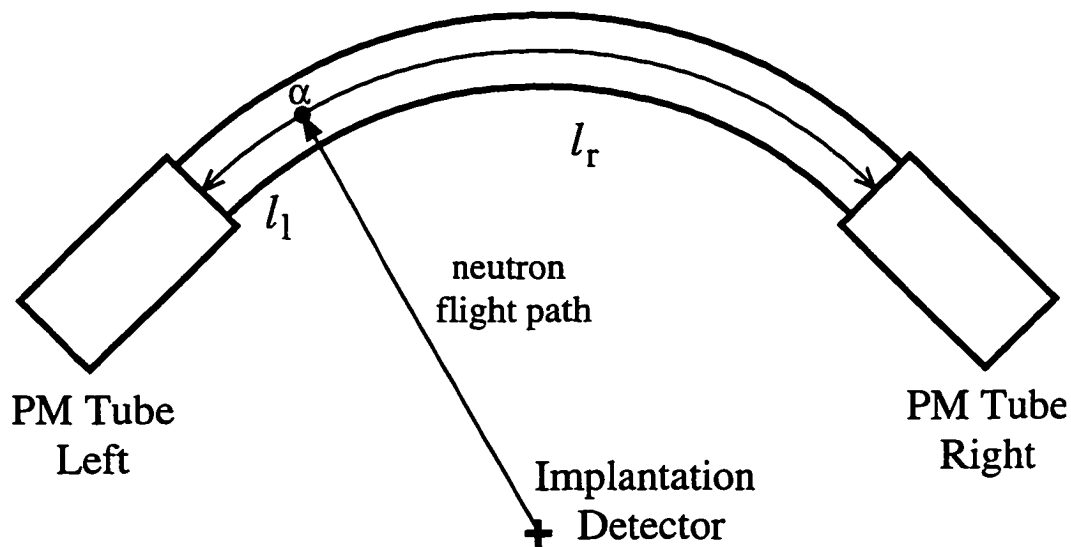


Figure 3.5 Schematic showing the geometry of a typical neutron decay. The symbol "PM" is an abbreviation for photomultiplier. Note that the diagram is not drawn to scale.

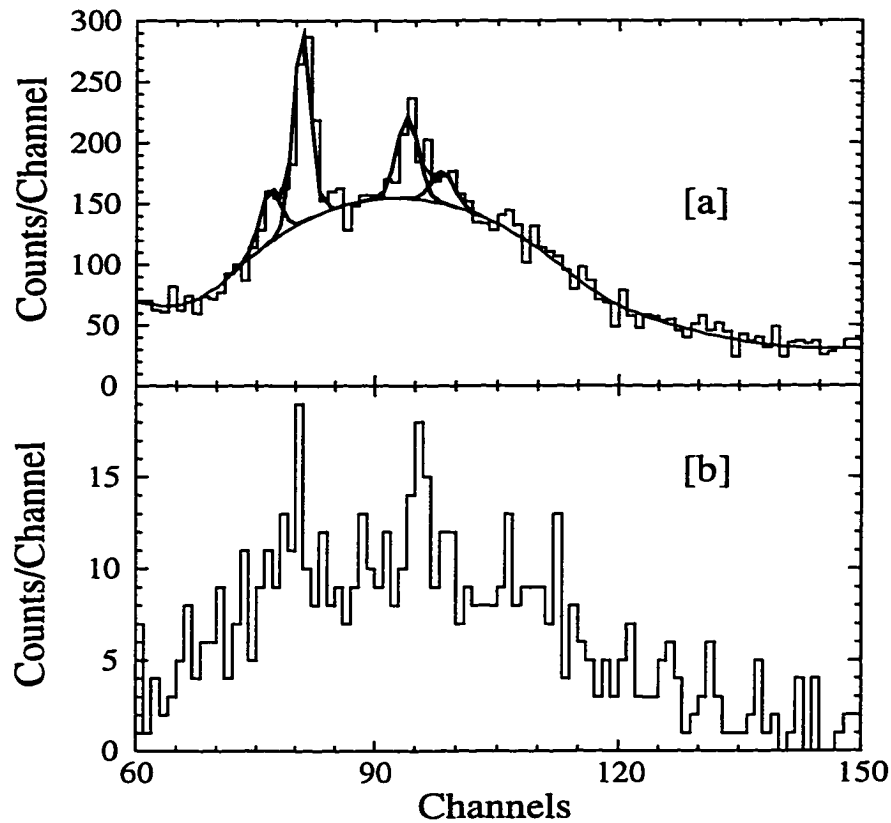


Figure 3.6 (a) Fit of the sum of the time-of-flight spectra of all fifteen neutron detectors. (b) Time-of-flight spectrum of one of the neutron detectors (number 1) for comparison.

The four neutron peaks shown in Fig. 3.6a were fitted simultaneously with Gaussian line shapes and a cubic background using the program FITS. Although the peak shapes are more properly hypergaussian (for example Fig. 2.7) with a low energy tail to account for scattered neutrons, there were insufficient statistics to fit the spectrum accurately using this line shape. Therefore Gaussian distributions were used to fit all of the ^{14}Be neutron peaks observed in the present experiment. Table 3.2 below lists the measured energies and widths of the four peaks. The energy of each peak was calculated by solving Eq. 2.12 for E_k (the kinetic energy

of the neutron); thus obtaining

$$E_k = \left[\frac{1}{\sqrt{1 - (v_n^2/c^2)}} - 1 \right] m_0 c^2, \quad (3.17)$$

where $m_0 c^2$ is the rest mass energy of the neutron (equal to 939.566 MeV/c²) and v_n is the velocity of the neutron, which has already been given by Eq. 2.13 (see Sec. 2.6). The distance used for this calculation was the calibrated distance found in Sec. 2.6, that is 100.9 ± 0.3 cm.

TABLE 3.2

RAW ¹⁴Be NEUTRON PEAKS

Energy (MeV)	Centroid (channels)	FWHM (channels)	FWHM (MeV)	Yield (counts)
3.50±0.07	76.6±0.4	3.1	0.46	155±12
2.98±0.02	80.70±0.11	2.7	0.31	460±20
1.90±0.02	94.0±0.3	3.7	0.21	260±16
1.67±0.03	98.6±0.7	2.9	0.14	81±9

NOTE: The abbreviation FWHM indicates full-width-at-half-maximum.

3.2.3 Correction for ¹¹Li contamination

In a previous experiment at MSU, Morrissey *et al.* [Mo96] measured the β -delayed neutrons from ¹¹Li using the same neutron detector array as the present experiment. Two of the neutron groups observed in this experiment (3.50 and 1.90 MeV) have energies consistent (within experimental error) with the ¹¹Li β -delayed neutron energies given in Table 3.3. This suggests that there was some ¹¹Li contamination in the data, as was apparent in Table 2.3, which shows that 3.7% of the total number of ions implanted were ¹¹Li. We discovered that one of the raw

neutron peaks listed in Table 3.3 (1.90 MeV) exhibited a half-life consistent with that of ^{11}Li . Because this peak was superimposed on the $2n$ distribution of ^{14}Be , the decay curve should be a mixture of both ^{14}Be and ^{11}Li . We eliminated the ^{14}Be component of the decay curve by subtracting the data that corresponded to the sum of two regions (channels 86–89 and 103–106, Fig. 3.6a) that included no sharp $1n$ peaks. Choosing the above regions ensured that the total area was the same as that of the $2n$ distribution under the 1.90 MeV peak so that ^{14}Be component could be subtracted directly. The program LIFES was used to fit the data of Fig. 3.7 with a single exponential curve. It was unnecessary to include a constant background, because it has already subtracted from the raw spectrum. The half-life obtained was 7.5 ± 0.9 ms, which is consistent (within error) with the accepted half-life [Aj90] of ^{11}Li (8.5 ± 0.2 ms). This measurement also indicates that there was significant contamination by this nuclide.

TABLE 3.3
RAW ^{11}Li NEUTRON PEAKS

No. ^a	Energy ^b (MeV)	Centroid (channels)	Width (channels)	Height (counts)	Yield (counts)
1	6.11 ± 0.61	141.5 ± 0.2	7.5 ± 0.2	24.5 ± 0.8	195 ± 8
2	3.48 ± 0.19	164.8 ± 0.2	5.7 ± 0.2	108.8 ± 0.8	660 ± 20
3	2.91 ± 0.12	174.8 ± 0.2	5.8 ± 0.2	452.2 ± 0.8	2800 ± 100
4	1.88 ± 0.12	200.8 ± 0.2	9.7 ± 0.2	282.5 ± 0.8	2920 ± 60
5	1.51 ± 0.47	212.8 ± 0.2	57.9 ± 0.2	161.1 ± 0.8	9930 ± 60

SOURCE: [Mo93]

^aAs numbered in Fig. 3.7.

^bUncertainties rounded to nearest 0.01 MeV.

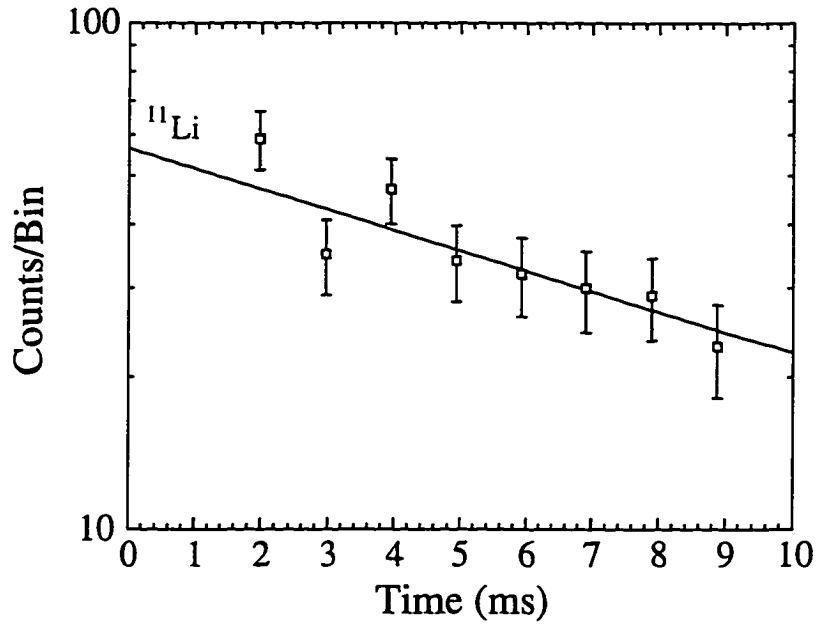


Figure 3.7 Fit of the ^{11}Li component of the decay curve where β - n coincidence has been applied.

Table 3.3 lists the energies, centroids, widths, heights, and yields of the β -delayed neutron states of ^{11}Li from the data shown in Fig. 3.8 [Mo93]. While the energies were listed in Ref. [Mo93], it was necessary to determine the centroids and widths directly from Fig. 3.8. The yields were determined by measuring the width and heights of the peaks shown in Fig. 3.8. A Gaussian distribution is often given (see, for example, Ref. [Le87b]) in the following form:

$$y = \frac{1}{\sigma\sqrt{2\pi}} e^{-\frac{(x-x_0)^2}{2\sigma^2}} = h \cdot e^{-\frac{(x-x_0)^2}{2\sigma^2}}, \quad (3.18)$$

where y is the number of counts, x is the channel number, x_0 , h , and σ are the centroid, height, and the standard deviation in the centroid of the Gaussian distribution,

respectively. Because what we measure is the full-width-at-half-maximum (Γ), we shall express Eq. 3.18 in terms of this quantity. By inserting the definition of Γ : $y(\pm\frac{1}{2}\Gamma) = \frac{1}{2}h$ into Eq. 3.18 and letting $x_0 = 0$, we get

$$\frac{1}{2}h = h \cdot e^{-\frac{(\pm\frac{1}{2}\Gamma)^2}{2\sigma^2}}. \quad (3.19)$$

Solving for σ in Eq. 3.19 yields

$$\sigma = \Gamma/[2\sqrt{2\ln(2)}] = 0.4247\Gamma. \quad (3.20)$$

Inserting Eq. 3.20 into Eq. 3.18 and setting $x_0 = 0$ gives us

$$y = h \cdot e^{-\frac{4\ln(2)}{\Gamma^2}x^2}. \quad (3.21)$$

If A represents the area (or yield) of the Gaussian distribution, then by integrating Eq. 3.21 from $-\infty$ to $+\infty$ we get the expression for A in terms of Γ and h:

$$A = \int_{-\infty}^{+\infty} h \cdot e^{-\frac{4\ln(2)}{\Gamma^2}x^2} dx = \frac{1}{2} \sqrt{\frac{\pi}{\ln(2)}} h\Gamma = 1.0645 h\Gamma. \quad (3.22)$$

Using the above equation we calculated the yields of the peaks listed in Table 3.3 using the measured widths and heights.

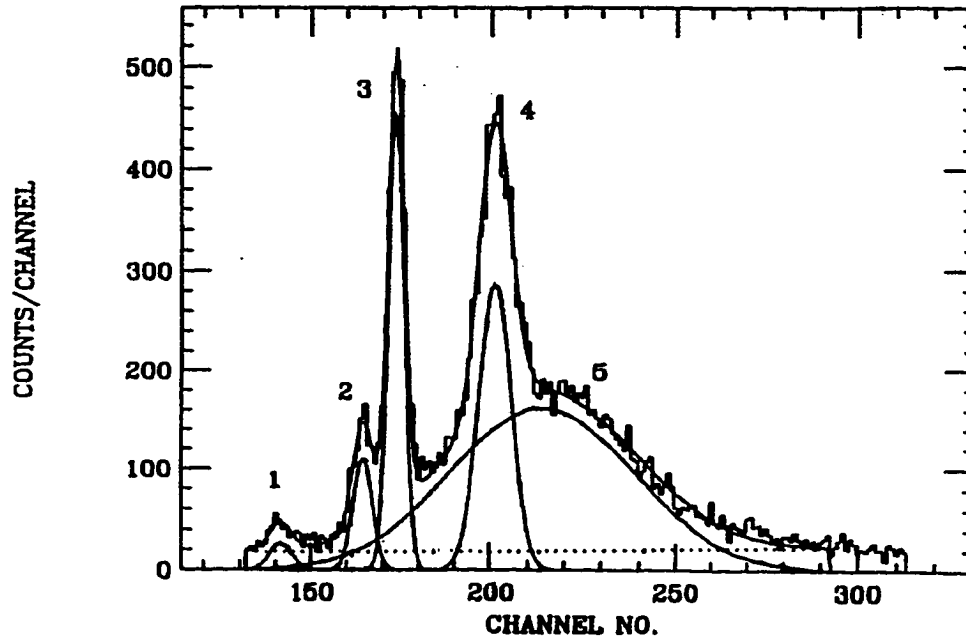


Figure 3.8 Raw ^{11}Li time-of-flight spectrum obtained from Ref. [Mo93].

Before subtracting the ^{11}Li contamination from the spectrum of Fig. 3.6a, it was necessary to normalize it to the ^{14}Be data of the present experiment. Because the peaks shown in Fig. 3.8 were fitted with Gaussian distributions, the only parameters necessary were the centroid, width, and height of each peak normalized to the ^{14}Be data. The centroids were easily found by using the neutron energies listed in Table 3.3 to calculate the flight times of the five peaks. Since the same detector array was used for the ^{14}Be and the ^{11}Li experiments, the neutron flight path was considered to be the same for both.[§] Solving Eq. 2.13 for C_n (the centroid of the neutron peak, see Sec. 2.6) we get

$$C_n = C_\beta + \frac{d}{k} \left(\frac{1}{v_n} - \frac{1}{v_\beta} \right), \quad (3.23)$$

[§]While the geometry of the detectors was the same for both experiments, it is possible that there was a difference in the calibrated flight paths (see Sec. 2.6). Because the calibrated flight path was not given in [Mo96], the difference was assumed to be small and was not considered here.

where C_β is the centroid of the prompt (or beta) peak (equal to 255.28 for the ^{14}Be data), d is the flight path distance (100.9 ± 0.3 cm), k is the conversion from time-of-flight channels to time (0.1 ns/chan), and v_n and v_β are the velocities of the neutron and β groups, respectively. The end point energy for the β decay of ^{11}Li (weighted by the Q values and branching ratios of the daughter states) ranges from 11.8 to 20.1 MeV, because some of the final daughter states are unknown [Aj90]. Using Eq. 2.12 and the average β decay energy (one-third of the end point energy, 3.9–6.7 MeV), we found that v_β ranges from 0.993c to 0.997c. The velocities of the emitted β particles for ^{11}Li β decay differs from those for ^{14}Be by no more than 0.2%. Given a neutron path length of about 1 m and a bin width of 0.1 ns/chan, the variation in the prompt peak centroid due to the distribution of β -particle velocities is only 0.067 channels, which is negligible. We used Eq. 2.12 and the rest mass energy of the electron (about $0.511 \text{ MeV}/c^2$) to calculate the velocities corresponding to the ^{11}Li neutron groups. The energies, velocities, and centroids (scaled to the ^{14}Be data) are listed in Table 3.4, where the error in the centroid is determined from the uncertainty in the measured energy. The determination of the other quantities listed in Table 3.4 will be discussed in the following paragraphs.

TABLE 3.4
CORRECTED ^{11}Li NEUTRON PEAKS

Energy (MeV)	Velocity (cm/ns)	Flight time (ns)	Centroid (channels)	Width (channels)	Height (counts)	Yield (counts)
6.11 ± 0.61	3.40 ± 0.17	29.6 ± 1.5	518 ± 15	30.0 ± 0.8	0.81 ± 0.17	25 ± 5
3.48 ± 0.19	2.57 ± 0.07	39.2 ± 1.1	613 ± 11	22.8 ± 0.8	3.4 ± 0.7	82 ± 17
2.91 ± 0.12	2.35 ± 0.05	42.8 ± 0.9	650 ± 9	23.2 ± 0.8	$14. \pm 3.$	340 ± 80
1.88 ± 0.12	1.89 ± 0.06	53.3 ± 1.7	755 ± 17	38.8 ± 0.8	7.4 ± 1.5	310 ± 60
1.55 ± 0.47	1.7 ± 0.3	$59. \pm 9.$	800 ± 100	231.6 ± 0.8	3.6 ± 1.6	900 ± 400

It was necessary to scale the time-of-flight axis of the ^{11}Li data to that of the ^{14}Be data so that the widths of the corrected ^{11}Li neutron peaks are consistent with that of the ^{14}Be data. First, the flight times (Table 3.4) were calculated by dividing the calibrated flight path (100.9 ± 0.3 cm) by the velocity given in Table 3.4. While the time-of-flight bin width for the ^{14}Be data has already been determined (0.1 ns/chan.), that of the ^{11}Li data has not. Thus we calculated the difference in channels and in flight time for every combination of peaks. We then divided the differences in time by their corresponding channel differences to get the time-of-flight conversion factor. The average conversion factor for the ^{11}Li data (weighted by the errors) was 0.40 ± 0.02 ns/chan. Thus the factor by which the widths were multiplied to make them consistent with the ^{14}Be data was $(0.40 \pm 0.02 \text{ ns}\cdot\text{chan.}^{-1}) / (0.1 \text{ ns}\cdot\text{chan.}^{-1}) = 4.00 \pm 0.02$. The new corrected widths are listed in Table 3.4.

The last step was to normalize the relative abundance (or areas of the neutron peaks) of ^{11}Li delayed neutrons groups in the ^{11}Li experiment to that found in the ^{14}Be experiment. Because, as shown by Fig. 3.7, the 1.90 MeV raw neutron peak appeared to come almost entirely from the decay of ^{11}Li , we used this peak to perform the above normalization. Since the yield of the 1.90 MeV group was 260 ± 16 and the yield of the 1.88 MeV ^{11}Li peak (Table 3.3) was 2920 ± 60 , the factor by which one must multiply the yields of the ^{11}Li neutron spectrum (Fig. 3.8) to scale the ^{11}Li peak at 1.88 MeV to the ^{14}Be peak at 1.90 MeV was 0.089 ± 0.006 . This factor only properly scales the relative abundance of ^{11}Li delayed neutrons at 1.90 MeV; it does not account for difference in neutron detection efficiencies at other energies. Thus it was necessary to calculate the neutron detection efficiency for the ^{11}Li experiment. The threshold used in this experiment was 0.35 MeV neutron energy [Mo93]. Given the light output function used in KSUEFF (Eq. 2.22):

$$T_e = a_1 \cdot T_p - a_2 [1 - \exp(-a_3 \cdot T_p^{a_4})], \quad (3.24)$$

where T_e is the electron kinetic energy (electron equivalent), T_p is the proton (or neutron) kinetic energy, and the a_i are the light coefficients, we were able to convert the threshold from neutron energy to electron equivalent energy. In the ^{11}Li experiment the threshold was 0.35 ± 0.01 MeV neutron energy. This threshold in terms of electron equivalent energy is 0.0275 ± 0.0018 MeV where the light coefficients [Ce79] for NE-102 (the same type of plastic as BC412) were used: $a_1 = 0.95$, $a_2 = 8.0$, $a_3 = 0.1$, $a_4 = 0.90$. We calculated the neutron detection efficiency of the ^{11}Li experiment by running KSUEFF with the above threshold. The neutron detection threshold of the ^{14}Be experiment was 0.168 ± 0.014 MeV ee (electron equivalent). The ratio of the neutron detection efficiency for the ^{14}Be experiment to that of the ^{11}Li experiment is shown in Fig. 3.9 (the vertical scale on the left side). Since both data sets were scaled to one another at 1.90 MeV, it was necessary to normalize the curve by the multiplicative factor 1.46 ± 0.18 so that it equals unity at 1.9 MeV. This curve would tell us how to scale the areas but not the heights. From Eq. 3.22, the area of a Gaussian distribution is proportional to the product of the width and height of the peak; therefore the heights scale inversely as the widths. As found previously, the ratio of the widths in the ^{14}Be experiment to that of the ^{11}Li experiment was 4.00 ± 0.02 , so that the ratio for heights is 0.2500 ± 0.0013 . Collecting all of above factors, we get the total normalization indicated by the vertical scale on the right side of Fig. 3.9 labeled "corrected ratio". Using the information listed in Table 3.4 and the functional form for a Gaussian distribution (where the centroid is located at x_0):

$$y = h \cdot e^{-\frac{4\ln(2)}{\Gamma^2}(x - x_0)^2} \quad (3.25)$$

we could reproduce the proper spectrum that accounts for the ^{11}Li contamination.

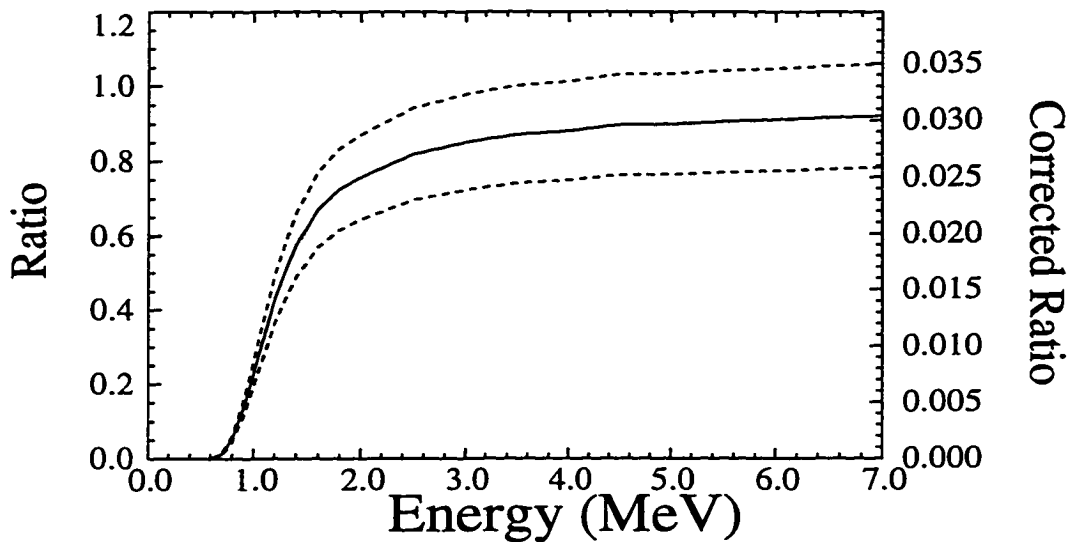


Figure 3.9 Ratio (solid line) between the neutron detection efficiency in the ^{14}Be experiment to that of the ^{11}Li experiment. The vertical scale labeled "Corrected Ratio" indicates the factor by which the heights given in Table 3.3 must be multiplied to yield the heights in Table 3.4. The dashed lines are the uncertainty in the corrected ratio.

The result obtained by subtracting this spectrum is shown in Fig. 3.10. The two remaining sharp peaks shown were fitted simultaneously with a cubic background and Gaussian line shapes using FITS. As mentioned previously in Sec. 3.2.2, the neutron peaks are more properly fit using hypergaussian line shapes, but there were insufficient statistics to do this; thus Gaussian line shapes were used. These sharp peaks indicate single-neutron decay or, possibly, sequential $2n$ decay through narrow intermediate states. Direct $2n$ decay, by contrast, is a three-body process where the decay energy is not shared in a unique proportion by the two neutrons, thus resulting in a distribution of energies. The polynomial background (labeled " $2n$ -distribution") mainly results from such direct $2n$ decay, or possibly but less likely from neutron decay to broad, closely-spaced $1n$ final states. The true background was fit separately and consisted of two parts: a constant level that represents random coincidences, and an increasing component (also a cubic

polynomial) on the high-energy (short time-of-flight) side representing the long tail of the β or prompt peak resulting from late-arriving scattered electrons or photons. The centroids, velocities, widths, energies, and yields of the two peaks shown in Fig. 3.10 are listed in Table 3.5, where the time-of-flight spectrum had a time bin width of 0.8ns/chan, compressed by a factor of eight relative to the raw spectrum shown in Fig. 2.6. Because the width of the 3.52 MeV peak (Fig. 3.10) was ill-defined, it was necessary to fix its width. At these energies we assumed that the natural width was negligible, and since the electronic width was only 0.13 channels (compressed scale of Fig. 3.10), the total widths of the two peaks are dominated by experimental width. Because the experimental width is, in turn, dominated by the systematic error in the flight path, it is inversely proportional to the velocity of the neutrons. Given the velocities listed in Table 3.5, we would expect the experimental widths for the two groups to differ by about 8% at most. Thus we fit the spectrum of Fig. 3.10 by fixing the width of 3.52 MeV peak equal to that of the 3.02 MeV peak, resulting in a common width of 2.3 channels (Table 3.5). The statistical error in the yields includes the error in subtracting the background and the ^{11}Li contamination. The systematic uncertainty includes the error in determining background, the ^{11}Li contamination, and the Gaussian distributions.

TABLE 3.5
CORRECTED ^{14}Be NEUTRON PEAKS

Energy (MeV)	Velocity (cm/ns)	Centroid (channels)	FWHM (channels)	FWHM (MeV)	Yield ^a (counts)
3.52±0.07	2.59 ±0.03	76.5±0.5	2.3	0.34	65± 9±22
3.02±0.03	2.401±0.011	80.3±0.2	2.3	0.27	175±15±22

^aBoth the statistical and systematic uncertainties, respectively, are given for the yields

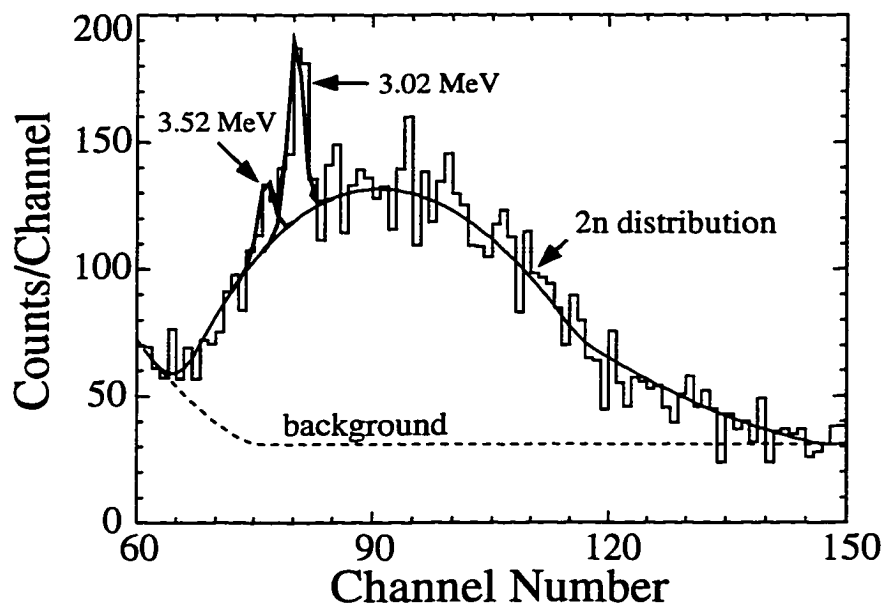


Figure 3.10 Time-of-flight spectrum for the sum of all 15 neutron detectors with ^{11}Li contamination removed. This spectrum has not been corrected for neutron detection efficiency. The bold lines indicate fits to the individual peaks. The x-axis scale is the same as that for Fig. 3.6.

3.3 Branching Ratios and $\text{Log}ft$ Values

3.3.1 Determination of branching ratios and $\text{log}ft$ values for $1n$ states

The next step in the analysis is to determine the branching ratios and $\text{log}ft$ [$\text{log}_{10}(ft)$] values for the neutron states. The branching ratio is the fraction of the total number of β decays that populate the state in question. We must normalize the yields obtained in Table 3.5 for both the solid angle and neutron detection efficiency of the detector array at the corresponding energy of each peak. The total solid angle of the detector array was 1.78 ± 0.03 sr ($14.2 \pm 0.2\%$ geometrical efficiency), and, from Fig. 2.14, we obtained neutron detection efficiencies of $19.6 \pm 0.6\%$ and $20.2 \pm 0.6\%$ for the two neutron groups, respectively. Given the total number of ^{14}Be β decays ($2.04 \pm 0.01 \pm 0.24$) $\times 10^6$, the computed branching ratios for these states are listed in Table 3.6.

TABLE 3.6

BRANCHING RATIOS AND $\log ft$ VALUES OF CORRECTED ^{14}Be NEUTRON GROUPS

Energy (MeV)	Branching Ratio (%)	Log ft	
		(g.s.)	(3.6810 MeV)
3.52 ± 0.07	$0.11 \pm 0.02 \pm 0.04$	$6.00 \pm \begin{smallmatrix} 0.06 & \pm & 0.14 \\ 0.04 & \pm & 0.20 \end{smallmatrix}$	$5.20 \pm \begin{smallmatrix} 0.07 & \pm & 0.14 \\ 0.08 & \pm & 0.20 \end{smallmatrix}$
3.02 ± 0.03	$0.30 \pm 0.03 \pm 0.05$	$5.67 \pm \begin{smallmatrix} 0.05 & \pm & 0.07 \\ 0.05 & \pm & 0.09 \end{smallmatrix}$	$4.91 \pm \begin{smallmatrix} 0.05 & \pm & 0.08 \\ 0.06 & \pm & 0.09 \end{smallmatrix}$

Because the β - n coincidence data has limited statistics, and the raw decay curve half-life has a rather large systematic uncertainty, we used the accepted half-life measured by Dufour *et al.* (4.35 ± 0.17 ms [Du88]) to compute $\log ft$ values. The Fermi integral (f) was calculated by using the method of Wilkinson and Macefield [Wi74], which assumes an allowed β transition. The end-point energy for the β decay is given by

$$E_0 = Q_{\text{g.s.}}(\beta^-) - Q_n - S_n - E_x, \quad (3.27)$$

where $Q_{\text{g.s.}}(\beta^-) = 16.22 \pm 0.11$ MeV [Au93] is the ground state ^{14}Be β decay energy, S_n is the neutron separation energy (0.97 MeV for $1n$ emission and 4.85 MeV for $2n$ emission), Q_n is the Q -value of the neutron decay, and E_x is the excitation energy of the final state.

Because we measure the kinetic energy of emitted neutrons E_n in the laboratory frame we need to compute Q_n . Let us represent the mass and velocity of the daughter nucleus by M and v , respectively, and that of the emitted neutron by m and V , respectively. Since the parent nucleus decays at rest, the center of mass is at rest, and the momenta of the daughter and emitted neutron are equal and opposite in direction; conservation of momentum yields:

$$Mv = mV. \quad (3.28)$$

Expressed in terms of energies, where E_r is the recoil energy of the daughter nucleus:

$$\begin{aligned} \frac{1}{2}M^2v^2 &= \frac{1}{2}m^2V^2 \\ M(E_r) &= m(E_n). \end{aligned} \quad (3.29)$$

The Q-value Q_n is equal to the total kinetic energy released or $E_r + E_n$. Thus $E_r = Q_n - E_n$, and inserting this expression into Eq. 3.29 and solving for Q_n gives

$$Q_n = \left(1 + \frac{m}{M}\right)E_n. \quad (3.30)$$

For example, for $1n$ emission from ^{14}B , the daughter is ^{13}B with atomic mass equal to about 13.0178 u, and the mass of the neutron is about 1.0087 u. Thus Eq. 3.30 yields

$$Q_n = [1 + (1.0087 \text{ u}/13.0178 \text{ u})]E_n = 1.0775 \cdot E_n. \quad (3.31)$$

Integral numbers for m and M will usually provide three or four figure accuracy.

The recoil of the daughter nucleus is already accounted for in the Wilkinson and Macefield method [Wi74]. The computation of $f(Z', E_0)$ is parameterized in the form:

$$f(Z', E_0) = f_{(z=0)} \exp \left[\sum_{n=0}^3 a_n \cdot (\ln E_0)^n \right], \quad (3.32)$$

where the a_n coefficients used are listed in Table 3.7 (see [Wi74]) and $f_{(z=0)}$ is the point nuclear phase space factor (or Fermi integral) for $Z=0$ [Wi74]:

$$\begin{aligned} f_{(z=0)} &= \int_1^{W_0} pW(W_0 - W)^2 dW \\ &= \frac{1}{60}(2W_0^4 - 9W_0^2 - 8) + \frac{1}{4}W_0 \ln(W_0 + p_0). \end{aligned} \quad (3.33)$$

The quantity $W \equiv (E + m_e c^2)/m_e c^2$ is the electron total energy in natural units, $W_0 \equiv (E_0 + m_e c^2)/m_e c^2$ is that at the β -decay end-point, and the momentum of the electron $p = (W^2 - 1)^{1/2}$. The symbols E and E_0 are the electron kinetic energy and its maximum kinetic energy at the end-point, respectively, and m_e is the electron mass. The parameterization is accurate to 0.1%, for $Z \leq 101$ and for $E_0 = 10 \text{ keV} - 25 \text{ MeV}$.

TABLE 3.7

THE a_n USED TO CALCULATE $\text{Log}ft$ VALUES FOR THE β DECAY OF ^{14}Be

Coefficient	β -decay End-point Energy (MeV)		
	0.501 – 3.162	3.163 – 12.589	12.590 – 25.044
a_0	0.172856	0.155095	0.019009
a_1	-0.0497409	-0.0166885	0.094523
a_2	0.0158284	0.0	-0.0234684

SOURCE: [Wi74]

The $\text{log}ft$ values corresponding to the two neutron groups are listed in Table 3.6. Because of the observation of a γ -ray decay (3.680 ± 0.001 MeV, see Sec. 3.4.1) and lack of γ - n coincidence data, two possibilities exist for the final state of the neutron decay, which are both listed in Table 3.7. This point will be discussed further below in Sec. 6.4.

3.3.2 Determination of the branching ratio for $2n$ emission

We next turn our attention to the $2n$ distribution shown in Fig. 3.10. Because the neutron detection efficiency varies as a function of time-of-flight channel number, represented as \mathcal{I} , one must correct the ^{14}Be spectrum for neutron efficiency channel by channel and sum for all appropriate \mathcal{I} which yield the total branching ratio for all detected neutron emission (the sum of $1n$ and $2n$ decay). The first step is to calculate the neutron energy as a function of time-of-flight channel number so that the detection efficiency for each channel number can be calculated. We get the neutron velocity v_n as a function of \mathcal{I} and the prompt peak centroid C_β (equal to 31.91 for Fig. 3.10) from Eq. 2.14 (note that C_n has been substituted by \mathcal{I}):

$$v_n = \frac{d}{k(\mathcal{I} - C_\beta) + (d/v_\beta)} \quad (3.39)$$

where the conversion from channels to time is $k = 0.8 \text{ ns/chan.}$, and the calibrated distance $d = 100.9 \pm 0.3 \text{ cm}$. Solving Eq. 2.11 for E_k (neutron kinetic energy) in terms of v_n yields

$$E_k = m_0 c^2 \left[\frac{1}{\sqrt{1 - (v_n^2/c^2)}} - 1 \right] \quad (3.40)$$

If we represent the raw number of counts as $\text{CNTS}(\mathcal{I})$, the number of counts in the corrected ^{11}Li spectrum as $\text{LI}_{\text{cor}}(\mathcal{I})$, and the background as $\text{BCK}(\mathcal{I})$, then the number ^{14}Be counts per channel \mathcal{I} with the ^{11}Li contamination subtracted, corrected for detection efficiency, is given by

$$\text{BE}(\mathcal{I}) = \frac{\text{CNTS}(\mathcal{I}) - \text{LI}_{\text{cor}}(\mathcal{I}) - \text{BCK}(\mathcal{I})}{\text{EFF}(\mathcal{I})} \quad (3.41)$$

It was assumed that the error in $\text{EFF}(\mathcal{I})$ was purely systematic; therefore the statistical error in $\text{BE}(\mathcal{I})$ is entirely dependent on the numerator of Eq. 3.41. We cannot use $[\text{LI}_{\text{cor}}(\mathcal{I})]^{1/2}$ as the absolute statistical error in $\text{LI}_{\text{cor}}(\mathcal{I})$, because this does not represent the statistical error in the number of raw measured counts. What we use instead is the relative statistical error in the raw number of ^{11}Li counts times the corrected number of ^{11}Li counts given by $\text{LI}_{\text{cor}}(\mathcal{I}) \cdot \{[\text{LI}(\mathcal{I})]^{1/2} / \text{LI}(\mathcal{I})\} = \text{LI}_{\text{cor}}(\mathcal{I}) / [\text{LI}(\mathcal{I})]^{1/2}$. (Here we assume no statistical error in the ^{11}Li correction; that is, the error is totally systematic). Using the standard rules of propagation of error, the expression above for the absolute statistical error in $\text{LI}_{\text{cor}}(\mathcal{I})$, and absolute statistical error in $\text{CNTS}(\mathcal{I})$ and $\text{BCK}(\mathcal{I})$ (equal to the square root of those quantities), the square of the absolute statistical error in $\text{BE}(\mathcal{I})$ is

$$[\delta \text{BE}_{\text{stat}}(\mathcal{I})]^2 = \frac{\text{CNTS}(\mathcal{I}) + \text{BCK}(\mathcal{I}) + \{\text{LI}_{\text{cor}}(\mathcal{I}) / [\text{LI}(\mathcal{I})]^{1/2}\}^2}{\text{EFF}(\mathcal{I})} \quad (3.42)$$

One must sum $[\delta \text{BE}_{\text{stat}}(\mathcal{I})]^2$ for all appropriate \mathcal{I} and take the square root of the result to find the total absolute statistical uncertainty in the total branching ratio.

The raw measured counts [CNTS(I)] have no systematic error. The systematic error in the background was obtained through visual inspection by choosing the minimum and maximum "reasonable" backgrounds and dividing the difference in both by two (channel by channel). The systematic error in the neutron efficiency curve was obtained similarly by finding the difference between the estimates of the error of the neutron efficiency curve (dashed lines Fig. 2.14) for energies corresponding to the channels I and dividing by two. The absolute systematic error in the corrected ^{11}Li counts [$\text{LI}_{\text{cor}}(\text{I})$] was found by finding the average systematic relative errors (weighted by their errors) in the corrected ^{11}Li yields (Table 3.4) (equal to about 24.9%), and assuming that this error was the same for all $\text{LI}_{\text{cor}}(\text{I})$. If the absolute systematic error in the background is represented by $\delta\text{BCK}(\text{I})$ and that of $\text{LI}_{\text{cor}}(\text{I})$ and $\text{EFF}(\text{I})$ are represented by $\delta\text{LI}_{\text{cor}}(\text{I})$ and $\delta\text{EFF}(\text{I})$, respectively, then by usual rules of propagation of error, the absolute systematic error in $\text{BE}(\text{I})$ is

$$\delta\text{BE}_{\text{sys}}(\text{I}) = \text{BE}(\text{I}) \left(\left\{ \frac{\sqrt{[\delta\text{LI}_{\text{cor}}(\text{I})]^2 + [\delta\text{BCK}(\text{I})]^2}}{[\text{LI}_{\text{cor}}(\text{I}) + \text{BCK}(\text{I})]} \right\}^2 + \left[\frac{\delta\text{EFF}(\text{I})}{\text{EFF}(\text{I})} \right]^2 \right)^{1/2} \quad (3.43)$$

where the $\delta\text{BE}(\text{I})$ are summed over the appropriate values of I.

Because the systematic error in the neutron detection efficiency is ill-defined near threshold, we excluded the region from 0.77–0.90 MeV. Thus the entire range over which $\text{BE}(\text{I})$, $[\delta\text{BE}_{\text{stat}}(\text{I})]^2$, and $\delta\text{BE}_{\text{sys}}(\text{I})$ were summed was $\text{I} = 61 - 123$. After computing the appropriate sums and dividing by the total number of emitted β particles $[(2.200 \pm 0.005 \pm 0.260) \times 10^5]$, we obtained a total neutron branching ratio (the sum of $1n$ and $2n$ emission) of $12.1 \pm 0.2 \pm 6.4\%$. From Table 3.6, we get a total $1n$ branching ratio equal to $0.41 \pm 0.03 \pm 0.07\%$. The difference between the total and $1n$ branching ratio, divided by two to account for the fact that either of the two neutrons can be detected, represents the branching ratio for $2n$ emission, equal to $5.9 \pm 0.1 \pm 3.2\%$.

3.4 Analysis of the γ -Ray Data

It was desirable to measure γ -rays, because γ - n coincidence data can, in principle, determine which excited levels of the ^{13}B and ^{12}B daughters are populated by the β -delayed neutron decay of ^{14}Be . The first step in this analysis is to perform an energy and detection efficiency calibration of the high purity Ge detector used for this experiment. With this information, we were not only able to determine the energies of the γ -ray states but also to estimate the branching ratios and $\log ft$ values corresponding to the β -transitions that populated these states.

3.4.1 Energy calibration of the γ -ray detector

Several sources were used to perform the energy calibration: the calibrated γ -ray lines of the NIST source (Table 2.4), the background lines that were observed during the experiment, and several single isotopic sources: ^{60}Co , ^{133}Ba , ^{137}Cs , ^{152}Eu , and ^{228}Th . The background lines consisted of the electron annihilation peak (equal to its rest mass, 511.003 keV [error negligible]) and some of the more prominent γ -ray lines from ^{214}Pb , ^{214}Bi , ^{228}Ac , and ^{40}K . The references for the accepted energies used in the calibration are given in Appendix B. All the calibration lines ranged in energy from about 80 keV to 2600 keV. The data points are plotted in Fig. 3.11 together with an unweighted least squares linear fit, where the y values represent the accepted values in keV, and the x values are the measured channel numbers. For an unweighted fit, all data points affect the fit equally, and the χ^2 is found by setting the standard deviation of the measured y -value $\sigma_i = 1$ [Pr86]:

$$\chi^2 = \sum_{i=1}^n \{ [y_i - y(x_i)] / \sigma_i \}^2 = \sum_{i=1}^n [y_i - y(x_i)]^2, \quad (3.44)$$

where y_i represents the y -value of the measured data point i , $y(x_i)$ represents the y -value of the fit calculated at x_i , and n is the total number of data points. For a

linear fit, $y(x_i) = a + b \cdot x_i$, where a and b are the constant and linear coefficients, respectively. The uncertainties in a and b were found by using the method described in Sec. 2.7.4 where it is necessary to multiply the result by $[\chi^2/(n - 2)]^{1/2}$ [Pr86]. The denominator, $(n - 2)$, represents the number of degrees of freedom, equal to the number of data points minus the number of parameters (two for a linear fit). The uncertainties in the data points are too small to be seen in Fig. 3.11.

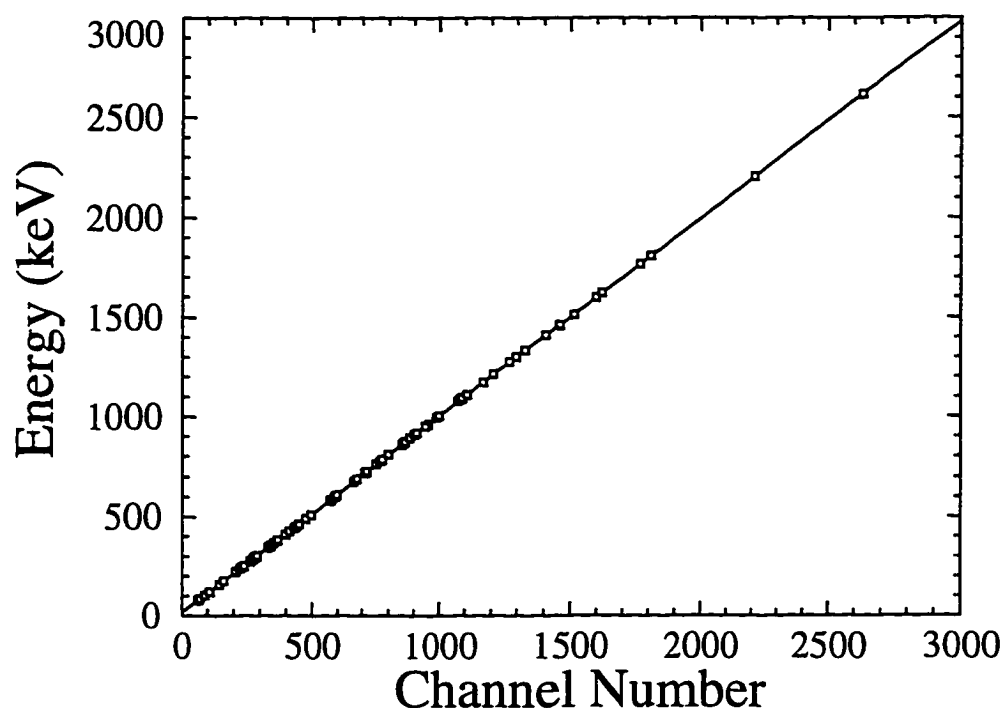


Figure 3.11 Plot of γ -ray energy calibration points as a function of channel number. The solid line is a linear fit to these points (see text).

Because it is impossible to distinguish the difference between the data points and the fit (Fig. 3.11), it is useful to plot the difference between the accepted energies and the corresponding calculated energies from the fit above (Fig. 3.12a). Notice that a non-linearity in the energy response of the detector is now very apparent as there is a definite curvature to the measured data points (relative to the linear fit). The error bars shown are the uncertainties in the accepted energies

(the error in channel numbers are too small to be seen). Typically, the energy calibration points for germanium detectors are fitted to a polynomial [Kn79d]. In this case, we chose the lowest order polynomial that adequately fit the data points (Fig. 3.12b): a quadratic. We found that higher order polynomials did not improve the fit. Notice that the curvature of the data points is no longer apparent with this polynomial. The best fit to the data (solid line) was

$$y = 17.12(11) \text{ keV} + [0.99045(12)]x \text{ keV/ch.} - [1.10(8) \times 10^{-6}]x^2 \text{ keV/ch}^2, \quad (3.45)$$

where y is the γ -ray energy in keV, x is the channel number, and the uncertainty in the coefficients are enclosed in parentheses. The dashed lines shown in Fig. 3.12b represent the uncertainty in the fit due to the statistical uncertainty in the coefficients above. For comparison, the uncertainty in the linear fit is also shown in Fig. 3.12a.

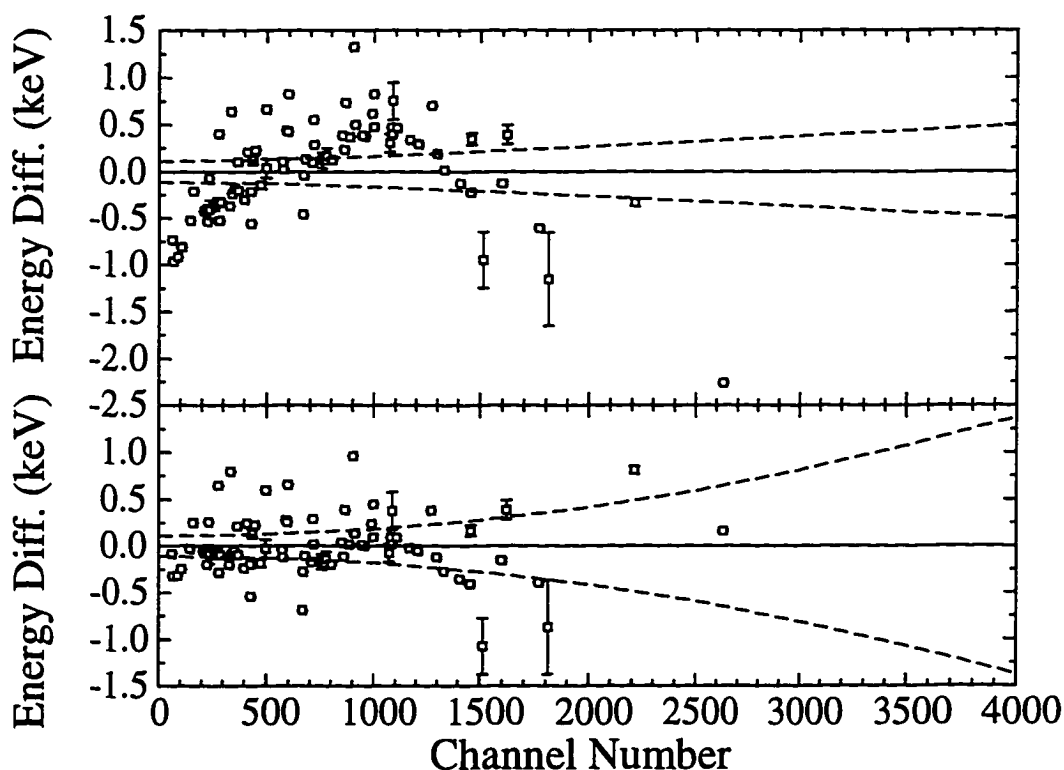


Figure 3.12 (a) Measured centroids versus difference between an unweighted linear fit and the accepted energies for the γ -ray energy calibration points. (b) A similar fit using a quadratic function. The dashed lines represent the statistical uncertainty in each fit.

Only one observed γ -ray line was due to the decay of ^{14}Be daughter; it was fitted with a Gaussian line shape and a constant background using the program FITS (Fig 3.12). The centroid was at channel number 3714.8 ± 0.3 and the integrated area of the peak was 143 ± 15 , where the uncertainties are statistical. The reduced χ^2 of the fit was 1.17. Using the calibration curve given in Eq. 3.45, the energy of this peak was 3680 ± 1 keV. The most likely daughter state that could correspond to this γ -ray energy is the ground state decay of the 3681 ± 5 keV level of ^{13}B [Aj91]. Another (less likely) possibility, corresponding to the 3684.51 ± 0.02 keV ground state transition in ^{13}C , will be discussed in Chap. 6, Sec. 6.4.

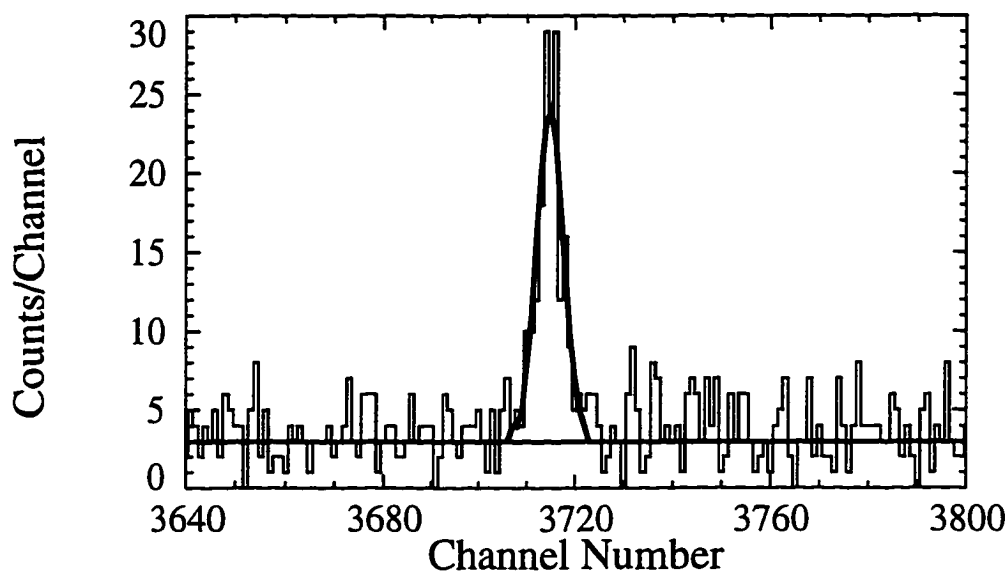


Figure 3.13 Fit of γ -ray peak due to daughter decay of ^{14}Be (see text).

3.4.2 Detection efficiency calibration of the γ -ray detector

This analysis consists of two steps: first, for each γ -ray line determine the total number of emitted γ -rays that impinge on the detector and, second, find the total number of γ -rays detected for each of those corresponding lines. This determination was simplified by the use of a standard source (the NIST source, see

Sec. 2.5.1) for which the total emission rates have been accurately calibrated. The elapsed time of the NIST calibration run was 316.16 ± 0.01 s (the start and stop times of each run are written to magnetic tape to the nearest 0.01 s).

The calibration run was performed 1163.427 ± 0.003 days (elapsed time above was used as the uncertainty in this value) after emission rates were determined. Because this period is about three years, which is a significant fraction of the half-lives of the nuclides present in the NIST source (^{155}Eu : 1737.80 ± 0.04 days, ^{154}Eu : 3135.0 ± 0.4 days, and ^{125}Sb : 1007.4 ± 0.4 days [Appendix B]), it was necessary to account for the decay of these nuclides since the emission rate determination. Equation 3.8 gives the exponential decay of a single isotope: $\mathcal{A} = \mathcal{A}_0 e^{-\lambda t}$. Dividing both sides of this equation by \mathcal{A}_0 gives the ratio between the final and initial activities: $\mathcal{A}/\mathcal{A}_0 = e^{-\lambda t}$, where $t = 1163.427 \pm 0.003$ days. This is the factor by which the emission rates listed in Table 2.4 must be multiplied to be corrected for the time of the NIST calibration run. The decay constants for the nuclides listed above are $(3.98865 \pm 0.00009) \times 10^{-4}$ days $^{-1}$ for ^{155}Eu , ^{154}Eu : $(2.2110 \pm 0.0003) \times 10^{-4}$ days $^{-1}$, and ^{125}Sb : $(6.8806 \pm 0.0003) \times 10^{-4}$ days $^{-1}$.

Since the sources were placed off-axis, it was necessary to calculate the solid angle subtended by the high purity Ge detector, and correct the emission rates for the difference in the solid angle of the Ge detector for the calibration run and ^{14}Be data run. This solid angle was calculated by using the method described by Wielopolski [Wi77] which is applicable for a cylindrical detector and cylindrical source. The geometry and size of the detector and source has already been given in Sec. 2.5.1. Here, we assumed a point source (height and radius of source equal to zero). The solid angle is calculated through the Monte Carlo method. Quite simply, the algorithm is to calculate a large number of randomly distributed vectors that originate from randomly distributed points in the source and determine the fraction

of those vectors that intercept any portion of the detector volume. This fraction, the geometrical efficiency, multiplied by 4π gives the solid angle in steradians. By performing enough iterations any desired statistical accuracy in the Monte Carlo calculation can be obtained, limited only by the CPU time of the computer. Because the details regarding this method and the FORTRAN code used are fully documented in [Wi77], they will not be repeated here. This program does not include self-absorption or self-scattering in the source (negligible for this analysis), nor does it take into account γ -rays that scatter out of the active volume of the detector without being detected (considered to be negligible with a high purity Ge crystal with the large dimensions used here [see Sec. 2.2]). The error in the calculated solid angles was assumed to be solely dependent on the uncertainties in the geometry of the detector and source. The specifications given by EG&G Ortec lists the HP Ge crystal dimensions to within 0.1 mm, which was assumed to be the uncertainty in these dimensions. Using the above information we determined that the solid angle subtended by the detector seen at the NIST source position was 0.51 ± 0.05 sr (geometrical efficiency $4.0 \pm 0.4\%$).

In Table 3.8 the numbers listed under the column entitled "Number Impinged" were found by first multiplying the emission rates listed in Table 2.4 by the total run time 316.16 ± 0.01 s, multiplying by the factors listed in Table 3.9 to correct for the radioactive decay of the source since the calibration date (Sept. 9, 1996) and multiplying by the geometrical efficiency 0.040 ± 0.004 to get the actual number of γ -rays that impinged on the detector.

The raw measured (detected) yields of the γ -ray lines of the NIST source is listed in column 4 of Table 3.8. It was desirable to obtain the intrinsic detection efficiency independent of the live time of the acquisition system, because it was different for the NIST calibration run and the ^{14}Be data run. We determined the live

TABLE 3.8

 γ -RAY DETECTION EFFICIENCY

Source	γ -ray Energy (KeV)	Number Impinged	Raw Measured Yield	Corrected Measured Yield	Efficiency (%)
^{155}Eu	86.062 \pm 0.005	72000 \pm 7000	5300 \pm 200	16800 \pm 600	23.4 \pm 2.3
^{155}Eu	105.306 \pm 0.002	50000 \pm 5000	4520 \pm 180	14400 \pm 600	28.9 \pm 2.9
^{154}Eu	123.070 \pm 0.001	360000 \pm 30000	35700 \pm 500	113900 \pm 1600	31.6 \pm 2.9
^{125}Sb	176.313 \pm 0.002	25000 \pm 2000	2690 \pm 80	8600 \pm 300	34.4 \pm 3.4
^{154}Eu	247.930 \pm 0.008	61000 \pm 6000	5440 \pm 120	17400 \pm 400	28.5 \pm 2.7
^{125}Sb	427.875 \pm 0.006	108000 \pm 10000	7660 \pm 100	24400 \pm 300	22.6 \pm 2.1
^{125}Sb	463.365 \pm 0.004	38000 \pm 4000	2630 \pm 60	8390 \pm 180	22.0 \pm 2.1
^{154}Eu	591.762 \pm 0.005	44000 \pm 4000	2390 \pm 60	7600 \pm 200	17.5 \pm 1.7
^{125}Sb	600.600 \pm 0.004	64000 \pm 6000	3760 \pm 80	12000 \pm 200	18.7 \pm 1.8
^{125}Sb	635.954 \pm 0.005	41000 \pm 4000	2230 \pm 60	7110 \pm 190	17.3 \pm 1.7
^{154}Eu	723.305 \pm 0.005	177000 \pm 16000	9150 \pm 120	29200 \pm 400	16.5 \pm 1.5
^{154}Eu	873.190 \pm 0.005	107000 \pm 10000	4910 \pm 80	15700 \pm 300	14.6 \pm 1.4
^{154}Eu	996.262 \pm 0.006	92000 \pm 8000	3940 \pm 70	12600 \pm 200	13.6 \pm 1.3
^{154}Eu	1004.725 \pm 0.007	159000 \pm 15000	6730 \pm 100	21500 \pm 300	13.5 \pm 1.3
^{154}Eu	1274.436 \pm 0.006	310000 \pm 30000	11600 \pm 130	37000 \pm 400	12.0 \pm 1.1
^{154}Eu	1596.495 \pm 0.018	15600 \pm 14000	610 \pm 20	1930 \pm 80	12.4 \pm 1.2

TABLE 3.9

CORRECTION FACTORS FOR THE RADIOACTIVE DECAY OF SOURCES

Source	Factor
^{155}Eu	0.628732 \pm 0.000007
^{154}Eu	0.773219 \pm 0.00003
^{125}Sb	0.44910 \pm 0.00014

time for the NIST calibration run (0.3135 with negligible uncertainty) by using a scaler that recorded the total number of start events and the corresponding number of start events while the computer was live. Thus corrected measured yields (column 5, Table 3.8) were found by dividing the raw yields by the live time (about 0.6865, the uncertainty was negligible).

The intrinsic detection efficiencies (column 6) were found by dividing the numbers of column 5 by the corresponding ones in column 3. A plot of these efficiencies as a function of energy is shown in Fig. 3.14, which was fitted to [Si76]:

$$\ln \varepsilon = bx + cx^2; x = \ln(a/E), \quad (3.46)$$

where ε is the efficiency in percent, E is the γ -ray energy in keV, and the coefficients a , b , and c are constants. Reference [Si76] cites several other semi-empirical formulae that have been fitted to measured γ -ray detection efficiency data. For the present analysis, we adopted the functional form of Eq. 3.46, because it required the fewest number of parameters and reproduced the γ -ray detection efficiency very well (Fig. 3.14). The coefficients were found by performing a fit to the γ -ray detection efficiency excluding the rising part of the curve (the four lowest energy data points that are affected by absorption of the γ rays in the material surrounding the detector). The constants were optimized by minimizing the reduced χ^2 . The coefficients found were $a = 7500 \pm 300$, $b = -0.002 \pm 0.003$, and $c = 0.0328 \pm 0.0003$, where the method described in Sec. 2.7.4 was used to find the uncertainty in the coefficients. The solid line of Fig. 3.14 represents the best fit to the data, and the dotted lines represent the uncertainty in this fit due to the error in the coefficients. This calculation is only a crude estimate because the effects of implanted ^{14}Be distribution, pileup and the systematic error in extending the curve to much higher energies was difficult to determine and was not included here.

3.4.3 Branching ratio and $\log ft$ value for the observed γ -ray state

Using Fig. 3.14, we can calculate the branching ratio and $\log ft$ value of the 3.681 MeV γ -ray line discussed in Sec. 3.4.1. The raw yield of this line, obtained from Fig. 3.13, was 143 ± 15 counts. The steps necessary to determine a branching ratio have already been outlined in Sec 3.3. Briefly, it requires normalizing the raw yield for geometrical efficiency (solid angle) and detection efficiency and dividing by the total number of corresponding β decays. Using the method of Wielopski [Wi77], the solid angle subtended by the γ -ray detector during the ^{14}Be data run was 0.57 ± 0.05 sr ($4.6 \pm 0.4\%$ geometrical efficiency). (This is slightly larger than that found for the energy calibration run (Sec. 3.4.2), because the implantation detector is on-axis.) From Fig. 3.14, the γ -ray detection efficiency obtained at the above energy was $6.6 \pm 0.4\%$. Thus the yield for the 3.681 MeV peak normalized for the geometrical and detection efficiencies was 48000 ± 5000 counts. A correction for dead time was unnecessary, because it was assumed that the same dead time affected both the γ -ray and half-life spectra. The total number of ^{14}Be β -decays was $(2.04 \pm 0.01 \pm 0.24) \times 10^6$, and, consequently, the branching ratio relative to ^{14}Be β -decay was $2.3 \pm 0.4\%$ (systematic error), which would correspond well to the known branching of the 3.681 ± 5 MeV [Aj91] ground state transition in ^{13}B . It is very unlikely that this γ -ray line would correspond to a transition in ^{12}B , because this would result from $2n$ emission of ^{14}B which is three-body process. Such a neutron transition would not populate a unique energy level in ^{12}B but rather a continuous distribution. These points will be discussed more fully in the discussion (Sec. 6.4). We must convert the level energy to the equivalent emitted kinetic energy so that we can compare this directly to our measured energy. It is necessary to see how the Q-value of the γ -transition is related to the measured energy of the γ -ray.

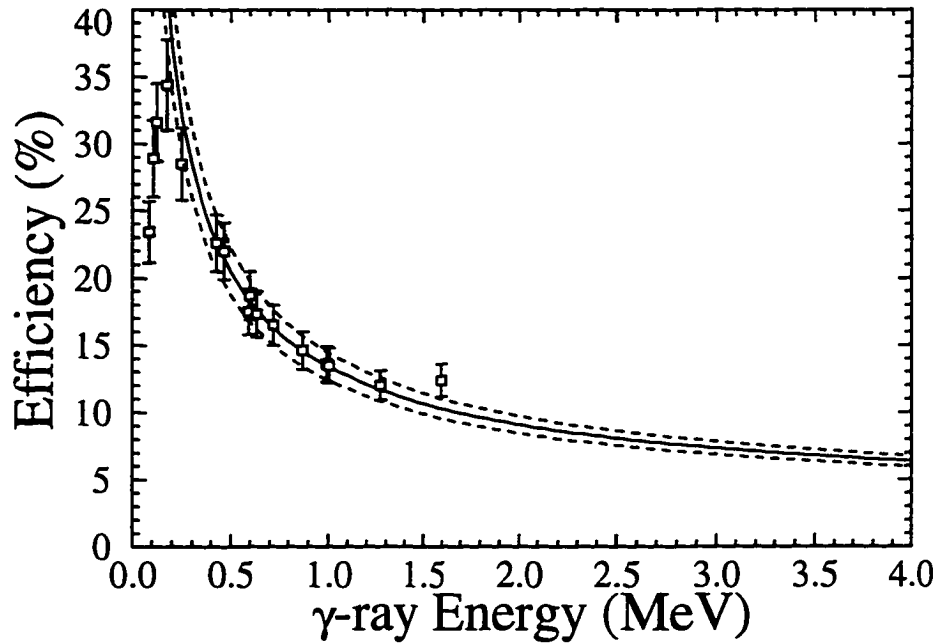


Figure 3.14 Plot of γ -ray detection efficiency as a function of γ -ray energy (see text for details).

Since the excited nucleus decays at rest, the conservation of momentum gives us:

$$p_R = p_\gamma, \quad (3.47)$$

where p_R and p_γ are the momenta of the recoiling nucleus and the emitted photon, respectively. Because the photon has zero rest mass, the relativistic relationship between its kinetic energy E_γ and momentum is $E_\gamma = c \cdot p_\gamma$, where c is the velocity of light in a vacuum. The kinetic energy of the recoiling nucleus is small enough relative to its rest mass energy, that its momentum can be expressed classically:

$$Mv = \frac{E_\gamma}{c}, \quad (3.48)$$

where M is the mass of the recoiling nucleus and v its velocity. Squaring both sides

of Eq. 3.48 and multiplying by $\frac{1}{2}$ yields

$$\frac{1}{2}M^2v^2 = \frac{E_\gamma^2}{2c^2}, \quad (3.49)$$

which simplifies to

$$E_R = \frac{1}{2}Mv^2 = \frac{E_\gamma^2}{2Mc^2}, \quad (3.50)$$

where E_R is the kinetic energy of the recoiling nucleus. For a reaction (or transition) the Q-value is defined as the difference between the total initial and total final kinetic energy of all particles: $Q = E_{\text{final}} - E_{\text{initial}}$. Because the initial nucleus is at rest, $E_{\text{initial}} = 0$. Thus, $Q = E_{\text{final}}$, and we get

$$Q = E_{\text{final}} = E_\gamma + E_R = E_\gamma + \frac{E_\gamma^2}{2Mc^2} = E_\gamma \left(1 + \frac{E_\gamma}{2Mc^2} \right). \quad (3.51)$$

We, therefore, find the quadratic expression:

$$\left[\frac{1}{2Mc^2} \right] \cdot E_\gamma^2 + E_\gamma - Q = 0 \quad (3.52)$$

that has the following solution for E_γ :

$$E_\gamma = Mc^2 \left(\sqrt{1 + 2 \frac{Q}{Mc^2}} - 1 \right). \quad (3.53)$$

Because $Q \ll Mc^2$ we can expand the square root term in a Taylor series. Keeping only the first term we get

$$E_\gamma \cong Q - \frac{Q^2}{2Mc^2}. \quad (3.54)$$

Except for very light ions and high Q, $E_\gamma = Q$ to a precision on the order of 10^{-5} .

If the 3.681 MeV γ -line results from a ^{13}B transition, then with a $1n$ separation energy of 0.97 ± 0.02 MeV [Au93] for ^{14}B and ^{14}Be ground state β -decay energy of 16.22 ± 0.11 MeV [Au93] the largest possible β -decay end

point energy (including error) $E_0 = (16.33 - 3.68 - 0.95) = 11.70$ MeV. If one assumes that the ^{14}B state that populates the ^{13}B state lies below the $2n$ threshold (5.85 ± 0.02 [Au93] see Fig. 1.7), then the smallest energy $E_0 = (16.11 - 5.87) = 10.24$ MeV. The range of possible branching ratios is 1.9–2.7%. Using this information with the method of Wilkinson and Macefield [Wi74] yields the following range of $\log ft$ values: 4.4–4.8.

3.5 Determination of the β -detection efficiency

We did not use information obtained from the ΔE and E-veto detectors (figures 2.4 and 2.5) to determine the total number of detected β decays, because this would impart an additional systematic uncertainty due to calculating the detection efficiency of the implantation detectors. This was unnecessary, because that number can be obtained directly from the raw β -decay curve (Sec. 3.1.1). Even so, it is still useful to calculate the β -detection efficiency of the implantation detectors.

Because the silicon surface barrier detectors (ΔE and E-veto) can be assumed to be nearly 100% efficient, we can use information obtained from figures 2.4 and 2.5 and Eq. 1 of Table 3.1 to compute the true activity at the end of the beam-on period. We used the long duty cycle runs (10.3 ms on/40 ms off), because the long beam-off period is equal to about 9 half-lives of ^{14}Be after which only 0.2% of the initial parent activity is present. Thus we can neglect any residual ^{14}Be activity present at the start of the beam-off period. We determined the number of ^{14}Be ions stopped in the implantation detector by summing the ^{14}Be group of Fig. 2.4, subtracting the same corresponding group in Fig. 2.5 (see Sec. 2.2), and correcting for the dead time (which was large). For the long duty cycle runs, the dead time was 27.19% (uncertainty negligible), which implies a live time of 72.81%, the factor by which the raw counts must be divided to correct for

dead time. The total number of stopped ^{14}Be ions (corrected for dead time) for all long duty cycle runs was $(4.99 \pm 0.13) \times 10^5$. The total elapsed time the beam is on is equal to the number of cycles (6.776×10^5) times the beam-on period (10.3 ± 0.1 ms) which is $(6.98 \pm 0.07) \times 10^6$ ms. Thus R , the rate of stopped ^{14}Be ions, is equal to 0.0716 ± 0.002 particles per ms. From Eq. 1 of Table 3.1, we derived an expression for the beam-on activity A for the parent nuclide: $A = R(1 - e^{-\lambda t})$, where λ is the decay constant for ^{14}Be and t is the elapsed time since the start of the beam-on period. We used the accepted half-life obtained by Dufour *et al.* (4.35 ± 0.17 ms [Du88]) to calculate λ (0.159 ± 0.006 ms^{-1} [Eq. 3.10]). At the end of the beam-on period $t = 10.3$ ms and $A = 0.058 \pm 0.002$ ms^{-1} which represents the total activity due to ^{14}Be at this point in time.

From Fig. 3.1, we obtained 1900 ± 300 counts/chan. (systematic error) for the first channel of the parent component spectrum which represents the activity at the beginning of the beam-off period. This represents the beam-off activity per channel summed for all cycles. By dividing this by the channel bin width (0.0617 ± 0.006 ms/chan) and by the total number of cycles (6.776×10^5) we get an initial beam-off activity (that is, the number of counts per ms per cycle) of 0.046 ± 0.008 ms^{-1} . This represents the detected activity at the same point of time as above. The above result divided by the beam-on activity \mathcal{A} yields a β -detection efficiency of $79 \pm 14\%$.

3.6 Missing Neutrons

Because the total $1n$ branching ratio is $0.41 \pm 0.03 \pm 0.07\%$, and the $2n$ branching ratio is $5.9 \pm 0.1 \pm 3.2\%$, the total observed neutron branching ratio is 10% at most (including systematic error). This is in sharp disagreement with the total neutron branching ratio measured by Dufour *et al.*, $86 \pm 4\%$ [Du88] (the sum

of the $1n$ and $2n$ multiplicities). Consequently, by subtracting our total branching ratio ($6.3 \pm 0.1 \pm 3.2\%$) from the total found by Dufour *et al.*, we find that 73–87% of the total neutron yield is "missing". In Ref. [Be95] we proposed that this was due a very strong neutron group or groups that have neutron energy below threshold (0.77 ± 0.13 MeV). Using Eq. 3.31 we find that an emitted neutron with an energy equal to threshold would have a Q-value of 0.83 ± 0.14 MeV. Given that the $1n$ -emission threshold is 0.97 ± 0.02 MeV, we deduced that most of the missing neutron yield resulted from $1n$ decay to a state in ^{14}B with an excitation energy between 0.95 and 1.82 MeV (including error). The end point energy of the corresponding β decay is in the range of 15.38 – 14.15 MeV and the predicted $\log ft$ is in the range of 3.6–3.8. We shall see, in the following description of the RIKEN experiment, how this information helped guide the setup for second experiment of this thesis.

CHAPTER 4

EXPERIMENTAL METHOD FOR THE RIKEN EXPERIMENT

This chapter describes the experimental method for the second of the two experiments described in this work. Because the experimental method for the second experiment was very similar to that of the first experiment, details that were already given in chapter 2 will not be repeated here. In Sec. 4.2, we shall see how the results of the first experiment guided the set up of this experiment. First, the method of ^{14}Be radioactive beam production and separation using the RIPS (see below) mass fragment separator is given. Next, the neutron detector array, its associated hardware, and the γ -ray detector used for γ - n coincidence are described. Last, the various calibration runs required to determine neutron detection efficiency, to perform an energy and detection efficiency calibration of the γ -ray detectors, and to make a time and distance calibration of the time-of-flight detectors is stated.

4.1 ^{14}Be Radioactive Beam Production at RIKEN

The second experiment was performed at the Institute of Physical and Chemical Research (RIKEN) at Wako, Saitama, Japan. The ^{14}Be beam was produced by projectile fragmentation of a 100 pnA 100 MeV per nucleon ^{18}O beam. The primary beam, produced by the K540 Ring Cyclotron [Ya88], impinged on a 8 mm thick ^9Be target that was placed just before the first quadrupole [Ku92] of the RIPS (RIKEN projectile-fragment separator) radioactive beam facility. This device

is a fragment mass separator that is used to collect and separate ^{14}Be ions. It consists of two 45° dipole magnets that bend in the same direction and twelve quadrupole and four sextupole magnets (Fig. 4.1). The RIPS beam facility was designed to produce high beam intensities by having a large acceptance mode (Table 4.1).

TABLE 4.1

MAXIMUM SETTINGS FOR RIPS

parameter	value
solid angle acceptance	5.0 msr
angular acceptance (circle)	80 mrad
momentum acceptance ($\Delta p/p$)	6.0 %
rigidity	5.56 Tm

SOURCE: Ref. [Ku92]

The first dipole magnet D1 (Fig. 4.1), set to 4.4129 T·m selects the fragments according to their mass-to-charge ratio (Eq. 2.2), which for this experiment was 3.5 (see Sec. 2.1). Undesired fragments were stopped inside this magnet. A thick concrete shielding wall separated D1 from the rest of RIPS to provide low background conditions. This dipole was insufficient to completely separate the desired fragments, since many isotopes can have the same approximate mass-to-charge ratio. Thus a dispersive wedged-shaped aluminum degrader (wedge angle 15.25 mrad and median thickness 2683 mg/cm^2 , corresponding to achromatic conditions [Ku92]) was placed at the first focus (F1) to further separate the fragments by inducing an energy loss that is sensitive to the mass and charge of the particles (see Sec. 2.1 and Ref. [Du86]). This energy loss allows the second dipole D2 (set to 3.5575 T·m) to focus different nuclides at different points along the focal plane of F2.

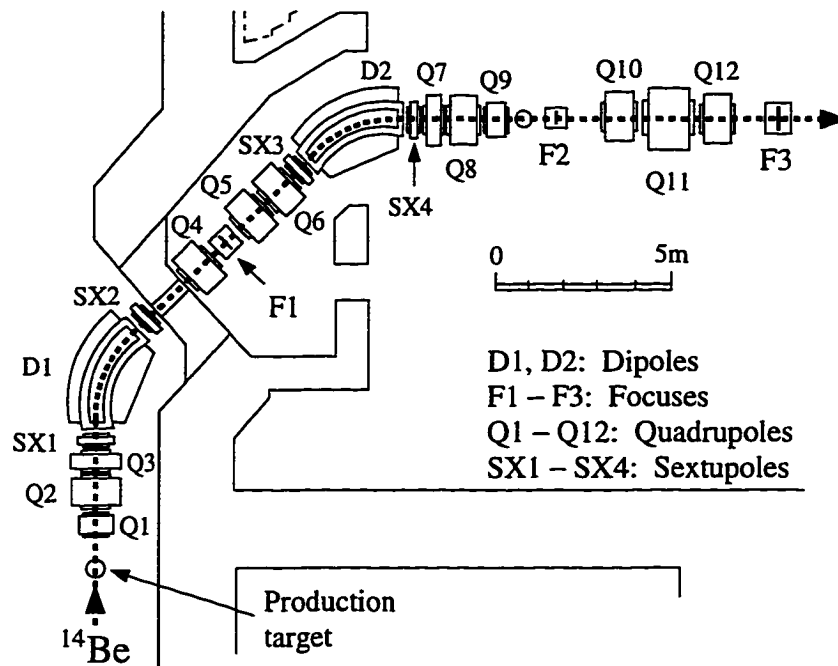


Figure 4.1 Diagram of the RIPS radioactive beam facility.

4.2 The RIKEN Neutron Detector Array and Associated Hardware

A schematic of the experimental apparatus used to perform the ^{14}Be decay study is shown in Fig. 4.2. Just as in the NSCL experiment, the ^{14}Be beam was energetic enough so that the apparatus shown in Fig. 4.2 could be placed in air. A thin Kapton[®] window (roughly 100 μm thick) was placed at the end of the beam line to separate the vacuum from the air. The ^{14}Be beam was stopped inside a stack of five thin (300 μm) silicon surface-barrier detectors (SSD) tilted at 45° to the beam axis. These detectors measured 48 mm by 48 mm and were separated from one another by 3 mm. The ΔE signal from each SSD provided redundant information on the relative number and species of particles interacting within the stack. The SSD detectors could not be used as the start detector, because, for each event, any number of the five detectors could register a β decay depending on its origin and direction. Therefore two sets of two thin plastic scintillators (each measuring 10 cm \times 10 cm \times 2

mm, BC408^{*}), placed in front of (upstream) and behind (downstream) the SSD's (Fig. 4.2), detected the β decay of implanted nuclei (known as " β detectors"). In Fig 4.2, the upstream scintillators are labeled $\beta u1$ and $\beta u2$, and the downstream ones are labeled $\beta d1$ and $\beta d2$. The logical AND of each set of scintillators ($\beta u1 \cap \beta u2$ and $\beta d1 \cap \beta d2$) was required to minimize triggering on noise. The logical OR of the scintillators ($\beta u1 \cap \beta u2, \beta d1 \cap \beta d2$) was the start for the acquisition system so that decay particles emanating in either direction would trigger the system. A diagram of the electronics associated with the β detectors is given in Appendix C.1.

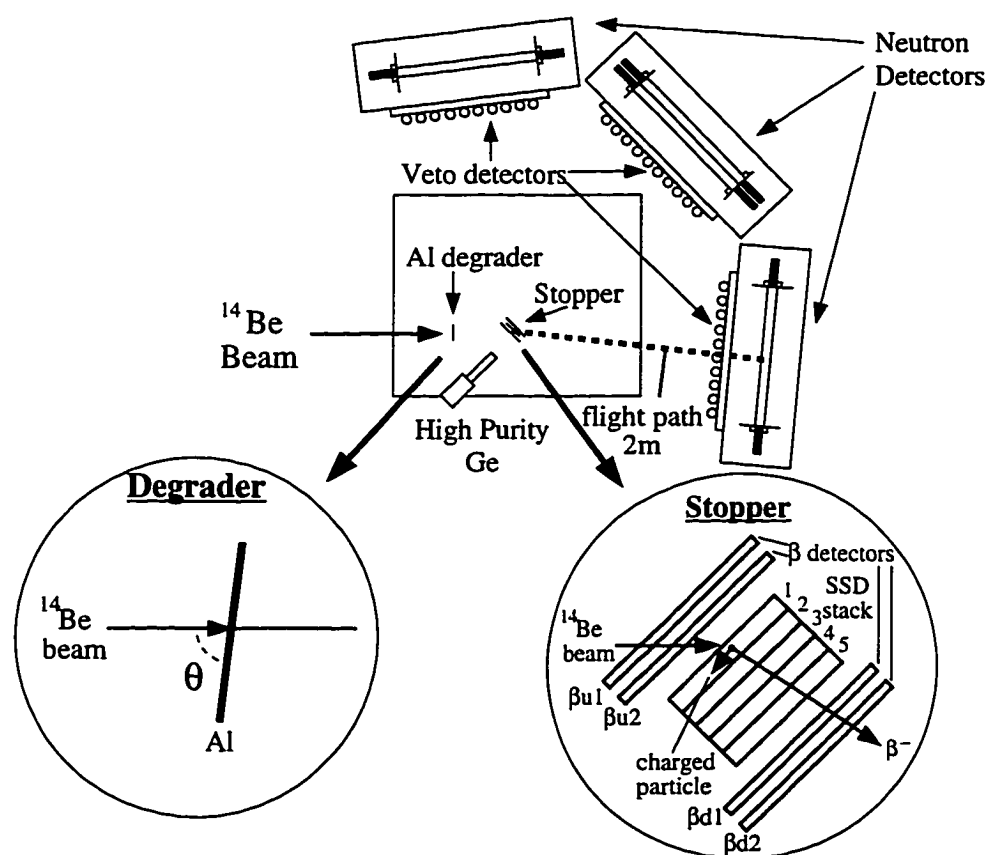


Figure 4.2 Schematic of experimental setup viewed from above with enlarged detail of the stopper (implantation detector) and the aluminum degrader. This figure is not drawn to scale, and it was, in part, obtained from [Ki93].

^{*}Density 1.032 g/cm² and hydrogen-to-carbon ratio 1.104 [Bi90].

A rotatable aluminum degrader was placed in front of the SSD's to adjust the depth to which the ^{14}Be ions were implanted so they were stopped in the center of the stack. Because the majority of the particles that interacted within the SSD stack were ^{14}Be (this will be discussed later), this nuclide gave the largest energy signal that was easily identified (Fig. 4.3). The relative number of ^{14}Be ions that stopped within a particular SSD could be determined on-line, which eliminated the need to calculate the energy losses, as was done in Sec. 2.2. The sum of the ^{14}Be peak (Fig. 4.3) for the second (Si_2), third (Si_3), and fourth (Si_4) SSD's (Fig 4.2) were found using both a 100 μm thick aluminum degrader and a 300 μm thick aluminum degrader. The ratios Si_2/Si_3 and Si_3/Si_4 were found for the 300 and 100 μm thick degraders, respectively, for several rotation angles. The ratios are plotted versus the effective thickness (t_{eff}) (Fig. 4.4) of the aluminum degrader. If θ is the interior angle between the degrader and beam axis, and t is the thickness of the degrader, then $\sin \theta = t/t_{\text{eff}}$, and

$$t_{\text{eff}} = t / \sin \theta. \quad (4.1)$$

The number of ^{14}Be ions stopped in SSD 3 was maximized by averaging the two thicknesses for which the ratios Si_2/Si_3 and $\text{Si}_3/\text{Si}_4 = 0.5$. This procedure was necessary, because the distribution of stopped ^{14}Be ions was not symmetric due to energy-loss straggling. This yielded an ideal effective thickness of 380 μm , achieved by using the 300 μm thick aluminum degrader rotated at 52° . The electronics associated with the SSD stack shown in Appendix C.2 indicates how the timing and energy signals were obtained. It was necessary to attenuate the energy signals to properly scale them for the ADC. Different attenuations were also required for the beam-on and beam-off signals.

Two thin plastic scintillators (about 1 mm thick) providing both energy and timing information were placed at the two intermediate foci F2 and F3 of RIPS (Fig. 4.1) to monitor the purity of the beam. A plot of the flight time from F2 to F3 versus the light output at F2 (proportional to the energy deposited) yielded clear Z and A separation (Fig. 4.5, also see Sec. 2.2). The energy loss (light output) is

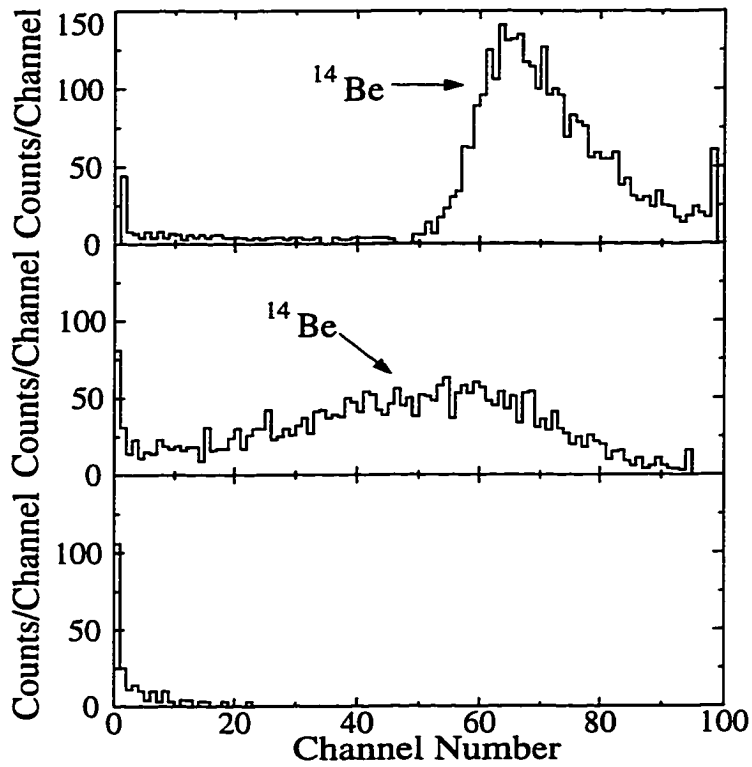


Figure 4.3 Energy spectra of SSD's 2-4 using an aluminum degrader with thickness of 300 μm tilted at 30° (see text).

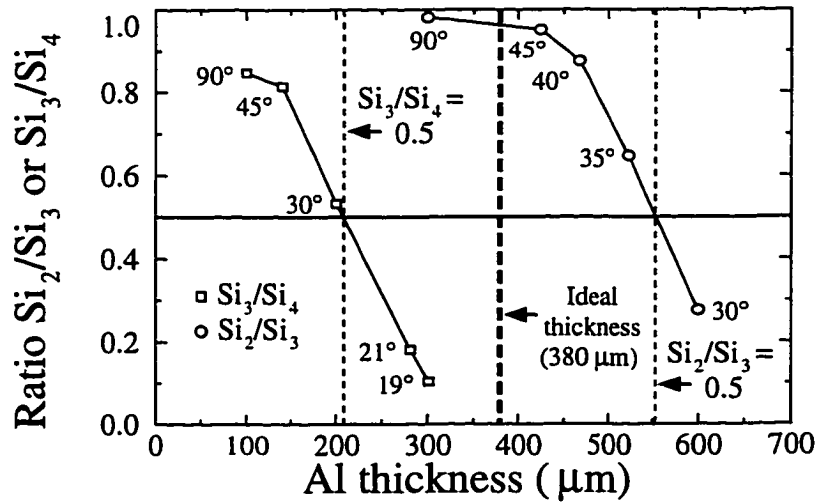


Figure 4.4 Plot of the ratios Si_2/Si_3 and Si_3/Si_4 versus the effective degrader thickness. The angle of the aluminum degrader relative to the beam axis (see text) for each data point is also indicated.

more strongly dependent on the charge q (Eq. 2.7) than the mass m , and the time-of-flight is proportional to m/q . Thus bands of increasing Z are seen with increasing ΔE_{F2} (y-axis, Fig. 4.5), and increasing m/q is associated with increasing $\text{TOF}_{(F3 - F2)}$ (x-axis). By summing the various groups that have been identified in Fig. 4.5, one can determine the purity of the beam. The relative yield and half-life of each nuclide present in the beam is listed in Table 4.1. In the off-line analysis, a similar plot (Fig. 4.6) was made requiring coincidence with the downstream β -detector. This yielded the number and species of particles which passed through these detectors. Thus the composition of the beam that stopped in the SSD stack was obtained by subtracting the yields of each nuclide shown in Fig. 4.6 from those obtained in Fig. 4.5. The relative amounts of the nuclides *stopped* in the SSD stack are also listed in Table 4.2. The purity of the beam stopped in the SSD stack was $68.7 \pm 0.5\%$. This may not seem like a very pure beam, but $28.34 \pm 0.15\%$ ($0.86 \pm 0.05\%$) of the beam was tritons (^3H), respectively, both having half-lives (12.3 yr and 13.8 s) that are long enough to be considered part of the constant background. The electronics associated with the F2 and F3 scintillators are shown in Appendix C.3.

TABLE 4.2
PURITY OF BEAM

Purity of beam			Purity of beam stopped		Purity of beam stopped excluding ^3H and ^{11}Be	
Isotope	Yield (%)	Half-life	Isotope	Yield (%)	Isotope	Yield (%)
^{14}Be	68.6 ± 0.4	4.35 ms	^{14}Be	68.7 ± 0.5	^{14}Be	97.0 ± 0.7
^{14}B	0.62 ± 0.09	14 ms	^{14}B	0.59 ± 0.09	^{14}B	0.83 ± 0.13
^{12}Be	0.25 ± 0.04	24 ms	^{12}Be	0.25 ± 0.04	^{12}Be	0.36 ± 0.05
^{11}Be	0.86 ± 0.05	13.8 s	^{11}Be	0.86 ± 0.05	—	—
^{11}Li	0.29 ± 0.03	8.7 ms	^{11}Li	0.30 ± 0.03	^{11}Li	0.42 ± 0.05
^9Li	0.72 ± 0.15	177 ms	^9Li	0.57 ± 0.14	^9Li	0.81 ± 0.20
^6He	0.65 ± 0.09	807 ms	^6He	0.43 ± 0.09	^6He	0.60 ± 0.11
^3H	28.01 ± 0.14	12.3 yr	^3H	28.34 ± 0.15	—	—

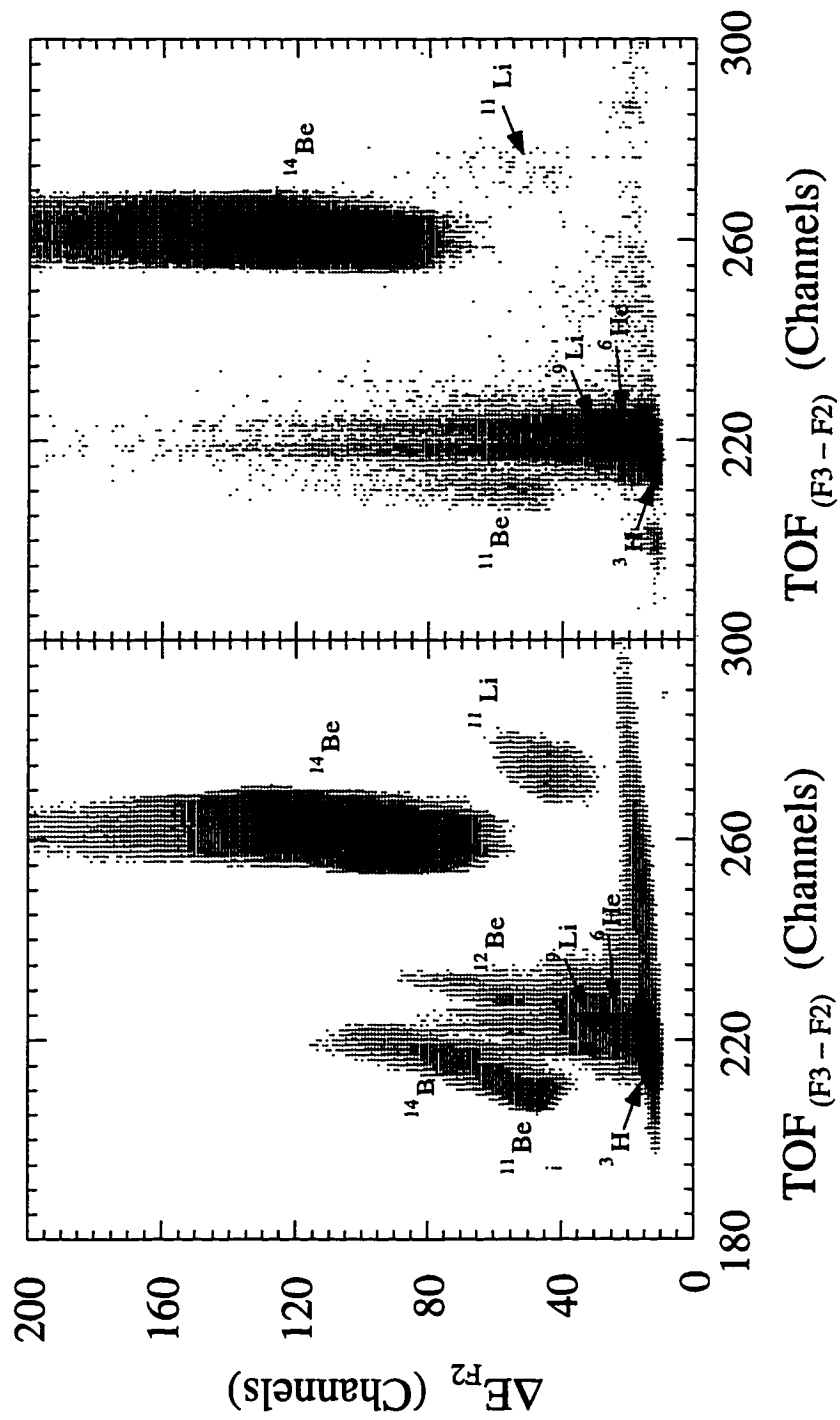


Figure 4.5 Plot of the energy deposited in the F2 scintillator versus flight time between F2 and F3. Figure 4.6 Same as Fig. 4.5 but gated in coincidence with the downstream β -detector.

The β -delayed neutrons were detected in three plastic scintillator arrays. The distance between the SSD stack and each neutron detector array varied from 200 to 203 cm. Each array consisted of either fifteen or sixteen long rectangular scintillator bars (BC412, 96 cm long by 6.1 cm high by 6.1 cm deep) that were stacked one on top of the other in the form of a "neutron wall" (Fig. 4.7). One of the arrays (Fig. 4.2) had two such walls stacked one behind the other to determine what percentage of the β -delayed neutrons were stopping in the front wall (as the beam sees it). We found that almost none of the neutrons of interest penetrated to the back wall (see below). A photomultiplier tube with both energy and timing outputs was optically coupled to either side of each scintillator bar. Because we believed that high thresholds prevented seeing all the neutrons (Sec. 3.6), we lowered the thresholds of the photomultiplier tubes as much as possible. The active area of each wall was about 96 cm by 96 cm (for sixteen bars) and the total solid angle was 579 ± 4 msr ($4.61 \pm 0.03\%$, geometrical efficiency). (The method by which this was calculated will be described in Sec. 4.6.).

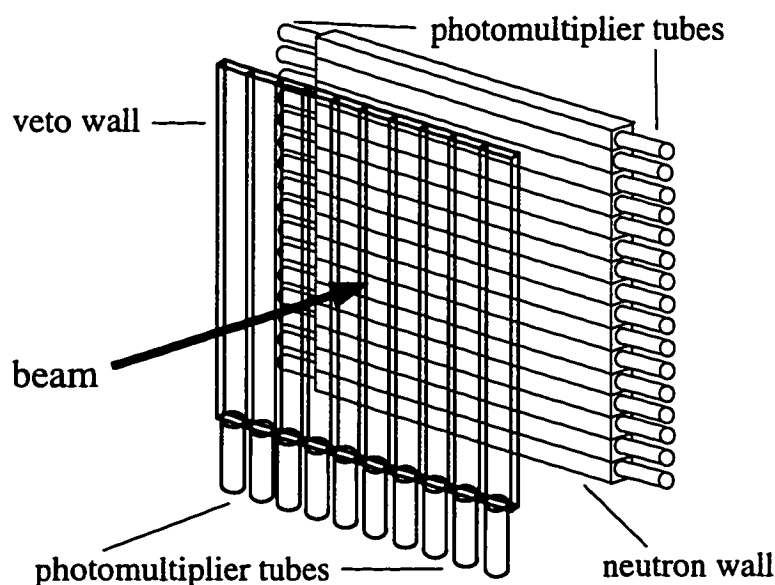


Figure 4.7 Diagram showing the geometry of the neutron and veto walls; it is not drawn to scale.

An accurate determination of the neutron position along the surface of the wall was necessary to measure the neutron energy by time-of-flight, because the flight path is not a constant. Vertical position was determined by simply noting which detector registered an event, and both timing and energy signals can be used to determine horizontal position. The stop for the acquisition system was the logical OR of all of the timing outputs, and in the off-line analysis we required that both photomultiplier tubes at each end of the scintillator bar⁴ registered an event to minimize triggering on noise. The flight time was determined from the mean of both sides. These flight times were then corrected so that they corresponded to the same flight path distance regardless of the location of the neutron interaction (see Sec. 4.5).

The type of module (model 4300B Lecroy [Le85]) used to digitize both timing and energy information is known as a FERA (Fast Encoding and Readout ADC). This module is distinguished from an ordinary ADC by its fast conversion capability, especially when used in conjunction with the model 4032 Lecroy FERA memory module [Le87c]. This module has a memory stack that allows the data to be read by the acquisition system only when the stack is full, thus minimizing the number of CAMAC reads and increasing the speed of the overall system [Le87c]. The energy signals were attenuated and TFC's (Time to FERA converters) were used to convert the timing information to a suitable form for the FERA's. The FERA and memory modules are coordinated by FERA drivers (model 4301 Lecroy FERA driver [Le]).

A wall of thinner plastic scintillators (100 cm wide by 80 cm high) was placed about 25 cm in front of each neutron wall so that it completely covered the thicker neutron wall as seen by the SSD stack. These walls consisted of ten scintillators paddles (BC412 10 cm wide by 80 cm long by 0.5 cm thick) that were placed vertically next to one another (Fig. 4.7). Each paddle had a photomultiplier tube

optically coupled to it that produced both timing and energy outputs. These walls were made thin enough and the threshold was made high enough so that they were sensitive to electrons but not neutrons. The prompt peak seen in the time-of-flight spectra could then be reduced by eliminating those events that simultaneously trigger any of paddles in a "veto wall" and any of the bars in the neutron wall that is behind that corresponding veto wall. The electronics associated with neutron and veto detectors, demonstrating the use of FERA modules, is given in Appendix C.4.

Gamma rays emitted in coincidence with β -delayed neutrons were measured with a high purity Ge detector. The Ge crystal was 6.2 cm long with a diameter of 5.7 cm and its front face 13.1 cm away from the SSD stack. The code of Wielopki [Wi77] (see Sec. 3.4.2) was used to calculate the solid angle of this detector (144 ± 7 msr). The γ -ray detector was positioned so that it did not block the beam nor the view of the of the SSD stack by the neutron detectors. A diagram of the electronics associated with high purity Ge detector is shown in Appendix C.5.

4.3 Beam-on/Beam-off Duty Cycles

Just as in the previous experiment, the beam was pulsed at regular intervals so that the ^{14}Be ions were implanted while the beam was on and decays were detected while the beam was off, providing clean conditions for the observation of the β -delayed neutron decay. A Clock Generator (an in-house electronic module built at RIKEN) was used to turn the beam on and off by producing an alternating logic signal that dephased the cyclotron RF with the desired period. The method of deriving neutron spectroscopic information is very similar to that in Sec. 2.3, except for the way the start signal is derived (see Sec. 4.2). The basic features of the time-of-flight neutron spectra are also very similar to that described in Sec. 2.3.

Several different duty cycles were used here: 10 ms on/20 ms off, 1 ms on/19

ms off, 2 ms on/18 ms off, and 10 ms on/90 ms off. The duty cycles with greatest percentage of beam-on time yields the most statistics, those with the longer beam-off periods allow the decay spectrum to be fit more accurately, and those with the shortest beam-on period have less build up of daughter and impurity activities. Because the statistics were low and most of the data was obtained with the 10 ms on/20 ms off duty cycle, we used this data set to analyze the activity spectrum.

4.4 Calibration Runs

4.4.1 Gamma ray calibration

An energy and detection-efficiency calibration of the γ -ray detector was performed by using a ^{152}Eu source (activity 4.7 μCi). A calibration was made both before and after the ^{14}Be data run, to determine if there was a drift or gain shift during the experiment (both found to be negligible). The calibration after the experiment was used because it had higher statistics. The source was placed as close as possible to the SSD position so that the solid angle subtended by the high purity Ge detector as seen by the source was nearly the same as that seen by the SSD stack.

4.4.2 Time-of-flight calibration run

The neutron time-of-flight spectra were calibrated by using a pulser that emitted very narrow pulses (0.5 ± 0.1 ns wide) that were spaced 10 ns apart for a fixed period of time. The method by which the calibration was carried out is the same as that for the previous experiment (see Sec. 2.5.2).

4.4.3 ^{17}N calibration run

A ^{17}N beam was used to measure the intrinsic detection efficiency of the

plastic neutron detectors. It was also used to make an accurate neutron flight path calibration. The energies and branching ratios of the β -delayed neutron peaks have already been given in Sec. 2.5.3. The duty cycle for this run was 3 s on and 7 s off.

4.4.4 Energy calibration of neutron detectors

There were also a series of calibrations that were not performed in the previous experiment, the first of which was a calibration of the energy signals or light output of the scintillators that were used as neutron detectors. The calibration was performed by using the Compton edges produced by ^{60}Co and ^{137}Cs γ -ray sources. The nuclide ^{137}Cs has a single edge at 477 keV and ^{60}Co has two edges at 963 keV and 1118 keV. Because the resolution of the neutron energy signals is not sufficient to resolve the two ^{60}Co edges, we used the average of the two edges (both lines have branching ratios of 100% [Appendix B]), 1041 keV, as the energy of the edge. For the ^{60}Co calibration the source was placed at the SSD location, and for the ^{137}Cs source a more accurate calibration was done by placing the source 75 cm in front of the center of each wall. The method by which the Compton edge energies were determined was given in Sec. 2.7.4 (Fig. 2.16).

4.4.5 SSD stack energy calibration

A relative calibration of the SSD energy signals was made using a pulser that injected the same quantity of charge into the pre-amplifier for each surface barrier detector. The sharp spike produced by the pulser and the noise peak of the pedestal (assumed to correspond to zero energy) gave two energy calibration points. It was assumed that the spectra were linear. This calibration was necessary to enable one to directly compare the energy spectra of the five SSD's.

4.4.6 Horizontal position calibration

We used a ^{106}Ru β source to perform the horizontal position calibration of the neutron detectors by placing it 10 cm from either end of the scintillator bar. This source emits β particles and γ rays of various energies through the β decay of ^{106}Ru and its daughter ^{106}Rh . The β decay of ^{106}Ru produces a single β -ray line with average energy 10.03 keV [de88], and that of the ^{106}Rh daughter produces a number of β particle lines with average energies in the range of 240 to 1508 keV [de88] and a large number of γ ray lines with energies in the range of 21 to 1840 keV [de88].

4.5 Flight Path Determination

The distance calibration consisted of two steps: first, correcting for the differing flight paths along the surface of each wall, using the horizontal and vertical position information, and then performing a distance calibration using a ^{17}N beam (see Sec. 2.6). This calibration minimized the error associated with systematic differences of the actual flight path from the geometrical flight path.

4.5.1 Geometrical flight path correction

The dimensions and geometry of the neutron walls with respect to the SSD location were carefully measured. Figure 4.8 shows a schematic view of the neutron detectors. The arrows emanating from the SSD stack and terminating at the center of each neutron wall indicate the perpendicular distance between the two. Because the center of each wall did not coincide with this perpendicular, it was necessary to account for the offset when calculating the horizontal position. In the lower left of Fig. 4.8 is a front view of neutron wall 1. Notice that the beam axis (beam level) does not intersect wall 1 exactly at the middle. The neutron is assumed to interact at the vertical center of each bar. This vertical position is found quite simply by noting which bar registered the interaction and then using the equations displayed in Fig. 4.8.

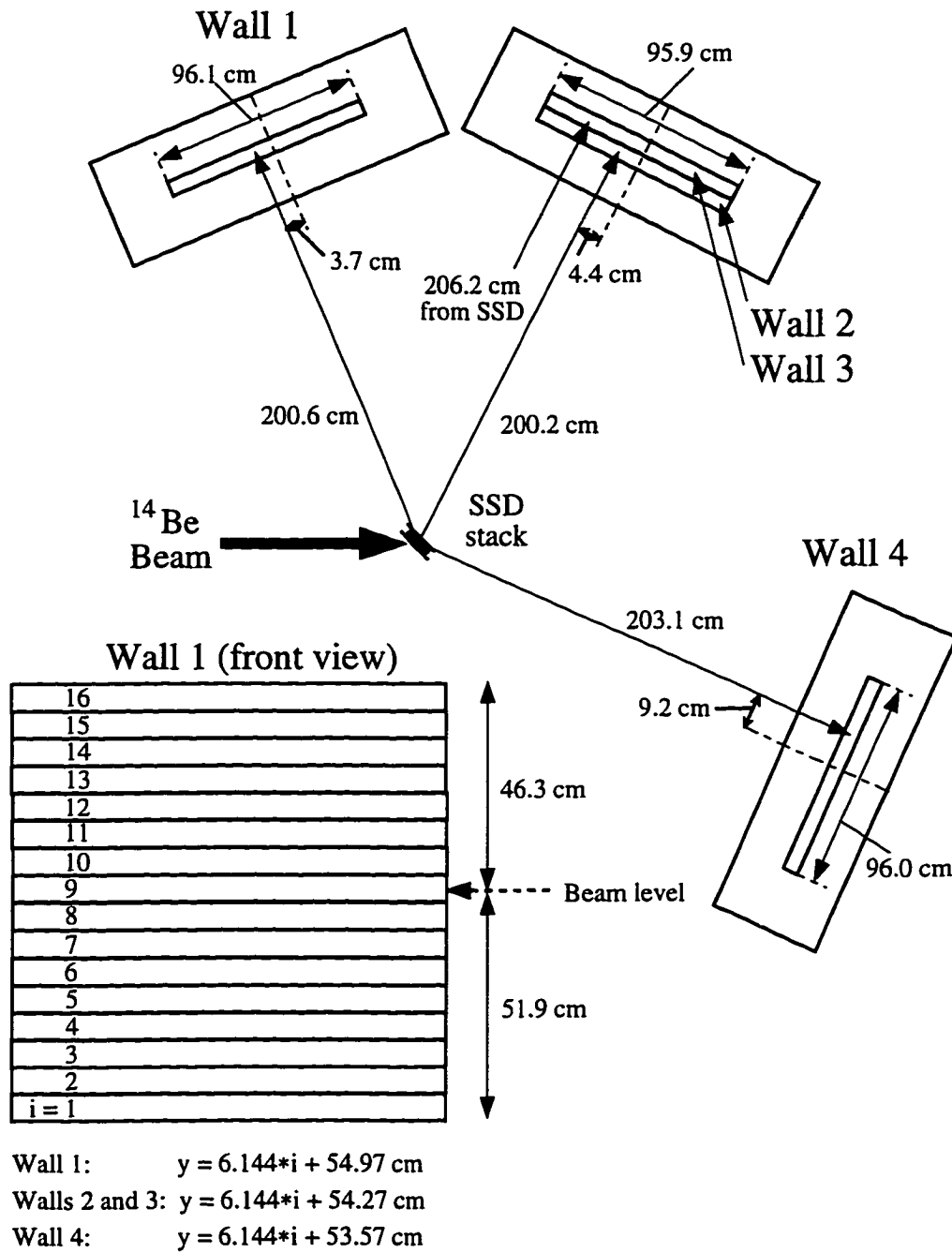


Figure 4.8 Schematic of the neutron detectors, as seen from above, showing the dimensions, geometry, and distance of these detectors from the SSD stack. A front view of neutron wall 1 is shown in the lower left corner (the geometries of the other walls are similar). The equations give the vertical position corresponding to each neutron bar i for each of the walls.

Now that the vertical and horizontal position of each scintillator bar has been determined, the next step is to find the horizontal position of each neutron interaction along its respective scintillator bar. A β source (^{106}Ru [see Sec. 4.4.6]) was used to perform the calibration. The source was placed 10 cm from the end of each bar (Fig. 4.9) giving two calibration points of known horizontal position. One can use both energy (light output) and timing information to perform the calibration. The energy method takes advantage of the fact that the scintillator light is attenuated by the plastic. The timing method, on the other hand, uses the fact that light takes a finite length of time to traverse the scintillator bar.

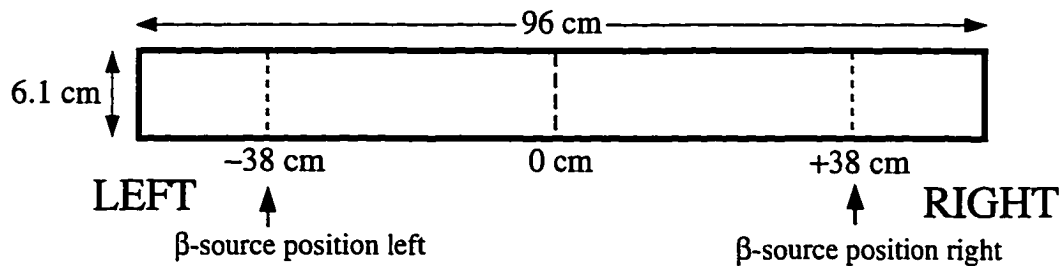


Figure 4.9 Diagram showing the geometry of a scintillator bar (as the beam sees it) and the locations of the β source used in the horizontal calibration.

If the neutron interacts at the extreme right position (Fig. 4.9), then the light output from the right photomultiplier tube R_E would be a maximum and that from the left photomultiplier tube L_E would be minimum. If the neutron interacted on the extreme left side, then R_E is a minimum and L_E is a maximum. Defining the horizontal position as positive to the right, $(R_E - L_E)$ is larger to the right and smaller to the left. This quantity is normalized by total light output $(R_E + L_E)$ and calibrated using the linear function:

$$X_{\text{pos}} = \text{offset} + \text{slope} \times \frac{R_E - L_E}{R_E + L_E}, \quad (4.2)$$

where X_{pos} is the horizontal position relative to the center of the bar (see Fig. 4.9), and the "offset" and "slope" are those of the calibration curve.

The same function as Eq. 4.2 can be used for the timing information, but in this case the difference $(R_T - L_T)$ increases to left. When the interaction is at the extreme right, R_T (right timing signal) is a *minimum* and L_T is a *maximum*; for the left side, the reverse is true, opposite to what occurs for the energy signals. In this case, the following function is plotted in Fig. 4.10:

$$X_{\text{pos}} = 1024 - 500 \times \frac{R_T - L_T}{R_T + L_T}, \quad (4.3)$$

for neutron bar 1, wall 1 (Fig. 4.8) with the β source placed at the left and right positions (Fig. 4.9). The quantity $(R_T - L_T)/(R_T + L_T)$ has been multiplied by 500 to give the resultant histogram a resolution roughly equivalent to that of raw timing signals, and an offset of 1024 has been added to place the two peaks near the center of the spectrum. The peaks corresponding to the energy signals look similar but have poorer resolution. The peaks shown in Fig. 4.10 were fitted with a symmetrical hypergaussian distribution (see Sec. 2.6 and Ref. [Di93]), where the exponent was equal to 1.35 and the reduced $\chi^2 = 2.64$. This peak shape yielded a better fit than an ordinary Gaussian distribution.

It was necessary to calibrate all horizontal position spectra (X_{pos} , Eq. 4.3) in terms of absolute position (cm). We shall use Fig. 4.10 as an example. The centroid and width of the peak corresponding to the left position are 1007.9 ± 0.4 and 3.0 channels, respectively, and those corresponding to the right position were 1032.2 ± 0.3 and 3.2 channels, respectively. Because the β source was placed 10 cm from either end of the scintillator bar, the peaks correspond to -38.05 cm and $+38.05$ cm, left and right, respectively.

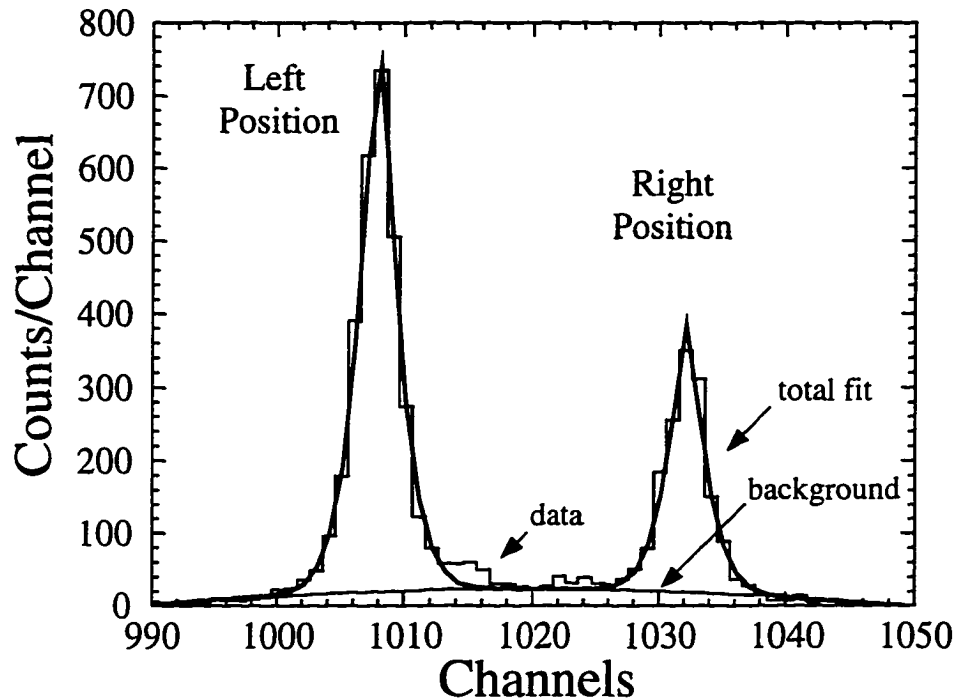


Figure 4.10 Typical horizontal position spectrum using timing information and the function of Eq. 4.3. The two peaks correspond to the left and right positions of the β source. The peaks are reversed in direction because the sign of $(R_T - L_T)$ is opposite to that of $(R_E - L_E)$ (Eq. 4.2).

Using these data, we obtained the following calibration curve:

$$Y_{\text{cm}(\text{bar } 1, \text{ wall } 1)} = 3.1317 \cdot X_{\text{pos}} - 3194.48. \quad (4.6)$$

(Note that extra significant digits have been retained in Eq. 4.6 to avoid round off error.) This was done for all horizontal position spectra. Because it was necessary to add the statistics of all time-of-flight spectra together in the analysis, the horizontal position resolution was found by adding all horizontal position spectra together. The result is plotted in figures 4.11a and 4.11b at a resolution of 0.2 cm/chan. Both timing (Fig. 4.11a) and energy (Fig. 4.11b) signals are shown for comparison. We found that hypergaussian distributions (Sec. 2.6 and Ref. [Di93]) fitted the peaks best. The widths of the two peaks in each case were averaged and yielded a resolution of 8.0 cm

(FWHM) using timing signals and 19.7 cm (FWHM) using energy signals. The timing signals were used for the analysis because of their superior resolution.

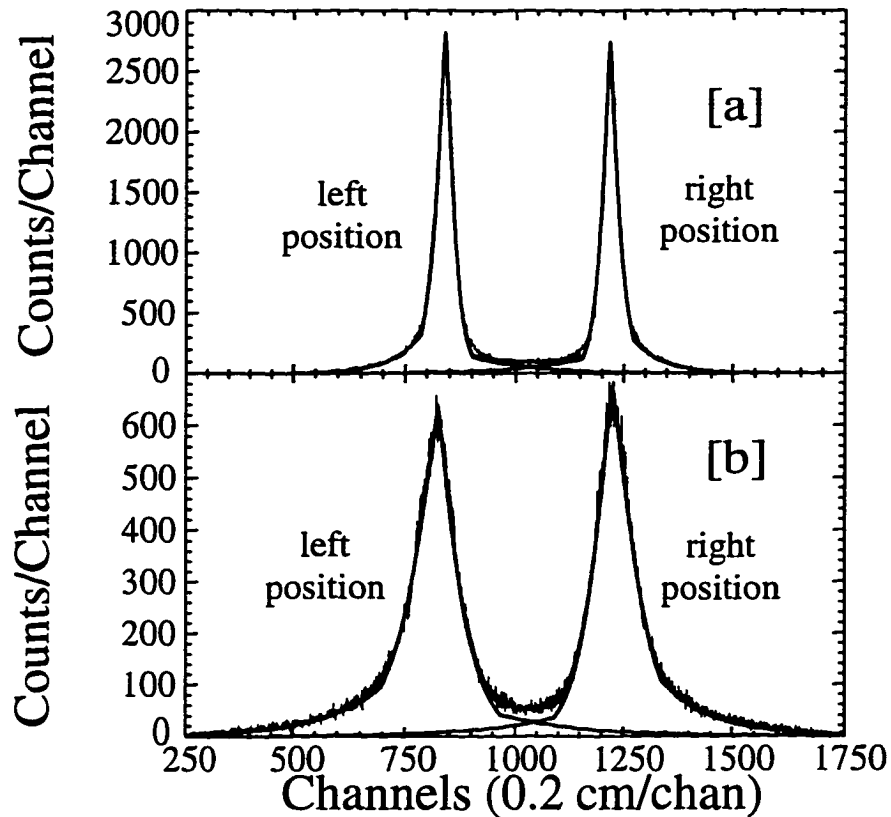


Figure 4.11 (a) A fit of the sum of all calibrated timing position spectra from which the timing horizontal position resolution was determined (b) The same as Fig. 4.11b but corresponding to energy signals.

Because the neutron walls were not centered (Fig. 4.8), it was necessary to add the following offsets to Eq. 4.6: wall 1, +3.7 cm; wall 2 and 3, +4.4 cm; and wall 4, +9.2 cm. Once the horizontal position x , vertical position y , and perpendicular distance z are obtained, the total distance d can be found from:

$$d = \sqrt{x^2 + y^2 + z^2}. \quad (4.7)$$

We normalized all the time-of-flight data so that all neutron events corresponded to the same flight path distance (two meters, a convenient value).

This minimized the loss of resolution due to the differing path lengths along the surface of the wall. If t_β is the flight time of the β particles, C_β is the centroid of the β (prompt) peak, C_n the channel number of a neutron time-of-flight event, and k is the conversion from time-of-flight to channels, then the flight time of the neutron is proportional to the channel difference Δch between the neutron channel number and the channel number corresponding to time zero ($C_\beta - t_\beta \cdot k$):

$$\Delta ch = C_n - (C_\beta - t_\beta \cdot k). \quad (4.8)$$

The quantity $t_\beta = d/v_\beta$, where v_β equals $0.995c$ (see Eq. 2.14 and Sec. 2.6), and d is the flight path distance of the neutron. If the distance to which all events are normalized is d_{std} (distance standard, here 2 m), then Δch becomes $\Delta ch \cdot (d_{std}/d)$ and the normalized channel number $C_{n_{cor}}$ (C_n corrected) is given by

$$C_{n_{cor}} = (C_\beta - t_\beta \cdot k) + \Delta ch \cdot (d_{std}/d). \quad (4.9)$$

This final result was applied to all time-of-flight spectra.

4.5.2 Distance calibration

Now that the time-of-flight spectra have been normalized to a nominal distance of two meters, it was still necessary to calibrate the flight path distance using a ^{17}N beam. We assumed that the ^{14}Be beam stopped at the center of SSD stack, and that the neutrons stopped at a depth equal to half the thickness of the neutron detectors at a vertical location equal to half its height. As was explained in Sec. 2.6, these assumptions are not necessary valid, and a distance calibration using a ^{17}N beam will minimize these systematic deviations of the actual flight path from the geometrical flight path. In this case, the neutron threshold was low enough to observe the 0.3838 MeV ^{17}N peak, which allowed the use of three neutron peaks (1.7003, 1.1709, and 0.3838 MeV) for distance calibration. Since the method is

very similar to that described in Sec. 2.6, the details will not be repeated here. The calibrated distance found from all three groups are listed in Table 4.3. The weighted average corresponding to the three peaks, 201.4 ± 0.7 cm, was used for the analysis.

TABLE 4.3
CALIBRATED DISTANCE CORRESPONDING TO ^{17}N NEUTRON PEAKS

Energy (MeV)	Velocity (cm/ns)	Distance (cm)
1.7003 ± 0.0017	1.8012 ± 0.0009	202.4 ± 1.3
1.1709 ± 0.0008	1.4953 ± 0.0005	202.4 ± 1.3
0.3828 ± 0.0009	0.8555 ± 0.0010	199.4 ± 1.3

4.6 Neutron Detection Efficiency Calibration

The measured intrinsic neutron efficiency was found from the neutron peaks listed in Table 4.3. The threshold of the start detectors were high enough that a correction was necessary to account for the differing detection efficiencies of these detectors of the β decays corresponding to the three neutron groups. (The threshold of the start detector in the NSCL experiment, on the other hand, was low enough that such a correction had a negligible affect on neutron detection efficiencies.) Then the corrected data points were compared to a Monte Carlo calculation used to produce a detection efficiency curve.

4.6.1 Raw detection efficiency

The raw detection efficiency was determined by a method that is similar to that already been given in Sec. 2.7.1 (see Eq. 2.16). A fit of the ^{17}N β delayed neutron peaks is shown in Fig. 4.12. The neutron groups shown there were fitted in a similar manner as in Fig. 2.7: a hypergaussian distribution with an exponential tail on the

long time-of-flight (low energy) side to account for scattered neutrons was used. A constant background was assumed as before to account for random coincidences. The centroids, yields, and widths of the peaks shown in Fig. 4.12 are listed in Table 4.4.

TABLE 4.4
INFORMATION REGARDING FIT OF ^{17}N PEAKS

Energy (MeV)	Centroid (channels)	FWHM (channels)	Yield (counts)
1.7003 ± 0.0017	1017.7 ± 1.0	24.2 ± 1.8	1300 ± 200
1.1709 ± 0.0008	1109.5 ± 1.3	32.4 ± 0.8	13000 ± 1000
0.3828 ± 0.0009	1500.8 ± 1.9	$98. \pm 10.$	8500 ± 1300

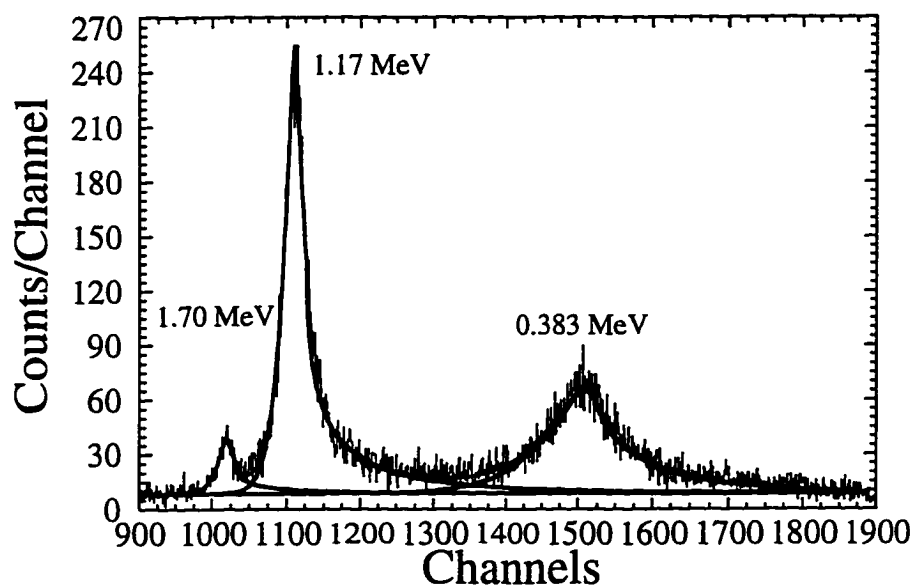


Figure 4.12 Time-of-flight spectrum of ^{17}N data showing the fit from which neutron detection efficiency was determined.

The number of ^{17}N β decays was determined from a fit to the ^{17}N activity curve using the program LIFE5 [Sc94]. Unfortunately the total ^{17}N decay curve was affected by an oscillatory distortion that made it impossible to fit (Fig. 4.13). It is

believed that this distortion was due to severe dead time caused the data transfer between from the CAMAC modules to the acquisition system which had a frequency (1 Hz) that is the same order of magnitude as the beam-off period (7 s). Fortunately, the event rate and corresponding dead time of a portion of the ^{17}N data was low enough so that this corresponding activity curve could be fitted (Fig. 4.14).

The ^{17}N beam was nearly 100% pure, as shown in Fig. 4.15 where the energy loss in the F2 scintillator versus the time-of-flight between the F2 scintillator and the F3 scintillator are plotted. The stronger group is ^{17}N and the much weaker one is an unidentified impurity. Figure 4.16 shows the same plot as Fig. 4.15 but in coincidence with the downstream β detector (in the off-line analysis). We found that the impurity accounted for only 0.1% of the total beam stopped in the SSD stack, where we used the method described in Sec. 2.2 (figures 2.4 and 2.5) and the sum of the groups shown in figures 4.15 and 4.16.

Because the impurity was so small, the ^{17}N activity spectrum was fitted with a single exponential component and a constant background. The regions in Fig. 4.14 bounded by long-dashed lines, consisting of the beginning of the curve (affected by rate dependent dead time) and the "little dip", were excluded from consideration. The fit was performed with the half-life fixed to the accepted value (4.174 ± 0.004 s [Oh76]) resulting in a background of 3.7 ± 0.2 counts per channel, and a reduced $\chi^2 = 0.989$. It was necessary to determine the total number of ^{17}N β decays by subtracting the background from the raw data (yield 82100 ± 300) to account for the "little dip" and other possible distortions from the true curve. This resulted in a ^{17}N yield of 77100 ± 400 where all uncertainties are statistical. Another fit was made in which the half-life was allowed to vary freely, resulting in a half-life of 3.93 ± 0.03 s, a background of 6.3 ± 0.2 counts per channel, and a corresponding reduced $\chi^2 = 0.987$. We used half of the difference between the

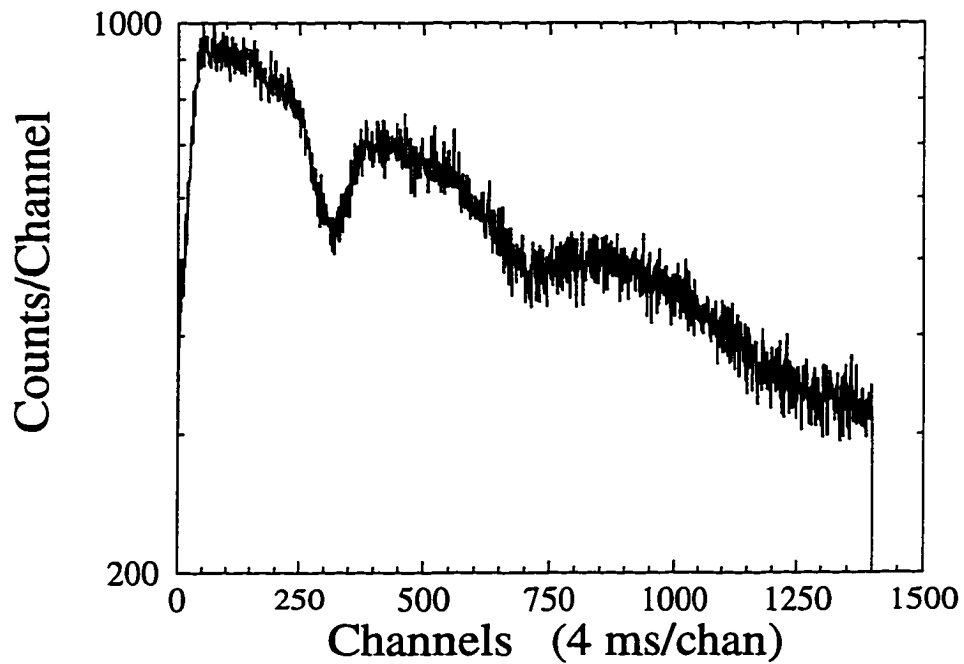


Figure 4.13 Plot of showing the severe distortion in the ^{17}N activity curve.

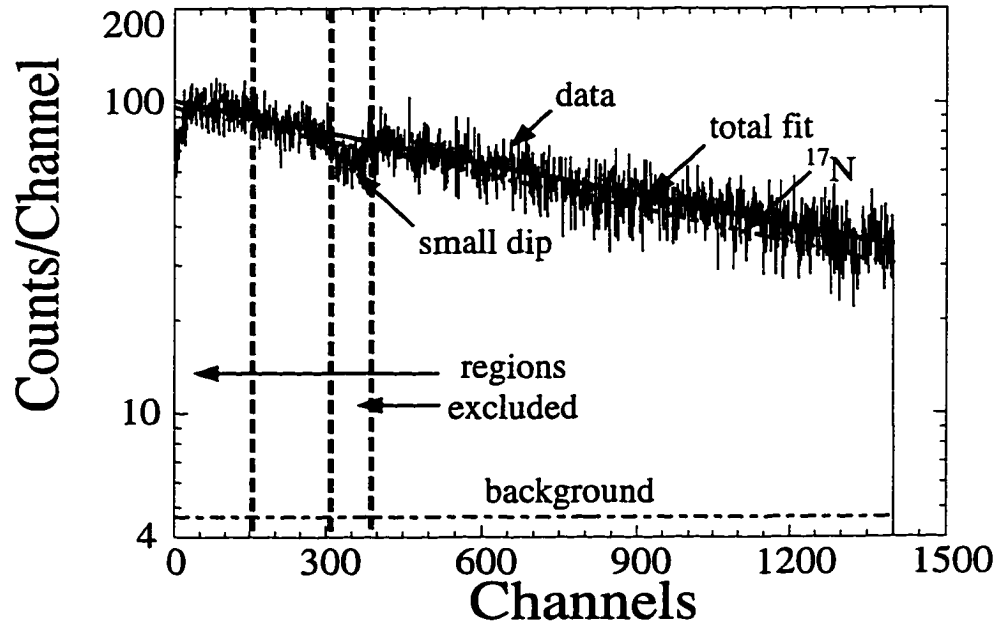


Figure 4.14 The ^{17}N decay curve that was fitted to obtain the total number of ^{17}N β decays. The vertical long-dashed lines indicate the regions excluded from consideration in the fit. See text for more details.

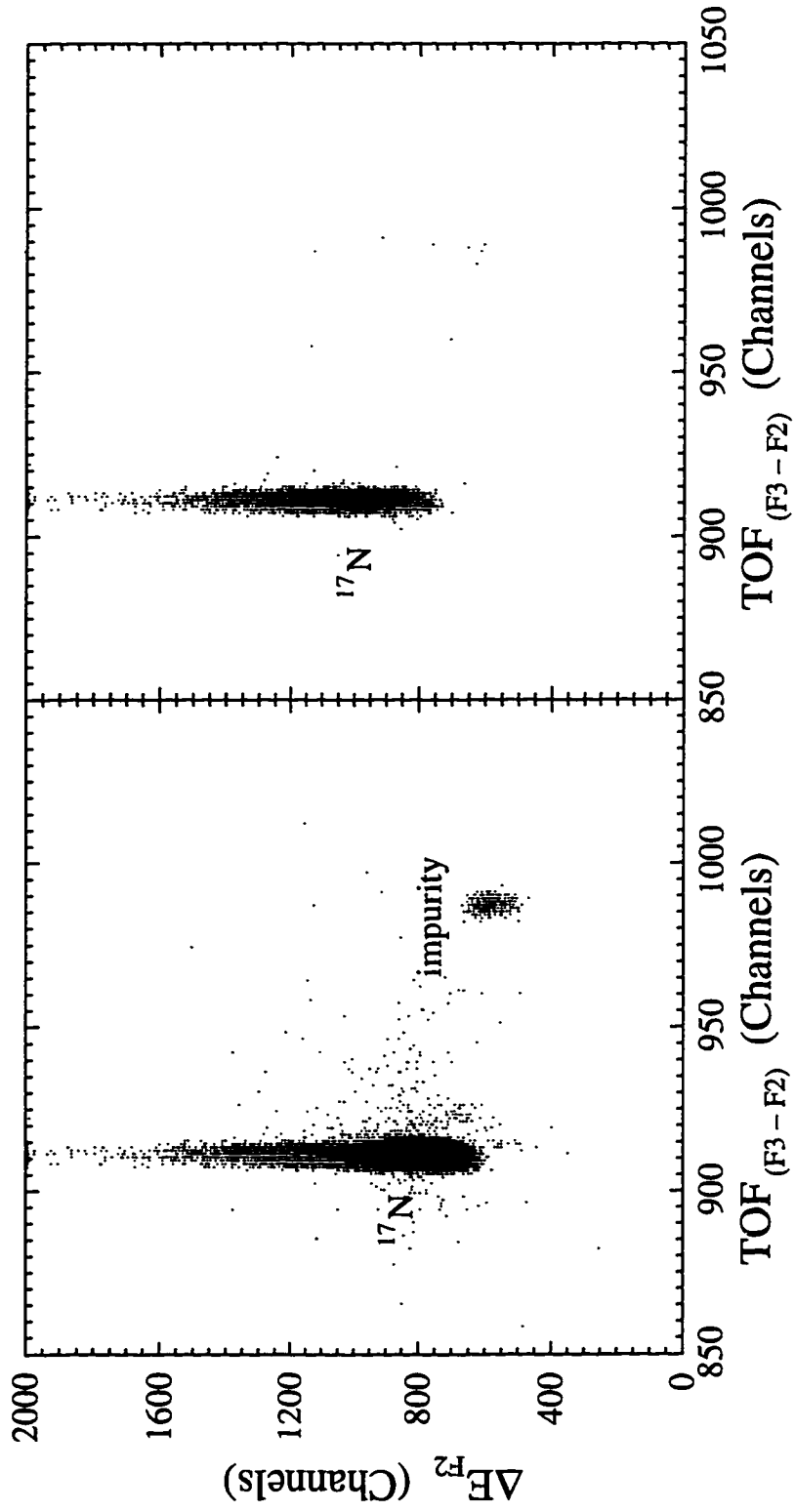


Figure 4.15 Plot of the energy deposited in the F2 scintillator versus flight time between F2 and F3 for the ^{17}N data. Figure 4.16 Same as Fig. 4.15 but gated in coincidence with the downstream β detector.

the yields corresponding to the two fits as the systematic uncertainty in the fit, resulting in a yield of 77100 ± 3600 . Next it was necessary to normalize this yield to the entire ^{17}N data set. Because the beam was very pure and the same beam-on/beam-off duty cycle was used for the entire data set (so that the buildup of daughters and impurities would be the same throughout), we could scale the data set by the total number of counts in the activity spectrum. The sum of the activity curve corresponding to the total ^{17}N data set (Fig. 4.13) was $(7.584 \pm 0.009) \times 10^5$ (statistical error), and that corresponding to the data set fitted in Fig. 4.14 was 82100 ± 300 (statistical error). Thus the ^{17}N yield found above (80900 ± 1800) was multiplied by the ratio 9.24 ± 0.03 to obtain the total ^{17}N yield, $(7.12 \pm 0.17) \times 10^5$.

The last step in calculating the raw measured detection efficiency is to find the solid angle subtended by the neutron walls. The solid angle of the front rectangular face of a parallelepiped Ω_p as viewed from the point p located at the rectangular coordinates (x_p, y_p, z_p) is given in Ref. [Wi84] as

$$\Omega_p = \tan^{-1} \left[\frac{(x_2 - x_p)(y_2 - y_p)}{z_p \sqrt{(x_2 - x_p)^2 + (y_2 - y_p)^2 + z_p^2}} \right] - \tan^{-1} \left[\frac{(x_1 - x_p)(y_2 - y_p)}{z_p \sqrt{(x_1 - x_p)^2 + (y_2 - y_p)^2 + z_p^2}} \right] - \tan^{-1} \left[\frac{(x_2 - x_p)(y_1 - y_p)}{z_p \sqrt{(x_2 - x_p)^2 + (y_1 - y_p)^2 + z_p^2}} \right] + \tan^{-1} \left[\frac{(x_1 - x_p)(y_1 - y_p)}{z_p \sqrt{(x_1 - x_p)^2 + (y_1 - y_p)^2 + z_p^2}} \right], \quad (4.10)$$

where the rectangular face is bounded by the four straight lines $x = x_1$, $x = x_2$, $y = y_1$, $y = y_2$ with $x_1 < x_2$ and $y_1 < y_2$. In this case the point p is on axis and defined to be located at $(0, 0, z_p)$. Equation 4.10 is valid only for a point source, which is not a bad assumption, considering that the dimensions of the SSD stack (4.8×4.8 cm) were small compared to the neutron flight path distance (about 200 cm). From the equations given in Fig. 4.8, we obtain the vertical position y of the center of each bar, $y_1 = y - 3.072$ cm and $y_2 = y + 3.072$ cm. The perpendicular distance from the SSD

stack to each wall, z_p , and the horizontal boundaries of each bar can also be found from Fig. 4.8. Bar number 16 was missing from walls 1 and 2, and the energy and timing signals from bar 12, wall 2 and bars 15 and 16, wall 4 were too noisy to be useful for analysis. All these bars were excluded from the calculation of the solid angle of the three walls. The uncertainty in the calculation of solid angle was assumed to be solely due to the uncertainty in the geometry of the walls: ± 0.1 cm in the x and y dimensions and ± 1 cm in z_p . The solid angles obtained were 194.8 ± 2.7 msr for wall 1, 194.8 ± 2.4 msr for wall 2, and 189.6 ± 2.6 msr for wall 4, where an extra significant digit has been retained to avoid round off error. The total solid angle of all three walls was 579 ± 4 msr ($4.61 \pm 0.03\%$ geometrical efficiency).

Now we must find the number of ^{17}N β -delayed neutrons corresponding to each group fitted in Fig. 4.12 that actually impinged on the neutron walls ("Neutrons Expected", Table 4.5). This is found by multiplying the total number of ^{17}N β decays, $(7.12 \pm 0.17) \times 10^5$ (^{17}N component Fig. 4.14) by the branching ratio of the corresponding group (Ref. [Oh76] and Sec. 2.5.3) and by the geometrical efficiency (0.0461 ± 0.0003). The detection efficiency is obtained by dividing the numbers listed in column 2 (Table 4.5) by the corresponding values in column 3; the result is listed in column 4.

TABLE 4.5

^{17}N NEUTRON DETECTION EFFICIENCY

Energy (MeV)	Neutron Yield	Neutrons Expected	Efficiency (%)
0.3828 ± 0.0009	8500 ± 1300	12500 ± 700	68 ± 11
1.1709 ± 0.0008	13000 ± 1000	16500 ± 900	78 ± 7
1.7003 ± 0.0017	1300 ± 200	2270 ± 160	59 ± 11

4.6.2 Corrected neutron detection efficiency

Because the threshold of the β (start) detectors was high enough so that the detection efficiency varied significantly as a function of the threshold, it was necessary to correct the raw efficiencies listed in Table 4.5. If a single decay channel is present, then the β detection efficiency of the start detectors will affect the half-life and time-of-flight spectra equally, and when the branching ratio is calculated (Eq. 2.16), this factor will cancel in the division. This is not the case for ^{17}N where there are four observed decay channels: the three β -delayed neutron transitions and β -delayed decay to the ground state of ^{17}O . If two or more decay channels are present that have different start efficiencies, then the half-life spectrum will be a mixture of different states each affected by a different β -detection efficiency, and each neutron peak will be affected by a different β -detection efficiency as well.

The β -detection efficiency was found by determining what fraction of the integrated β -decay energy distribution $N(E_e)$ (figures 1.5a, 1.5b, and 1.5c) was above threshold. From Eq. 1.38, we obtained the distribution for allowed β decay; multiplying this by the Fermi integral to account for the Coulomb field yields

$$N(E_e) \propto F(Z, \eta)(Q - E_e)^2(E_e + m_e c^2)\sqrt{E_e + 2E_e m_e c^2}, \quad (4.11)$$

where E_e is the kinetic energy of the electron, E_0 is the β -decay end point energy, $m_e c^2$ is the rest mass energy of the electron, and $F(Z, \eta)$ is the Fermi function in terms of the atomic number Z , and the momentum η of the emitted β particle is in units of $m_e c$. Reference [US52] tabulates the function $f(Z, \eta) = [\eta^2 \cdot F(Z, \eta)] / \varphi(Z)$ where $\varphi(Z)$ is a constant for a given Z and is independent of η . Thus

$$F(Z, \eta) = \frac{\varphi(Z) \cdot f(Z, \eta)}{\eta^2}. \quad (4.12)$$

The factor $\varphi(Z)$ could be ignored, because only the shape of the distribution was needed. The function $f(Z, \eta)$, for β^- decay, was calculated as given in Ref. [US52]:

$$f(Z, \eta) = \eta^{(2+2S)} e^{\pi\delta} |\Gamma(1 + S + i\delta)|^2, \quad (4.13)$$

where $\eta = \{[(E/m_e c^2) + 1]^2\}^{1/2} - 1$, $S = [1 - (Z^2/137^2)]^{1/2} - 1$, and $\delta = [Z \cdot (1 + \eta^2)^{1/2}] / (137\eta)$. The complex gamma function $|\Gamma(1 + S + i\delta)|^2$ was calculated with the following relation [US52]:

$$|\Gamma(a + ib)|^2 = |\Gamma(a)|^2 \cdot \prod_{n=0}^{\infty} [1 + b^2(n + a)^{-2}]^{-1}, \quad (4.14)$$

where a and b are real constants. (In this case, $a = S + 1$, and $b = \delta$.) The product of Eq. 4.14 was iterated until sufficient accuracy was obtained. Thus, if the threshold energy is represented by E_t and the end point energy by E_0 , then the β -detection efficiency is given by

$$\frac{\int_{E_t}^{E_0} N(E) dE}{\int_0^{E_0} N(E) dE}. \quad (4.15)$$

The correction factor by which the raw neutron efficiencies were multiplied was found by beginning with the definition of intrinsic detection efficiency: the number of detected neutrons divided by the number of neutrons incident on the detector. For each neutron state i , where the number of measured β decays is N_β (obtained from the fit of the activity spectrum), the geometrical efficiency is g_{eff} , and the branching ratio corresponding to the state in question is p_i , the neutron detection efficiency n_{eff} is given by

$$n_{\text{eff}_i} = \frac{N_i}{N_\beta \cdot g_{\text{eff}} \cdot p_i}. \quad (4.16)$$

We must determine N'_i and N'_β to find n'_{eff_i} , the corrected neutron detection efficiency (where primes indicate quantities corrected for the β -detection efficiency). The measured number of ^{14}Be β decays is equal to sum of the β decays for each decay channel j , which is N'_β scaled by the branching ratio and β -detection efficiency corresponding to the state j in question. Mathematically this is $N_\beta = N'_\beta \cdot p_1 \cdot b_{\text{eff}_1} + N'_\beta \cdot p_2 \cdot b_{\text{eff}_2} + \dots = N'_\beta \cdot (\sum_j p_j \cdot b_{\text{eff}_j})$ or $N'_\beta = N_\beta / (\sum_j p_j \cdot b_{\text{eff}_j})$, where b_{eff_i} represents the

β -detection efficiency for each decay channel j . Inserting N'_i (where $N'_i = N_i/b_{\text{eff}i}$) and N'_β into Eq. 4.16, we get

$$n'_{\text{eff}i} = \frac{(N_i/b_{\text{eff}i})}{(N_\beta \cdot g_{\text{eff}} \cdot p_i) / (\sum_j p_j \cdot b_{\text{eff}j})} \quad (4.17)$$

Rearranging the terms and applying Eq. 4.16 again, this becomes

$$n'_{\text{eff}i} = \frac{N_i}{N_\beta \cdot g_{\text{eff}} \cdot p_i} \left(\frac{\sum_j p_j \cdot b_{\text{eff}j}}{b_{\text{eff}i}} \right) = n_{\text{eff}i} \left(\frac{\sum_j p_j \cdot b_{\text{eff}j}}{b_{\text{eff}i}} \right). \quad (4.18)$$

The extreme right term enclosed in parentheses is the correction factor by which the measured neutron efficiency $n_{\text{eff}i}$ was multiplied to obtain the corrected efficiency.

A fit to the ^{17}N corrected neutron efficiencies was made by using the program KSUEFF [Ce79]. Because the threshold of the neutron detectors was very low and difficult to determine, an effective threshold was found by comparing the fit to the corrected data. The threshold of the start detectors was also not very well defined, because they do not measure the full energy of the emitted β particle. Thus, the threshold of the start detectors and the threshold of the neutron detectors were varied simultaneously until the reduced χ^2 of the fit was minimized. The resulting fit, shown by the solid line of Fig. 4.17a, corresponds to a neutron threshold 183 ± 16 keV (obtained by extrapolating the curve to zero energy, see Fig. 4.17b). The ^{17}N data points shown in Fig. 4.17a have already been corrected for the detection efficiency of the start detectors (Eq. 4.17) that corresponded to a start detector threshold of 0.97 ± 0.02 MeV. The dashed lines in Fig. 4.17a and Fig. 4.17b represent our estimate of the uncertainty in the neutron detection efficiency due to the error in both the *neutron* and *start* detector thresholds, where the method used to calculate the error outlined in Sec. 2.7 (see Fig. 2.15) was used. It should be emphasized that the purpose of the fit is **not** to determine these thresholds but rather to match the Monte Carlo calculations to the measured data by treating the thresholds as variable parameters. The corrected ^{17}N detection efficiencies are listed in Table 4.6.

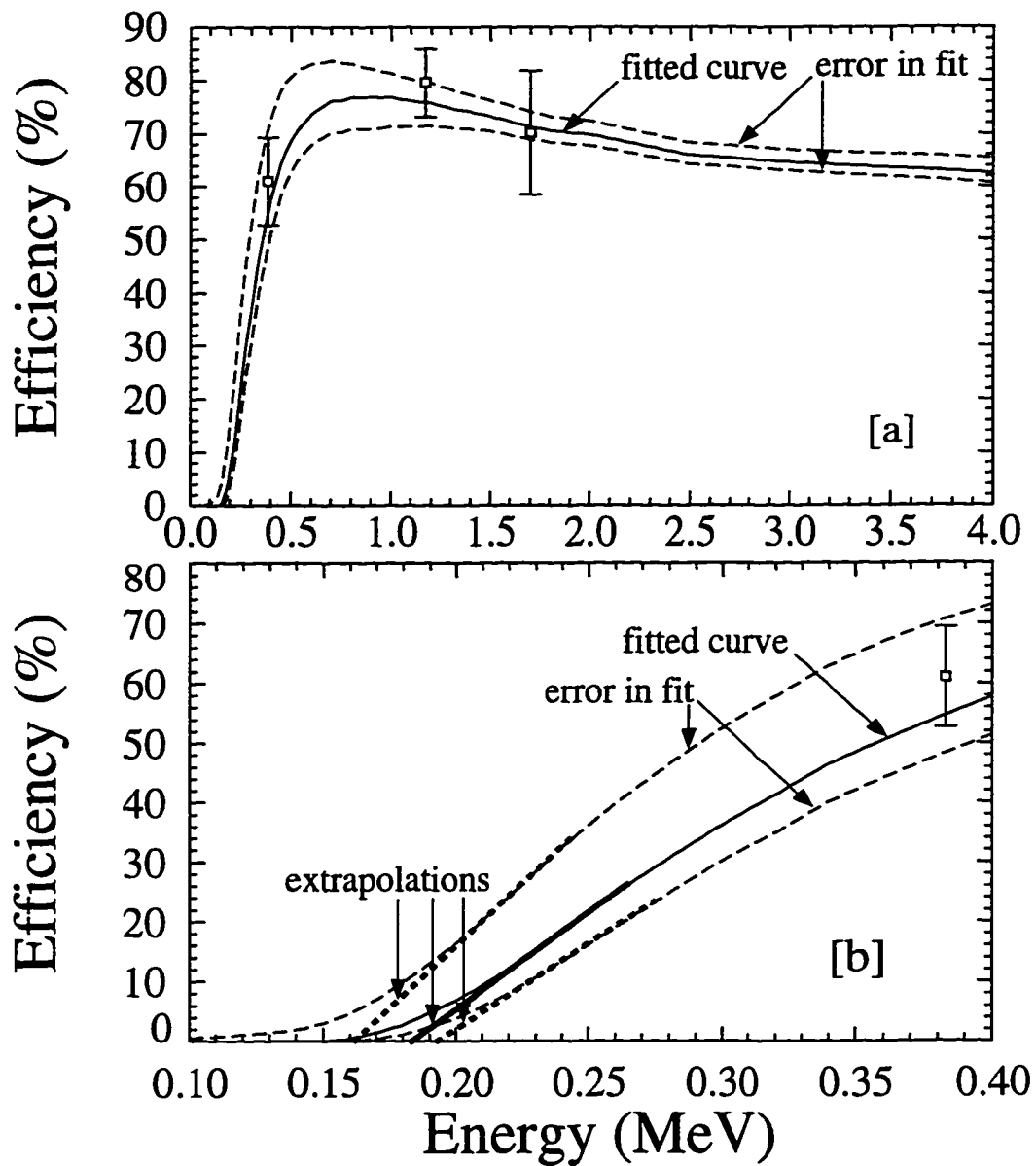


Figure 4.17 (a) Plot of the corrected neutron detection efficiencies obtained from the ^{17}N data and of the fitted efficiency curve. (b) Blow up of Fig. 4.18a showing how the curves were extrapolated to zero energy to obtain the threshold in terms of neutron energy.

TABLE 4.6
CORRECTED ^{17}N DETECTION EFFICIENCIES

Energy (MeV)	Corrected Efficiency (%)
0.3828 ± 0.0009	61 ± 8
1.1709 ± 0.0008	79 ± 7
1.7003 ± 0.0017	70 ± 12

Most of the β decay strength corresponded to a low energy neutron group at 287 ± 3 keV, which lies close to threshold. In this energy region, the detection efficiency curve rises sharply (Fig. 4.18a), and one would expect the systematic error to be large. Because the neutron detection efficiency varies less at energies farther from the threshold, the systematic error in the efficiency near 287 keV is dominated by the efficiency of the 0.3828 MeV ^{17}N β -delayed neutron group. One would also expect a large systematic error in the β -detection correction (Eq. 4.18). To see what the efficiency would be at low neutron energies without this correction, we matched the calculation given by KSUEFF [Ce79] (both for the data point and the extreme limits given by the error bar) by varying the neutron threshold to the raw detection efficiency at 0.3828 MeV ($68 \pm 11\%$, Table 4.5). The result at 287 keV was $45 \pm 14\%$ (Fig. 4.18). Compare this to the independent result from Fig. 4.17a ($41 \pm 13\%$) at the same energy. Both results are well within their respective systematic errors, indicating that the results are not sensitive to their errors in the β -detection efficiency correction.

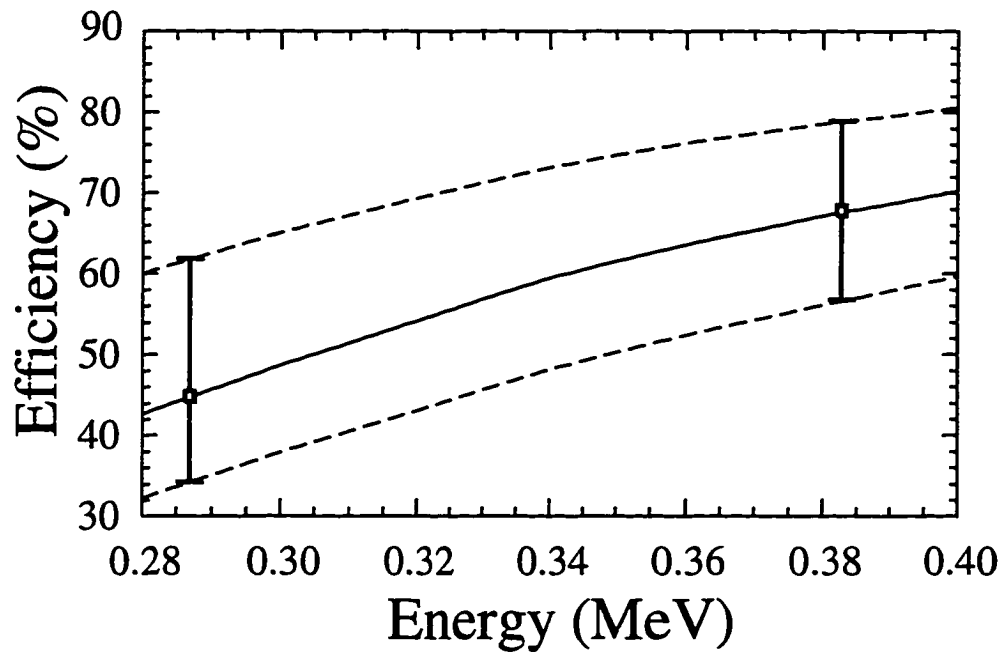


Figure 4.18 A fit to the uncorrected 0.3828 MeV ^{17}N data point (solid line) using KSUEFF [Ce79] where the dashed lines represent the systematic error and the left data point represents the corresponding efficiency at 287 keV.

CHAPTER 5

ANALYSIS AND RESULTS OF THE RIKEN EXPERIMENT

This chapter describes the analysis and presents the results for the second experiment performed at RIKEN. First, the analysis and results for the β decay activity spectrum (both ungated and that in coincidence with emitted neutrons) are presented. Second, the neutron time-of-flight analysis and results are described. Third, the analysis and results of the γ -ray data are discussed. Unlike the first experiment, we were able to measure charged-particle decay, and these results are also given. Last, we were able to determine the natural width of an observed low energy (287 keV) neutron group that corresponds to most of the β decay strength.

5.1 Analysis of β -decay Activity

5.1.1 Analysis of the ungated decay curve

The total number of β decays was determined by fitting the raw decay spectrum obtained from the Okuno TDC (an in-house electronic module built at RIKEN, see Appendix C.6). This device is capable of digitizing events for the full duration of the beam-off period. Because most of the statistics were taken with a duty cycle of 10 ms on/20 ms off, a fit of the raw activity spectrum corresponding to the 10 ms on/20 ms off ^{14}Be data was used to determine the total number of ^{14}Be β decays. The plot shown in Fig. 5.1 was fitted using the program GRAPH [Be92b], where the algorithm and differential equations used have been described in Sec. 3.1. The yield of each impurity (relative to ^{14}Be) along with the half-life of the nuclide in

question is listed in Table 4.2. The impurities ^{11}Be , ^6He , and ^3H were excluded because their half-lives (13.8 s, 807 ms, and 12.3 yr, respectively) were long enough to be considered as part of the constant background. Therefore, only the nuclides ^{14}B , ^{12}Be , ^{11}Li , and ^9Li were included as impurities, together with a small additional amount of ^{12}B corresponding to the daughter of ^{12}Be impurity.

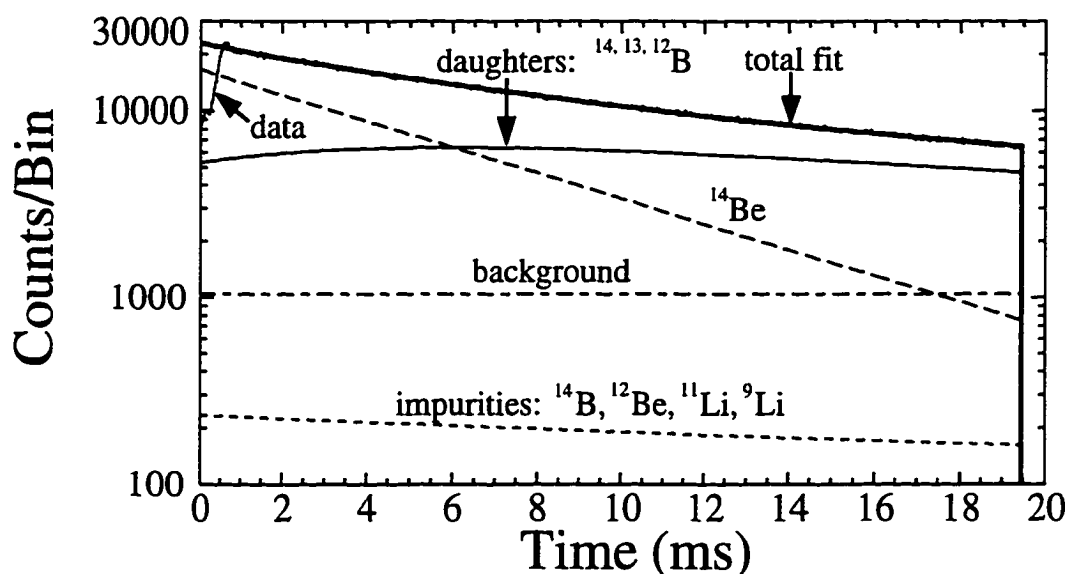


Figure 5.1 Fit of the raw 20 ms beam-off β -decay spectrum showing the parent, daughter, impurity, and background components.

Unlike the NSCL experiment (Fig. 3.1), it was necessary to correct the spectrum of Fig. 5.1 for rate dependent dead time. In almost all detector systems, the detector, electronics and acquisition system require a minimum amount of time (τ or the dead time period) to process and distinguish two separate events. Because it is difficult to separate the individual dead time contributions caused by the detector, electronics, and computer, we shall refer to the dead time of the total counting system, which is the fraction of time when the system is busy and unable to process additional events. There are two different models for describing the behavior of a counting system subject to dead time: extendable and non-extendable

(or paralyzable) dead time; both are diagrammed in Fig. 5.2. In the case of non-extendable dead time, after an event is initially processed, all other events are ignored for period of time equal to τ after the initial event (Fig. 5.2 [c]). If the system is subject to extendable dead time, then those events occurring during the period the computer is busy extend the dead time period by τ .

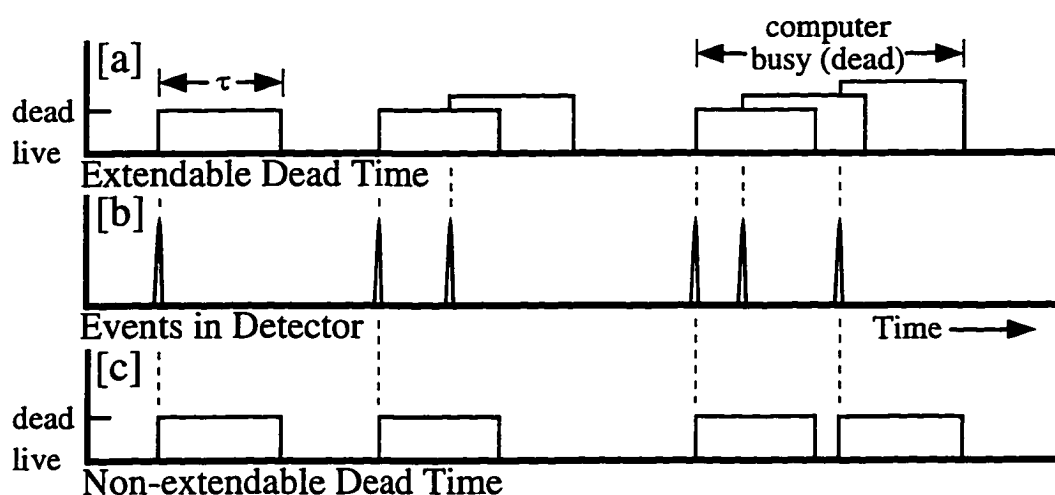


Figure 5.2 A diagram illustrating the difference between extendable and non-extendable dead time [Kn95e].

According to Ref. [Ao95] the activity spectrum (Fig. 5.1) was subject to non-extendable dead time. If the true interaction rate is given by n and the measured rate is given by m , then the fraction of the time that the counting system is dead is given by $m\tau$. The rate at which true events are lost is $nm\tau$, which is also equal to $n - m$. Therefore, [Kn79f]:

$$n - m = nm\tau, \quad (5.1)$$

and solving for n yields

$$n = \frac{m}{1 - m\tau}. \quad (5.2)$$

Thus the data in Fig. 5.1 were corrected by applying Eq. 5.2 to the raw spectrum

channel by channel. Since we did not have an independent means of measuring the dead time, τ was found by correcting the spectrum, allowing τ to vary, and optimizing the result by minimizing the χ^2 .

Figure 5.1 has already been corrected for the non-extendable dead time with $\tau = 0.920$ ms. Because the dead time was very large at the beginning of the curve (due to residual direct beam at the start of the beam-off period, see Sec. 3.2.2), it was necessary to exclude the first 0.82 ms from consideration in the fit, and to apply the same cut to all spectra corresponding to the ^{14}Be data. Due to the complexity of the fit it was not possible to determine the half-life accurately based on the fit to this curve. Thus, it was necessary to fix the value of the ^{14}Be half-life to that measured by Dufour *et al.*: 4.35 ± 0.17 ms [Du88]. It was also necessary to fix the relative abundances of the ^{14}B , ^{13}B , and ^{12}B daughters to the corresponding neutron multiplicities determined in Ref. [Du88]: $14 \pm 3\%$, $81 \pm 4\%$, and $5 \pm 2\%$ for $0n$, $1n$, and $2n$ neutron decay, respectively. Also the half-lives of the daughters were fixed to their accepted values of 13.8 ± 1.0 ms [Aj91], 17.36 ± 0.16 ms [Aj91], and 20.20 ± 0.02 ms [Aj90] for ^{14}B , ^{13}B , and ^{12}B , respectively. The intensities of the impurities (relative to the ^{14}Be yield) were fixed to the values listed in Table 4.2 (rightmost column). Thus for the fit shown in Fig. 5.1, only three parameters were varied: the dead time period τ , the ^{14}Be implantation rate, and the constant background. The resulting ^{14}Be yield (corresponding to the 10 ms on/20 ms off duty cycle and excluding the first 0.82 ms) was $(4.36 \pm 0.02) \times 10^6$ (statistical error), the ^{14}Be implantation rate equaled 224 particles per second, and the reduced χ^2 of the fit was 1.99. The total dead time corresponding to Fig. 5.1 (17.2%) was found by dividing the sum of the raw spectrum by the sum of the corrected spectrum (Fig. 5.1). The total dead time obtained from scaler information was 39.5%. Most likely this dead time is much higher than that found from Fig. 5.1 (17.2%), because a much higher portion of the dead time

corresponded to the sharp spike excluded in the software cut mentioned above. It was necessary to normalize the above ^{14}Be yield to the total data set, which was done by using the yield of the prompt peak. It was equal to $(4.225 \pm 0.017) \times 10^5$ for the total data set and $(3.640 \pm 0.015) \times 10^5$ for the data set corresponding to the 10 ms on/20 ms off duty cycle, yielding a total normalized yield of 5.07×10^6 .

The normalized ^{14}Be yield was checked by performing various other fits, including one similar to that done in Fig. 5.1 where the ^{14}Be half-life varied, resulting in a half-life of 4.47 ms and a normalized ^{14}Be yield of 5.17×10^6 . A portion of the data had dead time was low enough (about 5% during the counting period) to perform the fit without a dead time correction. The prompt β -peak yield corresponding to this data set was 3760 ± 60 . This fit of this data set was done both with the ^{14}Be half-life varying (resulting in a half-life of 4.99 ms and a normalized ^{14}Be yield of 4.37×10^6), and fixed to 4.35 ms (resulting in a normalized yield of 4.95×10^6). The normalized yields differed among each other by no more than 15.8%, determining the systematic error in the normalized ^{14}Be yield equal to $(5.07 \pm 0.05 \pm 0.40) \times 10^6$.

5.1.2 Analysis of the decay curve requiring β - n coincidence

A much better method to measure the ^{14}Be half-life (discussed in Sec. 3.1.2) is to use neutron coincidence. That is, we determined the yield of the neutron peak in the time-of-flight spectrum as a function of time by looking at the time-of-flight spectrum in coincidence with the raw activity spectrum. We found that this method was superior because almost all of the β -delayed neutron yield was accounted for by a single peak, and the background was much easier to determine in the time-of-flight spectrum (Fig. 5.3). We used the following cuts in the decay curve: 2.39–4.78 ms, 4.79–7.18 ms, 7.19–9.58 ms, 9.59–11.98 ms, 11.99–14.38 ms, 14.39–16.78 ms, and 16.79–19.19 ms. The error bars shown in Fig. 5.4 are statistical and include

the error in subtracting the background. We used the program LIFE5 [Sc94] (see Sec. 3.1.2 for more details) to perform the fit that consisted of a single exponential with no constant background. (The validity of excluding a constant background was checked by performing another fit where a constant background was included; the fitted background and the difference in the half-lives were negligibly small.) The half-life resulting from this fit was 4.36 ± 0.13 ms.

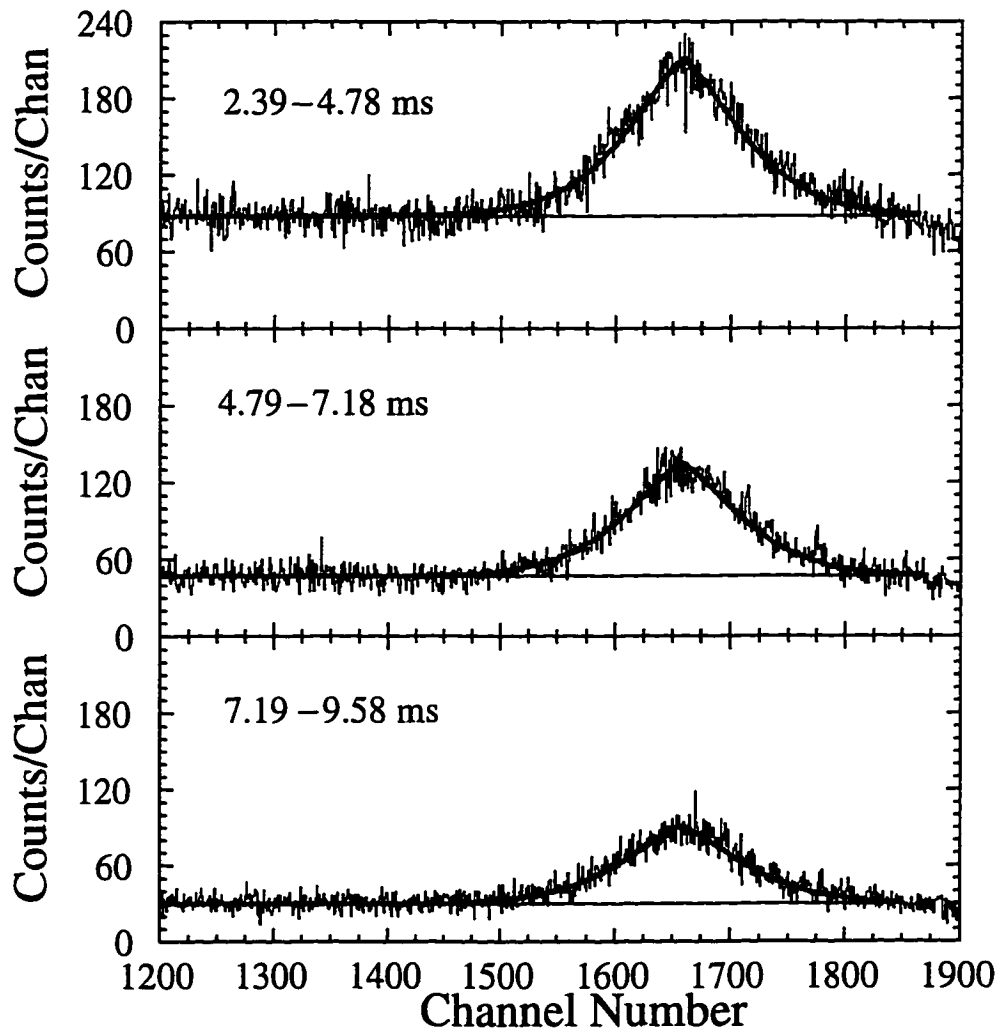


Figure 5.3 Portion of time-of-flight spectrum showing the ^{14}Be 287 keV β -delayed neutron peak as a function of elapsed time after the start of the beam-off period. The corresponding software cut on the activity spectrum is shown in the upper left of each plot.

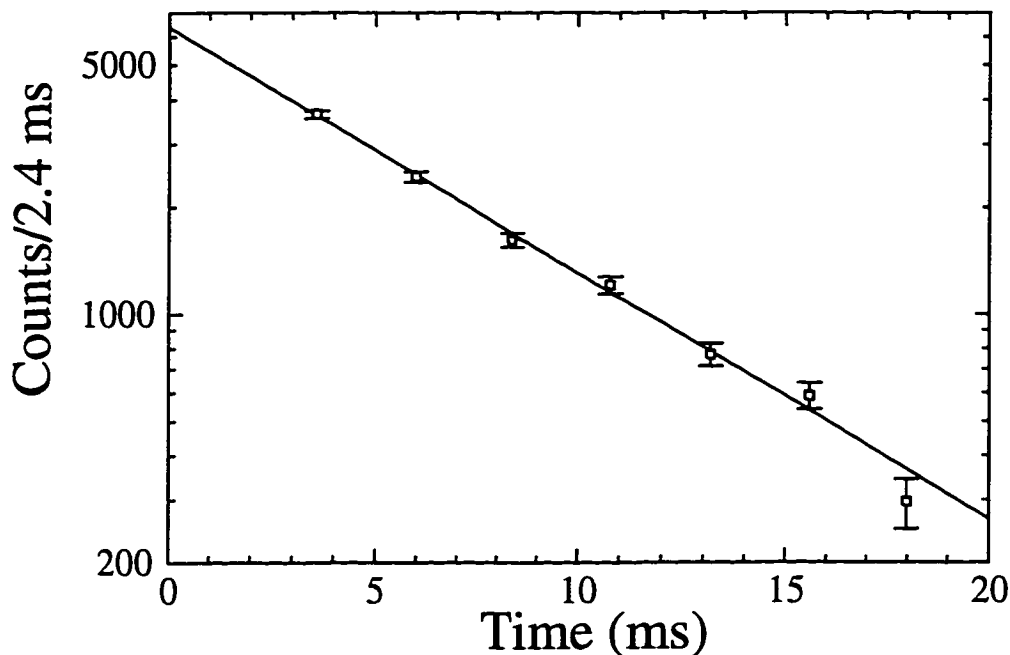


Figure 5.4 Plot of the decay curve requiring coincidence with the 287 keV neutron peak.

5.2 Analysis of the Neutron Time-of-Flight Data

5.2.1 Calibration of the time-of-flight data

Like the previous experiment, there were insufficient statistics to analyze individual neutron detector bars. Consequently, it was necessary to calibrate all forty-eight time-of-flight spectra so that equal flight times corresponded to equal channel numbers and all time-of-flight spectra could be added together. A pulser that emitted very narrow pulses spaced 10 ns apart was used. For the present experiment, the time-of-flight spectra were linearly calibrated to a common slope of 0.25 ns/chan (a convenient value) and an offset of -128 ns (so that time zero corresponded to channel 512). The method by which this was done has already been fully explained in Sec. 3.2.1.

5.2.2 Fit of the low energy neutron group

As in the previous experiment, we discovered that there was a small amount of beam-on contamination at the beginning of the beam-on period. This problem was indicated by a sharp spike present at the beginning of the half-life curve, which was eliminated by imposing a software cut that excluded all events associated with the first 0.82 ms of the activity spectrum.

Once this correction was applied, it was necessary to calculate the mean of the two timing signals from the photomultiplier tubes at both ends of the scintillator bar to correct for the finite velocity of light. The geometry of a typical neutron interaction is analogous to that shown in Fig. 3.5, except that the scintillator bar is straight. If the distance along the bar from the left and right edges of the bar to the site of the neutron interaction are represented by l_l and l_r (see Fig. 3.5), then taking the mean time effectively places neutron events at the center of a bar, where $(l_l + l_r)/2 = l/2$.

It is important to emphasize that this procedure only corrects for the differing times required for light to traverse the scintillator bar. It **does not** account for the different flight times of the neutrons to the scintillator. This was done by calculating the flight path distance for each neutron event (see Sec. 4.5.1) and normalizing its corresponding flight time to a common flight path distance of 2 m (see Eq. 4.9).

The corrected individual time-of-flight spectra were then added together. Figure 5.5 is a fit to the summed spectrum showing the low energy neutron group at 287 keV. The constant background was determined by averaging the number of counts per channel in a region where the time-of-flight spectrum was flat (channels 1200–1400). The peak was fitted using the program FITS [Di93]. We found that an asymmetric hypergaussian line shape without an exponential tail on the low energy (right or long time-of-flight) side fitted this peak best. Because there was insufficient range in the time-of-flight spectrum (Fig. 5.5), it is possible that the low

energy tail is cut off. This prevented an accurate determination of the background to the right of the peak, and increased the uncertainty in the background under the peak. The yield of the low energy neutron peak shown in Fig. 5.5 was $66600 \pm 300 \pm 4200$, where the systematic (second) error was dominated by the uncertainty in the background. The centroid of the peak shown in Fig. 5.5 was at channel number 1657 ± 2 and the width of this peak (FWHM) was 125 ± 4 channels. The equation for determining neutron kinetic energy E_k has already been derived (Eq. 3.17). Using this centroid, equations 3.17 and 2.14, the centroid of the prompt β -peak C_β (594.5 ± 0.7 [systematic error]), the conversion factor of channels to time k (0.25 ns/channel), and the calibrated distance d (201.4 ± 0.7 cm [Sec. 4.5.2]), we found the energy of the 287 keV neutron peak as listed in Table 5.1.

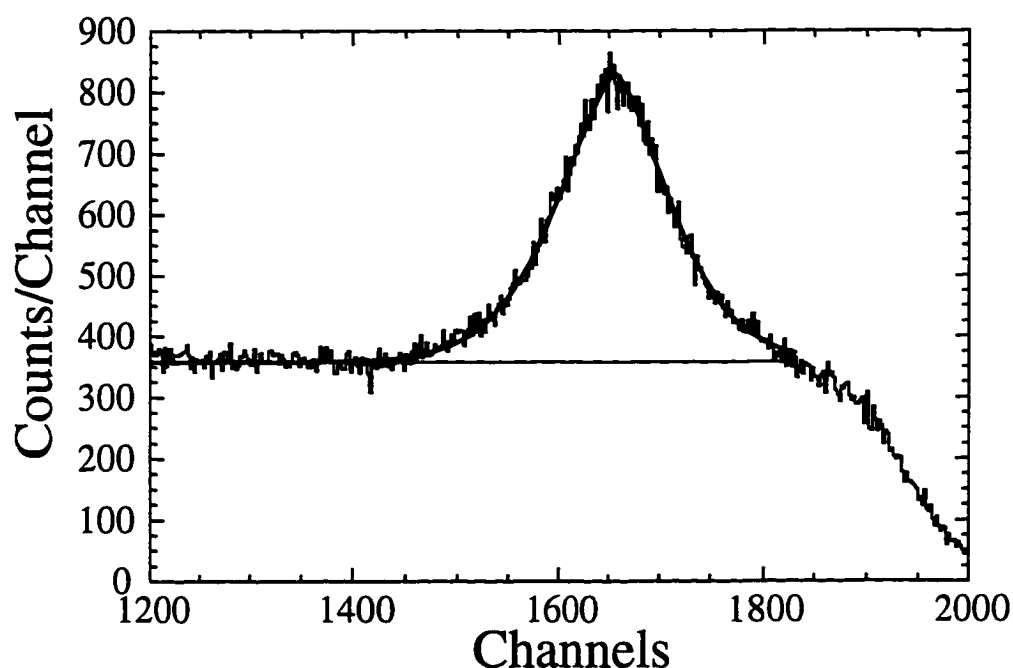


Figure 5.5 Portion of the time-of-flight spectrum showing the low energy neutron group at 287 keV.

TABLE 5.1
INFORMATION REGARDING ^{14}Be NEUTRON PEAKS

Energy (MeV)	Centroid (channels)	FWHM (channels)	FWHM (keV)	Yield (counts)
3.70 ± 0.11	876 ± 3	21	580	$370 \pm 20 \pm 90$
3.10 ± 0.08	905 ± 3	21	480	$370 \pm 20 \pm 80$
0.287 ± 0.003	1657 ± 2	126 ± 4	71 ± 1	$66600 \pm 300 \pm 4200$

NOTE: The centroids and widths (in channels) of the 3.70 and 3.10 MeV neutron groups are given in terms of the raw channel length (2048 channels full scale). These two peaks were also fitted with widths held fixed relative to one another.

5.2.3 Veto anti-coincidence and analysis of the high energy neutron peaks

Two β -delayed neutron groups were observed that were much higher in energy than the previous neutron group. It was necessary to look at the time-of-flight spectrum in anti-coincidence (in the off-line analysis) with the veto detectors (see Sec. 4.2) to see these groups, because they were located close to the prompt β -peak. This was unnecessary for the analysis of the low energy neutron group.

In the case of the veto detectors, only one photomultiplier tube was optically coupled to each paddle; thus, there was no mean time to calculate. The individual veto time-of-flight spectra were calibrated in the same way as the neutron detectors (see sections 5.2.1 and 3.2.1) by using a pulser that emitted very narrow pulses spaced 10 ns apart. This was necessary so that the same software cut could be applied to all veto spectra where events that occurred at an earlier time than the prompt peak were excluded from the anti-coincidence, minimizing the elimination of events coincident with noise. The sum of all veto time-of-flight spectra and the cut applied is shown in Fig. 5.6. (For illustration purposes, several veto bars that exhibited a high degree of noise have been excluded from this figure.) Only events

satisfying the cut shown in Fig. 5.6 corresponding to real events triggering both a veto wall and the respective neutron wall are eliminated.

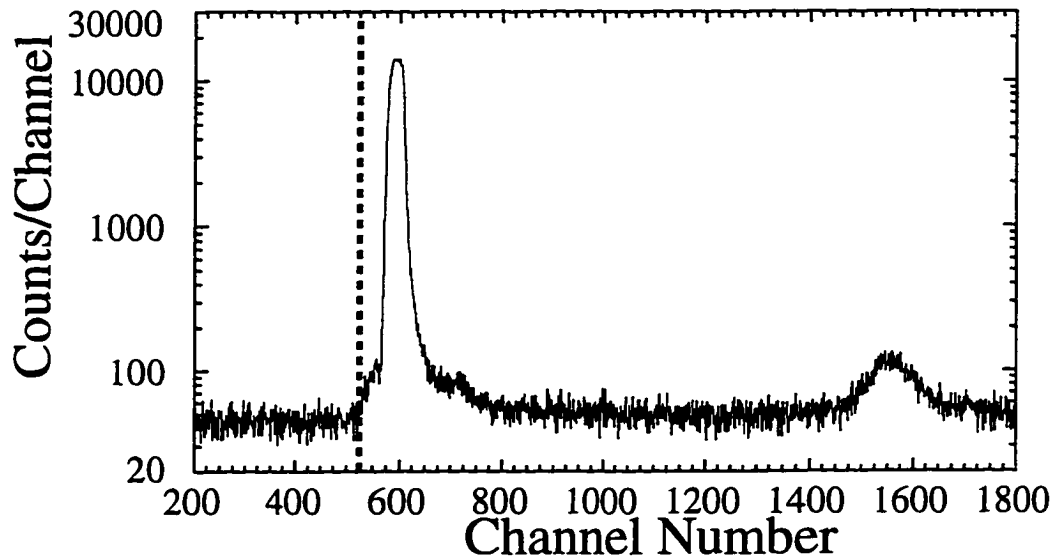


Figure 5.6 Plot of veto time-of-flight spectrum showing the lower software cut applied to the anti-coincidence data. Events corresponding to counts located to the left of the dashed line were not eliminated.

The neutron time-of-flight spectrum with no β veto applied is shown in Fig. 5.7a. There were several spurious peaks ("noise peaks") that were located just to the right of the prompt β peak. These peaks were determined not to be real, because they were almost totally eliminated when the β veto was applied (Fig. 5.7b). The low energy neutron peak (at 287 keV) and cosmic-ray peak are also labeled.

Figure 5.7b shows the result of applying the β veto. Note that the noise peaks are nearly eliminated, the constant background is smaller, and the β peak is dramatically reduced. In this plot it is just possible to see peaks that correspond to those observed in the NSCL experiment (labeled "higher energy neutron peaks").

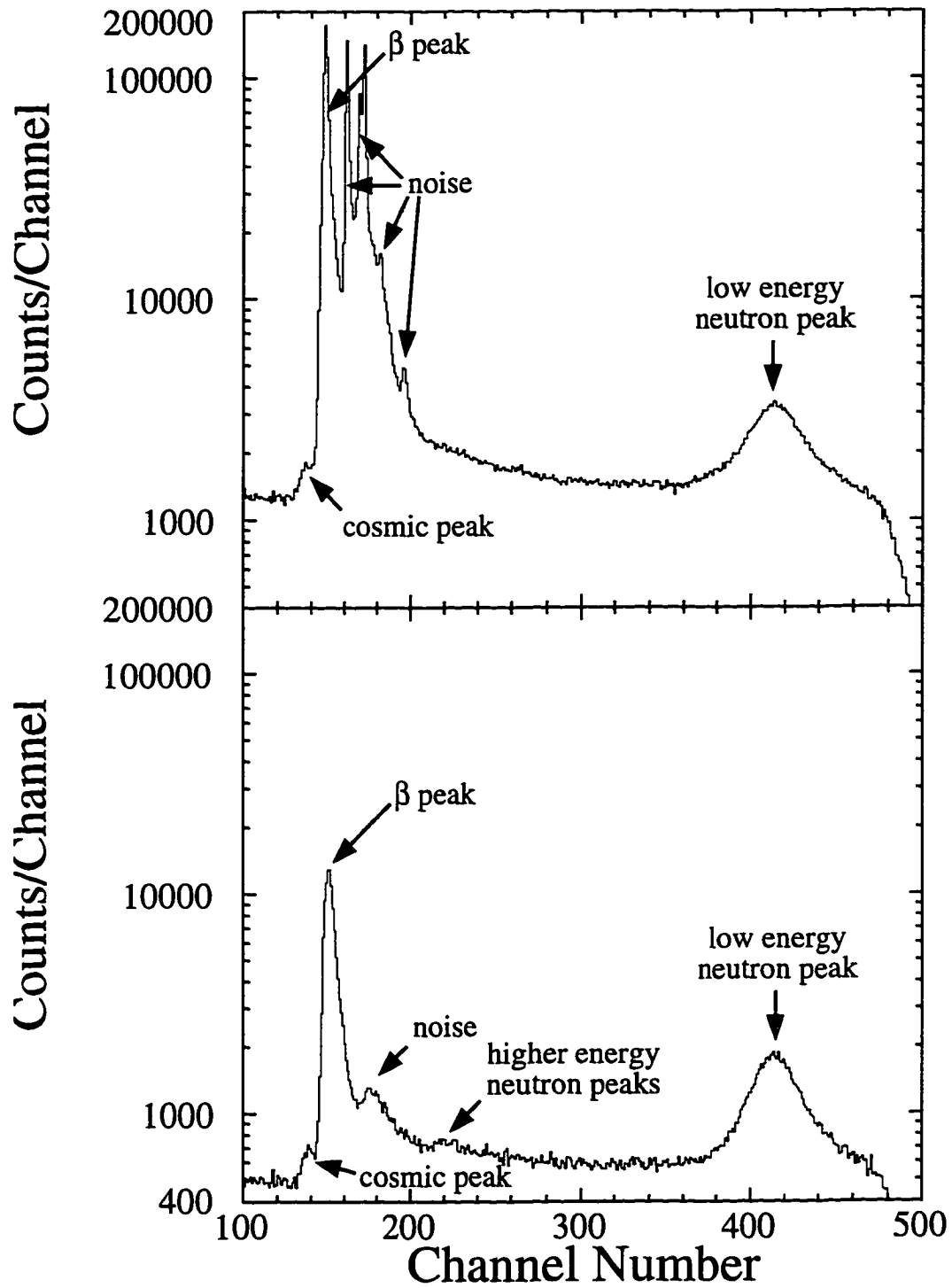


Figure 5.7 (a) Plot of the neutron time-of-flight spectrum without β veto (anti-coincidence) applied. (b) Same as Fig. 5.7a but with β veto applied. Note that the channel scale has been compressed by a factor of four relative to Fig. 5.5.

A fit of the corresponding enlarged time-of-flight spectrum is shown in Fig. 5.8. Although the neutron peaks are more properly fitted with a line shape that contains an exponential tail on the low energy (right) side, the peaks shown in Fig. 5.8 were too low in statistics to do this, and thus were fitted with a symmetric Gaussian line shape. The energy, centroid, width (FWHM) and fitted yield of these peaks are listed in Table 5.1, where the energies are calculated using the method outlined in Sec. 5.2.2.

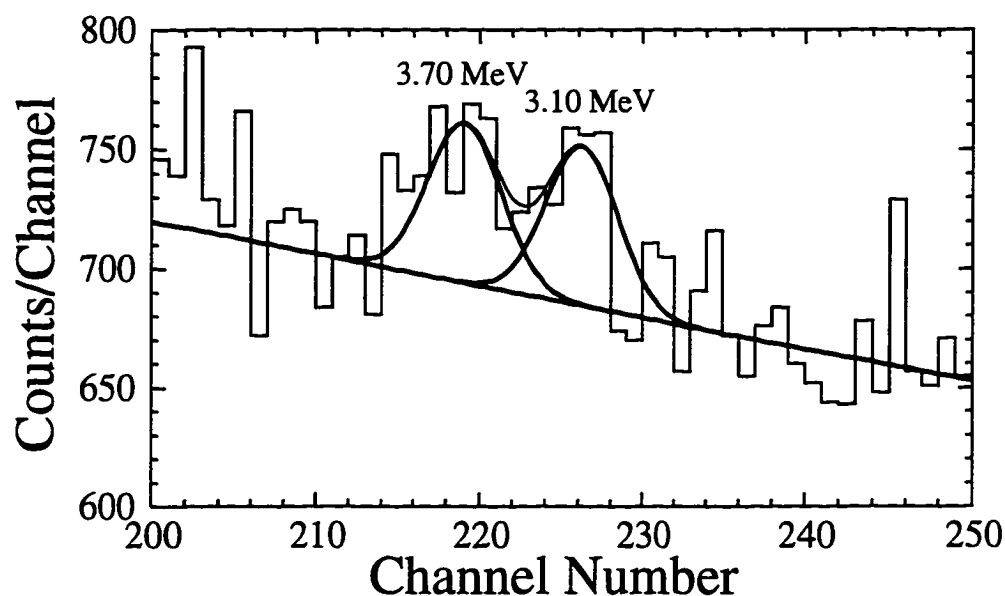


Figure 5.8 Enlarged portion of Fig. 5.7b showing a fit to the higher energy neutron groups.

Notice that in Fig. 5.6 the veto detectors still have some sensitivity to the neutron peak with energy 287 keV. Although the background was easier to determine in the veto detector time-of-flight spectrum than in the neutron time-of-flight spectrum (compare to Fig. 5.5), there were less statistics in the ^{17}N veto time-of-flight spectrum (Fig. 5.9), and the systematic error in the yields of the neutron groups shown in Fig. 5.9 was too large to accurately determine neutron detection efficiency. The yield of the 1.70 MeV β -delayed neutron peak is

especially difficult to determine in Fig. 5.9. Because of this we were unable to use the veto detectors to determine the branching ratio of the neutron groups.

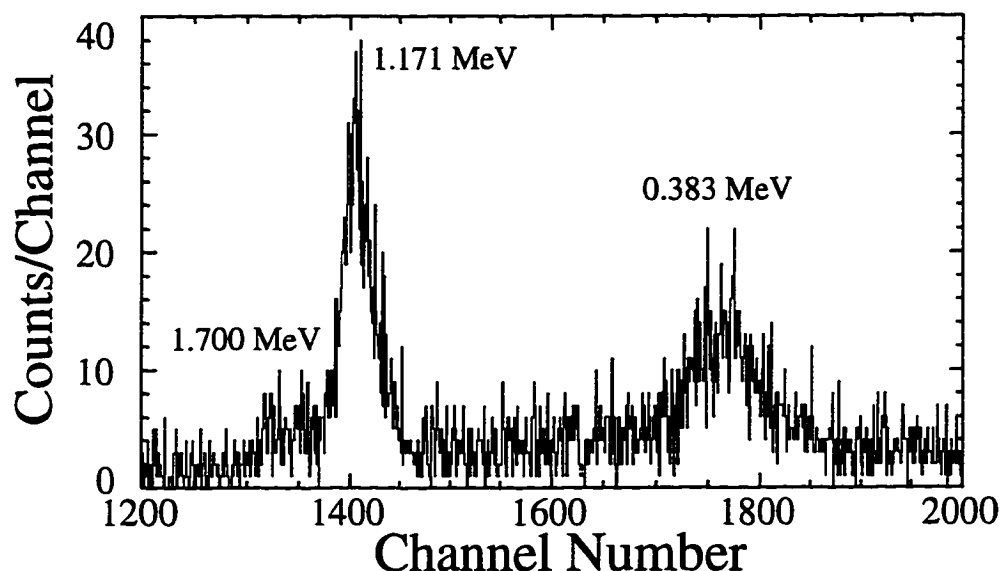


Figure 5.9 Plot of veto detector time-of-flight spectrum showing the ^{17}N β -delayed neutron groups.

5.3 Determination of Branching Ratio and Log ft Values of Neutron States

After calculating the energies and yields of all ^{14}Be β -delayed neutron peaks (Table 5.1), we can determine the branching ratios and log ft values corresponding to these neutron groups. The solid angle of the three neutron walls is 579 ± 4 msr (Sec. 4.2) and the efficiency was obtained from the fit of Fig. 4.18a. The detection efficiency of the 287 keV neutron group has already been mentioned in Sec. 4.6.2 ($41 \pm 1 \pm 13\%$), and those for the peaks listed in Table 5.1 were obtained from Fig. 4.18a and are listed in Table 5.2. By following the method that has already been described in Sec. 3.3.1 we obtain a branching ratio of $82 \pm 28\%$. Even though the systematic error in the branching ratio given by the fit of Fig. 4.18a is large, we can also place a lower limit of about 51% on this branching ratio simply by using the raw neutron detection efficiency given by the ^{17}N 0.383 MeV neutron group ($68 \pm 11\%$,

Table 4.5) This compares well with the lower limit obtained from Fig. 4.18a, which is 54%. The upper limit obtained from the branching ratio given by Fig. 4.18a is non-physical for it would imply an upper limit greater than 100%. The branching ratio is certainly no more than 100% and most likely is about 86% considering that the measured $2n$ multiplicity is $5 \pm 2\%$ (obtained from Ref. [Du88]) and the best value for the $0n$ branching ratio (obtained from [Du88]) is $14 \pm 3\%$. Thus the systematic limit given by this information result in a branching ratio of $82 \pm_{31}^4\%$, which is listed in Table 5.2.

TABLE 5.2
BRANCHING RATIOS AND $\text{Log}ft$ VALUES OF NEUTRON GROUPS

Energy (MeV)	Branching Ratio (%)	$\text{Log}ft$	
		(g.s.)	(3.681 MeV)
3.70 ± 0.11	$0.28 \pm 0.02 \pm 0.14$	—	—
3.10 ± 0.08	$0.29 \pm 0.02 \pm 0.12$	$5.67 \pm_{0.04}^{0.04} \pm_{0.24}^{0.15}$	$4.91 \pm_{0.05}^{0.05} \pm_{0.24}^{0.15}$
0.287 ± 0.003	$82. \pm 2. \pm_{31.}^4$	$3.70 \pm_{0.03}^{0.03} \pm_{0.04}^{0.20}$	—

Given the measured neutron energy and the branching ratio, one can calculate the $\text{log}ft$ value of the β decay that populates the state in ^{14}B corresponding to the neutron group in question. As in the NSCL experiment, a γ -ray line resulting from the β decay of ^{14}Be and corresponding to an electromagnetic transition in ^{13}B with accepted energy 3.681 ± 0.005 MeV [Aj91] (see Sec. 3.4.1) was observed. (The measurement of this γ -ray line will be discussed later in Sec. 5.4). Because, in the present experiment, there were insufficient statistics to obtain γ - n coincidence data, the $\text{log}ft$ values corresponding to both possible final ^{13}B states are listed in Table 5.2. After the analysis of the RIKEN data, we discovered that there is a β -delayed neutron

group with energy 3.613 ± 0.013 MeV [Aj81] corresponding to ^{13}B β -decay with a branching ratio of $0.16 \pm 0.03\%$ relative to ^{13}B β -decay. Because we lacked sufficient energy resolution to distinguish between a 3.613 and 3.70 MeV neutron groups, there is ambiguity in positively assigning the 3.70 MeV neutron peak as resulting from ^{14}Be β -delayed neutron decay. (This will be discussed in more detail in Sec. 6.3) Thus the $\log ft$ of this group is not listed in Table 5.2. Also in Sec. 6.2, we shall see why it was not likely that the 0.287 MeV neutron group be associated with the γ decay at 3.681 MeV.

5.4 Analysis of the γ -Ray Data

5.4.1 Energy calibration of the γ -ray detector

A ^{152}Eu source (activity 4.7 μCi) was used for the energy calibration of the Ge detector. The method used to perform this calibration has already been described in Sec. 3.4.1. Because there were fewer data points in the present experiment and because it was necessary to extend the calibration much further (from about 1.5 to 3.7 MeV as opposed to 2.6 to 3.7 MeV for the NSCL experiment), we did not trust a quadratic fit. Thus, Fig. 5.10 shows the difference between the accepted energies (Appendix B) and the corresponding calculated energies from the linear fit (the residuals). The corresponding calibration curve was

$$y = -(104.12 \pm 0.16) \text{ keV} + (1.1495 \pm 0.0003)x \text{ keV/channel.} \quad (5.5)$$

The γ -ray corresponding to the 3681 ± 5 keV ^{13}B [Aj91] ground state transition (Sec. 3.4.1) is shown in Fig. 5.11; the centroid of the peak was at channel number 3287.9 ± 1.8 (systematic error) and the raw yield was 150 ± 20 . The measured centroid and the calibration curve given by Eq. 5.5 yielded a measured energy of 3675 ± 2 keV.

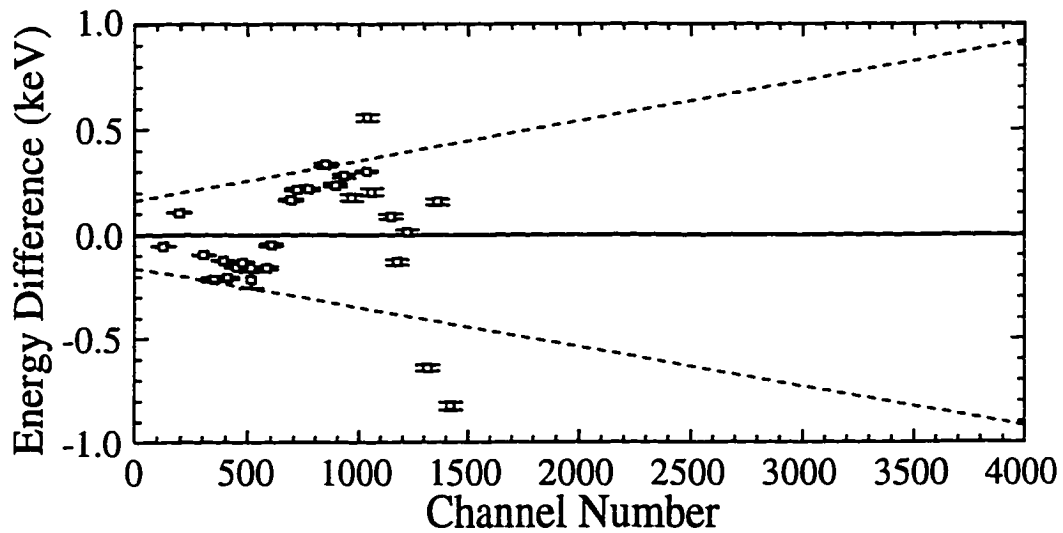


Figure 5.10 A plot showing the residuals for the linear fit used to determine the energy of the observed γ -ray line. The dashed lines represent the uncertainty in the fit, and the error bars are the uncertainties in the accepted energies.

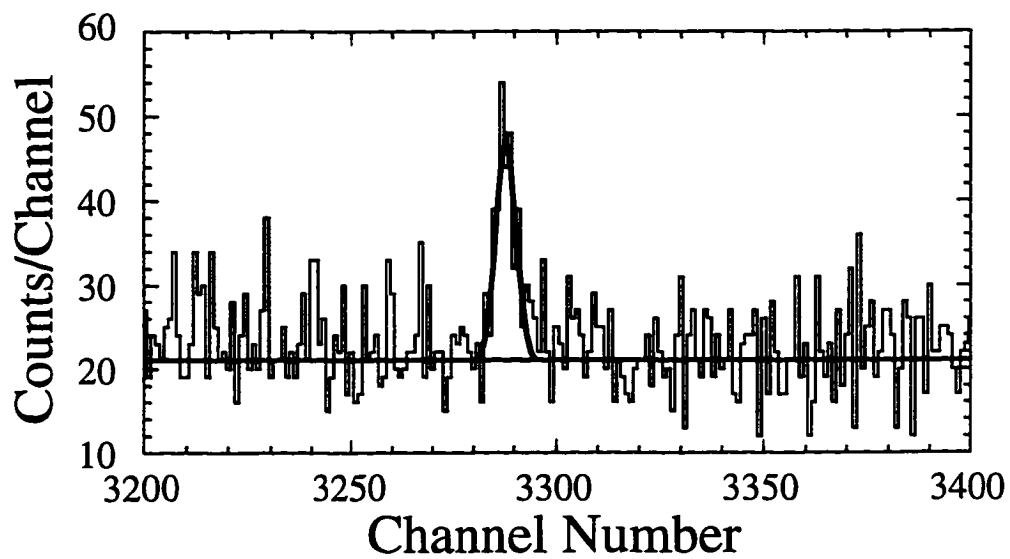


Figure 5.11 Fit of γ -ray peak due to daughter decay of ^{14}Be (see text).

5.4.2 Detection efficiency calibration of the γ -ray detector

This analysis consists of two steps: first, for each γ -ray line determine the total number of emitted γ -rays that impinge on the detector and, second, find the total number of γ -rays detected for each those corresponding lines. A ^{152}Eu source was used for this determination. Unlike the previous experiment, a calibrated source for which emission rates have been determined was not available for this experiment. The activity of this source was measured ($4.7 \pm 0.1 \mu\text{Ci}$), and using the accepted γ -ray intensities (Appendix B), the appropriate emission rates were calculated.

The elapsed time of the calibration run ($1132 \pm 1 \text{ s}$) was determined from the start and stop times that are written to tape by the acquisition system. Since the half-life of ^{152}Eu is 13.48 yr [Appendix B] and the activity was measured just one day after the calibration run, the correction of the activity for the time of the calibration run was negligible. Given the elapsed time and the fact that $1 \text{ Ci} = 3.7 \times 10^{10}$ disintegrations per second, the total number of ^{152}Eu (parent) decays occurring during the calibration run was $(1.97 \pm 0.04) \times 10^8$.

The γ -ray intensities* for ^{152}Eu were found from the appropriate reference in Appendix B. Thus the total number of emitted γ -rays for each line can be found by multiplying the total number of ^{152}Eu decays by its corresponding intensity. After calculating the emission rates, the procedure is analogous to that done in Sec. 3.4.2. The solid angle subtended by the high purity Ge detector was calculated using Ref. [Wi77] (also see Sec. 3.4.2). The geometry of Ge crystal was given in Sec. 4.2, where an uncertainty of 0.1 cm was assumed in all dimensions. This resulted in a solid angle of $144 \pm 7 \text{ msr}$ or a geometrical efficiency of $1.14 \pm 0.06\%$. Multiplying the total number of emitted γ -rays for each γ -ray line by the geometrical efficiency of the high

*The γ -ray intensity is a constant (usually expressed as a percentage) that when multiplied by the total number decays that populate the state from which the γ decay originates gives the number of emitted photons for that γ -ray line.

purity Ge detector gives the number of γ -rays for each line that impinged on the detector. Finally dividing these numbers into the corresponding measured yields normalized by the live time (25.8%, found from scaler information) gives the intrinsic detection efficiency, which is plotted in Fig. 5.12. The error bars of the measured data points are systematic, and the solid curve is a fit to these points (excluding the first two because of absorption in the material surrounding the detector) using [Si76]:

$$\ln \varepsilon = bx + cx^2; x = \ln(a/E), \quad (5.6)$$

where ε is the efficiency in percent, E is the γ -ray energy in keV, and the coefficients a , b , c are constants. The coefficients were optimized by minimizing the χ^2 , resulting in $a = (1.25 \pm 0.13) \times 10^5$, $b = -0.001 \pm 0.015$, and $c = 0.076 \pm 0.003$.

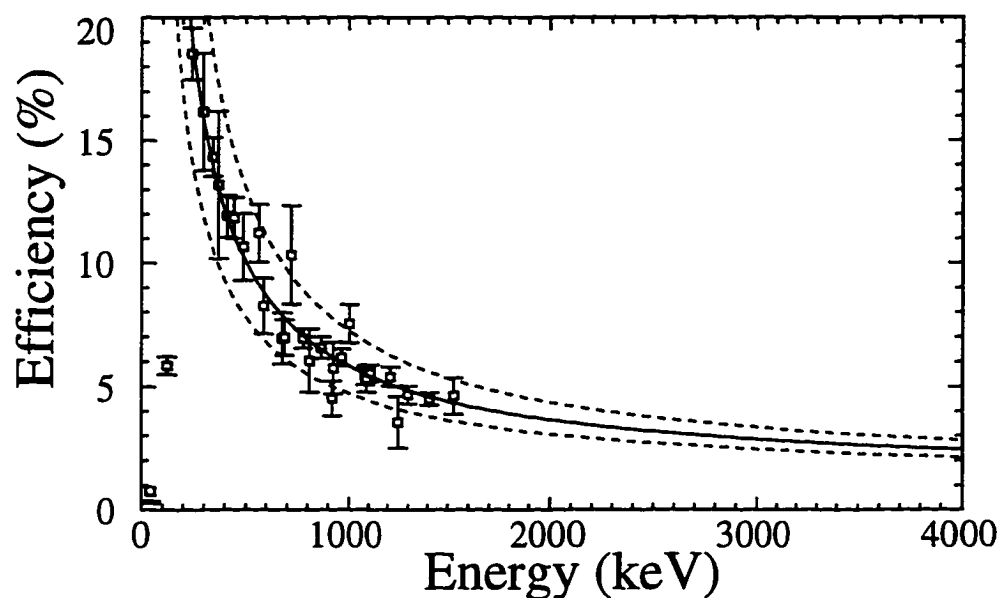


Figure 5.12 Plot of the γ -ray detection efficiency as a function of γ -ray energy (see text for details).

5.4.3 Branching ratio and $\log ft$ value for the observed γ -ray state

The detection efficiency for the 3675 ± 2 keV observed state found from Fig. 5.12 was $2.6 \pm 0.4\%$, and the raw measured yield for this group was 150 ± 20

(Sec. 5.4.1). Given the dead time corresponding to Fig. 5.11 (17.2% [Sec. 5.1.1]) and the geometrical efficiency of the Ge detector ($1.14 \pm 0.06\%$), the yield normalized (divided) by both is $(6.2 \pm 1.3) \times 10^5$. Because it was assumed that this group resulted from the β decay of ^{13}B , the total number of ^{13}B β decays ($4.16 \pm 0.10 \pm_{1.61}^{0.38}$) was found by multiplying the ^{14}Be β decay yield $[(5.07 \pm 0.05 \pm 0.40) \times 10^6]$ by the total $1n$ branching ratio (the sum of the branching ratios for the 0.287 and 3.10 MeV peaks equal to $82 \pm 2 \pm_{31}^4\%$ [Table 5.2]). Dividing the total number of ^{13}B β decays into the normalized γ -ray yield above gives a branching ratio of $15 \pm_{7}^3\%$ (systematic error).

The $\log ft$ of the β -transition that populates the ^{13}B 3681 ± 5 keV γ -ray state was found by using the method of Wilkinson and Macefield (see Ref. [Wi74] and Sec. 3.3.1). The end point energy of the corresponding β decay (9.756 ± 0.005 MeV) can be found from Eq. 3.27 where $S_n = Q_n = 0$, $Q_{g.s.}(\beta^-) = 13.4372 \pm 0.0011$ MeV [Au93], and $E_x = 3.681 \pm 0.005$ MeV. The end point energy for this state, its branching ratio ($15 \pm_{7}^3\%$), and its half-life (17.36 ± 0.16 ms [Aj91] for ^{13}B), resulted in $\log ft = 4.17 \pm_{0.11}^{0.25}$ (systematic error).

5.5 Analysis of Charged-Particle Data

It is possible that there were charged particle decay modes (other than the emitted β particles) that resulted from the β -decay of ^{14}Be . We used the energy signals of the SSD's to determine both the energy loss and position (along the beam axis) of β -delayed charged particles to investigate this possibility.

5.5.1 Relative gain matching of the SSD energy signals

A pulser that injected an equal amplitude pulse to each SSD pre-amplifier was used to calibrate the SSD energy spectra so that they could be gain matched with one another. A plot of the peak produced by the pulser for one of the SSD

energy signals (no. 1) is shown in Fig. 5.13. The peak on the left is the pedestal (caused by noise), which indicates zero energy, and the other is the peak produced by the pulser ("pulser peak"). The centroid of the pulser peak is at channel number 69.3 ± 0.8 (systematic error) and that of the pulser peak is 3645.3 ± 0.3 (systematic error). A linear calibration between the two points was assumed. All spectra were calibrated to the same (arbitrary) calibration curve so that equal energy signals corresponded to equal channel numbers.

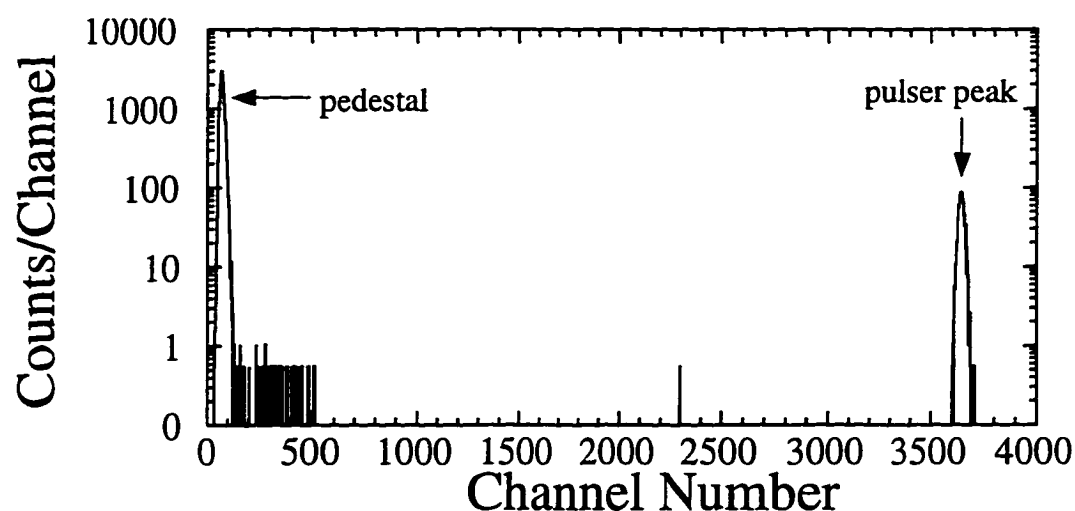


Figure 5.13 A typical energy spectrum (SSD 1) showing the pedestal and pulser peak.

5.5.2 Reduction of β peak interference

Figure 5.14 shows a typical calibrated SSD (no. 1) energy spectrum corresponding to the ^{14}Be data. The left peak is the pedestal. Because the β particles are lighter and are likely to be more energetic (average energy 4.4–5.4 MeV [Sec. 3.1.1]) than other charged particles, they deposit much less energy in the SSD. Thus, the two groups could be distinguished by their energy losses. The β group would also be expected to be the strongest group seen in the SSD energy spectrum. The very strong group just to the right of the pedestal group corresponds to emitted electrons

(the " β peak"). The dashed lines seen in Fig. 5.14 indicate a cut that was applied in the off-line analysis that will be described in detail below. Finally, the broad and indistinct group seen near channel number 260 is a charged-particle group. Note that this group is very difficult to see because of interference from the long tail of the β peak. (In fact, it was most easily seen in the SSD 1 energy spectrum.)

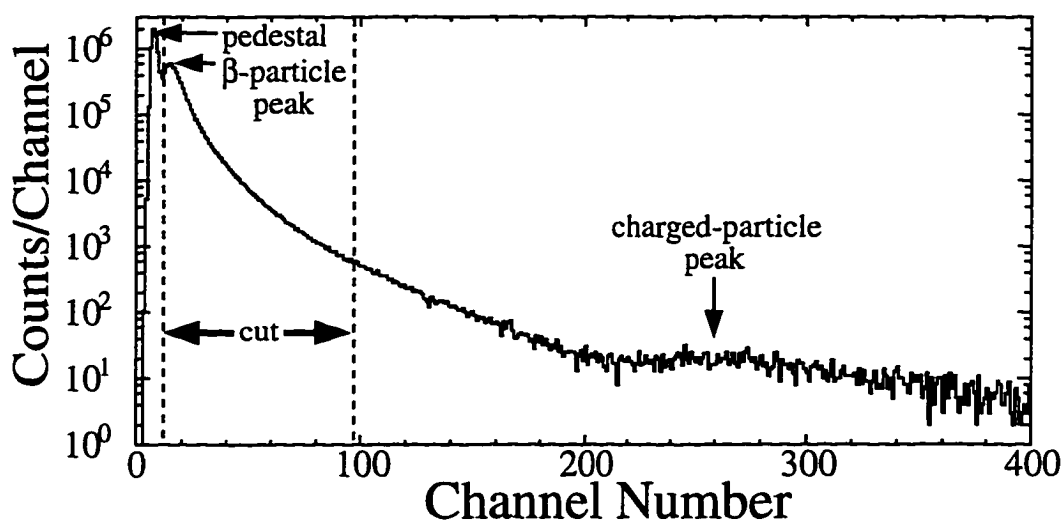


Figure 5.14 An energy spectrum of the ^{14}Be data from SSD 1 showing the various groups. The dashed lines indicate a cut that was used in the off-line analysis to separate the β -particle and charged-particle peaks (see text). The channel number are compressed by a factor of eight relative to Fig. 5.13.

Because the charged particles are much heavier, they have a much shorter range in silicon than the electrons. We thought that perhaps this information could be used to separate the two groups. A density of 2.33 g/cm^2 for silicon [Li91b] results in an areal thickness of 69.9 mg/cm^2 for one SSD (thickness $300 \mu\text{m}$ [Sec. 4.2]). From Ref. [Pa72], an electron with this range has a minimum energy of 0.23 MeV , which is much smaller than the average energies of the emitted β particles ($4.4\text{--}5.4 \text{ MeV}$). An electron that just penetrates all five SSD's has an energy of 0.71 MeV . Even though the range straggling of β particles is very large (differences of $20\text{--}400\%$ according to Ref. [Le87d]) due to their small mass, rough values serve here. The range of charged

particles of various possible species was calculated using the program STOPX (see Ref. [Aw83] and Sec. 2.2). Because protons are the lightest possible charged particles (other than electrons), they would have the longest range. For lower energy protons (1 MeV, for example), the range in silicon is only 3.7 mg/cm². Higher energy protons (10 MeV, for example) have a range (164.8 mg/cm²) larger than the thickness of an SSD. Heavier particles have much smaller ranges. The charged particles with the smallest range would be the daughters (¹⁴B, ¹³B, and ¹²B) that would have a small recoil energy. Before we can calculate its range, it necessary to calculate this recoil energy. The maximum recoil energy occurs at the end point energy where the electron possesses the maximum kinetic. In this case, conservation of momentum gives

$$p_r = p_e, \quad (5.7)$$

where p_e and p_r are the electron and daughter nucleus (recoil) momenta, respectively. Given that the recoil energy is small compared to the rest mass of the daughter nucleus and that the relativistic momentum of the electron has already been derived (Eq. 1.28), we get the following by squaring the result on both sides of the equation:

$$m_r^2 v_r^2 = 2m_r(\frac{1}{2}m_r v_r^2) = \frac{E_e^2 + 2E_e m_e c^2}{c^2}, \quad (5.8)$$

where m_r and v_r are the mass and velocity of the daughter nucleus, respectively, and E_e is the kinetic energy of the emitted electron. Equation 5.8 reduces to

$$E_r = \frac{E_e^2 + 2E_e m_e c^2}{2m_r c^2}, \quad (5.9)$$

where E_r is the recoil energy. The rest mass energy of the electron is about 0.511 MeV and the rest mass energies of the daughter nuclei were found by multiplying the most recent compilations [Au93] by the conversion factor 931.50 MeV·c²/u. At the respective end point energies (20.64 MeV, 13.44 MeV, and 13.37 MeV [Au93] for

^{14}B , ^{13}B , and ^{12}B , respectively), the recoil energies are 15.5 keV, 8.0 keV, and 8.6 keV, for ^{14}B , ^{13}B , and ^{12}B , respectively. Using STOPX [Aw83] we find that the range of these recoiling daughters are 0.033 mg/cm², 0.0091 mg/cm², 0.0093 mg/cm² for ^{14}B , ^{13}B , and ^{12}B , respectively. Because these ranges are so small compared to the thickness of an SSD (69.9 mg/cm²), we can conclude from the above information that most charged particles (except perhaps very energetic hydrogen isotopes) will stop within the same SSD from which the decay originally occurs, and most of the emitted electrons will pass through all of the SSD's.

With the conclusion above, we decided to look for charged particles deposited in a given SSD in coincidence with electrons traveling in only one direction (downstream or upstream) emitted from the same SSD. This would reduce the interference caused by electrons emitted from a different SSD that happen to pass through the SSD of interest. An example of this is shown in Fig. 5.15 that diagrams the geometry and cuts (in the off-line analysis) that we required to look at the charged particle group, on an event by event mode, deposited in SSD 2 in coincidence with β particles emitted from the same SSD traveling in the downstream direction.

Two different cuts were used in the analysis: "wide", channels 12–500 and "tight", channels 12–97 (the same tight cut shown in Fig. 5.14). Narrowing the tight cuts lessened the interference of the β particle tail but also reduced the statistics of the charged-particle peak. It was not possible to remove all the interference, and the cut shown in figures 5.14 and 5.15 represent the best compromise. The pedestal is excluded in all cuts, because this was present in all SSD's for all events.

In this example, one would only look at the energy spectrum of SSD 2 corresponding to events that satisfy all four cuts. Note that β particles originating from SSD 3 and SSD 4 traveling in the upstream direction, those originating from SSD 1 traveling in either direction, or those originating from SSD 2 traveling in the

upstream direction **do not** satisfy all four cuts. In other words, β particles that pass though SSD 2 that not are of interest are eliminated. A problem arises with SSD 1 and SSD 5, because the SSD's were adjacent only on one side in this case. In principle, the start detectors could also be used, but their detection efficiencies were not high enough to be useful.

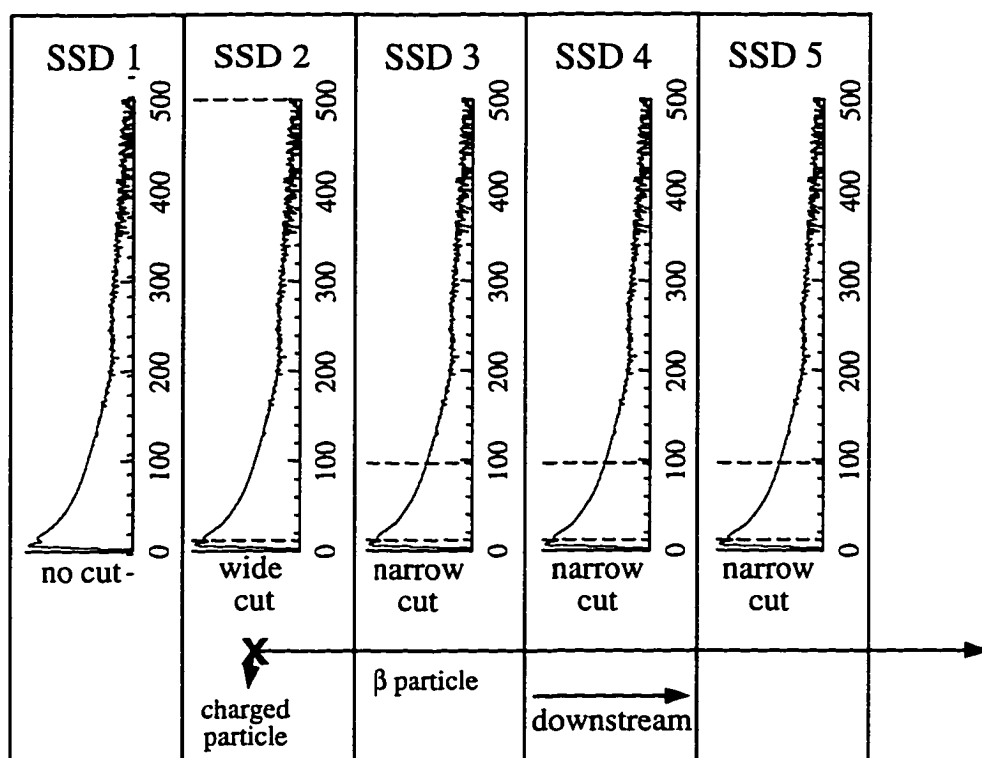


Figure 5.15 Diagram showing the geometry for a typical β decay and cuts used to reduce the interference caused by the β -particle peak for the type of event shown (see text). The spectra are only representative of typical energy spectra, and the channels have been compressed by a factor of eight relative to Fig. 5.13.

5.5.3 Half-life of the charged-particle group

We looked at all possible combinations and found that the sum of all gated spectra where the β particle originated from SSD 1 or SSD 2 gave the best results. Figure 5.16a shows the result plotted with same vertical and horizontal scales as Fig.

5.14. Figure 5.16b shows a fit (using the asymmetric hypergaussian line shape given by the program FITS [Di93]) to the same data, on a linear scale with the vertical axis enlarged to show the charged particle group more clearly. The half-life of this group was measured (using a method similar to that discussed in Sec. 5.1.2) by looking at Fig. 5.16 as a function of time (see Fig. 5.3 for an example).

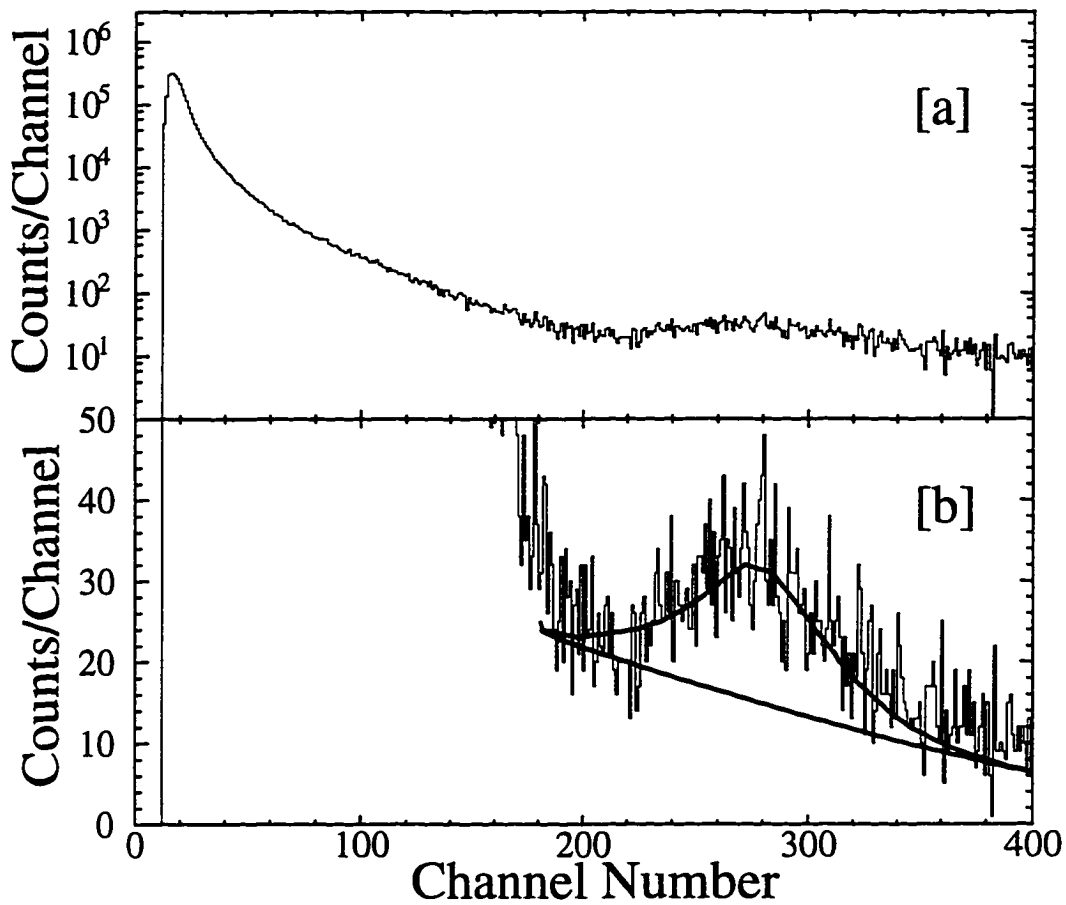


Figure 5.16 (a) Plot of SSD energy spectrum after cuts were applied that reduced the interference of the β -particle peak (see text). (b) Same as Fig. 5.16a showing a fit to the charged-particle group and plotted on a vertically enlarged linear scale.

The measured data points are plotted in Fig. 5.17 where the background has been subtracted and the error bars are statistical and include the background subtraction. The points did not fit very well to a single exponential curve (which

would be a straight line on this log plot) but did fit much better to what would be expected for a radioactive daughter decay. As in Fig. 5.1, the daughter rises initially due to the decay of the parent, and then exhibits an exponential decay later after the abundance of the parent is depleted. The mathematical form for a daughter decay has already been given (Eq. 5, Table 3.1). This function was fitted to the data by using the Marquadt method of performing a nonlinear least squares fit where the algorithms given by Ref. [Be92] were used. Because of the large uncertainty in the fit it was necessary to fix the value of the ^{14}Be half-life to the value measured here (4.36 ± 0.13 ms). Thus, the half-life of the daughter and the activities of the daughter and parent were varied. The fitted half-life was 12 ± 10 ms, with a reduced $\chi^2 = 0.278$.

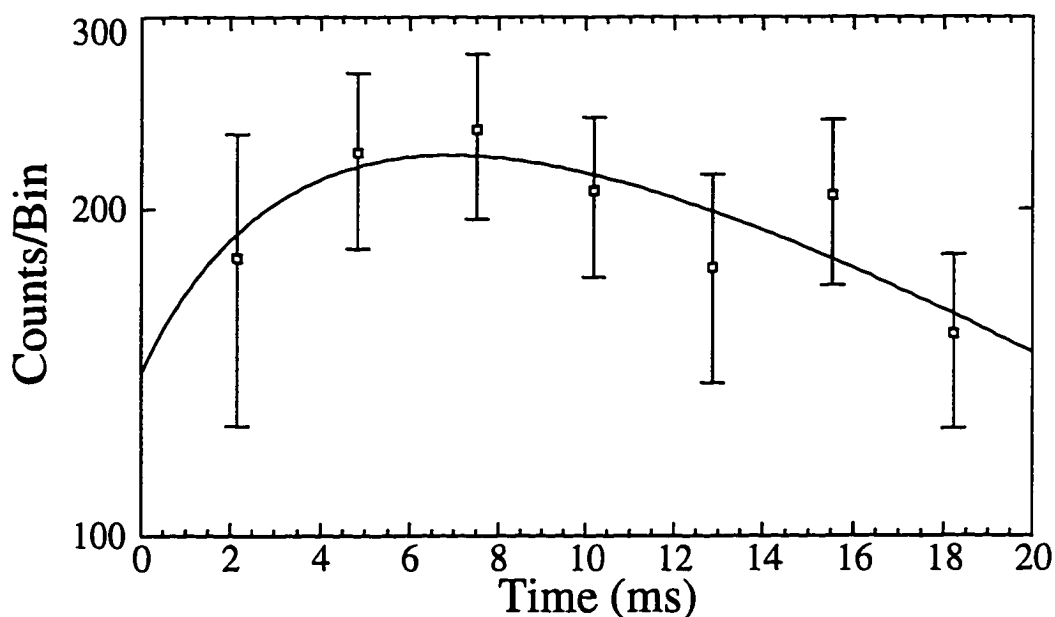


Figure 5.17 Fitted activity curve to the measured charged-particle data assuming a daughter decay using the procedure described in the text.

5.5.4 Absolute energy calibration of the SSD energy spectra

Although the pulser provided a relative energy calibration, it did not provide an absolute one. Thus, only a rough energy calibration could be made by measuring

the centroid of the noise pedestal (indicating zero energy) and the β group. At typical β -decay energies (a few MeV) the electrons are minimum ionizing, and their linear stopping power varied over a range small enough to make an energy estimate of the charged-particle group. For energies from 0.25 to 14.0 MeV, the average stopping power [Pa72] varied from $2.22 \text{ MeV}\cdot\text{cm}^2\text{g}^{-1}$ to $1.54 \text{ MeV}\cdot\text{cm}^2\text{g}^{-1}$ (in silicon). (Note: electrons below 0.25 MeV have insufficient range [Pa72] to penetrate a single SSD.) In Sec. 6.5, we shall see why we have identified the observed charged-particle group with ^{12}B β -decay. The average endpoint energy of ^{12}B weighted by the branching ratios to various daughter states [Aj90] is $13.20 \pm 0.04 \text{ MeV}$, the average β decay energy is one-third this $4.400 \pm 0.016 \text{ MeV}$, and the average energy loss for electrons at this average energy in an SSD is about $1.73 \text{ MeV}\cdot\text{cm}^2\text{g}^{-1}$. The deviation from the above average is no more than 28%, and this was taken as the systematic uncertainty in the energy loss. With a thickness of 0.0699 g/cm^2 , the energy loss was $0.12 \pm 0.03 \text{ MeV}$ for one SSD or $0.61 \pm 0.17 \text{ MeV}$ for the entire stack, which is small compared to the range of average β -decay energies for the ^{14}Be daughters (4.4–5.4 MeV).

The program FITS [Di93] was used to fit the pedestal in Fig. 5.16. The energy of the β group was assumed to be the same as the energy loss found above for one SSD. Because this was determined from the average energy loss corresponding to the average β -decay energy, it was necessary to compute the weighted average channel number of this group and not its centroid. Given the channel locations of the pedestal and charged particle groups (8.8 and 20.8 [512 channels full scale], respectively) and assuming linearity, we get the following calibration curve:

$$y = (11 \pm 3 \text{ keV/chan})x - 100 \pm 30 \text{ keV}. \quad (5.10)$$

In Eq. 5.10, y is the energy in keV, and x is the channel number (512 channels full scale). Because the systematic uncertainty in the calibration curve was dominated by the uncertainty in the β group energy, the uncertainty in the centroids was

negligible. From the fit shown in Fig. 5.16b, the centroid of the charged particle group was at channel number 271 yielding an energy of 2.9 ± 0.8 MeV, and the width was 71.0 ± 0.5 channels or 0.8 ± 0.2 MeV.

5.5.5 Branching ratio of the charged-particle group

Although the fit of Fig. 5.16b worked best for determining the half-life and centroid of the charged-particle group, it is not appropriate for determining the branching ratio of that group. The reason for this is that in SSD 1 and SSD 5 the emitted electron cannot be uniquely tracked as was done in Fig. 5.15. For example, if one wanted to look at the charged particle group in the energy spectrum of SSD 1 where the coincident β particle travels in the downstream direction (see Fig. 5.15) the following cuts would be used: SSD 1, wide; SSD 2, tight; SSD 3, tight; SSD 4, tight; SSD 5, tight. Notice that a β particle originating from SSD 5 traveling in an upstream direction also satisfies these same cuts. The problem arises because there is no SSD on the upstream side of SSD 1. Thus, we only analyzed energy spectra from SSD's 2–4 to avoid this ambiguity.

Figure 5.18 shows a fit of the sum of the energy spectra for SSD's 2–4 where a procedure similar to what is diagrammed in Fig. 5.15 was done for each of the three SSD's for β particles emanating in both directions. In Fig. 5.18, the charged-particle group was fitted with a Gaussian line shape and quadratic background (to account for interference from the long tail) using the program FITS [Di93]. The resulting yield was 330 ± 60 (systematic error) where the uncertainty in determining the background contributed the majority of the error. The yield of the β particle peak was $(2.460 \pm 0.007) \times 10^6$. Because β decay of daughters and impurities and coincident γ -ray decay also contribute to the yield of the β particle group, it was necessary to determine what fraction of this yield was due to the β decay of ^{14}Be . This was done by using the fit of the raw activity spectrum (Fig.

5.1) to find the ratio (0.43 ± 0.11) between the ^{14}Be yield and integrated sum of the raw data. This ratio was computed for fits to the activity curve corresponding to the various duty cycles (Sec. 4.3) to determine the systematic uncertainty in this ratio. Thus, the total yield of ^{14}Be β particles corresponding to the Fig. 5.18 was $(1.0 \pm 0.2) \times 10^6$, resulting in a branching ratio of $0.031 \pm 0.008\%$ for the charged-particle group (relative to ^{14}Be β decay).

With an impurity of $0.36 \pm 0.05\%$ (relative to ^{14}Be β decay, Table 4.2) of ^{14}Be , it should be expected that some of the charged-particle yield is due to the β decay of this impurity. We used the program GRAPH ([Be92b] and Sec.3.1.1) to calculate the relative amount of ^{12}B produced by the β decay of the ^{12}Be impurity corresponding to the fit shown in Fig. 5.1. The functional form for the activity of the impurity during the beam-off period is given by equations 3 and 6, Table 3.1 (where $f_i = 0.36 \pm 0.05\%$), and that for the daughter by equations 2 and 5 in the same table. The resulting branching ratio was about 0.08%, which is considerably larger than that found from the charged-particle data above ($0.031 \pm 0.008\%$). This point will be discussed in Sec. 6.5.

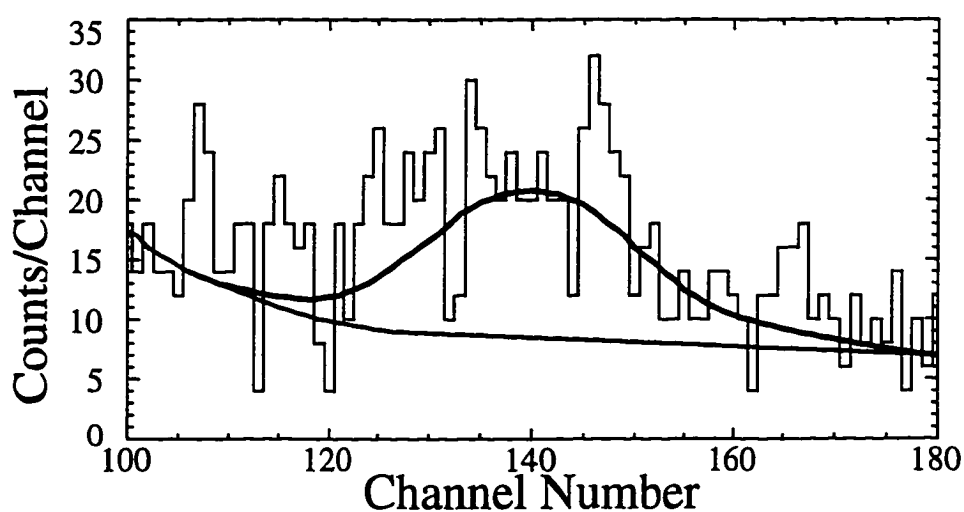


Figure 5.18 Fit to the charged-particle group that was used to determine its branching ratio (see text).

5.6 Determination of the Natural Width of the Low Energy Neutron Group

The 287 keV neutron group should be low enough in energy so that its natural width can be measured. First, we assumed that the observed total width is due to three sources: experimental line width (Γ_{exp}) due to systematic uncertainties in the flight path, electronic noise (Γ_{elect}), and the natural width (Γ_{nat}) intrinsic to the transition. These three widths are uncorrelated, so that

$$\Gamma_{\text{tot}} = \sqrt{\Gamma_{\text{exp}}^2 + \Gamma_{\text{elect}}^2 + \Gamma_{\text{nat}}^2}. \quad (5.11)$$

If the widths are expressed in terms of channel numbers which are proportional to the flight time, then solving Eq. 5.11 for Γ_{nat} yields

$$\Gamma_{\text{nat}} = \sqrt{\Gamma_{\text{tot}}^2 - \Gamma_{\text{elect}}^2 - \Gamma_{\text{exp}}^2}. \quad (5.12)$$

The electronic width (0.5 ± 0.1 ns) was estimated from the width of the pulser peaks used to calibrate the TDC spectra (Sec. 4.4.2). This electronic width, the known natural widths of the three observed ^{17}N neutron peaks ([Oh76] and Table 5.3, column 2), and the following equation found from Eq. 5.11 were used to determine the experimental width:

$$\Gamma_{\text{exp}} = \sqrt{\Gamma_{\text{tot}}^2 - \Gamma_{\text{elect}}^2 - \Gamma_{\text{nat}}^2}. \quad (5.13)$$

The total widths of the ^{17}N neutron groups are listed in Table 4.4. With each channel equal to 0.25 ns (Sec. 5.2.1), the total ^{17}N widths (in ns) are listed in Table 5.3 (column 3). Before calculating the experimental widths using Eq. 5.13, it was necessary to convert the ^{17}N natural widths to flight time. The flight time can be found from:

$$t = \frac{d}{v(E)}, \quad (5.14)$$

where the calibrated distance $d = 201.4 \pm 0.7$ cm (Sec. 4.5.2) and the neutron velocity

as a function of its energy was derived in Sec. 2.6 (Eq. 2.12). If the width in terms of energy is represented by $\Gamma(E)$ and that in terms of time is represented by $\Gamma(t)$, then

$$\Gamma(t) = \frac{d}{v(E + \frac{1}{2}\Gamma(E)) - v(E - \frac{1}{2}\Gamma(E))}. \quad (5.15)$$

Using Eq. 5.15, the corresponding natural widths in terms of flight time are listed in Table 5.3 (column 4). The corresponding experimental widths were calculated from Eq. 5.13 and are listed in Table 5.3 (column 5).

TABLE 5.3

VARIOUS WIDTHS ASSOCIATED WITH THE ^{17}N NEUTRON PEAKS

Energy (MeV)	Natural Γ (keV)	Total Γ (ns)	Natural Γ (ns)	Exp. Γ (ns)	Exp. Γ (cm)
0.383	54.8±0.4	24. ±2.	16.8 ±0.7	17.8±3.4	15. ±3.
1.171	63.2±0.2	8.1±0.2	3.62±0.16	7.2±0.2	10.8±0.4
1.700	60.5±3.2	6.1±0.5	2.0 ±0.2	5.7±0.5	10.3±0.9

NOTE: The symbol Γ represents the full-width-at-half-maximum, and Exp. is an abbreviation for experimental.

Because the experimental width is due to the uncertainty in the flight path, it should be a constant expressed in terms of distance. The width in terms of flight path $\Gamma(d)$ is calculated from

$$\Gamma(d) = v \cdot \{ [t + \frac{1}{2}\Gamma(t)] - [t - \frac{1}{2}\Gamma(t)] \} = v \cdot \Gamma(t), \quad (5.16)$$

where the total time t for each neutron group can be found by multiplying the neutron velocities given in Table 4.3 by the calibrated distance equal to 201.4±0.7 cm. The corresponding experimental widths in terms of flight path are listed in Table 5.3 (column 6), and the average of these values (weighted by the uncertainties) is 10.8±0.3 cm.

Using Eq. 2.12 again, the velocity of neutrons v at 0.287 ± 0.003 MeV is 0.744 ± 0.005 cm/ns, and multiplying this by the calibrated distance gives a total flight time of 271 ± 2 ns. With this information, the total calibrated flight path, the experimental width in terms of flight path (10.8 ± 0.3 cm), and the following equation:

$$\Gamma(t) = \frac{[d + \frac{1}{2}\Gamma(d)] - [d - \frac{1}{2}\Gamma(d)]}{v} = \frac{\Gamma(d)}{v}, \quad (5.17)$$

we get an experimental width of 14.5 ± 1.1 ns for the 0.287 MeV group. The total width of the group was 126 ± 4 channels or 31.4 ± 0.9 ns. Now that we have the total, electronic (0.5 ± 0.1 ns), and experimental width (14.5 ± 1.1 ns) for this neutron group, we find, applying Eq. 5.12, that the natural width of the group is 27.8 ± 1.2 ns. Because the velocity of neutrons at 0.287 MeV (0.744 ± 0.005 cm/ns) is much smaller than the velocity of light (about 30.0 ns/cm), classical mechanics could be used to calculate the above natural width in terms of energy:

$$E = \frac{1}{2}mv^2 = \frac{1}{2}m(d/t)^2. \quad (5.18)$$

In Eq. 5.18, E is the neutron energy, m is the neutron mass (about 1.675×10^{-27} kg), v is the neutron velocity, d is the calibrated distance, and t is the neutron flight time. Letting t represent the total flight time corresponding to the 0.287 MeV neutron group (271 ± 2 ns), the natural width in terms of energy can be found from:

$$\Gamma(E) = \frac{1}{2}m \left(\frac{d}{t + \frac{1}{2}\Gamma(t)} \right)^2 - \frac{1}{2}m \left(\frac{d}{t - \frac{1}{2}\Gamma(t)} \right)^2. \quad (5.19)$$

The resulting natural width for the 287 keV neutron group was 60 ± 5 keV, which is comparable to the natural width for the ^{17}N β -delayed neutron groups.

CHAPTER 6

DISCUSSION AND CONCLUSION

In this chapter the various results obtained from both experiments are discussed and compared to previous measurements and with each other. We also investigate what experimental improvements might be necessary to obtain γ - n and n - n coincidences in a future experiment. Next, $0n$ emission is addressed, its $\log f_{1t}$ value is calculated, and the implication of this are discussed. Using the information obtained in this work, we give the most likely decay modes for the various neutron, γ -ray, and charged-particle groups observed. Last, we compare the results with a shell-model calculation.

6.1 Discussion of ^{14}Be Half-life

While the half-life of ^{14}Be determined in the NSCL experiment, both ungated ($4.8 \pm 0.4 \pm 0.2$ ms) and in coincidence with neutrons (4.0 ± 1.2 ms) agree with the value measured by Dufour *et al.* 4.35 ± 0.17 ms [Du88], they had large uncertainties because of low statistics. The latter measurement suffered from a severe lack of statistics, because the higher threshold in the NSCL experiment prevented β - n coincidence with the strong neutron group at 287 keV. There was distortion due to rate dependent dead time in the RIKEN experiment that prevented a reliable half-life measurement of the raw activity spectrum. In contrast, the half-life determined from β - n coincidence with the

low energy neutron group was 4.36 ± 0.13 ms. This value is in excellent agreement with that measured in Ref. [Du88]. All of the values determined in this thesis and in Ref. [Du88] agree well with an earlier measurement (4.2 ± 0.7 ms [Cu86]) done at the NSCL.

6.2 Discussion of Low Energy Neutron State

The most important result of this thesis is the observation of the 287 keV neutron group in the RIKEN experiment. In Sec. 3.6, we mentioned that the total neutron branching ratio determined from the NSCL experiment accounted for only a small portion ($6.3 \pm 0.1 \pm 3.2\%$) of the total known neutron branching ratio ($86 \pm 4\%$, sum of the accepted $1n$ and $2n$ values [Du88]). The branching ratio of the 287 keV neutron group ($82 \pm 2 \pm_{31}^4\%$) compares well to the $1n$ branching ratio of $81 \pm 4\%$ [Du88] and explains the discrepancy between Dufour's measured $1n$ branching ratio [Du88] and that observed in the NSCL experiment.

Although the 0.287 MeV neutron group was not seen in coincidence with γ -ray decay, it is possible that there were insufficient statistics to see such a coincidence. The geometrical efficiencies of the neutron and γ -ray detectors were $4.61 \pm 0.03\%$ and $1.14 \pm 0.06\%$, respectively and the detection efficiencies corresponding to both groups are $41 \pm 13\%$ and $2.6 \pm 0.4\%$ for the 0.287 MeV neutron and γ -ray groups, respectively. With this information, the probability that a neutron and γ -ray from these corresponding groups are detected together in coincidence is the product of all these efficiencies ($0.0006 \pm 0.0002\%$). The expected number of coincident γ -rays would then be equal to the product of the above probability and the raw yield of the neutron peak, 66000 ± 4200 (systematic error). This would result in 0.37 ± 0.13 coincident γ -rays; obviously, one is not going to see these two groups in coincidence!

Because the coincidence measurement is inconclusive, this leads to two possible ^{14}B levels corresponding to the 0.287 MeV neutron group. Using Eq. 3.30, the Q-value of the above neutron group is 0.307 ± 0.003 MeV. Thus, if the two groups are not in coincidence, then the neutron decay populates the ground state of ^{13}B . With a $1n$ separation energy equal to 0.97 ± 0.02 MeV, the ^{14}B level energy is 1.28 ± 0.02 MeV. If the two groups are coincident, then the excitation energy of the observed γ -ray (3.68 MeV) must also be added to find the ^{14}B level energy, 4.96 ± 0.02 MeV. Because these level energies are below the $2n$ threshold (5.85 MeV [Aj91]), both are possible. (This group cannot correspond to $2n$ emission, because the two emitted neutrons would not share the decay energy in a unique proportion leading to distinct energy groups.) The former possibility is more likely because it corresponds to a lower ^{14}B level energy and agrees better with the shell model calculation given in Fig. 1.8. In Sec. 6.4, we shall investigate the possible decay modes of the observed γ -ray line and give an additional reason why the low energy neutron group results from a transition to the ground state of ^{13}B . Thus we assigned an energy of 1.28 ± 0.02 MeV to the ^{14}B level corresponding to the 0.287 MeV neutron group.

The $\log ft$ for this state ($3.70 \pm_{0.04}^{0.20}$) agrees very well with the predicted range given in Sec. 3.6 ($\log ft = 3.6 - 3.8$). Such a low $\log ft$ value implies a very strong allowed β transition. Because ^{14}Be is so far from stability, β decay from excited isomeric levels of ^{14}Be is very unlikely. Thus, we assume that all of the ^{14}Be decay originates from the 0^+ [Aj91] ground state. Given that the β decay is allowed and the initial state is 0^+ , the selection rules listed in Table 1.1 require a final state of 0^+ or 1^+ . A final 0^+ state is unlikely, because this would imply a superallowed Fermi decay, and the weakest known (highest $\log ft$) superallowed decay is the β^+ decay of ^{42}Ti [Ra75] with a $\log ft$ of $3.52 \pm_{0.17}^{0.11}$. One would expect β decay to the isobaric analog of the ground state of ^{14}Be to be a very strong superallowed $0^+ \rightarrow 0^+$ transition, because

these two states would have identical nuclear wave functions and shell-model configurations except for the difference between a neutron and proton. The ^{14}B level energy of the isobaric analog of the ^{14}Be ground state can be found from Eq. 1.45. The difference in Coulomb energy is 2.07 MeV (Eq. 1.51), and the binding energies of ^{14}Be and ^{14}B are 68.85 MeV and 85.42 MeV [Au93], respectively. The resulting analog state is 18.64 MeV above the ground state of ^{14}B or 2.42 MeV above the ^{14}Be ground state; thus, it is energetically impossible for the β decay to populate this state. Because of these reasons we have assigned a spin/parity of 1^+ to the 1.28 MeV level.

6.3 Discussion of Higher Energy Neutron States

In both the NSCL (Fig. 3.9) and RIKEN (Fig. 5.8) experiments, we observed two very weak neutron groups much higher in energy than the 287 keV neutron group. While the measured energies of the two higher energy neutron groups differ somewhat, they are in agreement within their mutual errors. The branching ratios ($0.11 \pm 0.02 \pm 0.04\%$ [NSCL] and $0.28 \pm 0.02 \pm 0.14\%$ [RIKEN]) of the group near 3.6 MeV are in sharp disagreement. The discrepancy is probably due to the ^{11}Li subtraction necessary in the NSCL experiment, and the fact that there is a ^{13}B β -delayed neutron group at 3.613 ± 0.013 MeV with branching ratio $0.16 \pm 0.03\%$ [Aj81] (relative to ^{13}B β decay). Given the systematic error in the measured energy of the 3.70 ± 0.11 MeV group, there is insufficient information to distinguish between the two neutron energies. Because of this ambiguity, we cannot say with any certainty that the 3.70 MeV group results from β -delayed neutron decay of ^{14}Be , and for this reason its $\log ft$ values are not listed in Table 5.2.

On the other hand, the branching ratios of the other high energy neutron group ($0.30 \pm 0.03 \pm 0.05\%$ [NSCL] and $0.29 \pm 0.02 \pm 0.12\%$ [RIKEN]) are in excellent agreement. Thus, we ascribe this group to the β -delayed neutron decay of ^{14}Be . As

mentioned above, there was one γ -ray line (at 3.680 MeV) observed in both experiments resulting from the β decay of ^{14}Be . As demonstrated in Sec. 6.2, it would not be possible to see a coincidence between the low energy neutron group and this γ -ray line. Taking the energy measured in the NSCL experiment (3.02 ± 0.03 MeV, the lower of the two), the corresponding ^{14}B level would be at 7.90 ± 0.04 MeV. This is well above the $2n$ separation energy (5.85 ± 0.02 MeV [Au93]), so this state would very likely decay by $2n$ emission. We adopt the value measured in the RIKEN experiment (3.10 ± 0.08 MeV), because the systematic error caused by subtracting a ^{11}Li impurity is negligible in this case. Thus, the corresponding ^{14}B level energy is 4.31 ± 0.09 MeV and $\log ft = 5.67 \pm_{0.04}^{0.04} \pm_{0.24}^{0.15}$. The corresponding $\log ft$ value obtained from the NSCL experiment, $5.67 \pm_{0.05}^{0.05} \pm_{0.07}^{0.09}$, is in excellent agreement.

6.4 Discussion of γ -ray State

In the NSCL (Fig. 3.12) and RIKEN (Fig. 5.11) experiments, one γ -ray line resulting from the β decay of ^{14}Be was observed. The measured energies determined were 3680 ± 1 keV (NSCL) and 3675 ± 3 keV (RIKEN). The most likely explanation of the disagreement between the two values is the fact that the RIKEN experiment was performed in an extremely clean γ -ray environment, and no background lines were seen except for the positron annihilation peak (energy 511.003 keV). This prevented using the higher energy background lines (for example, the 1764.4 keV and 2204.2 keV lines of ^{214}Bi , and the 2614.5 keV line of ^{208}Pb [Appendix B]) to improve the accuracy at higher energies. Because there were more γ -ray sources available for the NSCL experiment, the γ -ray energy determination for this experiment had many more calibration points and resulted in a better fit. For these reasons, we adopt the NSCL measurement of 3680 ± 1 keV.

Unfortunately, there are two possible candidates for this measured γ -ray line: the ground state decay of the ^{13}B 3681 ± 5 keV level and the ground state

decay of the ^{13}C 3684.51 ± 0.02 keV level. The emitted γ -ray energies can be found by applying Eq. 3.53 (where Mc^2 is the rest mass energy of the recoiling nucleus ^{13}B), resulting in 3680 ± 5 keV and 3683.95 ± 0.02 keV for ^{13}B and ^{13}C , respectively. Even though the adopted measured value is not in agreement with the ^{13}B energy, the error in extrapolating the NSCL calibration from the highest measured point (the 2614.5 keV ^{208}Pb line) to that of the observed 3680 ± 1 keV line was very difficult to determine and was not included in the uncertainty of the calibration. As mentioned in Sec. 6.2, there were insufficient statistics to obtain γ - n coincidence information that might identify this γ -ray line.

While the 3684.51 MeV ^{13}C ground state decay is well known (spin/parity of $3/2^+$, a multipolarity of M1+E2, and γ -ray intensity of 100% [Aj91]), little is known about the 3681 keV ^{13}B ground state decay other than its energy [Aj91]. Consequently, this information cannot be used to determine which state is more likely. The two possibilities are diagrammed in Fig. 6.1.

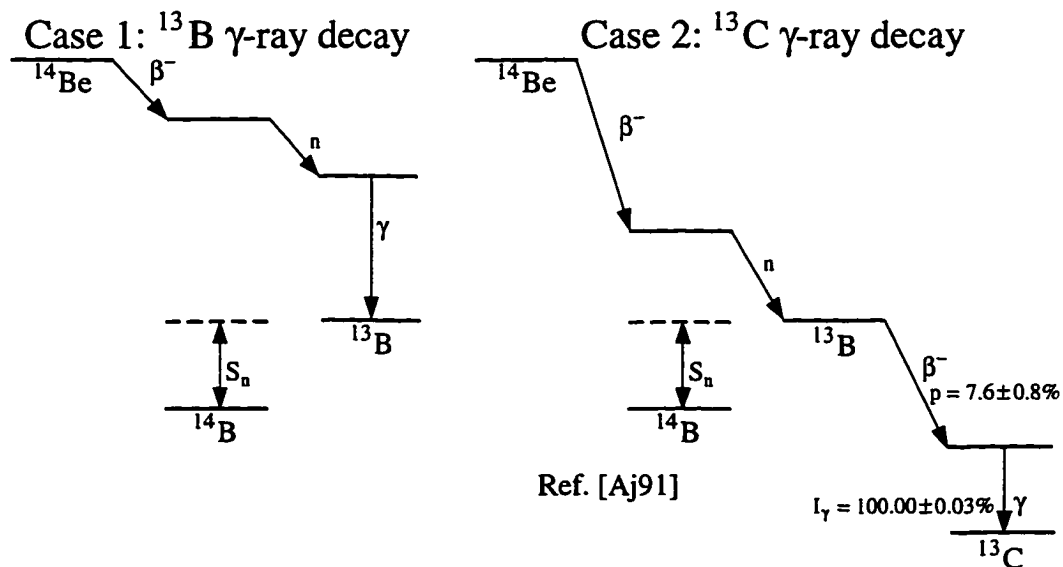


Figure 6.1 Diagram of the two possible decay schemes corresponding to the observed γ -ray decay with energy 3.680 MeV. The γ -ray intensity (I_γ) and branching ratio (p) are given where known.

In case 1 (Fig. 6.1), we do not know the identity of the ^{14}B level that populates the ^{13}B level in question, nor do we know the γ -ray intensity of the corresponding transition. One can use the geometrical efficiency of the γ -ray detector and the corresponding detection efficiency to determine the number of neutrons that would populate this ^{13}B state based on the observed yield of the γ -ray state. Since the total β decay yields have been measured $[(2.04 \pm 0.24) \times 10^6$ (NSCL) and $(5.07 \pm 0.40) \times 10^6$ (RIKEN)], we can determine the branching ratio of a hypothetical neutron transition (or transitions) that would correspond to the observed γ -ray decay. (In the following discussion we shall only calculate the larger systematic errors.) The raw yields of the observed γ -ray lines were 143 ± 15 (NSCL) and 150 ± 20 (RIKEN), the geometrical efficiencies of the high purity Ge detector were $4.6 \pm 0.4\%$ (NSCL) and $1.14 \pm 0.06\%$ (RIKEN), and the intrinsic detection efficiencies at 3.680 MeV were $6.6 \pm 0.4\%$ (NSCL) and $2.6 \pm 0.4\%$ (RIKEN). By normalizing the raw yields for the dead time (negligible for the NSCL experiment, and 17.2% for the other experiment) and the geometrical and detection efficiencies, and dividing the result by the corresponding number of β decays, we obtain the total branching ratio of the hypothetical neutron group(s) that correspond to this possible ^{13}B γ decay. For the NSCL experiment, the result was $2.4 \pm 0.4\%$, and for the RIKEN experiment it was $12 \pm 2\%$.

In Sec. 6.3, we demonstrated that the observed γ -ray line could not be in coincidence with the higher energy neutron group, because that would place the corresponding ^{14}B level above the $2n$ threshold. Therefore, two possibilities remain. One possibility is that the γ -ray transition is in coincidence with an unobserved neutron group. This is unlikely, because the hypothetical branching ratios found above are so high. Because we have already measured branching ratios on the order of 0.2%, let us assume this value as a lower threshold. Even for the NSCL experiment the hypothetical branching ratio is roughly a factor of ten higher than this threshold.

Although the γ -ray detection efficiency is only a crude estimate, it would have to be over ten times higher in the NSCL experiment (or about 66%) so that the hypothetical neutron state could not be seen. The situation for the RIKEN experiment is worse.

The other possibility is that the observed γ -ray line is in coincidence with the neutron group at 287 keV (branching ratio $82 \pm_{31}^4\%$). This is also unlikely because the hypothetical branching ratios are too low. For the RIKEN experiment (the highest one) it was $12 \pm 2\%$, a factor of 6.8 too low. Thus, the γ -ray detection efficiency for this experiment would have to be factor of 6.8 higher for the two to agree, and this is extremely unlikely.

In case 2 (Fig. 6.1), we assume that the observed γ decay corresponds to an electromagnetic transition in ^{13}C , where the β decay that populates this state originates from the ground state of ^{13}B [Aj91]. In this case, the γ -ray intensity and branching ratio of the corresponding β decay are accurately known ($100.00 \pm 0.03\%$, and $7.6 \pm 0.8\%$ [Aj91]). Normalizing the raw yields by the known γ -ray intensity, the β -decay branching ratio, and the detection and geometrical efficiencies results in the following hypothetical branching ratios (relative to ^{14}Be β decay): $30 \pm 6\%$ (NSCL) and $158 \pm 37\%$ (RIKEN). The observed 287 keV neutron group matches these branching ratio most closely of all possibilities. The γ -ray detection efficiency would only have to be about a factor of 2.7 lower for the NSCL experiment, and a factor of 1.9 higher for the other experiment for the two to agree. Because these represent the most reasonable values, we propose that the most likely identity of the observed γ -ray at 3680 ± 1 keV is case 2, the ground state decay of the ^{13}C 3684.51 ± 0.02 keV [Aj91] level. In addition, this conclusion requires that the low energy neutron group at 287 keV decays to the ground state of ^{13}B with the energy of the corresponding ^{14}B level equal to 1.28 ± 0.02 MeV.

6.5 Discussion of Observed Charged-particle Group

There was one observed charged-particle group with branching ratio $0.031 \pm 0.008\%$ (relative to ^{14}Be β decay) and energy 2.9 ± 0.8 MeV. The fit shown in Fig. 5.17 clearly indicates that this group results from the β decay of a ^{14}Be daughter: ^{14}B , ^{13}B , or ^{12}B . Unfortunately, the half-life measurement (12 ± 10 ms) was not certain enough to distinguish this among the half-lives of the three daughters (13.8 ± 1.0 ms [Aj91], 17.36 ± 0.16 ms [Aj91], 20.20 ± 0.02 ms [Aj90], for ^{14}B , ^{13}B , and ^{12}B , respectively).

After referring to [Aj90, Aj91], we found that only ^{12}B has known β decay branches to a states above the threshold for a charged-particle decay. This nuclide has two β -decay branches [Aj90] to the 7654.20 ± 0.15 keV and 10300 ± 300 keV levels of ^{12}C (branching ratios $1.5 \pm 0.3\%$ and $0.08 \pm 0.02\%$, respectively). Since the width of the 10300 keV state is very large (3000 keV [Aj90]), it is possible that part of the distribution may be below threshold and not energetically available to contribute to the charged-particle emission. Assuming a Gaussian distribution (Eq. 3.25) with centroid at 10300 keV and width (FWHM) of 3000 keV, the weighted average of the remaining distribution (equal to about 99% of the total peak yield) above the α -emission threshold (7366.57 ± 0.04 keV) is 10340 MeV. The difference between this value and the centroid (40 keV) is an order of magnitude smaller than the error (300 keV [Aj90]) and can be ignored. Because the recoil of the ^8Be nucleus is large, it is necessary to include its energy, which is detected in coincidence with the emitted α particles. Thus, the total decay energy or Q-value must be calculated. Given the α threshold above, the α -particle Q-values are 2900 ± 300 keV and 287.63 ± 0.16 keV, respectively. Both of these decay modes lead to ^8Be , which is particle unstable against prompt 2α emission [Aj88]. Using the program STOPX we determined that α -particles have the longest range of all the

particles produced by the β -decay above. Even at the measured energy of the observed group (2.9 MeV) the mean range of α particles is only 3.8% of the thickness of an SSD. Thus, almost all of the emitted particles stop in the SSD from which the β decay originates. Since the recoiling ^8Be particle and three α particles (the one from the β -delayed α decay of ^{12}B and the two from the ^8Be break up) are emitted in coincidence, the energy signals of all four particles would be added together. Because the first excited state of ^8Be [Aj88] is about 10.41 MeV above the ground state of ^{12}C , which is higher in energy than the highest ^{12}C level populated by the β -decay of ^{12}B [Aj90], the α -particle break up of ^8Be must originate from the ground state with a decay energy of 91.84 ± 0.04 keV [Au93]. Adding this energy to that of the two decay modes discussed above yields total measured energies of 3000 ± 300 MeV and 379.47 ± 0.16 keV for the transitions with branching ratios $0.08 \pm 0.03\%$ and $1.5 \pm 0.3\%$, respectively.

Because it seems most likely that the observed charged-particle group is due to the β -delayed α decay of ^{12}B , the branching ratio of the observed charged-particle group **relative to ^{12}B β decay** is found by dividing the branching ratio relative to ^{14}Be ($0.031 \pm 0.008\%$) by the branching ratio for $2n$ emission ($5.9 \pm 3.2\%$ [systematic error] found in this thesis). The result is $0.5 \pm 0.3\%$. Unfortunately, the measured energy (2.9 ± 0.8 MeV) and the branching ratio ($0.5 \pm 0.3\%$) are not consistent within mutual errors with either of the two decay modes mentioned above. The transition with energy 3000 keV is closer to the measured energy (2.9 MeV), but the other transition with branching ratio 1.5% is closer to the measured branching ratio (0.5%). Even so it seems that it is unlikely that the energy calibration could be off by an order of magnitude. The determination of the branching ratio has a large systematic uncertainty, because the statistics in the branching ratio determination were poor and it was very difficult to separate the interference from the tail of the β peak. In fact, the measured branching ratio ($0.5 \pm 0.3\%$) and that corresponding to the α decay from

the 10300 keV ^8Be level ($0.08 \pm 0.03\%$) do not disagree that badly when their mutual uncertainties are considered. The measured width of the group (Sec. 5.5.4, 800 ± 200 keV) also does not agree with the width of the 10300 keV level (3000 keV). On the other hand, it is difficult to determine the correct shape of the peak due to the interference from the β peak, which would prevent the observation of the lowest energy α particles. Moreover, if the observed group corresponded to the other possible α transition (at 379.47 ± 0.16 keV) this would place the centroid of the group at channel number 44 (Eq. 5.10), which would be extremely difficult to observe due to the very strong β peak (see Fig. 5.16a). Moreover, in Sec. 5.5.5 we found that (relative to ^{14}Be β decay) the branching ratio of ^{12}B corresponding to the ^{12}Be impurity was 0.08% and that corresponding to the charged-particle data was $0.031 \pm 0.008\%$. Because the branching ratio corresponding to the daughter of the ^{12}Be impurity is so small compared the other components in the fit of Fig. 5.1, its systematic uncertainty could be very large and was difficult to determine. Since ^{12}B ions resulting from either the ^{12}Be impurity or the β decay of ^{14}Be would be indistinguishable from one another, we cannot estimate how much of the charged-particle group is due to an impurity in the beam. This is not important for the present work, because based on the facts presented above, we believe that this branch corresponds to an already known daughter decay and not to $0n$ emission.

6.6 Discussion of Zero Neutron Emission

Now we turn our attention to β decay not resulting in the emission of delayed neutrons. This ^{14}Be β -decay branch must either decay to ^{14}B levels below the $1n$ threshold (0.97 ± 0.02 MeV [Au93]) or to final states that, for some reason, decay only by charged particle or γ -ray emission. Since there was not an independent means of determining the $0n$ multiplicity, the value calculated from the data presented here can only be found by subtracting the total neutron branching ratio ($88 \pm 2 \pm_{31}^4\%$, the sum

of the $1n$ and $2n$ branching ratios) from 100%, resulting in a $0n$ branching ratio of $12 \pm 2 \pm {}^3_4\%$. Because the systematic error in this value is so large, we adopt the accepted value, which was that measured by Dufour *et al.* [Du88], $14 \pm 3\%$.

According to Ref. [Aj91] the only known level in ${}^{14}\text{B}$ below the single-neutron threshold is the 1^- level at 0.74 ± 0.04 MeV [Aj91]. Before proceeding further, we should determine if there were enough statistics to see this possible γ -ray decay. We shall assume, for the sake of argument, that all of the β decay strength is to this state (with a branching ratio equal to $14 \pm 3\%$). The number of detected γ -rays for this supposed state is found from the product of the total number of β decays, the branching ratio above, the geometrical efficiency of the Ge detector, the corresponding intrinsic detection efficiency, and the live time for the data run. From figures 3.13 and 5.12 the γ -ray detection efficiency for the NSCL and RIKEN experiments were $16.1 \pm 1.6\%$ and $7.3 \pm 1.4\%$, respectively. The other necessary values have already been given in the previous section. The predicted yields for this hypothetical 0.74 MeV γ -ray peak are 2000 ± 600 (NSCL) and 700 ± 200 (RIKEN). Even for the RIKEN experiment this is about a factor of 4.7 higher than the yield of the 3680 keV γ -ray peak shown in Fig. 5.11 (150 ± 20), and would be easily observable. Thus, if such a state had existed, we should have seen it but did not. It is possible that there is an unknown level in ${}^{14}\text{B}$ corresponding to a low energy γ -ray (below about 0.2 MeV) that cannot be seen due to absorption in the material surrounding the detector, and the large Compton background.

For an energy range of 0.01 to 10 MeV and daughter Z from 6 to 95, Gove and Martin [Go71] have tabulated the ratio $\log_{10}(f_1^-/f_0^-)$ where f_0^- and f_1^- are the phase space factors of allowed and unique first-forbidden β^- transitions, respectively. Here, $Z = 5$, and, assuming a ${}^{14}\text{Be}$ ground state β decay, the transition energy is 16.22 ± 0.11 MeV [Au93]. Although the tables do not include $Z = 5$, they

were rather insensitive to Z for energies above a few MeV. It was also necessary to extrapolate the tabulation to 16.22 MeV. For $Z = 6$ and energies above 3 MeV, Fig. 6.2a shows an extrapolation to 17 MeV of the tabulated points from Ref. [Go71]. The following empirical function was used:

$$y = a + b \cdot \log(x) + c \cdot [\log(x)]^2, \quad (6.1)$$

where y is the ratio $\log_{10}(f_1^-/f_0^-)$, x is the β -decay energy in MeV, and a , b , and c are constants that were determined to be 0.5529, 1.742, and 0.08563, respectively. A function in the form of Eq. 6.1 was chosen, because it fit the points very well including a fit (Fig. 6.2b) over the entire energy range (0.1–10 MeV). The value of $\log_{10}(f_1^-/f_0^-)$ at 16.22 ± 0.11 MeV obtained from Fig. 6.2a was 2.79 ± 0.21 . The systematic error in this value was obtained from the fit of Fig. 6.2b, and several other fits including a quadratic and linear fit of the highest energy data points of Fig. 6.2a. Using this ratio, the $\log(f_1^- t)$ can be found from:

$$\log\left(f_0^- t \cdot \frac{f_1^-}{f_0^-}\right) = \log(f_0^- t) + \log\left(\frac{f_1^-}{f_0^-}\right), \quad (6.2)$$

where $\log(f_0^- t)$ is that for allowed decay, the same that was calculated in Sec. 3.3.1. The $\log(f_0^- t)$ corresponding to a decay energy of 16.22 ± 0.11 MeV is 4.6 ± 0.3 , and the resulting $\log(f_1^- t) = 7.4 \pm 0.3$. Even if it is assumed that this β decay branch decays to a state just below the $1n$ threshold (0.97 ± 0.02 MeV [Au93]) the result does not change to within two significant digits. The above result presents a problem, because this decay strength is considerably higher than most non-unique first-forbidden transitions, which have a $\log(f_1 t)$ (β^- or β^+ decay) in the range from about 9–11.5 [To71].

A further complication arises because of the 1^- ^{14}B level below the $1n$ threshold. A transition from the 0^+ ^{14}Be ground state to this level would correspond to a non-unique first-forbidden transition and would be expected to be more probable than the $0^+ \rightarrow 2^-$ transition, because non-unique transitions

typically have a lower $\log f_{1t}$ in the range of 6–9 [Ma69], and the energy difference is small. This brings up the question if the ground state spin of ^{14}B has been misidentified, for a ground state of 1^- or 0^- would explain the discrepancy. The original paper that assigns the spin/parity of the 2^- state [Al74] is quoted in Ref. [Aj91]. In Ref. [Al74], this assignment is based on the fact that the corresponding β transition decays to a well established 6.73 MeV 3^- level in ^{14}C

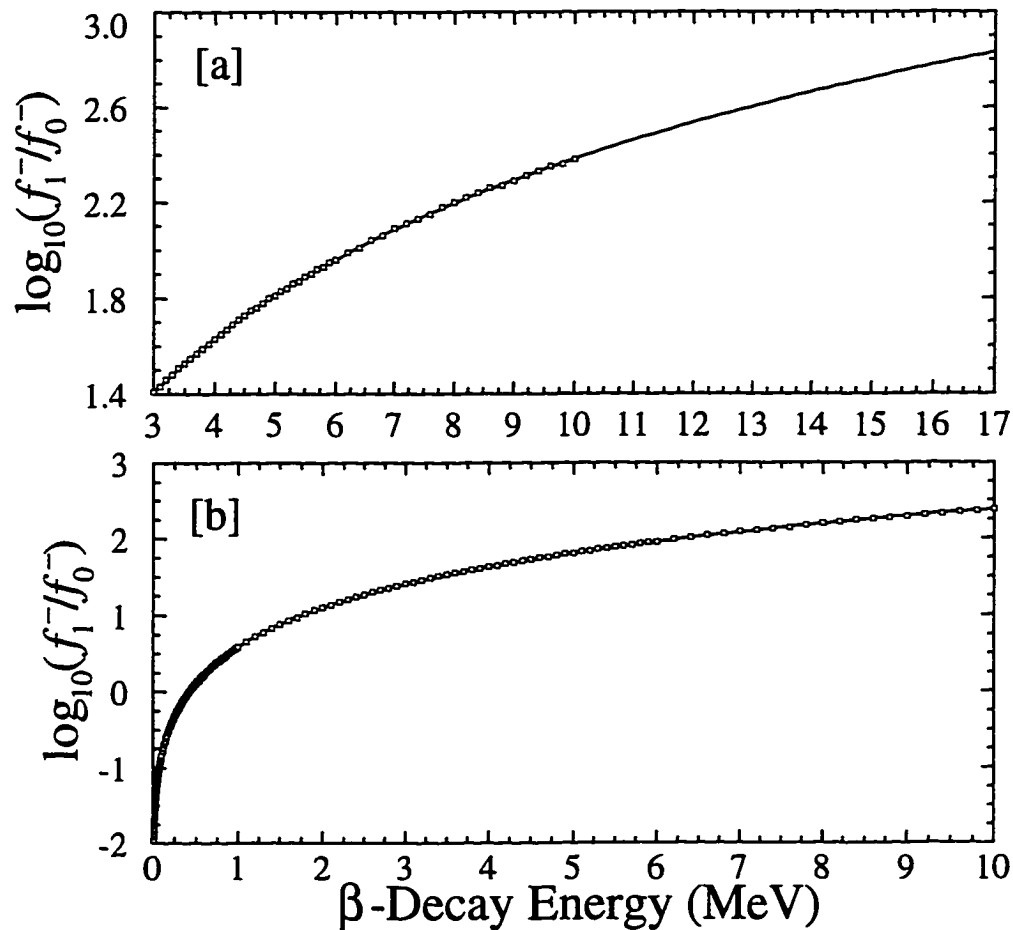


Figure 6.2 (a) For daughter $Z = 6$, an extrapolation of the tabulated values of $\log_{10}(f_1^-/f_0^-)$ obtained from Ref. [Go71] versus β decay energy using the function given in Eq. 6.1 (see text). (b) A fit to the same values as Fig. 6.2a for the entire energy range given in [Go71], again using Eq. 6.1.

[Al74] with branching ratio of $8.6 \pm_{4.0}^{1.7}\%$ [Al74] and $\log ft = 5.10 \pm_{0.08}^{0.30}$ [Al74]. Both of these measurements imply an allowed decay that would exclude the possibility of assigning a spin/parity of 1^- or 0^- to the ground state of ^{14}B . Unfortunately, the energy and intensity of the corresponding γ -ray was measured with sodium iodide (NaI) detectors, which have poor energy resolution. Moreover, the observed group is a small shoulder lying next to a much stronger peak (see Fig. 6.3), which appears difficult to measure. Finally, there were strong impurity decays in the data that were eliminated by putting a gate on the β -decay energy, but one can think that accidental coincidences might allow some "leakage" through this gate. No measurements of the state have been made since Ref. [Al74]. That reference also mentions that as much as half of the β -decay strength corresponding to the transition from the ground state of ^{14}B to the 6.73 MeV level in ^{14}C could be accounted for by a cascade decay from the 7.34 MeV level, which is populated by a β decay transition with branching ratio $<11\%$ [Al74]. The corresponding γ -ray decay was not observed. Thus, there could be considerable doubt in the corresponding branching ratio and possibly the identity of this state. A re-measurement of the ^{14}B decay to check the 2^- ground state assignment (which agrees with model expectations) is clearly in order.

It is also possible that an unobserved β -delayed charged-particle transition could account for some the β -decay strength. We made an estimate of the upper limit on the branching ratio of such a state by adding a Gaussian distribution (Eq. 3.25) to the spectrum shown in Fig. 5.16. This figure shows a typical SSD energy spectrum after the cuts diagrammed in Fig. 5.15 were applied to reduce the interference of the tail of the β peak (see Sec. 5.5.2). The added Gaussian distribution simulates a hypothetical charged particle group, where it was assumed that the width of this "simulated peak" is the same fraction of the total energy as

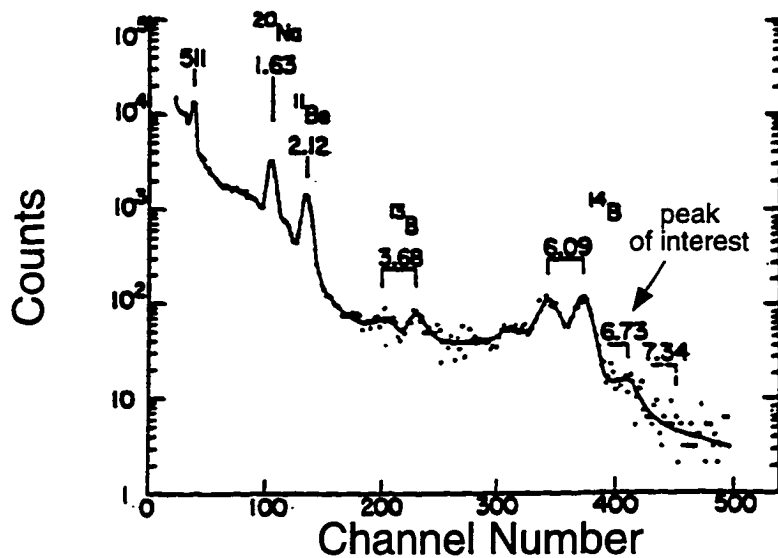


Figure 6.3 Plot obtained from Ref. [A174] showing measurement of 6.73 MeV γ -ray state ("peak of interest") that has established the spin/parity of the ^{14}B ground state (see text for details).

the observed charged-particle group. The width of the observed charged-particle group was 0.8 MeV and its energy was 2.9 MeV, which means that the width of the simulated peak should be about 0.28 times its energy. The limit is found by keeping the width constant and decreasing the height until the underlying peak can no longer be distinguished from the background. Then the branching ratio corresponding to this yield is calculated (see Sec. 5.5.5). An example of this is shown in Fig. 6.4, where a Gaussian peak having a width equal to 21 channels, a centroid at channel number 204 (corresponding to 2.1 MeV), and a height of 16 counts gives a yield of 350 counts. Given a β peak yield equal to $(1.0 \pm 0.2) \times 10^6$ (RIKEN), the minimum yields were divided by 0.6×10^6 to find the 2σ limit in the upper limit. The results of this calculation is shown in Fig. 6.5.

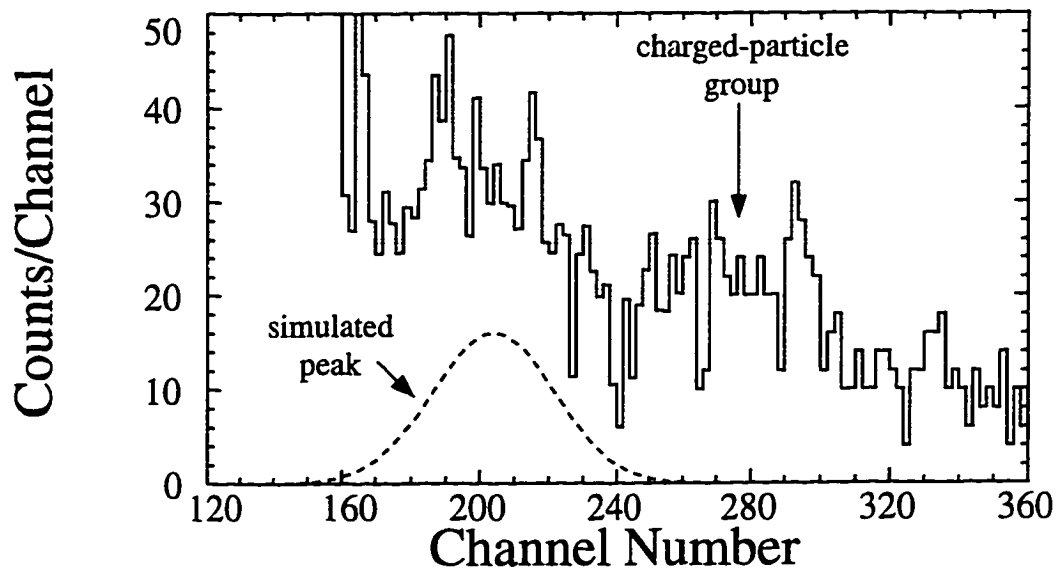


Figure 6.4 Plot showing an example of adding a Gaussian distribution "simulated peak" to determine the limit in the branching ratio of an unobserved charged-particle group. The one observed charged-particle group is shown above. Compare to Fig. 5.18.

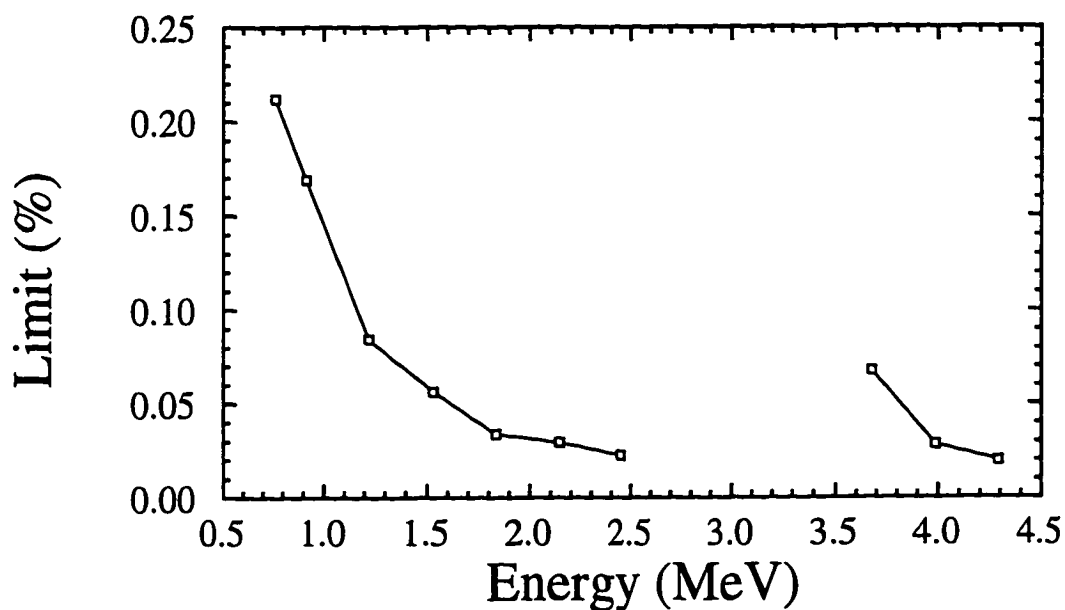


Figure 6.5 The 2σ upper limit in the branching ratio of an unobserved charged-particle group. The region from 4 to 6 MeV is excluded, because that is where the observed group is located. Energies below 1.3 MeV are also excluded, because the long tail of the β peak makes it increasingly difficult to determine the ratio.

6.7 Decay Scheme of ^{14}Be β decay

Figure 6.6 shows the revised level scheme for the β decay of ^{14}Be based on the information obtained from this thesis. All energies are given to the nearest 0.01 MeV. The energies and the spin/parities of previously known states (where uncertain assignments are enclosed in parentheses) were taken from the most recent compilation in Ref. [Aj91]. The two new levels established in this work are indicated by dashed lines with the level energies and spin/parities in boldface. We have determined that most of the β decay strength goes to a previously unobserved level in ^{14}B with energy 1.28 ± 0.02 MeV, spin/parity 1^+ , and a natural width of 60 ± 5 keV. The comparative half-life of this state ($\log ft = 3.70$) places it among the strongest allowed non-mirror Gamow-Teller transitions known. A much weaker higher-energy ^{14}B level (4.31 ± 0.09 MeV) has also been established in this thesis. We show the branching ratio and $\log ft$ values determined from the RIKEN experiment for two reasons: one, the lack of ambiguity due to the much reduced ^{11}Li contamination and, two, because even though the results of both experiments agree very well we chose the more conservative (larger) uncertainties of the two experiments. The $\log f_1 t$ value of the branch corresponding to $0n$ decay ($7.4 \pm_{0.4}^{0.3}$) has been determined from the best β decay branching ratio, which was measured by Dufour *et al.* [Du88]. Because of the evidence presented in Sec. 6.6 we have assigned the $0n$ decay mode to a ^{14}B ground state transition. This transition is much stronger than most non-unique first-forbidden decays. This, together with the non-observation of the expected β -decay branch to the (1^-) bound excited state brings up the interesting possibility that the ^{14}B ground state spin, though it agrees with both shell-model expectations and the sequence of negative-parity levels in ^{12}B , might have been misassigned.

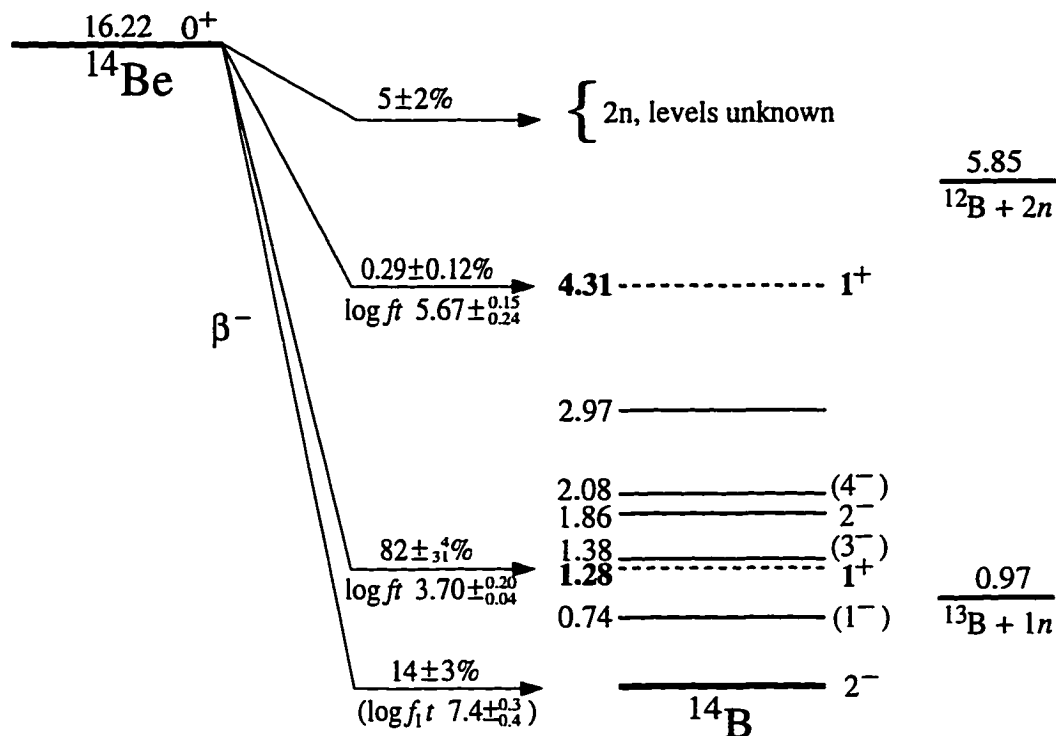


Figure 6.6 Decay scheme for the β^- decay of ^{14}Be . The numbers to the left of the parallel lines are the level energies for ^{14}B and the symbols to the right are the spin/parities. Numbers expressed as percentages are branching ratios determined from this work. The new ^{14}B levels established in this thesis are indicated by dashed lines and boldface type, and the other values were taken from Ref. [Aj91].

It is possible though unlikely that there are unobserved charged-particle transitions that would share the total β^- -decay strength, each with a higher $\log f_{1t}$. The one observed charged-particle group (see Sec. 6.5) could not have accounted for any of the $0n$ decay. Finally, we have adopted the best half-life measurement of ^{14}Be 4.36 ± 0.13 ms, determined from the β - n coincidence data of the RIKEN experiment.

6.8 Comparison to Shell-model Calculation

Figure 1.8 shows a shell-model calculation by Curtin and Brown where most of the β transition strength (98%) decays to a state that is 0.94 MeV above the

ground state of ^{14}B . A much weaker β decay transition (0.5%) is predicted to the 4.69 MeV level of ^{14}B . The present results agree rather well with this calculation. We have confirmed the prediction of a 1^+ low lying state in ^{14}B that receives most of the β decay strength (branching ratio 82%), with a predicted $\log ft$ of about 3.8 compared with the measured value of 3.7. The most significant difference between our measurements and the calculation was that this low-lying state is above the $1n$ threshold instead of just below it, but according to Ref. [Br96] the difference is well within the uncertainty of the calculation. The neutron group at 3.10 MeV would correspond quite well to a transition to a predicted 1^+ state at about 4.7 MeV with a calculated branching ratio of 0.5% and $\log ft$ value of 5.5.

A new calculation [Br96] was recently performed using the Millener and Kurath (MK) interaction [Mi75]. In this calculation, the final level energy was required to be that measured in this thesis (1.28 MeV), resulting in a branching ratio of 99% for this state and a transition to a higher energy level at 6.80 MeV with branching ratio 0.64% (excluding much weaker predicted transitions with branching ratios less than 0.16%). A similar calculation using the most recent WBT (Warburton and Brown, [Wa92]) interaction resulted in a 95.0% branching ratio for the transition to the 1.28 MeV level, and four other significant transitions to the 4.28 MeV, 6.29 MeV, 8.53 MeV, and 9.38 MeV levels with branching ratios 1.08%, 0.66%, 0.40%, and 0.38%, respectively (excluding weaker transitions with branching ratios less than 0.3%). The predicted transitions to the 1.28 MeV and 4.28 MeV level agree better than those of MK-interaction with the measurements presented in this thesis.

6.9 Comparison of Experimental Methods

In this section, we shall briefly compare the different experimental methods used for the two experiments and point out the advantages and disadvantages of each. While the measurements of coincident γ -rays were very similar between the

two experiments, both used high purity Ge detectors, the implantation of ^{14}Be ions, the start for the acquisition system, and the method of detecting neutrons differed.

6.9.1 Neutron detectors

In both experiments, the neutrons were detected in plastic scintillator bars. In the NSCL experiment the bars were curved to provide a uniform flight path, and in the RIKEN experiment they were flat and stacked in the form of a wall. The geometry of the NSCL experiment simplifies the data analysis, because no correction for flight path has to be performed, and thus the systematic error introduced by this route is eliminated. The detector array used in the RIKEN requires a flight path correction, but it is easier to build (compare figures 2.2 and 4.7), has thicker bars and, therefore, higher neutron efficiency. It also has additional advantage that the neutron walls are movable so that the flight path can be adjusted. For example, in a previous experiment [Ra96] using the same detector array as the RIKEN experiment, the β -delayed neutron decay of ^{19}C was measured with a flight path of 125 cm as opposed to 200 cm for the RIKEN experiment. This shorter flight path means that, while the flight path correction is larger and the neutron energy resolution is poorer, the geometrical efficiencies of the detectors are larger. The best flight path is a compromise between the two. The NSCL neutron detector array affords less systematic error in the determination of flight path, but the RIKEN neutron array is more flexible has higher efficiency.

6.9.2 Implantation and start detectors

The detectors in which ^{14}Be ions were stopped (implantation detector) in the two experiments were different. In the NSCL experiment, a plastic scintillator served as both the implantation detector and as the start detector. To maximize the start detection efficiency, it was necessary to calculate the amount of absorbing material

required so that the ^{14}Be ions would stop in the center of the implantation detector. Because the beam was stopped in a stack of five silicon surface-barrier detectors in the RIKEN experiment, the relative amount of ^{14}Be stopped in each detector and the amount of absorbing material could be determined on-line; thus, a range calculation was not necessary, making the RIKEN method superior. The start of the acquisition system for both experiments came from plastic scintillators giving similar results.

6.9.3 On-line monitoring of impurities

Different detectors were used to monitor, on-line, the relative amount of impurities. The energy signals of silicon surface-barrier detectors were used in the NSCL experiment; in the RIKEN experiment, the energy signals of the plastic scintillators were used. The silicon surface-barrier detectors yielded more cleanly separated energy groups (compare figures 2.4 and 2.5 to figures 4.5 and 4.6), making it easier to determine the relative amount of impurities. Even so, we found that the impurities were small for both experiments; thus, this did not make a significant difference in the analysis of the raw decay curve.

6.9.4 Other detectors present in the RIKEN experiment

There were two things that could be accomplished in the RIKEN experiment that could not be done in the other work: the measurement of charged-particle data and the ability to veto events corresponding to the prompt β -particles. We found that, for low energy neutron groups, (example, the observed 287 keV neutron group) applying the β veto was unnecessary, because these groups are well separated from the prompt β peak. Actually, it is possible that the veto detectors could worsen the neutron energy resolution due to scattering within these detectors. Therefore, it would not be advantageous to use these detectors in the case where the neutron groups of interest lie far from the prompt peak.

6.10 Future Work

Now that these two experiments has been presented, we shall discuss what future work is necessary to improve these results. The two most important experimental problems that need to be addressed are better coincidence information and a more accurate determination of neutron detection efficiency.

6.10.1 Gamma-neutron coincidence

The assignment of the level energies, decay modes, etc. can be made more reliable with better coincidence data. For example, it was argued that the 287 keV neutron group most likely resulted from a neutron decay to the ground state of ^{13}B , but decay to an excited ^{13}B level resulting in an emitted γ -ray (at 3.681 MeV) is not ruled out. Coincidence information would distinguish the two decays, but unfortunately there were insufficient statistics in either experiment to do this.

The coincidence statistics could be increased by a combination of increased geometrical efficiency, detection efficiency, and number of implanted ^{14}Be ions. In Sec. 6.2, we calculated that, with the geometrical and detection efficiencies of the RIKEN experiment, we should expect to see 0.37 γ -ray events coincident with the 287 keV neutron group. Let us assume that 100 γ -ray counts (a nice round number) would be required to see the coincidence easily. Thus we need to increase the product of the following by a factor of about 270:

$$\epsilon_{\text{geo}_n} * \epsilon_{\text{geo}_\gamma} * \epsilon_{\text{det}_n} * \epsilon_{\text{det}_\gamma} * (\text{total beam}), \quad (6.3)$$

where ϵ_{geo_n} and $\epsilon_{\text{geo}_\gamma}$ are the geometrical efficiencies of the neutron and γ -ray detectors, respectively, ϵ_{det_n} and $\epsilon_{\text{det}_\gamma}$ are the corresponding intrinsic detection efficiencies, and "total beam" represents the total number of ^{14}Be ions implanted.

One way to increase the implanted beam would be to decrease the beam-off period, but this not desirable, because it would be more difficult to fit the raw activity

spectrum. Let us say that doubling the beam time for the RIKEN experiment (for a total of two weeks) is a reasonable upper limit. It is very difficult to produce intense radioactive beams, especially for a nuclide as far from stability as ^{14}Be . Let us conservatively estimate that the ^{14}Be beam intensity could be doubled. Thus this combination would give an increase of a factor four in "total beam".

In the RIKEN experiment, it is doubtful that the neutron detection efficiency could be raised appreciably, because the threshold is so low (see Sec. 4.6.2). Thus, we shall assume that the neutron detection efficiency cannot be increased. The detection efficiencies of high purity Ge γ detectors is very low at energies as high as 3.68 MeV. Because our estimate of detection efficiencies given here are very rough approximations, it is difficult to tell if the difference in the detection efficiency in the two experiments is real or due to systematic error. Therefore, let us assume that we cannot raise the intrinsic efficiency of the γ -ray detector. Other detectors with much higher detection efficiencies could be used, such as bismuth germanate (BGO) and sodium iodide (NaI) scintillators. While the detection efficiencies of these types of detectors are much higher, the gain in efficiency might be negated by the loss of energy resolution that would greatly broaden the peaks, making the coincidence peaks much harder to see above the background.

Thus, there remains a factor of 67.5 that would have to be obtained by increasing the geometrical efficiencies of the detectors. The geometrical efficiency of the neutron detector arrays were 14.2% (NSCL) and 4.61% (RIKEN). With the addition of just three more neutron detectors in the NSCL experiment, the geometrical efficiency could be a factor of 3.70 higher than that of the RIKEN experiment. Although the low energy neutron group was not observed in the NSCL experiment, Fig. 5.7 shows that a flight path half of that used in the RIKEN experiment (1 m) would still yield more than sufficient neutron energy resolution

to measure this group. The geometrical efficiencies of the high purity Ge detector for the NSCL and RIKEN experiments were 4.6% and 1.14%, respectively. Four such detectors at a total distance of 76 mm (7 mm closer than in the NSCL experiment) would result in a gain of 18.5 in geometrical efficiency compared to the RIKEN experiment. The total combined gain in coincidence statistics would be 68.5, greater than the required factor of 67.5. To sum up, by using the NSCL detector array with three additional neutron detectors and with threshold equal to that used in the RIKEN experiment, four γ -ray detectors similar to the ones used in the NSCL experiment, twice the running time, and twice the beam intensity, one would probably have sufficient statistics to see the coincidence between the 287 keV neutron group and the 3.680 MeV γ -ray group if it were present. Many other scenarios could be devised, but the one above demonstrates that reasonable improvements in the set up would allow one to see such a coincidence. Unfortunately, it would be very difficult to see a coincidence with the other neutron group at 3.70 MeV, considering that even though the detection efficiency is 1.7 times higher at this energy, the yield of this group is 178 times smaller. Thus, the coincidence statistics would be 105 times less.

6.10.2 Neutron-neutron coincidence

Neutron-neutron coincidence data could also yield important information. For example, if the 3.70 MeV neutron group was coincident with the one at 0.287 MeV then that would show that the 3.70 MeV group is due to sequential single-neutron emission and that the 0.287 MeV neutron group cannot correspond to a ^{13}B ground state transition. The only additional information we need to determine if a n - n coincidence is possible is the detection efficiencies determined in the RIKEN experiment for the 3.10 MeV and 3.70 MeV groups (64% and 63%, respectively). Using a procedure similar to what was done in Sec. 6.2 for γ - n

coincidence we find that, given the low energy neutron yield of 66000, we should expect to see 36 counts in coincidence with either the 3.10 or 3.70 MeV group. This would be rather small to discern considering the background (see Fig. 5.8) but would not require much increase in statistics to observe. Given that the yields of high energy groups are a factor of 180 less than that of the low energy group, we find that, with the RIKEN set up, one should expect about 0.3 counts in either peak in coincidence with the other. This is comparable to what we obtained for γ - n coincidence (0.37 counts). Thus, with the same arguments used in that case, perhaps one could see a coincidence with the low energy neutron peak. None was seen in the RIKEN experiment with an improved setup.

6.10.3 Neutron detection efficiencies

The next question to address is how to obtain a more accurate determination of neutron detection efficiency. The first thing that could be done is to impose a constant threshold in all energy signals of the neutron detectors in the off-line analysis. This was not possible in the RIKEN experiment, because the energy signals were attenuated (see Appendix C.4). Consequently, they were too weak for a reliable threshold to be imposed that was low enough to get a more accurate determination of the detection efficiency of the 287 keV neutron group. Perhaps redoing the experiment with unattenuated the energy signals would allow a low enough threshold to get more accurate results.

Another thing that could be done in the RIKEN experiment is to lower the threshold of the start detectors so that the efficiency correction for these detectors (Sec. 4.6.2) would be less (but without triggering on excessive noise). While both of these things would lower the systematic uncertainty in the neutron detection efficiency, the largest source of error was in the use of the Monte Carlo code (KSUEFF).

According to Ref. [Ce79], the code agrees with available data to within 10% for neutron energies between 1 MeV to about 300 MeV and for thresholds of 0.1 MeV to above 22 MeV electron-equivalent energy. The main reasons why the code is unreliable below these limits is (1) the lack of available data on elastic scattering cross-section measurements of hydrogen and, especially, (2) the lack of information on the light output of scintillators for low energy protons. This information would improve calculations of the conversion of neutron energy to electron-equivalent energy for low energy neutrons. Also Ref. [Ce79] advises that improvements in the exact pulse height distribution would be necessary to make the calculation reliable below about twice the threshold. (In the RIKEN experiment the low energy neutron group was at 0.287 MeV and the threshold was 0.186 MeV *neutron* energy.) Because of this we have not relied on an **absolute** detection efficiency calculation at 0.287 MeV. What we have done is used the calculation to reproduce the shape of the detection efficiency curve and varied the threshold to match this curve to the data to extrapolate it to 0.287 MeV. Obviously, an absolute efficiency determination would be far more accurate and would require the above improvements to the code.

6.10.4 Other improvements

There are other things that would improve the set up. First, a renewed search for charged-particle decay is necessary to clarify the unusually high $\log f_{\beta} t$ value measured in this work (7.4). It is possible that the 0ν decay corresponds to several yet unobserved charged-particle transitions, each of which would share some of the transition strength. We need to improve the measurement of such transitions. Second, we have shown that to measure low energy neutrons (the 287 keV group, for example), the application of the β veto was unnecessary and removing the veto detectors might increase the energy resolution by reducing

neutron scattering. Third, the noise present in the time-of-flight spectra (Fig. 5.7) needs to be greatly reduced, because it was very troublesome for the measurement of high energy neutrons and for the determination of $2n$ multiplicity. Last, reducing the rate dependent dead time would decrease the systematic uncertainty in the fit of the raw activity spectrum. This could be reduced by decreasing the beam intensity, but then the run time would need to be increased. It would be far better to use a faster acquisition computer, faster electronics, and perhaps a less complicated set up with fewer detectors so that the rate dependent dead time could be reduced.

6.10.5 Future developments

The author is aware of another experiment performed at RIKEN [Ao96] in June 1995 that was designed for improved measurements of the β -delayed neutron decay of ^{14}Be . The most important difference between that experiment and the one presented here, is that electron energies have been measured directly to distinguish electrons corresponding to $1n$ and $0n$ decay (which have end point energies that differ by 1.28 MeV). In this experiment, the ^{14}Be ions were implanted into a 1 mm thick Si detector, and two thin plastic scintillators, one upstream and one downstream, served as the start for the acquisition system. The β decay energy was measured by placing thick plastic scintillators behind the start detectors.

The neutrons were measured with a new detector array [Yo96], designed for low energies. The scintillator bars (30.0 cm long by 4.5 cm wide by 2.5 cm deep) of this detector were made shorter than the second experiment of this thesis to minimize the absorption of light. Because of its smaller size, a shorter flight path of 50 cm was necessary to maintain the same solid angle. The detectors were also made thinner to maintain sufficient timing resolution. With these improvements, the threshold could

be set at 2 keV equivalent electron energy (a few tens of keV neutron energy), which was calibrated with low energy X-rays from ^{133}Ba and ^{241}Am sources.

Thus, the direct measurement of β decay energies would remove the ambiguity in determining the branching ratios introduced by using the Monte Carlo code to calculate neutron detection efficiency. This very low threshold reduces the systematic error in the efficiency determination of the low energy neutron group by making the detection efficiency a much less rapidly changing function at 287 keV. In fact, Ref. [Yo96] mentions that 80 keV neutrons from ^{11}Li (also measured in Ref. [Ao96]) were detected with this array.

At the time of this writing, the data analysis is continuing. Preliminary results given in Ref. [Ao96] report an energy of 288 ± 6 keV and branching ratio of $73 \pm 15\%$ for the low energy neutron group. These are in good agreement with the corresponding results obtained in this thesis.

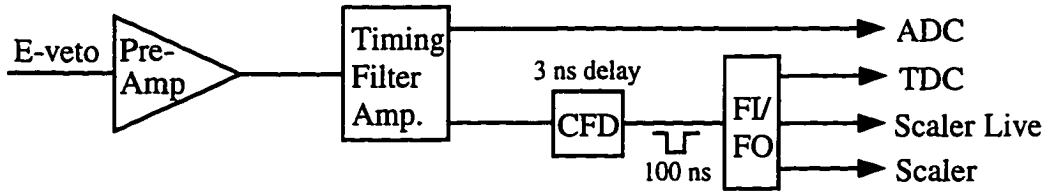
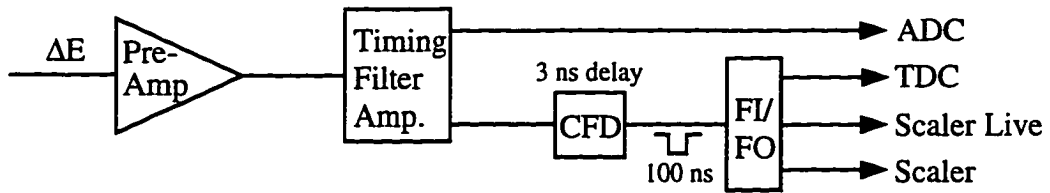
6.11 Conclusion

In conclusion, we have shown that the ^{14}Be half-life determined in this thesis agrees very well that measured by Dufour *et al.* [Du88] and has a smaller error. Most of the β transition strength corresponds to a low energy neutron group at 287 keV. We lack sufficient statistics to perform γ -n and n-n coincidence, and the observed charged-particle decay most likely corresponds to an already known daughter decay mode. It has been demonstrated that γ and n coincidence experiments with the neutron group at 287 keV are certainly possible in a future experiment with reasonable experimental constraints, while that with the much weaker group at 3.10 MeV is not. The unusually strong unique first-forbidden β -decay transition strength to the ^{14}B ground state might be shared among several unobserved states, the limits of which have been given in Fig. 6.5. It appears that

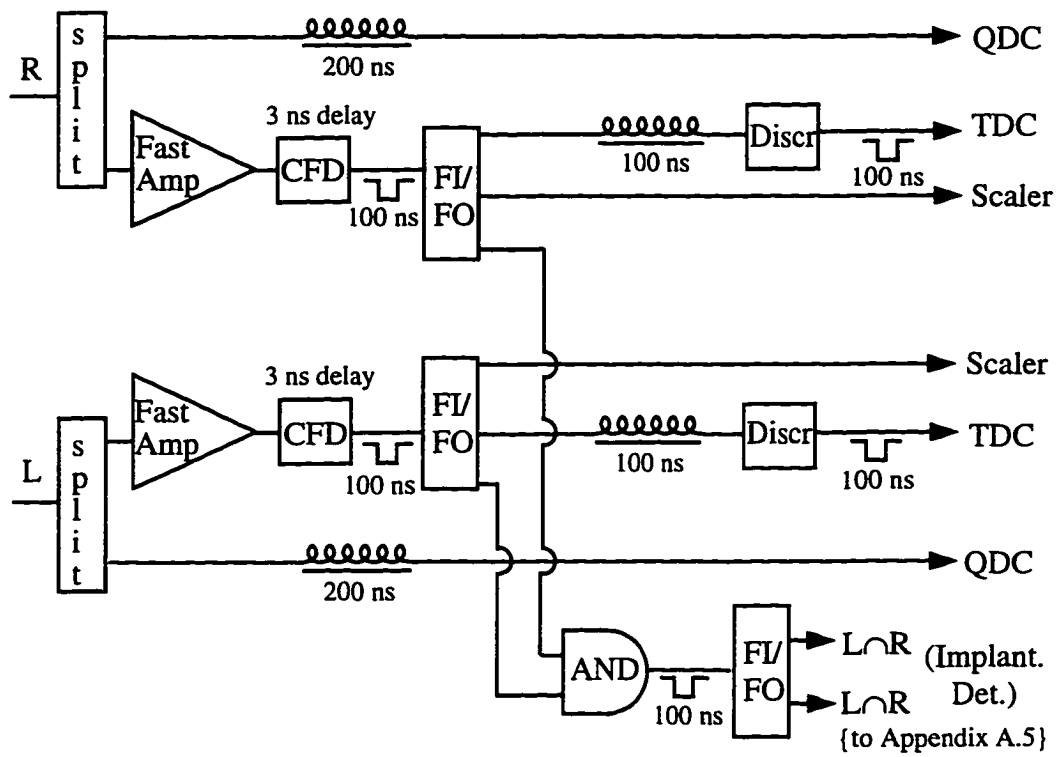
the WBT shell-model calculation gives the best prediction of the ^{14}Be β decay to 1^+ states in ^{14}B , correctly predicting that a large portion of the β decay strength goes to low-lying states. Because there is still some disagreement between the prediction and the measurements presented here, more work needs to be done in this area. There also seems to be some doubt about the spin/parity assignment of 2^- to the ground state of ^{14}Be (Sec. 6.6). Because the measurement that established that assignment was done with NaI detectors, perhaps newer measurements with high purity Ge detectors might clarify this and help explain the unusually high $\log f_1 t$ value measured for $0n$ emission. Of course, one must determine if the detection efficiency at 6.73 MeV is sufficient for such a measurement. Lastly, we expect that additional experiments including the one performed at RIKEN in June 1995, will yield improved results and shed more light on the β -delayed neutron decay of ^{14}Be .

APPENDIX A
ELECTRONICS DIAGRAMS FOR THE NSCL EXPERIMENT

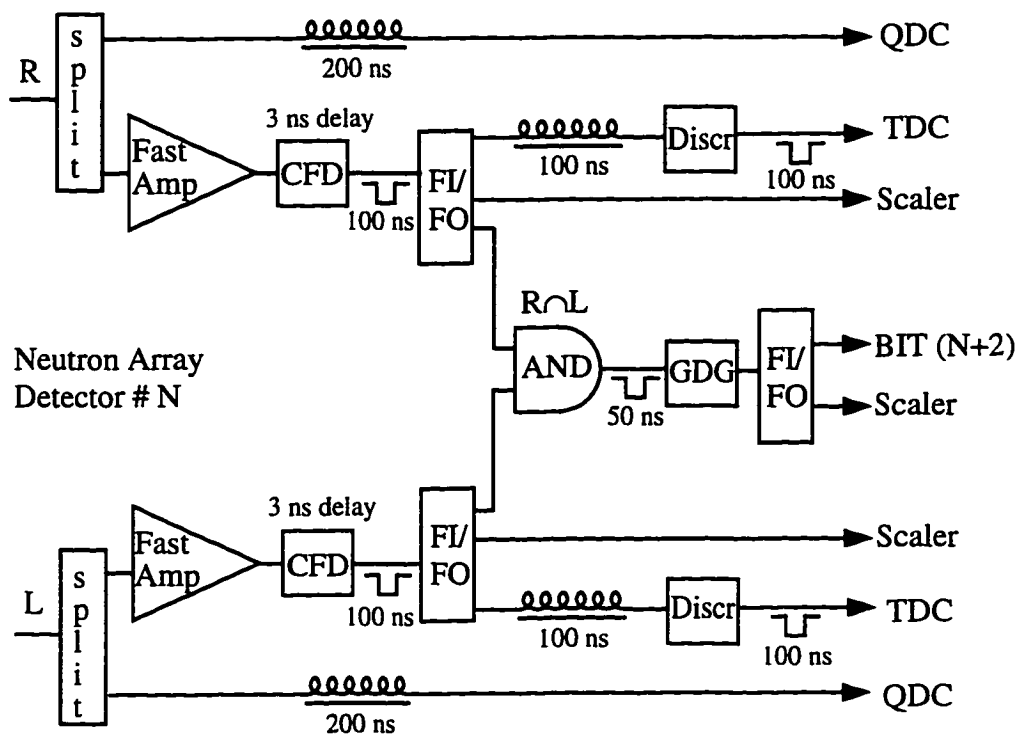
A.1 DIAGRAMS FOR E AND ΔE DETECTORS



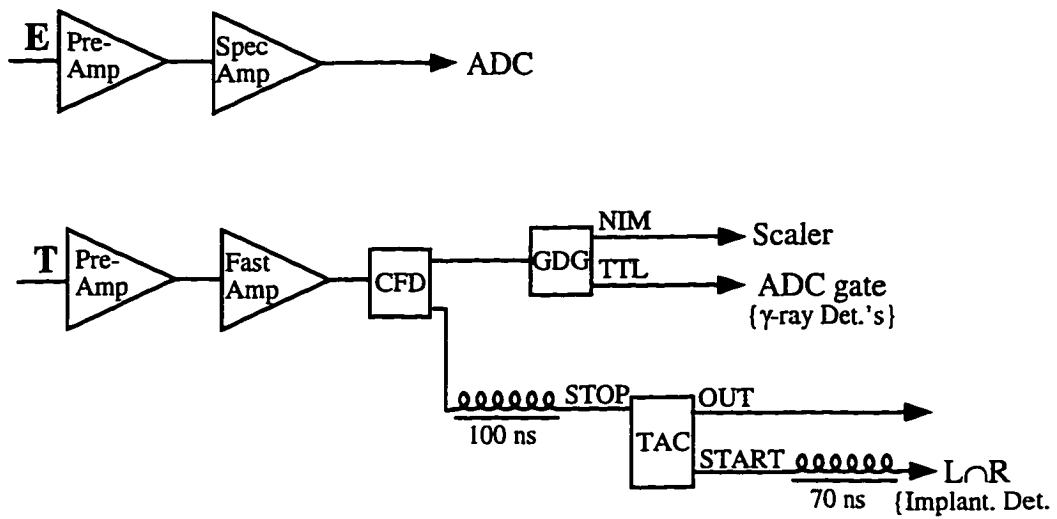
A.2 DIAGRAM OF IMPLANTATION DETECTOR ELECTRONICS



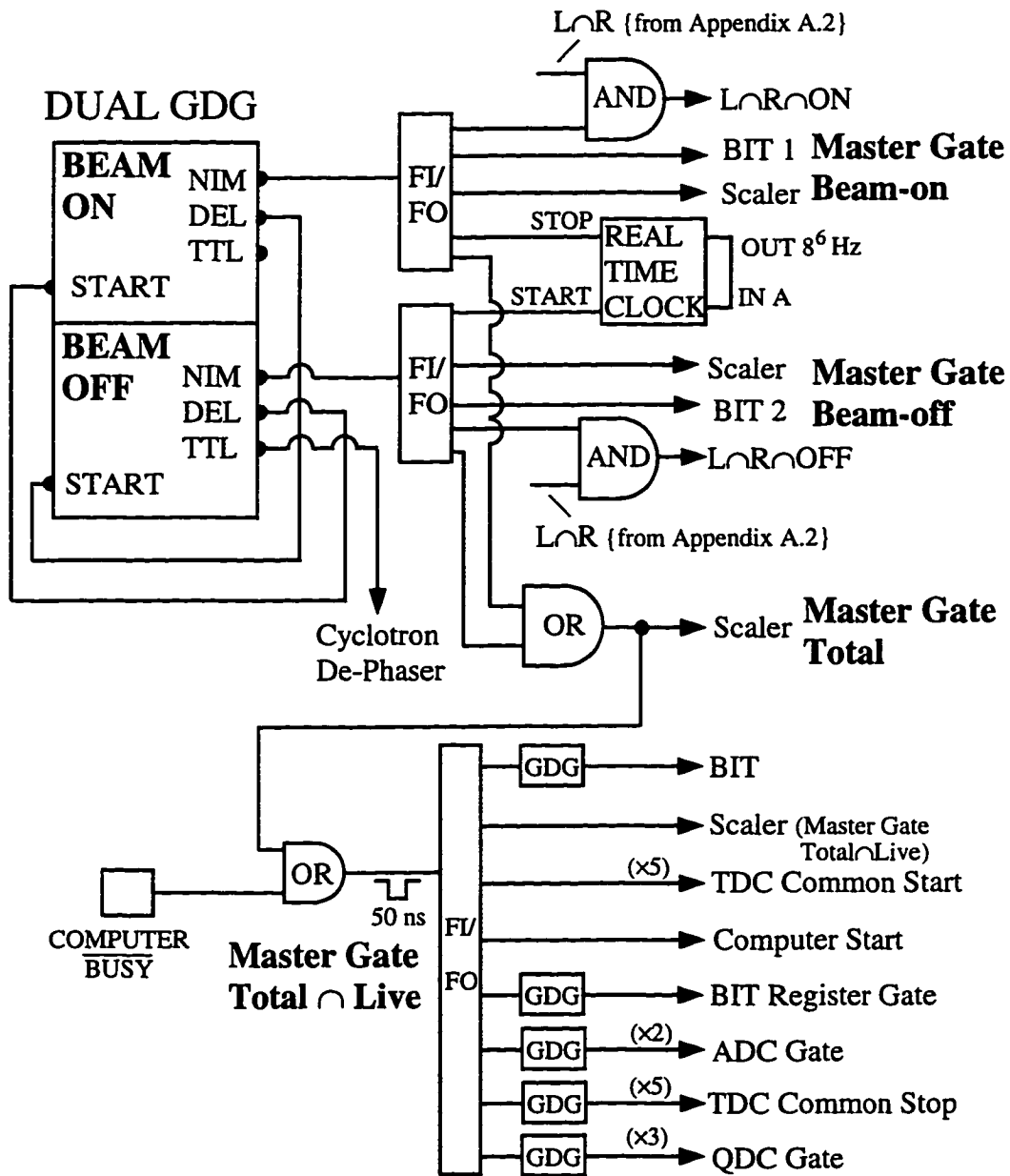
A.3 DIAGRAM FOR NEUTRON ARRAY DETECTORS



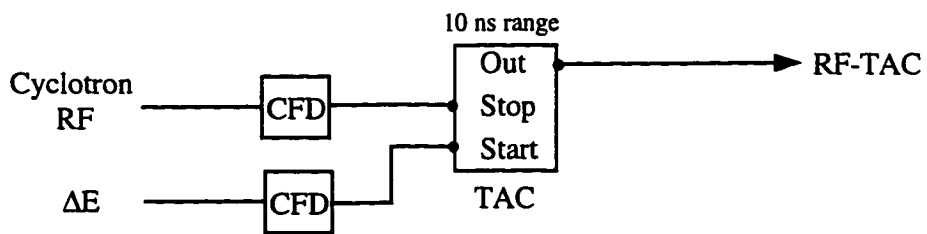
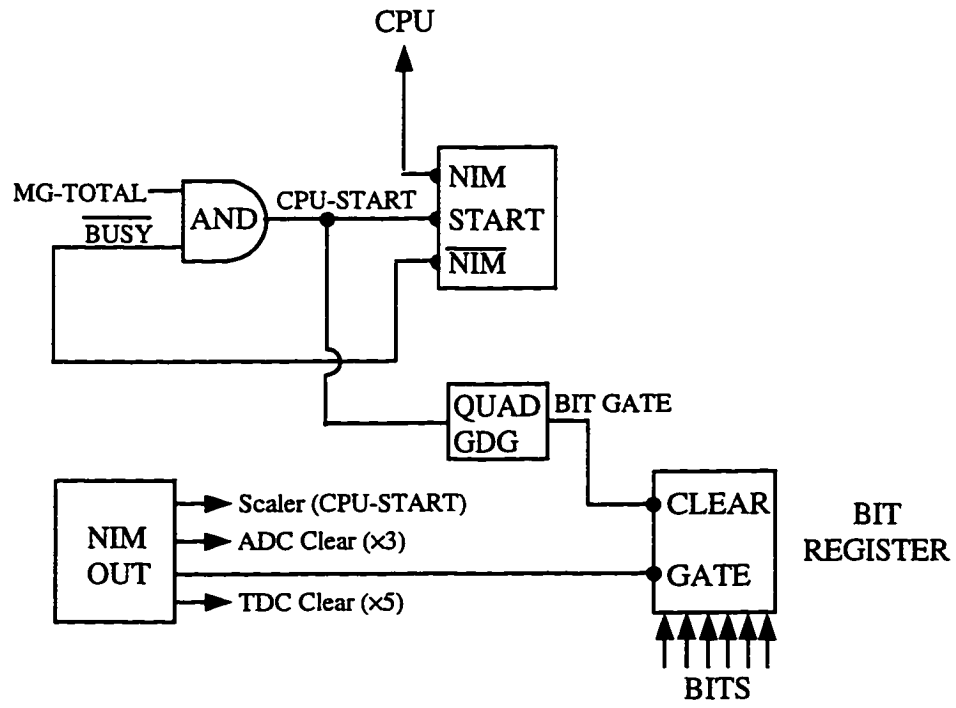
A.4 DIAGRAM FOR HP-Ge γ -RAY DETECTOR



A.5 DIAGRAM FOR ELECTRONICS ASSOCIATED WITH THE MASTER GATE



A.6 DIAGRAM OF ELECTRONICS ASSOCIATED WITH THE CPU AND THE CYCLOTRON-RF



A.7 DEFINITION OF TERMS AND SYMBOLS USED IN APPENDIX A

<u>ooooo</u>	– delay
┌┐	– pulse width
(x#)	– repeated # number of times
ADC	– analog to digital converter
CFD	– constant fraction discriminator
DEL	– delayed output
Discr	– discriminator
E	– energy
Fast Amp	– fast timing amplifier
FI/FO	– fan in/fan out
GDG	– gate and delay generator
Implant. Det.	– impantation detector
L	– left
MG	– master gate
NIM	– Nuclear Instrument Module output
QDC	– charge to digital output
R	– right
RF	– radio frequency
Spec Amp	– spectroscopy amplifier
Split	– splitter
T	– time
TAC	– time to amplitude converter
TDC	– time to digital converter

APPENDIX B REFERENCES FOR γ -RAY SOURCES

[⁶⁰Co]: P. Anderson, L. P. Ekström, and J. Lyttkens, Nucl. Data Sheets, **48**, 251 (1986).

[²¹²Bi, ²¹²Pb, ²¹²Po]: A. Artna-Cohen, Nucl. Data Sheets **66**, 171 (1992).

[¹⁵⁴Eu]: R. G. Helmer, Nucl. Data Sheets **69**, 507 (1993).

[¹²⁵Sb]: J. Katakura, M. Oshima, K. Kitao, and H. Iimura, Nucl. Data Sheets **70**, 217 (1993).

[²⁰⁸Tl]: M. J. Martin, Nucl. Data Sheets **47**, 797 (1986).

[²²⁴Ra, ²²⁰Rn, ²²⁸Th]: M. J. Martin, Nucl. Data Sheets **49**, 83 (1986).

[¹⁵²Eu]: L. K. Peker, Nucl. Data Sheets **58**, 93 (1989).

[¹³³Ba]: S. Rab, Nucl. Data Sheets **75**, 491 (1995).

[¹⁵⁵Eu]: C. W. Reich, Nucl. Data Sheets **71**, 709 (1994).

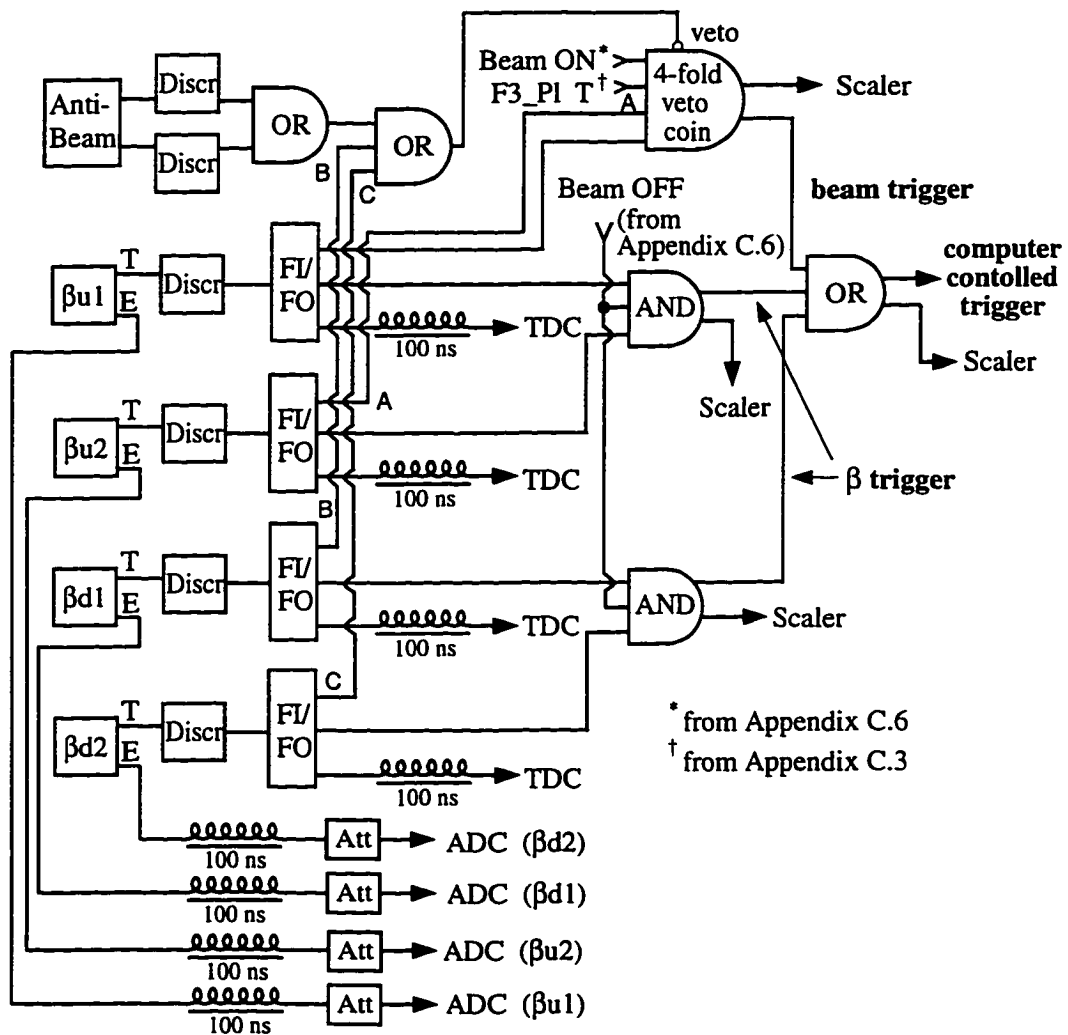
[¹³⁷Cs]: J. K. Tuli, Nucl. Data Sheets **72**, 355 (1994).

[²¹⁴Bi, ²¹⁴Pb]: Y. A. Akovali, Nucl. Data Sheets **76**, 127 (1995).

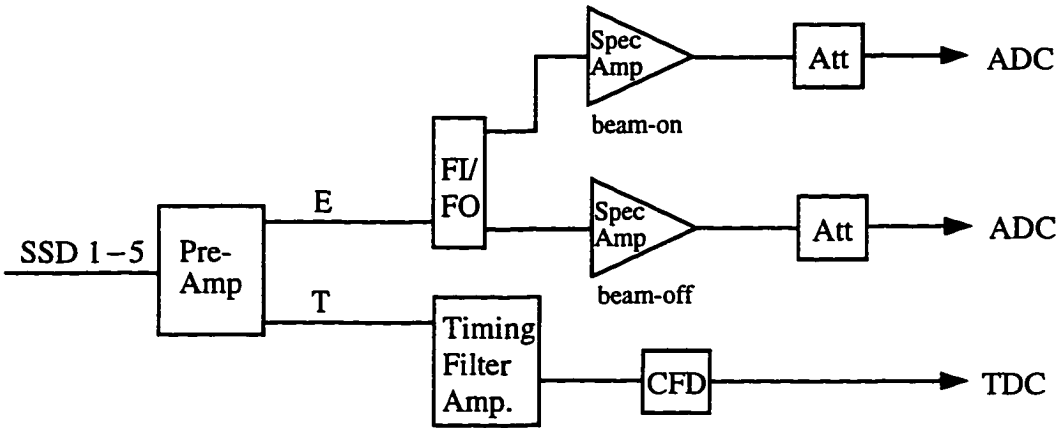
[⁴⁰K]: P. M. Endt, Nucl. Phys. A **521**, 1 (1990).

APPENDIX C
ELECTRONICS DIAGRAMS OF THE RIKEN EXPERIMENT

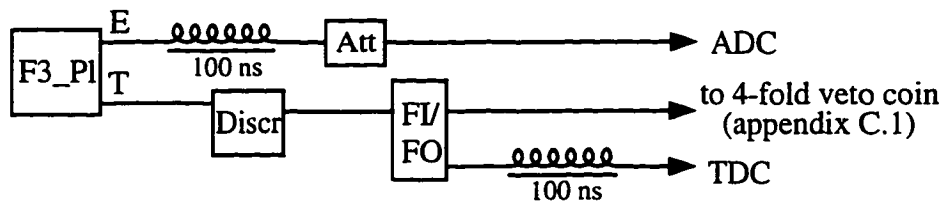
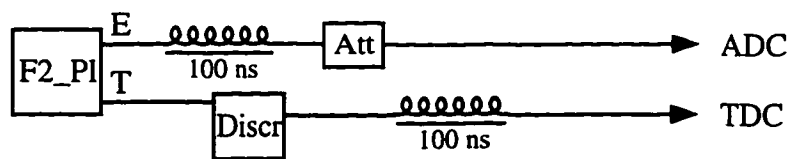
C.1 ELECTRONICS DIAGRAM FOR START (BETA) DETECTORS



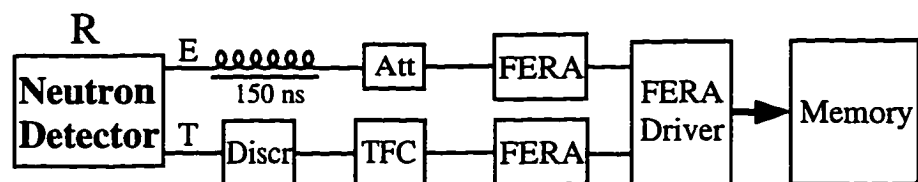
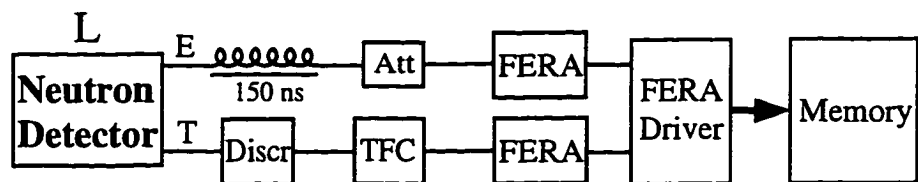
C.2 ELECTRONICS DIAGRAM FOR THE SSD STACK



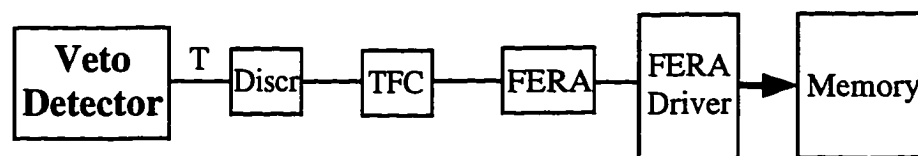
C.3 ELECTRONICS ASSOCIATED WITH F2 AND F3 SCINTILLATORS



C.4 ELECTRONICS ASSOCIATED WITH NEUTRON AND VETO DETECTORS

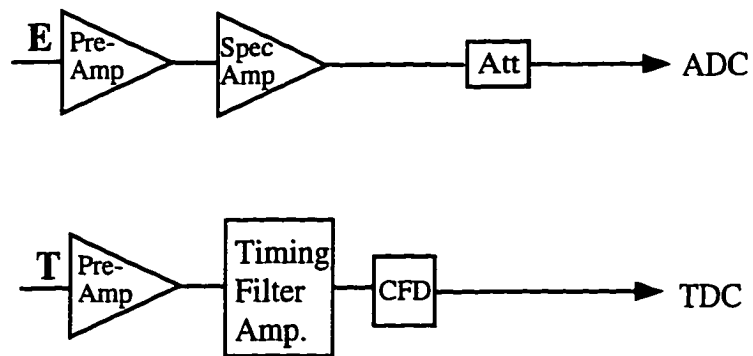


No. 1-16
Walls 1-4

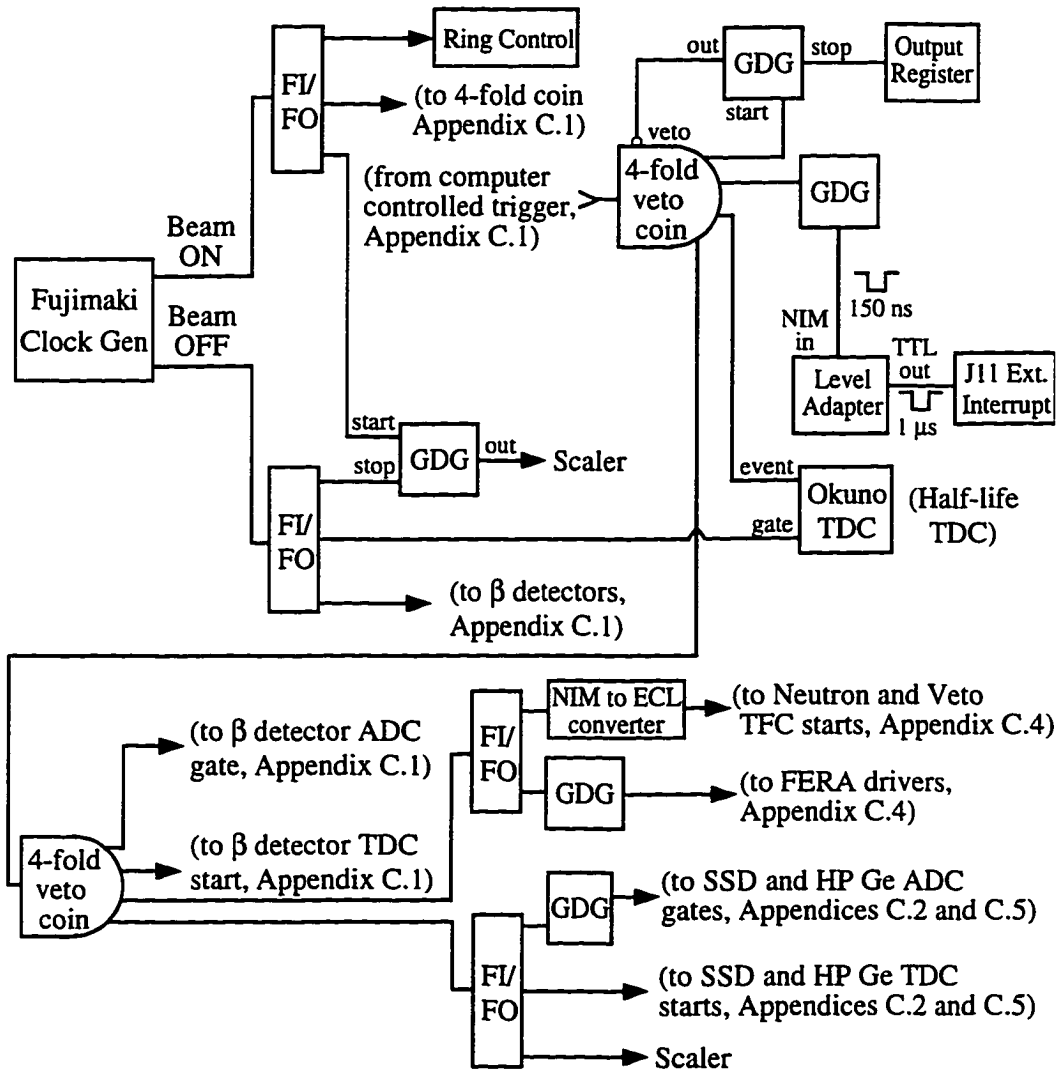


No. 1-10
Walls 1-3

C.5 ELECTRONICS ASSOCIATED WITH HP Ge DETECTOR



C.6 ELECTRONICS ASSOCIATED WITH BEAM-ON AND -OFF SIGNALS



C.7 DEFINITION OF NEW TERMS USED IN APPENDIX C

Att	– attenuator
β_d	– beta downstream detector
β_u	– beta upstream detector
Coin	– coincidence
Ext	– external
FERA	– Fast Encoding and Readout ADC
F2_P1	– Focus 2 plastic scintillator
F3_P1	– Focus 3 plastic scintillator
TFC	– time to FERA converter
Ring Control	– Ring Cyclotron RF control

NOTE: See A.7 for definition of other terms.

REFERENCES

- [Ab65] M. Abramowitz and I.A. Stegun, *Handbook of Mathematical Functions* (Dover, New York, 1965).
- [Aj81] F. Ajzenberg-Selove, Nucl. Phys. **A360**, 1 (1981).
- [Aj82] F. Ajzenberg-Selove, Nucl. Phys. **A375**, 1 (1982).
- [Aj88] F. Ajzenberg-Selove, Nucl. Phys. **A490**, 1 (1988).
- [Aj90] F. Ajzenberg-Selove, Nucl. Phys. **A506**, 1 (1990).
- [Aj91] F. Ajzenberg-Selove, Nucl. Phys. **A523**, 1 (1991).
- [Aj93] F. Ajzenberg-Selove, Nucl. Phys. **A564**, 1 (1993).
- [Al74] D.E. Alburger and D.R. Goosman, Phys. Rev. C **10**, 912 (1974).
- [Ao96] N. Aoi, K. Yoneda, H. Miyatake, H. Ogawa, Y. Yamamoto, E. Ideguchi, T. Kishida, T. Nakamura, M. Notanim H. Sakurai, T. Teranishi, S.S. Yamamoto, Y. Watanabe, A. Yoshida, and M. Ishihara, *RIKEN Accelerator Progress Report 1995* **29**, 67 (1996), unpublished.
- [Au93] G. Audi and A. H. Wapstra, Nucl. Phys. **A565**, 1 (1993).
- [Aw83] T.C. Awes, computer program STOPX, Oak Ridge National Laboratory (1983).
- [Be69] P.R. Bevington, *Data Reduction and Error Analysis for the Physical Sciences* (McGraw-Hill, New York, 1969).
- [Be92] P.R. Bevington and D. Keith Robinson, *Data Reduction and Error Analysis for the Physical Sciences*, 2nd. Ed., (McGraw-Hill, Inc., New York, 1992) p. 146.
- [Be92b] M. Belbot, computer program GRAPH, University of Notre Dame (1992), unpublished.

[Be95] M. Belbot, J.J. Kolata, K. Lamkin, R.J. Tighe, M. Zahar, R. Harkewicz, D. J. Morrissey, N.A. Orr, R. M. Ronningen, B.M. Sherrill, J.A. Winger, M. Carpenter, *Phys. Rev. C* **51**, 2372 (1995).

[Bi90] Bicron Corporation product catalog, (1990), unpublished.

[Bo69] A. Bohr and B.R. Mottelson, *Nuclear Structure*, vol. 1 (W.A. Benjamin, Inc., 1969, New York), p. 190.

[Bo73] J.D. Bowman, A.M. Poskanzer, R.G. Koteling, and G.W. Butler, *Phys. Rev. Lett.* **31**, 614 (1973).

[Br96] B. A. Brown, private communication.

[Ca90] R.F. Casten, *Nuclear Structure from a Simple Perspective* (New York, Oxford University Press, 1990), p. 47–137.

[Ce79] R.A. Cecil, B.D. Anderson and R. Madey, *Nucl. Instr. and Meth.*, **161**, 439 (1979).

[Cu85] M.S. Curtin, Ph.D. thesis, Michigan State University (1985), unpublished; B.A. Brown, private communication.

[Cu86] M.S. Curtin, L.H. Harwood, J.A. Nolen, B. Sherrill, Z.Q. Xie, and B.A. Brown, *Phys. Rev. Lett.* **56**, 34 (1986).

[de88] D. de Frenne, E. Jacobs, M. Verboven, G. de Smet, *Nucl. Data Sheets* **53**, 73 (1988).

[Di93] S. Dixit, Ph.D. thesis, University of Notre Dame (1993), unpublished.

[Du86] J.P. Dufour, R. Del Moral, H. Emmermann, F. Hubert, D. Jean, C. Poinot, M.S. Pravikoff, A. Fleury, H. Delagrangé, K.H. Schmidt, *Nucl. Instrum. Methods A* **248**, 267 (1986).

[Du88] J.P. Dufour, R. Del Moral, F. Hubert, D. Jean, M.S. Pravikoff, A. Fleury, A.C. Mueller, K.-H. Schimdt, K. Summerer, E. Hanelt, J. Frehaut, G. Giraudet, *Phys. Lett. B* **206**, 195 (1988).

[Go71] N. B. Gove and M. J. Martin, *Nucl. Data Tables*, **10**, 205 (1971).

[Go87] Goodfellow product catalog, no. 8, p. 73 (1987/88), unpublished.

[Ha79] M.L. Halbert, *Nucl. Data Sheets* **28**, 179 (1979).

[Ha91] R. Harkewicz, D.J. Morrissey, B.A. Brown, J.A. Nolen, Jr., N.A. Orr, B.M. Sherrill, J.S. Winfield, and J.A. Winger, *Phys. Rev. C* **44**, 2365 (1991); R. Harkewicz, Ph. D. thesis, Michigan State University (1992), unpublished.

[Ke81] J. Kelley, computer program ALLFIT, Massachusetts Institute of Technology, (1981), unpublished.

[Ki93] T. Kishida, T. Nakamura, G. Liu, Y. Watanabe, A. Yoshida, N. Aoi, M. Hirai, M. Ishihara, H. Okuno, H. Sakurai, T. Teranishi, H. Miyatake, T. Shirakura, E. Ideguchi, S. Shimoura, S.S. Yamamoto, M.D. Belbot, J.J. Kolata, M. Zahar, *RIKEN Accelerator Progress Report 1993* **27**, 46 (1994), unpublished.

[Kn79] G.F. Knoll, *Radiation Detection and Measurement*, (John Wiley and Sons, New York, 1979) p. 42.

[Kn79b] G.F. Knoll, *Radiation Detection and Measurement*, p. 50.

[Kn79c] G.F. Knoll, *Radiation Detection and Measurement*, p. 99.

[Kn79d] G.F. Knoll, *Radiation Detection and Measurement*, p. 449.

[Kn79e] G.F. Knoll, *Radiation Detection and Measurement*, p. 96.

[Kn79f] G.F. Knoll, *Radiation Detection and Measurement*, p. 97.

[Kr88] K.S. Krane, *Introductory Nuclear Physics* (John Wiley and Sons, New York, 1988), p. 275–295.

[Kr88b] K.S. Krane, *Introductory Nuclear Physics*, p. 297.

[Kr88c] K.S. Krane, *Introductory Nuclear Physics*, p. 116–125.

[Kr88d] K.S. Krane, *Introductory Nuclear Physics*, p. 25–38.

[Kr88e] K.S. Krane, *Introductory Nuclear Physics*, p. 121.

[Kr88f] K.S. Krane, *Introductory Nuclear Physics*, p. 123.

[Kr88g] K.S. Krane, *Introductory Nuclear Physics*, p. 294.

[Kr88h] K.S. Krane, *Introductory Nuclear Physics*, p. 388–392.

[Kr88i] K.S. Krane, *Introductory Nuclear Physics*, p. 44–59.

- [Ku64] R.J. Kurz, Lawrence Radiation Laboratory Report No. UCRL-11339, (1964), unpublished.
- [Ku92] T. Kubo, M. Ishihara, N. Inabe, H. Kumagi, I. Tanihata, K. Yoshida, T. Nakamura, H. Okuno, S. Shimoura, K. Asahi, Nucl. Instrum. Methods B **70**, 309 (1992).
- [La80] R.D. Lawson, *Theory of the Shell Model* (Oxford University Press, Oxford, 1980).
- [Le] "CAMAC Model 4301 Fast Encoding and Readout ADC (FERA) System Driver User's Manual", Lecroy Corporation operator's manual, unpublished.
- [Le85] "CAMAC Model 4300B 16 Channel, Fast Encoding and Readout ADC (FERA)", Lecroy Corporation product documentation (1985), unpublished.
- [Le87] W.R. Leo, *Techniques for Nuclear and Particle Physics Experiments*, (Springer-Verlag, Berlin, 1987), p. 40.
- [Le87b] W.R. Leo, *Techniques for Nuclear and Particle Physics Experiments*, p.81.
- [Le87c] "ECLine Programmable Trigger Product Summary", Lecroy Corporation (1987), unpublished.
- [Li91] D.R. Lide, ed., *CRC Handbook of Chemistry and Physics*, 72nd ed., (CRC press, Boca Raton, 1991) p. 14-19.
- [Li91b] D.R. Lide, ed., *CRC Handbook of Chemistry and Physics*, 72nd ed., p. 4-94.
- [Ma63] D.W. Marquardt, J. Soc. Ind. Appl. Math. **11**, 431 (1963).
- [Ma69] P. Marmier and E. Sheldon, *Physics of Nuclei and Particles* (Academic Press, New York, 1969), p. 372.
- [Mi75] D.J. Millener and D. Kurath, Nucl. Phys. **A255**, 315 (1975).
- [Mi88] D. Mikolas, B.A. Brown, W. Beneson, L.H. Harwood, E. Kashy, J.A. Nolen, Jr., B. Sherrill, J. Stevenson, J.S. Winfield, Z.Q. Xie, and R. Sherr, Phys. Rev. C, **37**, 766 (1988).
- [Mo93] D.J. Morrissey (1993), unpublished.
- [Mo96] D.J. Morrissey, K.N. McDonald, D. Bazin, B.A. Brown, R. Harkewicz, N. A. Orr, B.M. Sherrill, G. A. Souliotis, M. Steiner, J.A. Winger, S.J. Yennello, B.M. Young, S. Lukyanov, G. Chubarian, Yu.Ts. Oganessian, "Single Neutron Emission Following ^{11}Li β -Decay", submitted to Phys. Rev. C, (1996).

- [Na88] National Institute of Standards and Technology Certificate of Standard Reference Material, SRM 4275C-69.
- [Oh76] H. Ohm, W. Rudolph, K.-L. Kratz, Nucl. Phys., **A274**, 45 (1976).
- [Or73] "Ortec RC014 Real Time Clock Technical Data Sheet", EG&G/Ortec, May 1973.
- [Pa72] L. Pages, E. Bertel, H. Joffre, and L. Sklavenitis, At. Data **4**, 1 (1972).
- [Pr86] W.H. Press, B.P. Flannery, S.A. Teukolsky, W.T. Vetterling, *Numerical Recipes: The Art of Scientific Computing*, (Cambridge University Press, Cambridge, 1986) p. 507.
- [Ra75] S. Raman, T.A. Walkiewicz, H. Behrens, At. Data Nucl. Data Tables, **16**, 451 (1975).
- [Ra96] G. Raimann, A. Ozawa, R.N. Boyd, F.R. Chloupek, M. Fujimaki, K. Kimura, T. Kobayashi, J. J. Kolata, S. Kubono, L. Tanihata, Y. Watanabe, K. Yoshida, Phys. Rev. C, **53**, 453 (1996).
- [Sa85] J.J. Sakurai, *Modern Quantum Mechanics* (Addison-Wesley Publishing Company, Inc., Redwood City, California, 1985), p. 203–217.
- [Sc92] K.W. Scheller, private communication.
- [Sc94] K.W. Scheller, J. Görres, J.G. Ross, M. Wiescher, R. Harkewicz, D.J. Morrissey, B.M. Sherrill, M. Steiner, N.A. Orr, and J.A. Winger, Phys. Rev. C **49**, 46(1994); K.W. Scheller, Ph. D. thesis, University of Notre Dame, 1993, unpublished.
- [Sh91] B.M. Sherrill, D.J. Morrissey, J.A. Nolen, Jr., and J.A. Winger, Nucl. Instr. and Meth. in Phys. Res. B, **56/57**, 1106 (1991).
- [Si76] R. Singh, Nucl. Instrum. Methods **136**, 543 (1976).
- [Sw58] N.V.V.J. Swamy and A.E.S. Green, Phys. Rev. **112**, 1719 (1958).
- [Ta72] K. Takahashi, Prog. Theor. Phys. **47**, 1500 (1972).
- [Ti87] D.R. Tilley, H.R. Weller, and H.H. Hasan, Nucl. Phys. **A474**, 1 (1987).
- [To71] I.S. Towner, E.K. Warburton, G.T. Garvey, Ann. Phys. **66**, 674 (1971).

[Tu92] P.J. Turner, computer program XVGR, version 2.09, Oregon Graduate Institute of Science and Technology, Software Documentation Series, SDS3, 91-3 (1992), unpublished.

[US52] U.S. Department of Commerce, National Bureau of Standards Applied Mathematics Series, vol. 13, Tables for the Analysis of Beta Spectra, (United States Government Printing Office, Washington, 1952), p. 1.

[Wa92] E.K. Warburton and B.A. Brown, Phys. Rev. C, **46**, 923.

[Wa94] Waterloo Maple Software, computer program MAPLE v, Release 3 SUN SPARC SOL23, University of Waterloo (1994).

[Wi74] D.H. Wilkinson and B.E.F. Macefield, Nucl. Phys. **A232**, 58 (1974).

[Wi77] L. Wielopolski, Nucl. Instrum. Methods **143**, 577 (1977).

[Wi84] L. Wielopolski, Nucl. Instrum. Methods **226**, 436 (1984).

[Wi86] M. Weissbluth, *Atoms and Molecules*, 2nd. Ed. (Academic Press, Inc., San Diego, 1978), p. 80–87.

[Wi92] J.A. Winger, B.M. Sherrill, D.J. Morrissey, Nucl. Instrum. Meth. Phys. Res. **B70**, 380 (1992).

[Wo54] R.D. Woods and D.S. Saxon, Phys. Rev. **95**, 577 (1954).

[Ya88] Y. Yano, in Twelfth International Conference on Cyclotrons and Their Applications, Berlin, Germany, edited by B. Martin and K. Ziegler (World Scientific, Singapore, 1991) p. 13.

[Yo96] K. Yoneda, N. Aoi, H. Miyatake, H. Ogawa, Y. Yamamoto, E. Ideguchi, T. Kishida, T. Nakamura, M. Notani, H. Sakurai, T. Teranishi, S.S. Yamamoto, Y. Watanabe, A. Yoshida, and M. Ishihara, *RIKEN Accelerator Progress Report 1995* **29**, 182 (1996), unpublished.

[Zi80] J.F. Ziegler, *The Stopping Powers and Ranges of Ions in Matter*, vol. 3 and 5 (Peragamon Press, New York, 1980).